Department of Chemical and Metallurgical Engineering

Hydrogen supply in proton exchange membrane fuel cell systems

Kaj Nikiforow

Aalto University

DOCTORAL DISSERTATIONS

Aalto University publication series
DOCTORAL DISSERTATIONS 110/2018
VTT SCIENCE 177

Hydrogen supply in proton exchange membrane fuel cell systems

Kaj Nikiforow

A doctoral dissertation completed for the degree of Doctor of Science (Technology) to be defended, with the permission of the Aalto University School of Chemical Engineering, at a public examination held at the lecture hall Ke2 of the school on 8th June 2018 at 12.

Aalto University
School of Chemical Engineering
Department of Chemical and Metallurgical Engineering
Chemical engineering research group

Supervising professor
Professor Ville Alopaeus, Aalto University, Finland

Thesis advisor
Dr. Jari Ihonen, VTT Technical Research Centre of Finland Ltd, Finland

Preliminary examiners
Associate professor Masoud Rokni, Technical University of Denmark, Denmark
Associate professor Karl Erik Birgersson, National University of Singapore, Singapore

Opponent
Professor Göran Lindbergh, KTH Royal Institute of Technology, Sweden

Aalto University publication series
DOCTORAL DISSERTATIONS 110/2018

VTT SCIENCE 177

ISBN 978-952-60-8029-1 (printed)
ISBN 978-952-60-8030-7 (pdf)
ISSN 1799-4934 (printed)
ISSN 1799-4942 (pdf)
http://urn.fi/URN:ISBN:978-952-60-8030-7

ISBN 978-951-38-8642-4 (printed)
ISBN 978-951-38-8641-7 (pdf)
ISSN 2242-119X (printed)
ISSN 2242-1203 (pdf)
http://urn.fi/URN:ISBN:978-951-38-8641-7

Unigrafia Oy
Helsinki 2018

Finland

441 697
Printed matter

Aalto University

Abstract

Aalto University, P.O. Box 11000, FI-00076 Aalto www.aalto.fi

Author
Kaj Nikiforow

Name of the doctoral dissertation
Hydrogen supply in proton exchange membrane fuel cell systems

Publisher School of Chemical Engineering

Unit Department of Chemical and Metallurgical Engineering

Series Aalto University publication series DOCTORAL DISSERTATIONS 110/2018

Field of research Chemical Engineering

Manuscript submitted 1 February 2018 **Date of the defence** 8 June 2018

Permission to publish granted (date) 24 April 2018 **Language** English

☐ **Monograph** ☒ **Article dissertation** ☐ **Essay dissertation**

Abstract

Proton exchange membrane fuel cells (PEMFCs) are a fuel cell type that operate at low temperature and are commonly fueled with hydrogen gas. A PEMFC is seen as a promising power source for various applications including road vehicles, marine vessels, backup power, and grid balancing. Commercial PEMFC products are already available. The main factors limiting their widespread use are the lack of an extensive hydrogen distribution network, their price, and their durability.

To work efficiently, a PEMFC requires a set of components for fuel supply, oxidant supply, and cooling. This set of components is called the balance of plant (BoP). The PEMFC and the BoP together form a PEMFC system. The BoP contributes to a substantial fraction of the total system price and considerably affects system performance and durability.

This thesis examines the hydrogen supply in PEMFC systems with electrical power in the range 5 to 50 kW. In particular, components and methods for realizing hydrogen purge, hydrogen humidification, and hydrogen recirculation are evaluated theoretically and experimentally. Effort is put on examining solutions that improve system efficiency and durability while decreasing cost.

Hydrogen purge is a widely used approach for removing impurities and liquid water from a dead-end anode. In this work, methods for determining PEMFC membrane permeability, fuel purity, as well as the amount and composition of purged gas are developed and demonstrated. These methods can be used as inidicators of fuel supply or PEMFC system malfunctioning. Further, the effects of hydrogen purge on an 8 kW PEMFC system performance are studied by varying the cathode inlet humidity. Results show that PEMFC stack efficiency improves by 0.7% when increasing cathode inlet dew point temperature from 52 °C to 58 °C. The role of the purge shifts at these high-humidity conditions from impurity removal towards liquid water removal.

A humidifier can be employed to increase the anode inlet gas humidity and, consequently, to increase the PEMFC efficiency and durability. In this work, a bubble humidifier for a 50 kW PEMFC pilot plant using PEMFC stack waste heat is modelled and characterized. One commonly cited disadvantage of a bubble humidifier is the high hydrostatic pressure drop. The modelling results suggest that efficient humidification is achieved with only 5 mbar hydrostatic pressure drop.

Hydrogen recirculation is commonly applied to increase the gas flow velocity in a PEMFC. Ejectors have attracted attention because of their low price and high durability compared to mechanical pumps. However, ejector sizing and control still lack established methods. In this work, a 2-dimensional (2D) computational fluid dynamics (CFD) modelling approach for ejectors is validated against experimental data using three different turbulence models. In addition, a discrete control system for ejector is developed. Finally, the low-price and robust combination of a single fixed geometry ejector and a discrete control system is tested with a 5 kW PEMFC system by performing load transients from 2 kW to 4 kW within a fraction of a second.

Keywords PEMFC, hydrogen purge, hydrogen humidification, hydrogen recirculation

ISBN (printed) 978-952-60-8029-1 **ISBN (pdf)** 978-952-60-8030-7

ISSN (printed) 1799-4934 **ISSN (pdf)** 1799-4942

Location of publisher Helsinki **Location of printing** Helsinki **Year** 2018

Pages 192 **urn** http://urn.fi/URN:ISBN:978-952-60-8030-7

Tekijä
Kaj Nikiforow

Väitöskirjan nimi
Vedynsyöttö protoninvaihtopolttokennojärjestelmissä

Julkaisija Kemian tekniikan korkeakoulu

Yksikkö Kemian tekniikan ja metallurgian laitos

Sarja Aalto University publication series DOCTORAL DISSERTATIONS 110/2018

Tutkimusala Kemian laitetekniikka

Käsikirjoituksen pvm 01.02.2018 **Väitöspäivä** 08.06.2018

Julkaisuluvan myöntämispäivä 24.04.2018 **Kieli** Englanti

☐ **Monografia** ☒ **Artikkeliväitöskirja** ☐ **Esseeväitöskirja**

Tiivistelmä

Protoninvaihtopolttokenno (PEMFC) on polttokennotyyppi, joka toimii matalassa lämpötilassa ja käyttää polttoaineena vetykaasua. PEMFC:tä pidetään lupaavana teholähteenä moneen sovellukseen, mm. tieliikenteeseen, laivoihin, varavoimasovelluksiin ja sähköverkon vakautukseen. Kaupallisia tuotteita on jo saatavilla. Tärkeimmät PEMFC:iden yleistymistä rajoittavat tekijät ovat kattavan vetyjakeluverkoston puuttuminen sekä PEMFC:iden hinta ja kestävyys.

Toimiakseen tehokkaasti, PEMFC tarvitsee joukon komponentteja polttoaineensyöttöön, hapettimensyöttöön ja jäähdytykseen. Näistä komponenteista käytetään englanninkielistä nimitystä balance of plant (BoP). Yhdessä PEMFC:n kanssa BoP-komponentit muodostavat PEMFC-järjestelmän. BoP-komponentit muodostavat merkittävän osan PEMFC-järjestelmän hinnasta ja ne vaikuttavat keskeisesti PEMFC-järjestelmän suorituskykyyn ja kestävyyteen.

Tässä väitöskirjassa tarkastellaan vedyn syöttöä 5-50 kW PEMFC-järjestelmissä. Erityisesti arvioidaan teoreettisesti ja kokeellisesti komponentteja ja menetelmiä vetyhuuhtelun, vedyn kostutuksen ja vedyn kierrätyksen toteuttamiseksi. Pyrkimyksenä on tarkastella ratkaisuja, jotka parantavat järjestelmän hyötysuhdetta ja kestävyyttä mutta laskevat sen hintaa.

Vetyhuuhtelua käytetään poistamaan epäpuhtauksia ja nestemäistä vettä anodilta umpiperäisissä järjestelmissä. Tässä työssä kehitetään menetelmiä, joilla PEMFC:n membraanin kaasunläpäisevyys, polttoaineen puhtaus sekä vetyhuuhtelun määrä ja koostumus pystytään määrittämään. Näitä menetelmiä voidaan käyttää vedynsyötön tai PEMFC-järjestelmän toimintahäiriön indikaattoreina. Lisäksi, vetyhuuhtelun vaikutuksia 8 kW PEMFC-järjestelmän suorituskykyyn tutkitaan varioimalla syötetyn ilman kosteutta. Tulokset osoittavat että PEMFC kennoston hyötysuhde paranee 0,7 % nostamalla ilman kastepiste 52 °C:sta 58 °C:een. Vetyhuuhtelun päätehtävä muuttuu korkealla kosteustasolla epäpuhtauksien poistamisesta nestemäisen veden poistamiseen.

PEMFC:lle syötettävä vety voidaan kostuttaa kostuttimen avulla ja siten parantaa PEMFC:n hyötysuhdetta ja kestävyyttä. Tässä työssä 50 kW PEMFC-järjestelmälle tarkoitettu ja sen hukkalämpöä käyttävä kuplakostutin karakterisoidaan ja mallinnetaan. Kuplakostuttimen merkittävimpänä haittana pidetään sen korkeaa hydrostaattista painehäviötä. Mallinnustulokset kuitenkin osoittavat, että tehokas kostutus voidaan saavuttaa vain 5 mbar hydrostaattisella painehäviöllä.

Vedyn kierrätystä käytetään PEMFC-järjestelmissä lisäämään kaasun virtausnopeutta virtauskanavissa. Mielenkiinto ejektoreita kohtaan on lisääntynyt sillä ne ovat halvempia ja kestävämpiä kuin mekaaniset pumput. Tässä työssä verrataan 2-uloitteisen numeerisen virtausdynamiikkamallin (CFD) ja kolmen eri turbulenssimallin ennusteita mittaustuloksiin. Lisäksi kehitetään diskreetti ejektorinsäätömenetelmä. Lopuksi diskreetin säätömenetelmän ja ejektorin yhdistelmää kokeillaan 5 kW PEMFC-järjestelmässä nostamalla PEMFC-järjestelmän sähköteho kahdesta neljään kilowattiin sekunnin murto-osassa.

Avainsanat PEMFC, vetyhuuhtelu, vedyn kostutus, vedyn kierrätys

ISBN (painettu) 978-952-60-8029-1 **ISBN (pdf)** 978-952-60-8030-7

ISSN (painettu) 1799-4934 **ISSN (pdf)** 1799-4942

Julkaisupaikka Helsinki **Painopaikka** Helsinki **Vuosi** 2018

Sivumäärä 192 **urn** http://urn.fi/URN:ISBN:978-952-60-8030-7

Preface

The work presented in this thesis was conducted at VTT Technical Research Centre of Finland Ltd during the years 2011-2013 and 2016-2018 and at Aalto University during the years 2013-2016. The work at VTT was conducted under the TopDrive and DuraDemo projects that were funded by Tekes (the Finnish Funding Agency for Innovation), the PEMBeyond project that was funded by the European Union's Seventh Framework Programme for research, technological development and demonstration, and the EL-TRAN project that was funded by the Academy of Finland. I would like to acknowledge the Graduate School of Chemical Engineering (GSCE), VTT, and the Walter Ahlström foundation for financial support, which has allowed me to concentrate on this thesis.

This thesis would not have been possible without the help of many people that I have had the opportunity to work with during the past seven years. For this, I would like to acknowledge them all.

Especially, I want to thank my supervisor, Professor Ville Alopaeus and my instructor, Dr. Jari Ihonen. Ville Alopaeus, with his proficiency in chemical engineering and his attention to details, has guided me through the process of thesis writing. Jari Ihonen's expertise in the field of proton exchange membrane fuel cells and his never-ending innovation of new ideas and solutions has provided me with an inspiring working environment.

I also want to thank my co-authors, technicians at VTT, and other colleagues both at VTT and at Aalto University, who have made this work possible.

Last but not least, I want to thank my family – my wife, my two sons, and my yet unborn daughter – for being there and counterbalancing my work.

Espoo, Finland, January 2, 2018

Kaj Nikiforow

Contents

List of Publications

This doctoral dissertation consists of a summary and the following publications, which are referred to in the text by Roman numerals.

I. H. Karimäki, L.C. Pérez, K. Nikiforow, T.M. Keränen, J. Viitakangas, J. Ihonen, J. 2011. The use of on-line hydrogen sensor for studying inert gas effects and nitrogen crossover in PEMFC system. Published in: International Journal of Hydrogen Energy, volume 36, issue 16, pages 10179-10187. ISSN: 0360-3199. DOI: 10.1016/j.ijhydene.2011.04.230.

II. K. Nikiforow, H. Karimäki, T.M. Keränen, J. Ihonen. 2013. Optimization study of purge cycle in proton exchange membrane fuel cell system. Published in: Journal of Power Sources, volume 238, pages 336-344. ISSN: 0378-7753. DOI: 10.1016/j.jpowsour.2012.11.153.

III. K. Nikiforow, J. Ihonen, T. Keränen, H. Karimäki, V. Alopaeus. 2014. Modeling and experimental validation of H_2 gas bubble humidifier for a 50 kW stationary PEMFC system. Published in: International Journal of Hydrogen Energy, volume 39, issue 18, pages 9768-9781. ISSN: 0360-3199. DOI: 10.1016/j.ijhydene.2014.04.058.

IV. K. Nikiforow, P. Koski, H. Karimäki, J. Ihonen, V. Alopaeus. 2016. Designing a hydrogen gas ejector for 5 kW stationary PEMFC system – CFD-modeling and experimental validation. Published in: International Journal of Hydrogen Energy, volume 41, issue 33, pages 14952-14970. ISSN: 0360-3199. DOI: 10.1016/j.ijhydene.2016.06.122.

V. K. Nikiforow, P. Koski, J. Ihonen. 2017. Discrete ejector control solution design, characterization, and verification in a 5 kW PEMFC system. Published in: International Journal of Hydrogen Energy, volume 42, issue 26, pages 16760-16772. ISSN: 0360-3199. DOI: 10.1016/j.ijhydene.2017.05.151.

VI. K. Nikiforow, J. Pennanen, J. Ihonen, S. Uski, P. Koski. 2018. Power ramp rate capabilities of a 5 kW proton exchange membrane fuel cell system with discrete ejector control. Published in: Journal of Power Sources, volume 381, pages 30-37. ISSN: 0378-7753. DOI: 10.1016/j.jpowsour.2018.01.090.

Author's Contribution

I: The use of on-line hydrogen sensor for studying inert gas effects and nitrogen crossover in PEMFC system

H. Karimäki took part in designing and building the PEMFC system, conducted system characterization, took part in inert buildup measurements, and was the main writer of the manuscript. L.C. Pérez took part in measurements and in writing the manuscript. K. Nikiforow took part in building the PEMFC system, in inert buildup measurements, and in reviewing the manuscript. T.M. Keränen, J. Viitakangas, and J. Ihonen took part in designing the PEMFC system and the experiments and reviewed the manuscript.

II: Optimization study of purge cycle in proton exchange membrane fuel cell system

K. Nikiforow took part in designing and modifying the PEMFC system, conducted the measurements, compiled and interpreted the results, and was the main writer of the manuscript. H. Karimäki took part in designing and modifying the PEMFC system, interpreting the results, and writing the manuscript. T.M. Keränen and J. Ihonen took part in designing the PEMFC system, interpreting the results, and reviewing the manuscript.

III: Modeling and experimental validation of H_2 gas bubble humidifier for a 50 kW stationary PEMFC system

K. Nikiforow was responsible for designing, characterizing, and modelling the bubble humidifier. K. Nikiforow also compiled and interpreted the results and was the main writer of the manuscript. J. Ihonen took part in designing the bubble humidifier, designing the experiments, interpreting the results, and reviewing the manuscript. T. Keränen and H. Karimäki took part in designing and characterizing the bubble humidifier, interpreting the results, and reviewing the manuscript. V. Alopaeus took part in interpreting the results and reviewing the manuscript.

IV: Designing a hydrogen gas ejector for 5 kW stationary PEMFC system – CFD-modeling and experimental validation

K. Nikiforow designed the ejector inner dimensions, participated in building the test setup, conducted the experiments, performed the CFD simulations, compiled the data, and was the main writer of the manuscript. P. Koski was responsible for ejector manufacturing and participated also in building the test setup,

in interpreting the results, and reviewing the manuscript. H. Karimäki, J. Ihonen, and V. Alopaeus took part in interpreting the results and reviewing the manuscript.

V: Discrete ejector control solution design, characterization, and verification in a 5 kW PEMFC system

K. Nikiforow designed the PEMFC system, took part in designing the ejector primary flow control solution (EPC), sized and tested the EPC, conducted the measurements, compiled the results, and was the main writer of the manuscript. P. Koski took part in the experimental work and in designing the EPC, in interpreting the results, and in reviewing the manuscript. J. Ihonen took part in designing the EPC and the experiments, in interpreting the results, and in reviewing the manuscript.

VI: Power ramp rate capabilities of a 5 kW proton exchange membrane fuel cell system with discrete ejector control

K. Nikiforow made the modifications to the PEMFC system and to the control software, conducted the experiments, compiled the experimental data, and was the main writer of the paper. J. Pennanen implemented the model, conducted the simulations, and compiled the simulation results. J. Ihonen took part in designing the experiments, in interpreting the results, and in writing the paper. S. Uski participated in writing the manuscript. P. Koski reviewed the manuscript.

List of Abbreviations and Symbols

Latin symbol	Explanation	Value/unit
A	Area	m^2
a_i	Activity of species i	-
b	Cell pressure drop coefficient	bar/(kg/s)
C_p	Isobaric heat capacity	J/(mol·K)
$\underline{C_i}$	Specific heat capacity of i	J/(kg·K)
c	Concentration	mol/m^3
D_i	Diffusion coefficient of i	m^2/s
d	Diameter	m
E	Voltage	V
e	Elementary charge	$1.6022 \cdot 10^{-19}$ C [1]
F	Faraday constant	96485 C/mol [1]
f_p	Purge fraction	-
Fo	Fourier number	-
ΔG	Gibbs energy change	J/mol
ΔH	Heat of combustion	J/mol
ΔH_{vap}	Heat of vaporization	J/mol
h	Heat transfer coefficient	$W/(m^2 \cdot K)$
I	Current	A
K_v	Flow coefficient	m^3/h
k	Thermal conductivity	$W/(m^2 \cdot K)$
M_w	Mole weight	kg/mol
m	Mass	kg

Latin symbol	Explanation	Value/unit
$\dot{m}$	Mass flow rate	kg/s
N_A	Avogadro constant	$6.0221 \cdot 10^{23}$ mol^{-1} [1]
N_i	Number of i	-
n	Amount of substance	mol
$\dot{n}$	Molar flow rate	mol/s
P	Power	W
p	Pressure	bar (=10^5 Pa)
p_i^{vap}	Vapor pressure of species i	bar (=10^5 Pa)
$\dot{Q}$	Heat transfer rate	W
q	Charge	C
R	Universal gas constant	8.3145 J/(mol·K) [1]
Re	Reynolds number	-
RH	Relative humidity	%
R_i	Heat transfer resistance	K/W
r	Radius	m
Sh	Sherwood number	-
T	Temperature	°C
T_{dew}	Dew point temperature	°C
t	Time	s
t_{lrf}	Load current ramp-up timing relative to fuel supply ramp-up	s
u_f	Fuel utilization	-
V	Volume	dm^3 (=10^{-3} m^3)
$\dot{V}$	Volume flow rate	nlpm (lpm @ NTP)
v	Velocity	m/s
W	Work	J
y_i	Gas phase mole fraction of species i	-
ΔZ	Height	m
z_i	Mole fraction of species i	-

Greek symbol	Explanation	Value/unit
Δ	Change in quantity	-
η	Efficiency	%
λ	Stoichiometric ratio	-
μ	Dynamic viscosity	Pa·s
ν_i	Stoichiometric coefficient of i	-
ρ	Density	kg/m^3
Ω	Ejector entrainment ratio	-

Subscript	Explanation
an	Anode
aq	Aqueous phase
b	Bubble
cat	Cathode
e	Electrical
ej	Ejector
f	Fuel
ff	Fuel feed stream
gas	Gas (phase)
h	Heating water
in	Inlet, inside
liq	Liquid (phase)
$meas$	Measured
out	Outlet, outside
p	Purge
p, in	Ejector primary inlet
pp	Per pass
r	Recirculated stream
ref	Reference
s	Stack

Subscript	Explanation
s, in	Ejector secondary inlet
sim	Simulated
tot	Total

Superscript	Explanation
$*$	Ideal gas
0	Standard conditions (T = 25 °C, p = 1 bar)

Abbreviation	Explanation
1D	One-dimensional
2D	Two-dimensional
3D	Three-dimensional
AC	Alternating current
AD	Mean absolute deviation (see Eq. 64)
BD	(Water) back-diffusion
BoP	Balance of plant
CFD	Computational fluid dynamics
DC	Direct current
DEA	Dead-end anode
DEFC	Direct ethanol fuel cell
DMFC	Direct methanol fuel cell
EOD	Electro-osmotic drag
EPC	Ejector-primary-gas-control-system
EVM	Eddy viscosity model
GDL	Gas diffusion layer
HOR	Hydrogen oxidation reaction
ICE	Internal combustion engine
LHV	Lower heating value
MEA	Membrane electrode assembly
NTP	Normal temperature (273.15 K) and pressure (1.01325 bar)

Abbreviation	Explanation
OCV	Open circuit voltage
ORR	Oxygen reduction reaction
PEMFC	Proton exchange membrane fuel cell (the single cell unless otherwise noted)
PFSA	Perfluorosulfonic acid
PV	Photovoltaic
RANS	Reynolds-averaged Navier–Stokes
RD	Mean relative deviation (see Eq. 65)

1. Introduction

Modern society relies on energy being available for transportation, industry and residential heating or cooling, among others. Along with increasing population and growing personal income, the energy demand is expected to increase [2].

Fossil fuels have fulfilled a large portion of our energy demand for several decades. The use of fossil fuels is, however, not sustainable because of their limited reserves and the emissions associated with them.

Interest in renewable and sustainable energy has increased in the past decades. The total renewable power capacity has increased by 150% from 800 GW in year 2004 to 2017 GW in year 2016. In the same period of time, the sum of solar (photovoltaic, PV) and wind power capacity increased more than 15 times from 50.6 GW to 790 GW. [3,4]

The power output of both PV and wind power plants depends on prevailing weather conditions. For this reason, power generation from these sources is unpredictable in the long term and is likely to mismatch with the demand for power. In addition, the electric grid is unevenly loaded from these sources, and, therefore, energy storage is needed. [2]

The concept of the Hydrogen economy was first published in 1972 [5]. The idea behind this concept is to found the energy infrastructure on hydrogen as energy storage [2]. The excessive energy from PV and wind power can be stored as hydrogen by splitting water with electrolysis, for example.

Fuel cells are devices that can convert the energy stored in hydrogen back to electricity while emitting only water and heat. Fuel cells have no moving parts in contrast to combustion engines, which makes their operation efficient and silent [6].

Proton exchange membrane fuel cells (PEMFCs) are one type of fuel cells especially suited for applications where rapid load changes are expected (e.g. automotive, grid balancing, backup power) [7]. PEMFCs are, however, still too expensive for large-scale commercialization, but research is ongoing to reduce their price [8].

PEMFCs, like other fuel cell types, require a set of system components for fuel supply, oxidant supply, and cooling, for example. This set of components is called the balance of plant (BoP), and it makes up a substantial fraction of the total system cost [9]. The purpose of the BoP is to ensure optimal operating conditions for the PEMFC. Thus, careful design of the BoP is a key to cost efficient and durable PEMFC systems.

1.1 Thesis objective

The primary task of a hydrogen supply system in a PEMFC is to deliver hydrogen to a fuel cell. Without a hydrogen supply, the PEMFC cannot operate. The hydrogen supply system also has secondary tasks, such as preventing the buildup of impurities (contaminants and inert gases), removing liquid water, humidifying the hydrogen, and recirculating hydrogen. These tasks are important for efficient and long lasting PEMFC operation. The objective of this thesis is to study devices and methods for hydrogen supply that could improve PEMFC system performance and durability.

Hydrogen purge is an efficient way of removing inert gases and other impurities as well as liquid water from an anode. However, it has not been clear how the anode inert gas content, system humidity level, and hydrogen purge parameters affect the PEMFC and fuel efficiencies. Methods for measuring the required quantities were developed, and the aforementioned questions were studied in publications [I] and [II].

Although hydrogen humidification adds system complexity and cost, it is often employed because it improves PEMFC efficiency. A bubble humidifier has a simple design and working principle and is, thus, a good humidifier candidate for PEMFC systems. However, downsides such as hydrostatic pressure drop and the lack of controllability are factors often considered to outweigh the benefits. In publication [III], a bubble humidifier was designed, characterized, and modelled, and improvements on its design and control were discussed.

Hydrogen recirculation is typically employed in PEMFC systems because it improves PEMFC performance. Mechanical pumps often employed for hydrogen recirculation have been proven too unreliable. Ejectors, on the other hand, are seen as promising devices for this application. However, the limited working range of ejectors and the challenges in ejector primary flow control are seen as factors limiting their usability. Publications [IV]-[VI] examined the possibility of using the simplest thinkable approach to hydrogen recirculation – a single ejector with discrete primary flow control.

1.2 Thesis structure

The thesis first gives a brief introduction to PEMFC technology and PEMFC systems in Chapter 2. Chapter 3 provides an overview of hydrogen supply in PEMFC systems and describes the three secondary tasks of the hydrogen supply system: hydrogen purge, hydrogen humidification, and hydrogen recirculation.

Chapters 4-6 discuss the three secondary tasks of hydrogen supply in more detail and present the methods employed and results obtained in publications [I]-[VI]. Chapter 4 focuses on inert buildup and hydrogen purge, which was studied experimentally in publications [I] and [II]. Chapter 5 presents design, characterization, and modelling of a bubble humidifier for hydrogen humidification based on publication [III]. Chapter 6 presents methods and results of the work done in publications [IV]-[VI], which targeted hydrogen recirculation with a single, fixed geometry ejector and a discrete primary flow control.

A summary of the results is given in Chapter 7. The publications that thesis is based on are attached at the end.

2. Background

This chapter introduces proton exchange membrane fuel cell (PEMFC) technology. The PEMFC itself is introduced in Section 2.1, and the auxiliary components needed for successful operation of a PEMFC, i.e. the PEMFC system, are introduced in Section 2.2.

2.1 Proton exchange membrane fuel cell

A PEMFC, like other types of fuel cells, is an electrochemical cell; it converts the chemical energy of a fuel to electricity. Its function, therefore, resembles that of a battery. The main difference between fuel cells and batteries is, however, that fuel and oxidant are continuously supplied to fuel cells whereas batteries are closed systems. Therefore, fuel cells can, in principle, output electrical energy as long as fuel and oxidant are supplied. In this sense, the function of fuel cells closely resembles that of internal combustion engines (ICEs). The main difference between ICEs and fuel cells is, however, that fuel cells do not output mechanical energy like ICEs but electrical energy.

This work focuses solely on PEMFCs although a number of other fuel cell types exist. An introduction to PEMFC structure, its working principle, and factors that affect PEMFC voltage, power, and efficiency follow. A key factor in PEMFC technology, namely water management, is introduced in Section 2.1.3.

2.1.1 Structure and working principle

The basic structure of a PEMFC is shown in Figure 1. It consists of a membrane electrode assembly (MEA), gas diffusion layers (GDLs), gaskets, and end plates sandwiched together. The MEA is a polymer membrane (electrolyte) with catalyst layers (electrodes) attached to both sides. To enable normal PEMFC operation, the polymer membrane should be 1) proton conductive, 2) impermeable to gases, and 3) an electrical insulator [10]. The purposes of the GDLs is to enable the transport of 1) reactant gases to the catalyst, 2) water away from the catalyst, and 3) heat and electrons from the catalyst to the end plate, and 4) to give mechanical support to the MEA [6]. The end plates provide mechanical support, function as electron conductors, and contain gas channels for distributing the reactants over the entire cell [10].

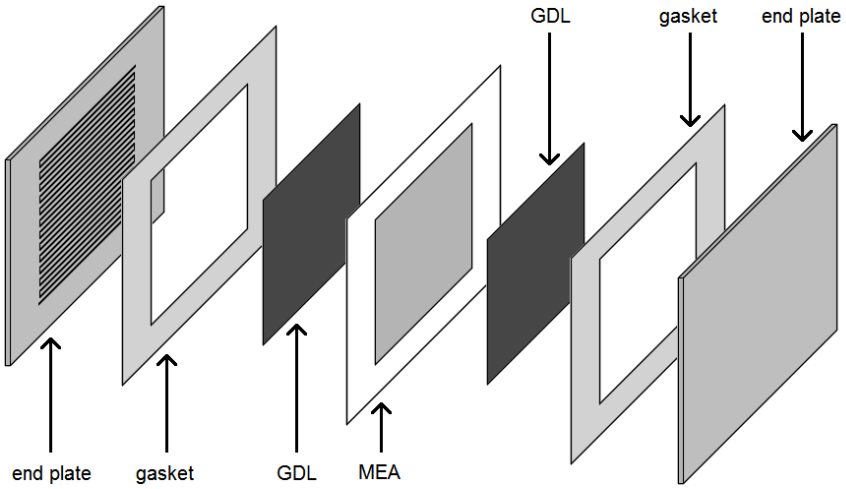

Figure 1. The structure of a PEMFC. The cell active area (gray area in MEA) is typically hundreds of cm^2 at most. The thickness of MEA is tens of micormeters while the thickness of the GDL is typically around 200 µm. Figure modified from [11].

Several PEMFCs can be connected electrically in series to form a PEMFC stack. The end plates between two adjacent cells then serve as both anodic and cathodic end plates and are called bipolar plates. Stacking cells together enables higher output voltages, as in batteries.

PEMFCs use pure hydrogen gas as the fuel. Hydrogen rich reformate gas can also be used as the fuel but, in that case, special attention is required because of the fuel's higher impurity content. Reformate gas typically contains at least the impurities CO_2 and CO but might also contain significant amounts of N_2, H_2O, and CH_4 depending on the fuel and production process [12–15]. Liquid fuels, such as methanol or ethanol, can also be used. However, in such a case, the fuel cell is called a direct methanol fuel cell (DMFC) or a direct ethanol fuel cell (DEFC).

Hydrogen is fed to the PEMFC on the anode side, where it transfers from the gas channels through the GDL to the anode catalyst sites (see Figure 2). The catalyst splits hydrogen into protons and electrons. The protons pass through the membrane to the cathode, and the electrons pass through an external circuit, thus producing an electrical current.

The oxidant used in PEMFCs is commonly air, but pure oxygen can also be used. Either way, the oxidant is fed to the cathode, and the oxygen transfers through the GDL to the cathode catalyst sites. At these sites, oxygen reacts with the protons and the electrons and water is produced. Depending on operating conditions, the water produced may transfer to the anode side or leave the cell with the oxidant stream as shown in Figure 2.

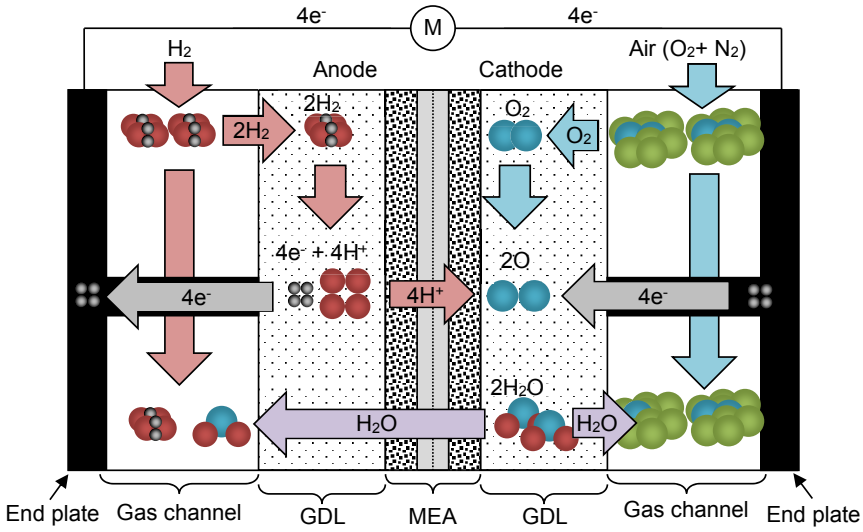

Figure 2. The reactions occurring and the transport of reactants and products in a PEMFC (single cell) when one oxygen molecule reacts with two hydrogen molecules and forms two molecules of water.

2.1.2 Current, voltage, power, and efficiency

The voltage of a PEMFC is a function of current drawn. Consequently, the output power is not a linear function of current, and the cell efficiency is not constant. This section briefly explains how cell current, voltage, power, and efficiency are interrelated.

The half-cell reactions (hydrogen oxidation reaction, HOR, and oxygen reduction reaction, ORR), the overall reaction, and the Gibbs energy changes at standard state (ΔG^0) per mole of water formed [16] are:

HOR: $H_2(gas) \rightarrow 2H^+(aq) + 2e^-$ $\Delta G^0 = 0 \frac{J}{mol}$ (1)

ORR: $½O_2(gas) + 2H^+(aq) + 2e^- \rightarrow H_2O(liq)$ $\Delta G^0 = -237140 \frac{J}{mol}$ (2)

Overall: $H_2(gas) + ½O_2(gas) \rightarrow H_2O(liq)$ $\Delta G^0 = -237140 \frac{J}{mol}$ (3)

The Gibbs energy change (ΔG) for a chemical reaction is [6]:

$$\Delta G = \Delta G^0 + R \cdot T \cdot ln \prod a_i{}^{\nu_i} \quad (4)$$

where a_i is the activity and ν_i is the stoichiometric coefficient of species i. For an ideal gas (denoted by superscript *) [6]:

$$a_i^* = \frac{p_i^*}{p^0} \quad (5)$$

The Gibbs energy change equals the maximum attainable work per mole (n) in a reaction. The electrical work (W_e) is obtained by multiplying the charge (q) by the voltage (E) [6]:

$$\Delta G = \frac{W_e}{n} = \frac{q \cdot E}{n} \tag{6}$$

The number of electrons transferred per molecule of water produced (according to Eq. 3) is 2. Thus, the charge transferred per mole water produced is:

$$\frac{q}{n} = 2 \cdot N_A \cdot (-e) = -2 \cdot F \tag{7}$$

where N_A is the Avogadro constant, e is the elementary charge, and F is the Faraday constant. Combining Eqs. 6 and 7 gives an equation for the reversible open circuit voltage (OCV) for a hydrogen fuel cell:

$$E = \frac{\Delta G}{-2 \cdot F} \tag{8}$$

Further, combining Eqs. 4 and 8 gives the Nernst equation:

$$E = E^0 - \frac{R \cdot T}{2 \cdot F} \cdot ln \frac{a_{H_2O}}{a_{H_2} \cdot a_{O_2}^{1/2}} \tag{9}$$

which relates the reversible OCV to the standard state reversible OCV (E^0), the temperature (T), and the activities (a_i).

The standard state reversible OCV can be calculated from the reaction Gibbs energy change at standard state ($\Delta G^0 = -237140\,\mathrm{J/mol}$): $E^0 = 1.229\,\mathrm{V}$. The actual OCV is notably lower (typically around 1.0 V) mainly because of hydrogen crossover [17] and internal currents [6]. Also the temperature and the reactant activities affect the reversible OCV, as seen in Eq. 9.

When current is drawn from a cell, the voltage drops further. This is called voltage polarization and is mainly caused by three types of irreversibilities or losses: activation losses, ohmic losses, and concentration losses [6]. Other commonly used terms for these irreversibilities include overpotential, overvoltage, or voltage drop. The aforementioned irreversibilities have their most pronounced influence on cell voltage at different current levels (Sections I, II, and III), which gives the cell voltage polarization curve its characteristic shape (Figure 3 a).

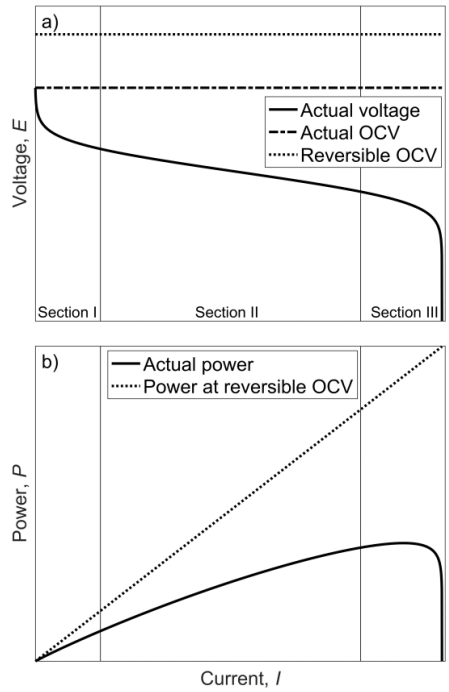

Figure 3. Typical PEMFC a) current-voltage (*I-E*) curve (also called polarization curve) and b) current-power (*I-P*) curve.

The activation losses in Section I cause a notable drop in cell voltage with increasing current. The activation losses are caused by reaction kinetic limitations. The activation loss of HOR is negligible compared to the activation loss of ORR in PEMFCs. [6]

The ohmic losses in Section II cause a nearly linear voltage drop with increasing current. The ohmic losses arise from the resistance of the electrolyte and the current carrying parts of the cell [6]. These resistances follow Ohm's law and, for that reason, have a linear relationship with current.

The mass transfer starts to limit the achievable current in Section III. The cell current-voltage behavior starts to deviate from the linear relationship, and, at some current, the cell voltage suddenly drops. This is the current that corresponds to the maximum mass transfer rate.

The PEMFC power output is:

$$P = I \cdot E \tag{10}$$

A typical PEMFC current-power (*I-P*) curve is shown in Figure 3 b. The power increases typically almost linearly with current in Sections I and II and is roughly half of the maximum power. In other words, the other half is converted into heat. In Section III, the mass transfer limited current is reached, and the power collapses.

Fuel cell efficiency (η_{cell}) is commonly related to the lower heating value (LHV) of hydrogen combustion at standard state:

$$H_2(gas) + ½O_2(gas) \rightarrow H_2O(gas) \quad \Delta H^0 = -241830 \frac{J}{mol} [16] \qquad (11)$$

and is defined as follows:

$$\eta_{cell} = \frac{\Delta G}{\Delta H^0} = \frac{E}{1.253\ V} \qquad (12)$$

Consequently, the shape of the current-efficiency curve is identical with the current-voltage (*I-E*) curve shown in Figure 3 a. At zero current, the maximum efficiency is obtained, but the power is zero.

2.1.3 Water management

Water management is a key factor for operating a PEMFC successfully. This is because the polymer membrane must be hydrated in order to be proton conductive. Water is formed in the cathode reaction, which, in principle, would suffice to keep the membrane hydrated. In practice, however, the water formed at the cathode is distributed unevenly within the cell.

The membrane in PEMFCs is most commonly made of perfluorosulfonic acid (PFSA) polymer [18,19]. In PFSA, sulphonated side chains form hydrophilic clusters, which absorb water. Within these hydrated regions and between them, protons are able to move, thus giving rise to proton conductivity. [6] Therefore, the membrane needs to be hydrated to be proton conductive. The higher the water content, the higher the membrane proton conductivity [6,20]. Dehydration decreases membrane conductivity, increases ohmic losses, and, subsequently, decreases PEMFC performance. [21]

When water is produced at the cathode, the membrane absorbs part of it while the rest of it eventually leaves the fuel cell with the cathode gas. Ideally the water formed in the reaction would suffice to maintain the membrane hydrated as the water absorbed by the membrane is not consumed. However, various water transport mechanisms cause the water to distribute unevenly within the cell.

The most important water transport mechanisms are electro-osmotic drag (EOD), back-diffusion (BD), and convection. Pressure and temperature differences also cause water transport. [19]

EOD is a result of protons moving from the anode towards the cathode and dragging along water molecules [19]. Thus, the EOD is always in the direction away from the anode towards the cathode. As a result of EOD and water generation, water builds up at the cathode while the anode remains drier. The concentration difference tends naturally to even out by diffusion. This form of water transport is called back-diffusion [19].

Convective water transport act along cell in contrast to the other water transport mechanisms. Dry reactant gases fed to the cell will dry out the cell inlet. Water will condense at the end of the cell when the reactant gas flow has

become saturated. [6] If the liquid water is not removed, it will buildup and prevent reactant gases from reaching the reaction site – a condition called flooding [21,22].

Water generation at the cathode and the various water transport mechanisms (mainly EOD and convective water transport) result in uneven water distribution within the cell unless care is taken. One part of the cell may suffer from dehydration while another part floods. Particularly at high current density levels, the cathode water concentration will increase due to water generation, and the anode may be dehydrated due to the EOD [21].

Both flooding and membrane dehydration should be avoided throughout the cell. Flooding prevents reactants from reaching the reaction sites and, therefore, causes a performance decrease and possibly permanent damage to the PEMFC [23]. As a consequence of water generation, the EOD, and the reactant gas flows, flooding is more likely to occur at the cathode close to cell outlet, but anode flooding is also possible [I,II]. Membrane dehydration, on the other hand, besides decreasing PEMFC performance through decreased proton conductivity, also speeds up membrane aging [23].

Theory and practice have shown that membrane dehydration in PEMFCs cannot be avoided at operating temperatures above approximately 60°C without external humidification. Because of this and because more humid operating conditions result in better performance, external humidification is commonly employed. [6,24] Reactant gas inlet humidities should, however, be controlled to avoid flooding in the cell.

2.2 Proton exchange membrane fuel cell system

PEMFC stacks in operation consume reactants and produce heat. The reactants typically need to be humidified before entering the PEMFC stack. Therefore, equipment for preparing and feeding the reactants and for removing heat is needed. This equipment together with the PEMFC stack forms a PEMFC system.

PEMFC systems can be classified according to their reactant pressure level, operating temperature level, fuel supply method, and oxidant supply method (see Table 1). Pressurizing reactants not only improves PEMFC performance (see Nernst equation, Eq. 9) but also consumes energy and adds system complexity [25]. This work focuses on non-pressurized systems.

Table 1. PEMFC system classifications.

Factor	*Classification*
Operating pressure	Non-pressurized (~0-0.3 barg) / Pressurized (~0.5-2 barg)
Operating temperature	Low (< 50 °C) / Moderate (50-80 °C) / High (> 80 °C)
Fuel supply	Open anode / Dead-end anode (with or without recirculation)
Oxidant supply	Free-breathing / Forced convection

PEMFC stack performance improves with increasing temperature through the improved reaction kinetics [6,26]. However, maintaining the electrolyte suffi-

ciently hydrated at elevated temperatures is challenging [6], and a PEMFC performance decrease associated with dehydration is possible. The focus of this work is on PEMFC systems operating at moderate (50-80 °C) temperatures.

Fuel can be supplied to a PEMFC stack in open anode mode or in dead-end anode (DEA) mode. In open anode mode, the fuel is fed in excess and the not utilized fuel is vented out. This mode is employed mainly in test setups and when reformate gas is used as fuel. In the DEA mode, the anode outlet is closed with a valve, and the PEMFC stack is fed with the amount fuel that is utilized. With time, impurities enrich in the anode, and a hydrogen purge (also called anode purge) must be performed (i.e. the anode outlet valve is opened) to remove the impurities. Alternatively, a bleed valve can be employed to pass a small bleed stream that prevents impurities from enriching. Conceptually, the bleed valve does not differ from open anode operation. Hydrogen recirculation can be employed in both open anode and DEA modes to increase the flow rate through the stack although hydrogen recirculation in open anode systems is uncommon. This work focuses on systems with DEA and occasional hydrogen purges and with hydrogen recirculation.

When system simplicity or energy density [J/m^3] is crucial (e.g. in portable applications), the cathode can be made free-breathing. In this case, the air enters the cathode by free convection and no blower is needed. The relatively slow air supply rate, however, limits fuel cell power output [10]. Therefore, if high power density [W/m^3] is needed, forced convection with an air blower or compressor must be employed. The PEMFC stack air supply in this work is realized with blowers.

Figure 4 shows a typical but simplified schematic of a non-pressurized PEMFC system with DEA and using ambient air as the oxidant and pressurized hydrogen as fuel. This system consists of three subsystems: 1) fuel supply, 2) oxidant supply, and 3) cooling. The oxidant supply and cooling subsystems are briefly discussed below. The fuel supply subsystem is discussed in more detail in Section 3.

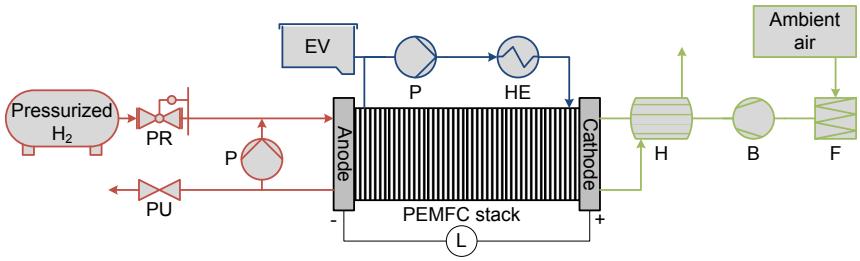

Figure 4. Simplified schematic of the PEMFC system. B: blower, EV: expansion vessel, F: filter, H: humidifier, HE: heat exchanger, L: electrical load, P: pump, PR: pressure reducer, PU: purge valve.

When using ambient air as the oxidant, the oxidant supply subsystem typically contains at least an air filter, a blower, and a humidifier, as shown in Figure 4.

Recirculation is not a viable option to humidify the air because of the high inert content (~79%) in air. Instead, a humidifier – typically a membrane humidifier [27] or a spray tower [28] – is employed. Operation without an air humidifier has also been demonstrated [24] but with a notable performance decrease compared to a humidified system. Pure oxygen can be used as the oxidant in applications where air is not available [29,30].

The cooling subsystem consists of at least a cooling water recirculation pump, a heat exchanger, and an expansion vessel. The operating temperature range focused on in this work is 60-70 °C. The low operating temperature necessitates using a larger heat exchanger because of the low temperature difference. In stationary applications, the size of the heat exchnager is not a problem [27,28], but in e.g. transport applications, the size of the system is a critical factor.

Details of the electrical subsystem do not fall within the scope of this thesis. However, some general characteristics are worth mentioning. The maximum stack output current is typically ca 1 A/cm^2 cell area in non-pressurized systems and ca 2 A/cm^2 cell area in pressurized systems. The maximum stack output voltage is relative to the number of cells in the stack, which might range from a few to a few hundred, depending on the application. Because the voltage varies with load current, a DC/DC converter is usually employed to maintain constant output voltage. Additionally, the electrical subsystem can be hybridized to limit the required PEMFC stack size.

3. Hydrogen Supply in a PEMFC System

The main purposes of the hydrogen supply system in a PEMFC system are: 1) to maintain a suitable pressure level at the anode, 2) to maintain a sufficient fuel flow rate through the stack, 3) to guarantee a sufficient fuel inlet humidity level, and 4) to prevent excessive hydrogen discharge to the surrounding air. In its simplest form, the hydrogen supply can simply comprise a pressure reducer that reduces the pressure of hydrogen in the storage tank to a suitable level. In practice, however, the hydrogen supply comprises many components that deal with the aforementioned tasks. This chapter introduces the principles of hydrogen supply in PEMFC systems.

3.1 Overview

The hydrogen fed to the PEMFC stack is not 100% hydrogen but contains impurities that are either inert or poisonous to the PEMFC. In addition, some nitrogen and carbon dioxide will permeate through the membrane to the anode when air is employed as the oxidant. The impurities are not consumed, unlike fuel, and are, therefore, enriched in the anode. The enriched impurities decrease PEMFC performance either by decreasing fuel concentration (Nernst equation) or by poisoning the PEMFC [31]. This thesis focuses on inert impurities that are not poisoneous to the PEMFC, such as nitrogen (N_2), and their effect on fuel cell performance.

The performance decrease associated with inert gas buildup can be mitigated by allowing fresh fuel to flush out the impurities either intermittently (hydrogen purge) or continuously (bleed). The fraction of hydrogen purged is termed the purge fraction (f_p). The higher the purge fraction, the more hydrogen is lost but the lower the impurity concentration will be in the anode.

Anode gas recirculation is often applied in multi-kW PEMFC systems. The recirculation serves the purpose of increasing the gas flow rate, thus enhancing convective mass transfer and preventing water droplet formation due to water BD (back-diffusion) from the cathode. Water droplet formation occurs especially close to the cell outlet, where the anode gas is also hydrogen depleted. Recirculation also humidifies the anode inlet gas, which is completely dry unless a humidification is employed.

The effects of the purge fraction and recirculation rate are best visualized by solving the balance equations. This is done in the next section.

3.2 Anode material balances

Figure 5 shows the anode side streams for which the steady state material and species balance equations are solved. The stream denoted by subscript *ff* represents fresh fuel from storage. Subscript *in* denotes the anode inlet stream, which is a combination of the fresh fuel stream and the recirculated stream denoted by *r*. Subscript *out* denotes the anode outlet stream, which is split into the recirculated stream and the purged stream, denoted by *p*. Subscript *s* refers to species consumption or transport inside the stack.

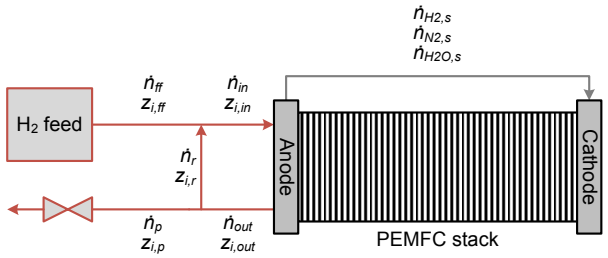

Figure 5. Streams in a PEMFC fuel supply system.

The molar flow rate is denoted by $\dot{n}_j$ where the subscript j refers to the stream. The hydrogen consumption rate ($\dot{n}_{H_2,s}$), the nitrogen permeation rate ($\dot{n}_{N_2,s}$), and the water transport rate ($\dot{n}_{H_2O,s}$) are all assumed to occur away from the anode. Normally nitrogen permeation and water transport occur towards the anode and, therefore, they might take negative values. In contrast, the hydrogen consumption rate is always positive, and it is calculated, based on Eq. 7, as follows:

$$\dot{n}_{H_2,s} = \frac{I \cdot N_{cell}}{2 \cdot F} \tag{13}$$

where I is the current applied, N_{cell} is the number of cells in the PEMFC stack, and F is the Faraday constant.

The mole fractions are denoted by $z_{i,j}$ where the subscript i refers to species (H_2, N_2, or H_2O) and the subscript j refers to the stream. For simplicity, N_2 represents all inert compounds entering the anode with the fuel or diffusing from the cathode through the membrane. The diffusion of hydrogen to the cathode or hydrogen consumption in the reaction with oxygen diffused from the cathode is not considered.

The total material balance equations are:

$$\dot{n}_{ff} + \dot{n}_r = \dot{n}_{in} \tag{14}$$

$$\dot{n}_{in} = \dot{n}_s + \dot{n}_{out} = \left(\dot{n}_{H_2,s} + \dot{n}_{N_2,s} + \dot{n}_{H_2O,s}\right) + \dot{n}_{out} \tag{15}$$

$$\dot{n}_{out} = \dot{n}_r + \dot{n}_p \tag{16}$$

and the species balance equations are:

$$\dot{n}_{ff} \cdot z_{i,ff} + \dot{n}_r \cdot z_{i,r} = \dot{n}_{in} \cdot z_{i,in} \tag{17}$$

$$\dot{n}_{in} \cdot z_{i,in} = \dot{n}_{i,s} + \dot{n}_{out} \cdot z_{i,out} \tag{18}$$

$$\dot{n}_{out} \cdot z_{i,out} = \dot{n}_r \cdot z_{i,r} + \dot{n}_p \cdot z_{i,p} \tag{19}$$

Purged gas and recirculated gas are recognized to have the same composition as the anode outlet gas (i.e. $z_{i,out} = z_{i,r} = z_{i,p}$). Combining these equations yields the total material and species balance equations for the entire fuel supply system:

$$\dot{n}_{ff} = \dot{n}_s + \dot{n}_p \tag{20}$$

$$\dot{n}_{ff} \cdot z_{i,ff} = \dot{n}_{i,s} + \dot{n}_p \cdot z_{i,p} \tag{21}$$

With this notation, the purge fraction (f_p) is defined as follows:

$$f_p = \frac{\dot{n}_p \cdot y_{H_2,p}}{\dot{n}_{ff} \cdot y_{H_2,ff}} = 1 - \frac{\dot{n}_{H_2,s}}{\dot{n}_{ff} \cdot z_{H_2,ff}} \tag{22}$$

and it is related to the fuel efficiency (η_f) – also known as the total fuel utilization ($u_{f,tot}$) – as follows:

$$u_{f,tot} = \eta_f = \frac{\dot{n}_{H_2,s}}{\dot{n}_{ff} \cdot z_{H_2,ff}} = 1 - f_p \tag{23}$$

The fuel utilization per pass ($u_{f,pp}$), which is a measure of the recirculation rate, is defined as follows:

$$u_{f,pp} = \frac{\dot{n}_{H_2,s}}{\dot{n}_{in} \cdot z_{H_2,in}} = \frac{1}{\lambda_f} \tag{24}$$

where λ_f is the fuel stoichiometric ratio at inlet. The steady state balance equations can be solved by assuming 1) the stack pressure drop is a linear function of the inlet mass flow rate:

$$\Delta p_s = p_{in} - p_{out} = b \cdot \dot{m}_{in}, \tag{25}$$

2) the anode outlet gas is saturated at stack temperature:

$$z_{H_2O,out} = \frac{p_{H_2O}^{vap}(T_s) \cdot RH_{out}}{p_{out}}, \tag{26}$$

and 3) continuous purging (i.e. bleed). For operation with intermittent purges and the same purge fraction, the results would be similar except that the concentrations would vary around those with continuous purging.

The results are plotted in gas phase mole fractions ($y_{i,j}$) to visualize possible water condensation and because the gas phase mole fractions are typically measured, not the total mole fractions. The gas phase mole fractions are computed by limiting water gas phase mole fraction according to Eq. 26 and keeping the ratio of hydrogen and nitrogen mole fractions constant.

The parameters in Table 2 are used for example calculations (unless otherwise noted) in Section 3 to illustrate the effect of the purge fraction, anode gas recir-

culation rate, fuel purity, and nitrogen permeation rate on the anode gas composition. For simplicity, the anode outlet humidity and the nitrogen permeation rate are assumed constant.

Table 2. Parameters for the model. The parameters are chosen based on the PEMFC systems studied in this work (see sections 4.2.1 and 6.5).

Parameter	*Value*	*Explanation*
T_s	60 °C	Cell temperature
$p_{H_2O}^{vap}(T_s)$	0.199 bar [32]	Water vapor pressure at cell temperature
RH_{out}	100%	Cell outlet relative humidity
I	120 A	Cell current
N_{cell}	1	Number of cells in stack
$y_{H_2,ff}$	0.9999	Hydrogen mole fraction in fuel
$y_{N_2,ff}$	0.0001 (= 100 ppm)	Nitrogen mole fraction in fuel
$y_{H_2O,ff}$	0.0000	Water mole fraction in fuel
$u_{f,tot}$	0.99	Total fuel utilization
$u_{f,pp}$	0.60	Fuel utilization per pass
p_{in}	0.25 barg	Cell inlet pressure
b	$1.5 \cdot 10^4$ bar·(kg·s^{-1})$^{-1}$	Cell pressure drop coefficient
$\dot{n}_{N_2,s}$	$-3.7 \cdot 10^{-7}$ mol/s (*)	Nitrogen permeation rate (anode to cathode)

(*) For a fully hydrated membrane at 60 °C, with 25 µm thickness, with 200 cm^2 area, and exposed to 0.9 bar N_2 partial pressure difference [33,34].

Despite the simplified approach employed here, some generally valid observations about the effects of purge fraction and recirculation rate can be made. First, decreasing the purge fraction (i.e. increasing total fuel utilization) increases anode impurity (represented here by N_2) concentration and decreases fuel concentration, as discussed is Section 3.1. Employing a low purge fraction can result in impurity concentrations that are several orders of magnitude higher in the fuel cell than in the fuel, as seen in Figure 6 a. For example, a purge fraction of $f_p = 10^{-3}$ results in 1933 times higher N_2 mole fraction in the anode inlet stream compared to the fuel. With a zero purge fraction, the N_2 partial pressure on the anode side approaches that on the cathode side. This would result in an excessive decrease in performance especially in non-pressurized PEMFC systems. The water concentration, which depends on the fixed outlet relative humidity, changes only a little with purge fraction; the observed change is due to a change in pressure drop.

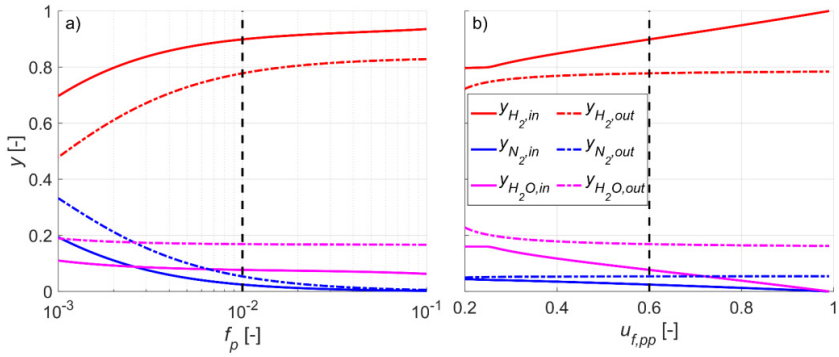

Figure 6. Gas phase mole fractions at anode inlet and outlet at varying a) purge fraction (f_p) and b) fuel utilization per pass ($u_{f,pp}$). Solved from material balance equations. The dashed line indicates conditions shown in Table 2.

Second, an increase in the recirculation rate (i.e. a decrease in fuel utilization per pass) causes inlet concentrations to approach the outlet concentrations (Figure 6 b). Therefore, increasing the recirculation rate theoretically (but not in practice) decreases PEMFC performance. The outlet concentrations remain nearly unchanged over most of the recirculation rate range. The change in outlet concentrations observed at high recirculation rates is due to an increased water outlet mole fraction as a conequence of the increased pressure drop. In reality, the outlet concentrations also depend on water transport and the N_2 permeation rate, both of which are functions of the recirculation rate.

Third, the anode gas recirculation humidifies the anode inlet (Figure 7 b). Without recirculation, the anode inlet gas equals the dry hydrogen supply from the storage unless a humidifier is employed. The anode inlet humidity increases with increasing recirculation rate. For example, a roughly 35% (i.e. a relatively low) fuel utilization per pass is required to achieve a 55 °C dew point temperature (corresponding to a 80% relative humidity) at the anode inlet even though the anode outlet is assumed saturated with water. In practice, the recirculation rate is limited by the power consumption, when employing a mechanical pump, or the achieved recirculation rate, when employing an ejector.

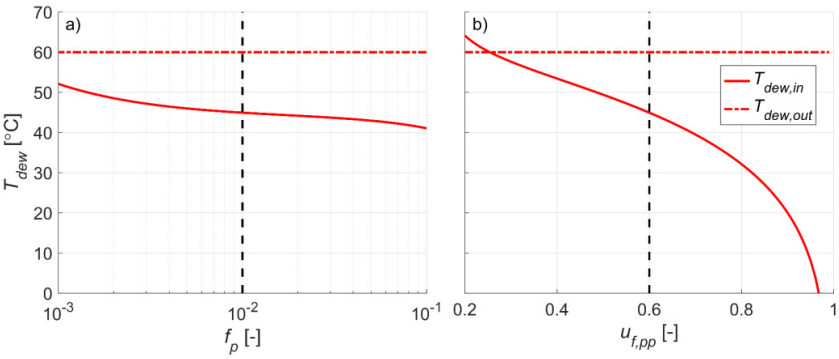

Figure 7. Anode inlet and outlet dew point temperatures at varying a) purge fraction (f_p) and b) fuel utilization per pass ($u_{f,pp}$). Solved from material balance equations. The dashed line indicates conditions shown in Table 2.

The anode inlet dew point temperature exceeds that of the anode outlet at approximately 25% fuel utilization per pass. This is possible because of the increase in pressure difference between the inlet and the outlet while the anode outlet partial pressure remains constant. The effect of the purge fraction on inlet humidity is minor (Figure 7 a).

The effects of fuel impurity concentration and the N_2 permeation rate are shown in Figure 8 a and b. The relative effect of fuel concentration at the simulated conditions (Table 2) is minor ($0.6 \cdot 10^{-7}$ mol/s) compared to the N_2 permeation rate ($3.7 \cdot 10^{-7}$ mol/s); decreasing the concentration of impurity in fuel by an order of magnitude does not significantly decrease the concentrations in the fuel cell, as seen in Figure 8 a. Instead, the N_2 permeation rate accounts for most of the impurity buildup at these conditions. An increase either in fuel impurity concentration or in the membrane permeation rate results in a higher recirculated stream impurity content and, subsequently, necessitates an increase in purge frequency or bleed rate.

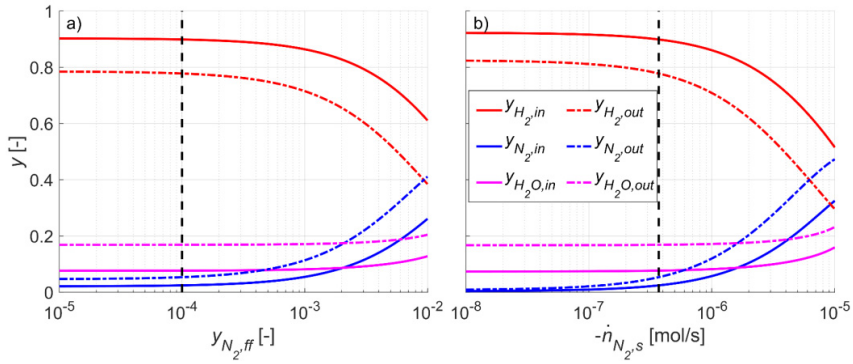

Figure 8. Gas phase mole fractions at anode inlet and outlet at varying a) N_2 mole fraction in fuel ($y_{N_2,ff}$) and b) N_2 permeation rate ($\dot{n}_{N_2,s}$). Solved from material balance equations. The dashed line indicates conditions shown in Table 2.

It is important to distinguish between steady state and dynamic behavior. The above discussion solely considers steady state. The time required for concentrations to reach a steady state (or pseudo steady-state with intermittent purges) depends mainly on anode volume and current level. Based on experience from PEMFC systems presented in sections 4.2.1 and 6.5, the steady state is typically reached in tens of minutes, the temperatures and, consequently, the water concentrations taking the longest time to stabilize. Steady state is likely never reached in applications with load changes several times within a minute. In applications with long periods (thousands of hours) of constant operation, the steady state is of primary importance, and the way steady state is reached (i.e. system dynamics) is of minor importance.

3.3 Hydrogen purge

One purpose of the hydrogen purge is to remove accumulated impurities. A purge fraction that is too high results in poor fuel efficiency. A purge fraction that is too low results in high concentration polarization and reduced fuel cell

efficiency. The Nernst equation (Eq. 9) can be used for estimating the effect of a decrease in hydrogen partial pressure on cell voltage [6]:

$$\begin{aligned}\Delta E_{Nernst} &= E - E_{ref} \\ &= \left(E^0 - \frac{R \cdot T}{2 \cdot F} \cdot ln \left[\frac{\frac{p_{H_2O}}{p^0}}{\frac{p_{H_2}}{p^0} \cdot \left(\frac{p_{O_2}}{p^0}\right)^{\frac{1}{2}}} \right] \right) \\ &\quad - \left(E^0 - \frac{R \cdot T}{2 \cdot F} \cdot ln \left[\frac{\frac{p_{H_2O}}{p^0}}{\frac{p_{H_2}}{p^0} \cdot \left(\frac{p_{O_2}}{p^0}\right)^{1/2}} \right] \right)_{ref} \\ &= \frac{R \cdot T}{2 \cdot F} \cdot ln \frac{p_{H_2}}{p_{H_2.ref}} \end{aligned} \quad (27)$$

where the hydrogen partial pressure (p_{H_2}) is averaged over the cell, and the reference hydrogen partial pressure ($p_{H_2.ref}$) corresponds to the reference cell voltage (E_{ref}). The power decrease per cell due to concentration polarization is:

$$\Delta P_{Nernst} = I \cdot \Delta E_{Nernst} \quad (28)$$

On the other hand, the power lost per cell due to hydrogen vented out in purges (at an average rate of $\overline{\dot{n}_{H_2,p}}$) is computed by applying Faraday's law of electrolysis:

$$\Delta P_{fuel} = \frac{\bar{I}_p}{N_{cell}} \cdot E_{ref} = \frac{\overline{\dot{n}_{H_2,p}} \cdot 2 \cdot F}{N_{cell}} \cdot E_{ref} \quad (29)$$

where $\bar{I}_p$ is the average rate of hydrogen lost in purges converted to electrical current, and E_{ref} is a reference cell voltage (same as above). ΔP_{Nernst} and ΔP_{fuel} are plotted in Figure 9 as a function of purge fraction and fuel utilization per pass.

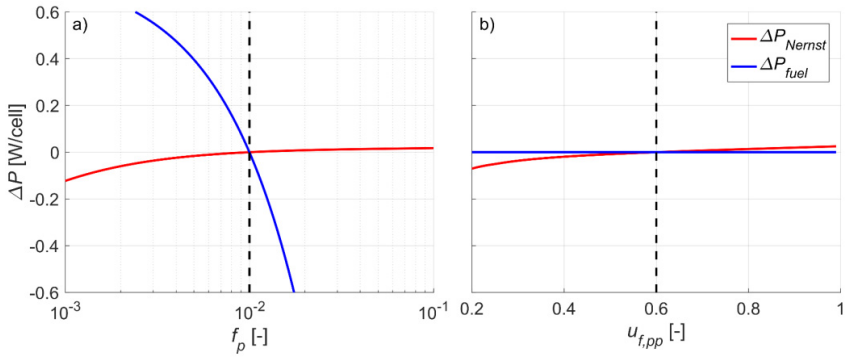

Figure 9. Change in cell power output due to concentration polarization and hydrogen lost in purges at varying a) purge fraction (f_p) and b) fuel utilization per pass ($u_{f,pp}$). Solved from material balance equations. The values are relative to the dashed line indicating conditions shown in Table 2. $E_{ref} = 650$ mV is assumed.

As seen in Figure 9 a, the cell net output power is much more sensitive to total fuel utilization than to concentration polarization at the simulated conditions. One could draw the conclusion that the optimal purge fraction is very low (<0.001). However, in publication [II], it is shown that the measured concentration polarization can be notably higher than the theoretical one. In addition, these simulations (like numerous others, e.g. [35–38]) do not account for the effects of water transport and condensation.

Water condenses when water vapor partial pressure exceeds water vapor pressure. Liquid water in anode gas channels is harmful in two ways; it 1) restricts the gas flow in gas channels and 2) prevents hydrogen from reaching the catalyst sites. The uneven flow distribution between cells that occurs from the water droplets plugging the gas channels induces further growth of existing droplets.

Fuel starvation is a condition in which hydrogen cannot reach the reaction site, either locally because of water droplets blocking them or globally because of no hydrogen present. When local fuel starvation occurs, the cell regions suffering from hydrogen shortage adapt their electrode potentials to a higher level. The potential difference between the anode and the cathode remains constant because of the highly conductive bipolar plates. The elevated electrode potentials enable unwanted reactions (water splitting and corrosion of the carbon support on the cathode and oxygen reduction at the anode) and a reversed current. Local fuel starvation has, therefore, negative effect on cell lifetime, but it is difficult to detect before irreversible damage to the PEMFC has occurred because of the unchanged cell voltage. [23,39]

The other main purpose of the hydrogen purge is, thus, to remove liquid water from the gas channels and guarantee stable performance even when operating at very humid conditions, i.e. at conditions where the reactant gases are close to saturated or even oversaturated with water. A PEMFC typically achieves maximum performance at such high-humidity conditions. The effect of humidity level on the optimal purge parameters is difficult to study by modelling, but some experimental studies about the subject have been conducted (e.g. [40,41]). This is also the main topic in publication [II].

A hydrogen purge can be triggered based on various criteria: a predefined voltage drop [42], [II], time-based [43], the applied load current [37,44], the anode pressure [V], or a predefined impurity concentration [35,37], for example. The choice of triggering criterion is governed by the expected drive cycle and by the operating conditions. The primary purpose of a hydrogen purge at dry operating conditions is to remove inert gases and, for this reason, either a time-based or a coulomb counter-based purge trigger would be suitable. Flooding can be expected at humid operating conditions, and cell voltage deviation is one of the best indicators of that.

The liquid water is removed most efficiently with a high-flow-rate purge. Therefore, the purge valve should have a sufficiently low flow resistance, i.e. a high K_v-value. An excessively high K_v-value, however, depressurizes the anode

rapidly as soon as the valve is opened. This results in a pressure difference between the anode and cathode and causes unnecessary stresses on the polymer membrane [23].

While a high flow rate efficiently removes liquid water, it also results in a large amount of hydrogen being vented out. Therefore, the purge length (i.e. the time the valve is kept open) should be relatively short, typically few hundred milliseconds. The typical response time of a solenoid valve is a few tens of milliseconds. In other words, the valve may not have time to fully open before it is closed during very short purges.

An alternative to a hydrogen purge is a hydrogen bleed [36,45], i.e. to continuously vent out a fraction of the anode outlet gas. Hydrogen bleed can also be employed in parallel with hydrogen purge. This might be necessary when using low grade hydrogen to avoid excess buildup of impurities in the anode loop. A correctly sized and fast reacting proportional valve can also be employed both as a bleed valve and as a purge valve.

The main difference between a hydrogen purge and a bleed is the maximum flow rate encountered through the stack during operation. During a hydrogen purge, the flow rate is normally multiplied whereas a continuous bleed adds typically at most a few percent (depends on total fuel utilization) to the flow rate. Because of this, the purge is often preferred as it efficiently removes liquid water, thus stabilizing PEMFC operation.

Another difference between a hydrogen purge and a bleed is the rapid pressure decrease during a purge. This easily leads to an excessive pressure difference between the anode and cathode, especially in pressurized systems, and, subsequently, complicates pressure management.

3.4 Hydrogen humidifiers

As seen in Figure 7 b, the anode inlet humidity (expressed in dew point temperature) is relatively low even with hydrogen recirculation unless high recirculation rate is applied. For example, a typical fuel utilization per pass of 0.6 results in an anode inlet dew point temperature of 45 °C which corresponds to a relative humidity of only 48% at the cell operating temperature (60 °C). For best PEMFC performance, the anode inlet relative humidity should be close to 100%.

The anode inlet is further dehydrated at high power levels because of the EOD (electro-osmotic drag) prevailing over BD (back-diffusion) and because the fuel that is fed is drier (unless the recirculation rate is increased in the same proportion). Anode inlet dehydration can be mitigated by feeding air and fuel to the cell in counterflow mode because water is then transported from the humid cathode outlet stream to the dry anode inlet stream. Despite the advances in polymer technology that enable the use of thinner membranes (18 μm membranes were available in 2007), which in turn facilitates membrane hydration [25], inlet gas humidification is often applied to increase PEMFC performance and durability [21]. Gas humidifiers are commonly employed not only on the cathode side but also often on the anode side in addition to hydrogen recirculation [27,28].

Humidifiers typically employed for anode gas humidification can be classified as either a gas-to-gas type or a liquid-to-gas type. From system complexity point of view, the gas-to-gas type humidifiers are more attractive since liquid water is not needed. Liquid water must either be refilled or condensed from PEMFC stack outlet gas streams. A gas-to-gas type humidifier can be placed between the streams where a transfer of humidity is required without the need for any additional system components.

Possible humidifier types and their advantages and disadvantages are listed in Table 3. An example of a gas-to-gas humidifier is the enthalpy wheel [46,47]. Examples of liquid-to-gas humidifiers are the water atomizer [48–50], spray tower [28], and bubble humidifier [51,52]. A membrane humidifier can be operated both in gas-to-gas [53,54] and in liquid-to-gas [55] modes.

Table 3. A summary of the advantages and disadvantages of humidifiers with respect to hydrogen gas humidification based on references [6,28,46–55] and the author's own experience.

Gas-to-gas		
Humidifier type	**Advantages**	**Disadvantages**
Enthalpy wheel	- Compact size - Low gas pressure drop	- Gas leakages - Power consumption - Require maintenance
Membrane humidifier	- No power consumption - Compact size	- Gas leakages - Moderate gas pressure drop (~20-50 mbar [47], times two) - High price
Liquid-to-gas		
Humidifier type	**Advantages**	**Disadvantages**
Water atomizer	- Gas tight - Low gas pressure drop - Controllable humidity	- Inefficient heat transfer - Sensitive to control (oversaturation possible) - Power consumption
Membrane humidifier	- Compact size - No power consumption	- Gas leakages possible - High price
Spray tower	- Gas tight - Low gas pressure drop - Low power consumption	- Large size (several times that of a membrane humidifier)
Bubble humidifier	- Gas tight - Low power consumption	- Large size (several times that of a membrane humidifier)

A characteristic feature of gas-to-gas humidifiers is that the mass transfer is not limited to water – other gases are also transferred between the two streams [47]. This introduces a safety risk through possible leakages when humidifying hydrogen since the cathode outlet air is the only possible humidity source. Therefore, gas-to-gas type humidifiers are not considered here for hydrogen humidification.

The water atomizer humidifiers have the advantages of being small, enabling humidity control with short delay, and having practically no gas pressure drop [48–50]. However, unless the humidified gas requires cooling (e.g. after compression), a heat exchanger is needed [48,49] since water evaporation is a heat-intensive process. A heat exchanger causes a drop in gas pressure and adds to the humidifier size, especially if the available temperature difference is low (e.g.

PEMFC stack coolant). Heating with electricity reduces size and weight but adds parasitic power consumption. In addition, a liquid water flow control mechanism is required for water atomizers [48,49]. Finally, water-atomizing humidifiers permit over-saturating the gas, which can lead to PEMFC flooding.

Liquid-to-gas membrane humidifiers are compact in size, they require no power to operate, and they can easily make use of the waste heat rejected from a PEMFC stack through the cooling circuit. However, as with the gas-to-gas membrane humidifier, gas leakages might occur in the liquid-to-gas version, which introduces a safety risk when humidifying hydrogen. Further, impurities in the heating water have been reported to plug the humidifier [50], thus limiting its lifetime. In addition, the price of membrane humidifiers is high [47,48]. For example, the price of the two membrane humidifiers used for humidifiying the cathode inlet air in the 50 kW PEMFC pilot plant [27] was thousands of euros per piece. On the other hand, the membrane humidifier for a mass-produced 80 kW PEMFC system was estimated to cost approximately $100 in 2010 [25].

The spray tower (with a packed bed [28]) and the bubble humidifier both bring the heated water and the gas in direct contact with each other. Although these humidifiers are relatively large and heavy, the good contact between phases ensures efficient heat and mass transport. For example, the approach dew point temperatures achieved with the bubble humidifier studied in publication [III] were notably lower compared to those achieved with water atomizing humidifiers [48,49]. The achieved humidification performance depends, however, on humidifier sizing and, therefore, direct comparison cannot be made. Both the spray tower and the bubble humidifier are gas tight and consume little power but the gas pressure drop in a bubble humidifier is higher than in a spray tower due to the water bed.

3.5 Hydrogen recirculation

As shown in Figure 6 b, an increase in recirculation rate results in a higher average N_2 concentration in the anode gas channels. Therefore, a decrease in PEMFC performance with an increase in the recirculation rate could be expected (Figure 9 b). However, a higher average N_2 concentration decreases the N_2 permeation rate, thus partly cancelling out the increase in the average N_2 concentration caused by the increase in recirculation rate. In addition, an increase in recirculation rate enhances convective mass transfer and prevents water droplet formation inside the PEMFC, as mentioned in Section 3.1. In general, the higher the recirculation rate, the better and more stable the PEMFC performance, especially at high-humidity conditions.

The recirculation rate in systems with a mechanical pump (Figure 4) is limited by pump power consumption (given a pump with high enough performance). At some point, the added recirculation rate does not pay off. The power consumption of recirculation will typically be low (depends on recirculation rate and system flow resistance) relative to the power consumption of the cathode blower. Furhermore, the recirculation can be varied with a variable rotating speed pump to meet the requirements of the prevailing operating conditions. Therefore, the sizing and operation of a mechanical hydrogen recirculation pump is simple.

Mechanical pumps for hydrogen recirculation are relatively expensive. Experience has also shown that the operating conditions in PEMFC systems can be too demanding for mechanical pumps to meet the system lifetime requirements [27]. These qualities have resulted in a greater interest in other hydrogen recirculation solutions.

3.5.1 Hydrogen recirculation with ejectors

Ejectors are a valid alternative to mechanical pumps in PEMFC systems for anode gas recirculation. Their operation relies on transferring momentum directly from a primary gas to a secondary gas. A high-pressure primary gas is supplied to the primary inlet port after which it enters the nozzle (Figure 10). In the nozzle, the primary gas is accelerated to high velocity (up to several Mach) and its pressure is reduced. The high-velocity primary gas meets the almost stagnant secondary gas downstream of the nozzle, and the transfer of momentum equalizes the velocities of the two gases as they mix. The gas mixture decelerates in the ejector diffuser, and, as a result, the pressure increases. The primary gas in PEMFC applications equals the fresh hydrogen feed from storage, the secondary gas equals the recirculated gas, and the ejector outlet gas equals the anode inlet gas (Figure 11).

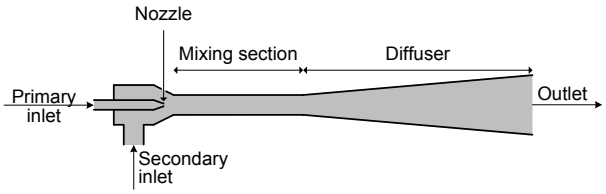

Figure 10. Ejector main parts.

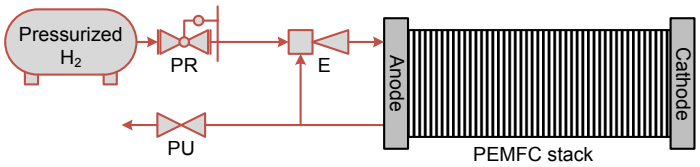

Figure 11. Simplified schematic of the PEMFC fuel supply system with an ejector. PR: pressure reducer, PU: purge valve, E: ejector.

Ejectors are more durable and less expensive than mechanical pumps because they have no moving parts. These are the main reasons why ejectors have received growing interest recently. In addition, the solid construction of ejectors makes it easy to seal them. Ejectors also make use of the hydrogen storage pressure energy – an energy source otherwise lost – which makes them more energy efficient than mechanical pumps.

Ejectors, however, have qualities that make their usage more challenging than mechanical pumps. First, the primary gas flow rate of an ejector is proportional to the primary inlet pressure. Therefore, the primary gas pressure (or flow rate) of an ejector must be controlled to match the hydrogen consumption rate. Otherwise, the anode pressure will vary in a DEA (dead-end anode) setup. Second,

the recirculation rate achieved with an ejector varies with the primary gas flow rate (i.e. the hydrogen consumption rate) and cannot be controlled. Therefore, the ejector must be sized carefully to achieve an adequate flow rate when needed. Third, the hydrogen purge with an ejector is not as efficient as in systems with hydrogen fed passively through a pressure reducer since the ejector nozzle limits the flow rate of the primary gas. Instead, either the primary pressure of the ejector must be increased during a purge or a hydrogen supply line bypassing the ejector must be implemented.

3.5.2 Model-based ejector sizing

Ejector sizing is conducted with models that predict the effect of ejector dimensions and boundary conditions on ejector performance. Ejectors have been modelled with various approaches ranging from simplified 1D models [56–58] to complex CFD models in 3D [59–61].

The 1D models are based on isentropic flow relations and the balance equations of mass, energy, and momentum. These models consider only the main ejector dimensions, such as the diameters of the nozzle and mixing section. The computation is inherently relatively light. While satisfactory accuracy has been obtained with the 1D models, their accuracy is usually limited to specific operating conditions or a range of operating conditions. Further, their accuracy relies largely on experimental parameters [62] applied to account for non-idealities in ejector operation.

At the other end of the model spectrum, CFD models are based on actual ejector geometry. The modelling domain is spatially discretized, and the balance equations are solved in every discretized portion, “cell”, separately. Consequently, CFD models in 3D can provide more accurate predictions of ejector performance for a wider range of conditions [60]. However, the number of degrees of freedom in a 3D model (millions) is considerably higher than in a 1D model (dozens), and more time and computational resources (memory and CPU) is required to both setup the model and solve it.

A 2D CFD model is lighter than a 3D CFD model both computationally and in model setup, and it provides more accurate predictions of ejector performance than a 1D model. A 2D CFD model does not require parameter tuning like 1D models do. Moreover, 2D modelling conducted with CFD can be employed for checking the effects of various ejector dimensions, which are neglected in 1D models. However, a 2D CFD model is limited to the axissymetric part of an ejector and, therefore, cannot capture the phenomena resulting from the non-axisymmetric parts. The degree to which the non-axisymmetry affect ejector performance depends on the ejector design.

The flow in ejectors is typically turbulent, which adds modelling complexity. In CFD, turbulence is typically modelled by employing Reynolds-averaged Navier–Stokes (RANS) equations. In practice, this means that the flow (pressure and velocity) is decomposed into a mean part and a fluctuating part. The fluctuating part (the Reynolds stress term) can be modelled with an eddy viscosity model (EVM), which relates the Reynolds stress term to mean velocities. Example of EVMs are the k-ε and the k-ω models. Many alternative approaches for

turbulence modelling exist but the RANS equations coupled with EVMs are usually a good compromise between accuracy and computational cost.

Because of the trade-off between accuracy and effort, the ejector is, in many cases, best designed by stepwise increasing the modelling complexity (Figure 12). The initial screening of possible ejector designs is conducted with simple models. The modelling complexity can be increased with a limited number of designs once some estimate of the ejector performance in the intended system is obtained. Ultimately, the final adjustments of the design (before manufacturing) are made with a complex model.

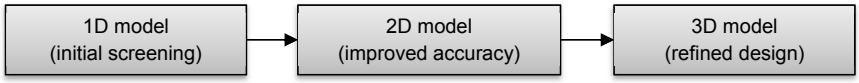

Figure 12. Ejector design approach.

4. Hydrogen Purge

Impurities enter the anode both with the fuel and through the membrane. The impurities will build up in a DEA setup to a high level and will impair fuel cell stack performance unless hydrogen purges or a bleed is applied. In addition, a fraction of the water formed at the cathode is transported to the anode. At high-humidity conditions, water might condense and cause an uneven flow between anode gas channels. The high flow velocity achieved during a hydrogen purge flushes out condensed water and maintains stable PEMFC performance.

The impaired stack performance resulting both from impurity buildup and from anode gas channel flooding is possible to detect by monitoring the cell voltages. However, even though cell voltages would decrease at these conditions, the cause for the decrease in voltages may be difficult to track down. Possible causes for decreased cell voltages include a decrease in anode gas recirculation rate and an increase in impurity content. A decrease in recirculation rate might be a result of liquid water plugging the gas channels, for example. An increase in impurity content might be a result of an increased rate of inert gas permeation through the membrane, a variation in fuel purity level, or inefficient hydrogen purges.

A better view of the prevailing conditions can be obtained with additional measurements, and the operating parameters can be optimized. For example, by measuring the anode gas composition, the purge frequency and length can be optimized to result in stable operation without purging hydrogen in excess. In addition, added instrumentation in a fuel cell system can, at best, aid in detecting the malfunction of a component and help in choosing the best strategy for continued operation. On the other hand, extra transmitters are usually avoided to keep the system cost as low as possible and to avoid potentially failing components that the system operation depends on.

In publications [I] and [II], methods for determining some key figures of hydrogen supply and recirculation were developed. In publication [I], a method for determining fresh fuel purity and the membrane inert gas permeation rate in a fuel cell system was developed. In publication [II], the same but updated fuel cell system was used to develop methods for determining the purged gas volume and composition.

4.1 Inert buildup and hydrogen purge calculations

The calculations used to determine some key figures of hydrogen supply and recirculation are presented below.

4.1.1 Fuel quality and inert gas membrane permeability

In a system with DEA, the concentration of inert gases (mainly nitrogen) in the anode gas increases between hydrogen purges due to fuel impurities and membrane permeability. The rate of increase in inert concentration can be used to estimate the inert concentration in the fuel and the membrane permeability. Using the notation in Section 3.2 and assuming ideal gas ($y_{i,j} = z_{i,j}$) at constant pressure and temperature, the inert gas (here represented by nitrogen, N_2) buildup rate ($\dot{n}_{N_2,an}$) is:

$$\dot{n}_{N_2,an} = n_{an} \cdot \frac{dy_{N_2,an}}{dt} = \frac{p_{an} \cdot V_{an}}{R \cdot T_{an}} \cdot \frac{dy_{N_2,an}}{dt} = \dot{n}_{N_2,ff} - \dot{n}_{N_2,s} \tag{30}$$

where $\dot{n}_{N_2,ff}$ is the rate of inert gas entering with fuel:

$$\dot{n}_{N_2,ff} = y_{N_2,ff} \cdot \dot{n}_{H_2,s} = y_{N_2,ff} \cdot \frac{I \cdot N_{cell}}{2 \cdot F} \tag{31}$$

and $-\dot{n}_{N_2,s}$ is the molar flow rate of inert gases entering the anode through the membrane. Combining Eqs. 30 and 31 gives:

$$\dot{n}_{N_2,an} = y_{N_2,ff} \cdot \frac{I \cdot N_{cell}}{2 \cdot F} - \dot{n}_{N_2,s} \tag{32}$$

Differentiating $\dot{n}_{N_2,an}$ with respect to I and assuming that membrane permeability, anode pressure, and temperature are independent of the load current $\left(\frac{d\dot{n}_{N_2,s}}{dI} = \frac{dp_{an}}{dI} = \frac{d\frac{1}{T_{an}}}{dI} = 0\right)$ gives the following expression for the inert gas mole fraction in fuel:

$$y_{N_2,ff} = \frac{2 \cdot F}{N_{cell}} \cdot \frac{d\dot{n}_{N_2,an}}{dI} = \frac{2 \cdot F}{N_{cell}} \cdot \frac{p_{an} \cdot V_{an}}{R \cdot T_{an}} \cdot \frac{d}{dI}\left(\frac{dy_{N_2,an}}{dt}\right) \tag{33}$$

Substituting Eq. 33 into Eq 32 gives an expression for the rate of inert gases entering the anode through the membrane:

$$-\dot{n}_{N_2,s} = \dot{n}_{N_2,an} - y_{N_2,ff} \cdot \frac{I \cdot N_{cell}}{2 \cdot F} = \dot{n}_{N_2,an}\{I = 0\} \tag{34}$$

As mentioned above, Eqs. 33 and 34 are valid when the membrane permeability can be assumed independent of the load current. This is not exactly true since membrane permeability is known to be a function of at least the membrane pressure difference, humidity, and temperature [34,63]; all of which depend, at least to some degree, on the load current. Further, current density affects membrane permeability [63], and the fuel and oxygen crossovers (both of which consume fuel) have been neglected in this analysis. Neglecting gas crossover might not be a valid assumption in the future as new PEMFCs employ thinner membranes with higher gas crossover rates.

The error associated with using gas phase mole fractions ($y_{i,j}$) instead of total mole fractions ($z_{i,j}$) is related to the anode gas volume (V_{an}). Therefore, the use of gas phase mole fractions, which usually are measured, can be used even though some water condensation occurs.

Eqs. 33 and 34 can be used to detect variations in fuel purity and membrane permeability, especially in applications with a repeated load cycle. Even though the results are only approximations and might deviate from actual ones, the measurements give the overall trends and help detect a change in the determined quantities.

4.1.2 Purge gas amount and composition

The hydrogen purge serves two purposes. First, it removes condensed water from the channels, thus stabilizing fuel cell performance under humid operating conditions. Second, it removes inert gases from the anode, which, when accumulated, decrease fuel cell performance. Knowledge of the purged amount and composition gas give an indication of purge efficiency and aids in choosing the correct purge parameters for the prevailing operating conditions.

The total fuel utilization ($u_{f,tot}$), i.e. the fuel efficiency (η_f), of a fuel cell is the ratio of the hydrogen consumption rate to the hydrogen supply rate. The difference between supply and consumption rates equal the rate at which hydrogen is lost, mainly in hydrogen purges. Thus, dividing the average hydrogen lost rate by the purge frequency gives the average of hydrogen lost during one purge. However, this does not give the total amount of purged anode gas vented during a purge, which typically also contains water and nitrogen. Even if fuel efficiency is corrected with measured water and nitrogen concentrations, the amount of purged gas determined this way is not very accurate because the purged gas composition depends on purge length, as will be shown in Section 4.3.2.

The approach to determining the purged gas amount depends on how the system is operated. In systems where the hydrogen supply rate is kept constant during a purge, the amount of gas purged (n_p) can be determined from the anode pressure difference before (1) and after (2) the purge:

$$n_p = \left(p_{an,1} - p_{an,2}\right) \cdot \frac{V_{an}}{R \cdot T_{an}} \tag{35}$$

In systems where the anode pressure is kept constant by supplying hydrogen through a pressure reducer, the amount of purged gas (n_p) can be determined by numerically integrating the difference between the fuel supply rate ($\dot{n}_{ff}$) and the hydrogen consumption rate ($\dot{n}_{H_2,s}$) during a purge:

$$n_p = \int \left(\dot{n}_{ff} - \dot{n}_{H_2,s}\right) dt \tag{36}$$

This requires measuring the fuel supply rate with a transmitter that has a short response time. Figure 13 shows an example of a measured hydrogen flow rate profile during a hydrogen purge in a system with the anode pressure maintained constant with a pressure regulator.

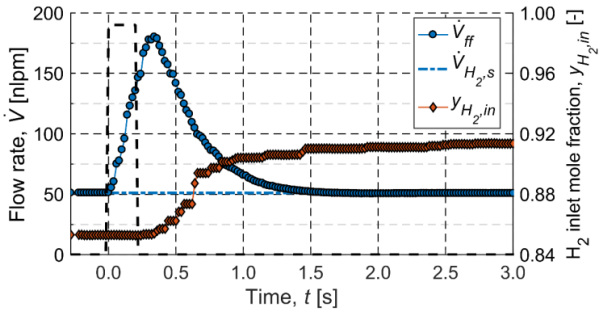

Figure 13. Example of hydrogen flow rate and mole fraction profiles during a hydrogen purge. Operating parameters: $t_p = 200$ ms; $T_{dew,cat\ in} = 52$ °C; $\Delta E_{trigger} = -3$ mV. The dashed lines show the purge valve control signal (on/off). Data in figure is from measurements conducted for publication [II].

In both of the above cases, the change in anode gas temperature (hydrogen supply is usually colder than anode gas) might introduce an error. However, unless the temperature change during the purge is significant, the error should be small. In addition, the pressure change in the case of constant hydrogen supply rate might not be uniform due to hydrogen recirculation. Therefore, computing the amount of purged gas separately in different parts of the anode might give results that are more accurate.

The composition of purged gas can be determined based on the hydrogen balance. The gas phase mole fractions ($y_{i,j}$) are again used because they are measured whereas the total mole fractions ($z_{i,j}$) are not (for reasoning, see section 4.1.1). The amount of hydrogen supplied during a purge is:

$$n_{H_2,ff} = y_{H_2,ff} \cdot n_p \tag{37}$$

where $y_{H_2,ff}$ is the hydrogen mole fraction in fuel. The amount of hydrogen in the anode before ($n_{H_2,an,0}$) the purge is:

$$n_{H_2,an,0} = y_{H_2,an,0} \cdot n_{an} \tag{38}$$

and the amount of hydrogen in the anode after ($n_{H_2,an,1}$) the purge is:

$$n_{H_2,an,1} = y_{H_2,an,1} \cdot n_{an} \tag{39}$$

It is assumed that the total amount of anode gas remains unchanged ($n_{an,0} = n_{an,1}$). This implies that the same amount of gas (n_p), but with a different composition, exits the anode during the purge. The amount of hydrogen in the purged gas is the difference between the amount of hydrogen supplied ($n_{H_2,ff}$) and the amount of hydrogen accumulated in the anode ($y_{H_2,an,1} \cdot n_{an} - y_{H_2,an,0} \cdot n_{an}$) during the purge. The purged gas hydrogen mole fraction is, therefore:

$$\begin{aligned} \overline{y_{H_2,p}} &= \frac{y_{H_2,ff} \cdot n_p - (y_{H_2,an,1} - y_{H_2,an,0}) \cdot n_{an}}{n_p} \\ &= y_{H_2,ff} - (y_{H_2,an,1} - y_{H_2,an,0}) \cdot \frac{n_{an}}{n_p}, \end{aligned} \tag{40}$$

which is the same result that is obtained when a perfectly mixed anode is assumed (see Appendix A). Similar equations can be obtained for the other gas components.

As the gas concentrations in the anode loop are non-uniform, volume-based averaging is necessary before applying Eq. 40. An example of a change in the hydrogen mole fraction at the anode inlet during a hydrogen purge measured in publication [II] is shown in Figure 13.

As discussed earlier in this section, the purged gas composition does not necessarily equal anode outlet gas composition before the purge. This is because the anode outlet gas concentration changes as the purge process proceeds. Immediately after opening the purge valve, the gas close to the purge valve vents out. Simultaneously, the flow rate from other parts of the anode starts gradually to increase – first upstream of the anode gas recirculation pump and through the stack. Ultimately, with a high enough pressure difference between the anode inlet and purge valve, the gas flow in the recirculation pump might even reverse.

If the purge valve is open long enough, the purged gas hydrogen content gradually increases as the hydrogen depleted gas flows out and fresh fuel enters the anode. The purged gas hydrogen content increases as the flow rate through the stack increases, thus decreasing the fuel utilization per pass. When the fresh fuel front reaches the purge valve, the hydrogen content in the purged gas increases further. When the purged gas hydrogen content increases from the initial one, the purged gas can be thought of as being a mixture of fresh fuel ($n_{p,ff}$) and anode outlet gas ($n_p - n_{p,ff}$), as concluded in Appendix A:

$$y_{H_2,p} \cdot n_p = y_{H_2,ff} \cdot n_{p,ff} + y_{H_2,out,0} \cdot \left(n_p - n_{p,ff}\right) \tag{41}$$

Thus, the fraction of fresh fuel in purged gas can be expressed as follows:

$$\frac{n_{p,ff}}{n_p} = \frac{y_{H_2,p} - y_{H_2,out,0}}{y_{H_2,ff} - y_{H_2,out,0}} \tag{42}$$

This quantity can be used as a measure to determine a suitable purge length for the system. If $n_{p,ff}/n_p = 0$, the purged gas has the same H_2 mole fraction as the anode outlet gas before the purge. This might be an indication of a too short purge resulting in inefficient for water removal. From fuel efficiency point of view, the case of $n_{p,ff}/n_p = 0$ is optimal because minimum amount of H_2 is lost relative to total purged gas volume. The value of $n_{p,ff}/n_p$ cannot be less than zero. On the other hand, if $n_{p,ff}/n_p \gg 0$, the purged gas contains much hydrogen as a result of a too long purge. This results in poor fuel efficiency. The optimal $n_{p,ff}/n_p$ naturally depends on the system and the operating conditions.

The purged gas amount could, in principle, also be determined from the change in measured anode gas composition. However, this is possible only if the purge is sufficiently short and the purged gas composition is the same as the anode gas composition before the purge (see Eq. 40).

4.1.3 Recirculation rate

The hydrogen recirculation rate is challenging to measure as the anode gas typically consists of at least hydrogen, nitrogen, and both gaseous and condensed water. The total mass or volume flow rate can be determined with standard devices but usually not without introducing a significant flow resistance, which decreases the recirculation rate or adds power consumption. Gas composition transmitters are needed to be able to determine the composition of the recirculated gas and the fuel utilization per pass (or alternatively the stoichiometric ratio of hydrogen at the anode inlet).

The recirculation rate can be determined from the material balances if gas composition transmitters are available and the fuel feed composition is known. Using the notation introduced in Section 3 but again, gas phase mole fractions ($y_{i,j}$) instead of total mole fractions ($z_{i,j}$), the anode inlet molar flow rate is (Eq. 14 and Eq. 17):

$$\dot{n}_{in} = \dot{n}_{ff} + \dot{n}_r = \frac{\dot{n}_{ff} \cdot y_{i,ff} + \dot{n}_r \cdot y_{i,r}}{y_{i,in}} \tag{43}$$

or

$$\dot{n}_r = \dot{n}_{ff} \cdot \frac{y_{i,ff} - y_{i,in}}{y_{i,in} - y_{i,r}} \tag{44}$$

The recirculation rate can thus be computed when the molar feed rate and the mole fractions of one component are known in the feed, at the anode inlet, and in the recirculated gas (or in the anode outlet gas, $y_{i,r} = y_{i,out}$). The feed rate in a DEA setup equals the hydrogen consumption rate ($\dot{n}_{ff} = \dot{n}_{H_2,s} = \frac{I \cdot N_{cell}}{2 \cdot F}$), and the feed is typically almost pure (>99.9%) hydrogen. Therefore, the recirculation rate can be approximated based on load current and, e.g. the humidity measurements, as in publication [I]:

$$\dot{n}_r = \frac{I \cdot N_{cell}}{2 \cdot F} \cdot \frac{y_{H_2O,in}}{y_{H_2O,out} - y_{H_2O,in}} \tag{45}$$

The accuracy of Eq. 45 depends mainly on the accuracy of the humidity measurements. This accuracy decreases with an increase in recirculation rate because of the decrease in the water mole fraction difference in the nominator, as pointed out by Koski et al. [45]. Furthermore, humidity measurements close to the dew point decrease accuracy because of possible water condensation.

Assuming only three gas components (the three main components are usually hydrogen, water, and nitrogen), the anode gas composition at any point can be determined by one additional measurement of the concentration of either hydrogen or nitrogen at the anode inlet, at the anode outlet, or in the recirculation line. The remaining gas compositions are calculated using Eqs. 14-19 and recalling that $z_{i,out} = z_{i,r} = z_{i,p}$.

Alternatively, if a mass flow transmitter (e.g. a coriolis flow meter) is employed instead of a concentration transmitter, the composition in the recirculation line can be computed by solving the following set of equations:

$$\dot{m}_r = \sum \dot{m}_{i,r} = \sum \left(M_{w,i} \cdot \dot{n}_{i,r} \right) = \dot{n}_r \cdot \sum \left(M_{w,i} \cdot y_{i,r} \right) \tag{46}$$

$$\sum y_{i,r} = 1 \tag{47}$$

where $\dot{m}$ is the mass flow rate, M_w is the molar mass, and the summation is carried for all species $i = H_2, H_20, N_2$. Again, only three components must be assumed.

If neither a hydrogen concentration transmitter nor a mass flow transmitter is employed, the mass flow rate at the anode inlet or outlet can be estimated from the stack pressure drop, although with limited accuracy. Water condensation in gas channels might drastically change the flow resistance inside the stack. In addition, the pressure drop is not only a function of the mass flow rate but also of the gas composition and the temperature.

With knowledge of the molar flow rate of the recirculated gas and the gas composition, the fuel utilization per pass (or alternatively the anode inlet hydrogen stoichiometry) can be computed with Eq. 24.

4.2 Experimental setup and measurements

4.2.1 Test bench [I,II]

The test bench used in inert buildup and hydrogen purge measurements is shown in Figure 14. Hydrogen was fed through a pressure reducer and hydrogen recirculation was realized with a diaphragm pump (GD Thomas 118ZC20/24). Air was fed with a 24 VDC blower (Domel 497.3.265) and humidified using a membrane humidifier (PermaPure FC300-1660-10HP). The deionized cooling water was pumped (Johnson Pump, CM30P7-1) through a liquid-to-liquid heat exchanger (SWEP, B5Hx20/1PSC-S) with tap water flowing through the cold side.

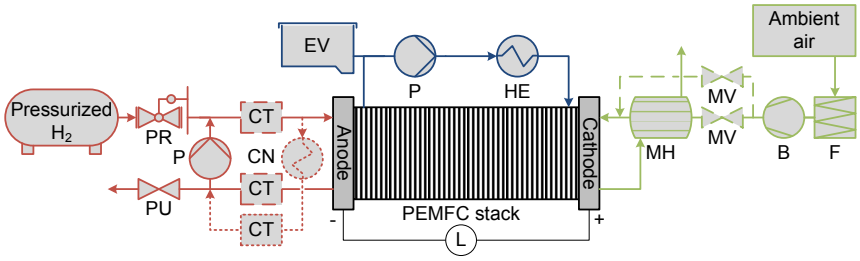

Figure 14. Simplified 8 kW PEMFC system scheme. B: blower, CN: condenser (and gas-liquid separator), CT: H_2 concentration transmitter, EV: expansion vessel, F: filter, HE: heat exchanger, L: electronic load, MFC: mas flow controller, MH: membrane humidifier, MV: manual valve, P: coolant pump, PU: purge valve. Dotted components are present only in 1st generation setup and dashed components are present only in 2nd generation setup.

In the initial (1st generation) test bench, used for inert buildup measurements, an aged Nedstack P8 64-cell stack with a 200 cm² active single cell area was employed. The anode inlet H_2 concentration was measured with a concentration transmitter (H2scan, HY-OPTIMA 740) placed in a slipstream. The slipstream was dried with an ice bath because the H_2 concentration transmitter did not tolerate condensed water.

In the 2nd generation test bench, used for hydrogen purge measurements, the aged stack was replaced with a new Nedstack P8 64-cell stack with a 200 cm^2 active single cell area. In addition, new H_2 concentration transmitters (Applied Sensor HPS-100) were used. The new transmitters tolerated water condensation, and they could be placed directly in the recirculation stream. The slipstream was removed. In the 2nd generation test bench, a setup for controlling the cathode inlet humidity was implemented with a humidifier bypass line and two manual valves, as shown in Figure 14.

4.2.2 Inert buildup measurements [I]

The measurements were conducted by operating the PEMFC system at constant load current levels ranging from 25 A to 175 A at 25 A steps, without hydrogen purges, and with a constant air flow rate corresponding to the air stoichiometry of 2.5 at 175 A current level. Each current level was maintained for several minutes, and the decrease in the H_2 mole fraction was recorded. The slipstream setup used for measuring the H_2 mole fraction caused a short (in the order of seconds) delay in mole fraction readings, which was negligible with the long measurement times employed.

4.2.3 Hydrogen purge measurements [II]

The objective of the hydrogen purge measurements was to find out how various purge parameters and system humidity levels affect purge efficiency (the removal of liquid water and inert gases) and system efficiency. The varied parameters were the purge length (t_p), the cathode inlet humidity ($T_{dew,cat,in}$), the criteria triggering a purge ($\Delta E_{trigger}$), and the purge type (single or double). $\Delta E_{trigger}$ is defined as the measured change in average cell voltage since the last purge.

The measurements were performed by first allowing the system to stabilize at operating conditions (120 A load current, 200 mbarg anode pressure, 2.5 air stoichiometry, and 60-60.5 °C coolant inlet temperature). After stabilization, 10 consecutive purge cycles were performed. The results were averaged from the successful purge cycles recorded.

4.3 Results and discussion

4.3.1 Inert buildup [I]

Figure 15 a shows the inert gas buildup at various stack load current levels as a function of time. The amount of inert gas ($n_{N_2,an}$) was calculated from measured hydrogen mole fractions using the ideal gas law. The solid straight lines show the linear fits made to the measurements.

The inert buildup rates calculated from the linear fits, few of which are shown in Figure 15 a, were plotted as a function of the stack current in Figure 15 b. As shown in the figure, the inert buildup rate is linearly proportional to the current. Assuming that membrane permeability is independent of the load current, the

slope of the line is proportional to the fuel purity, and the intercept equals membrane permeability, as discussed in Section 4.1.1.

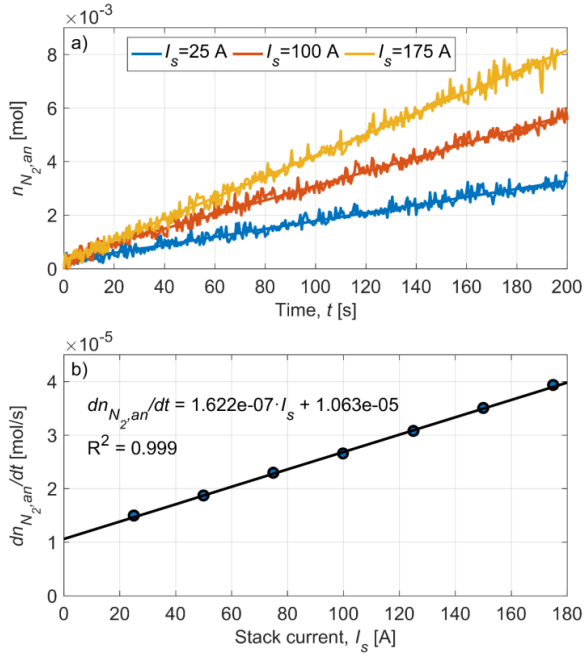

Figure 15. a) Amount of inert gas in anode loop ($n_{N_2,an}$) relative to t = 0 s and calculated from measured hydrogen mole fractions and plotted as a function of time with load currents 25 A, 100 A, and 175 A. Operating conditions: $p_{an,in} = 200$ mbarg; $p_{cat,in} = 130$ mbarg; anode gas recirculation pump control = 100%; $T_s = 58$ °C; inert concentration at t = 0 s varies in the range of 2.5 to 7.9 mole-% at the anode inlet and in the range of 8.0 to 9.8 mole-% at the anode outlet. b) The calculated inert gas buildup rate ($n_{N_2,an}/dt$) as a function of load current.

The inert concentration in fuel can be calculated using Eq. 33 and the slope ($d\dot{n}_{N_2,an}/dI$) in Figure 15 b:

$$y_{N_2,f} = \frac{2 \cdot 96\,485 \frac{\mathrm{C}}{\mathrm{mol}}}{64} \cdot 1.622 \cdot 10^{-7} = 5 \cdot 10^{-4} \tag{48}$$

In other words, according to measurements, the fuel used was 99.95% pure hydrogen. The measurements were conducted with grade 2.5 hydrogen (purity ≥ 99.5%).

The anode outlet humidity readings fluctuated during the inert buidup measurements presumably due to water condensation. This made the determination of water concentration unreliable. Therefore, water concentrations averaging between the anode inlet and outlet was employed in the calculations.

The partial volumes of anode inlet gas and anode outlet gas were not measured. The results presented here are based on estimated partial volumes (40% anode inlet and 60% anode outlet of the total anode volume 2.6 dm³). In contrast, the results presented in publication [I] were based on the assumption that the entire anode loop had the same H_2 concentration. The partial anode volumes

clearly affected the results, and, for precise measurements, the partial anode volumes should be determined.

4.3.2 Purge gas volume and composition [II]

Figure 16 shows the averaged flow rate profiles measured with three different hydrogen purge strategies: a) a double purge with $t_p = 200$ ms, b) a single purge with $t_p = 200\ ms$, and c) a single purge with $t_p = 400$ ms. The purges were performed with a $\Delta E_{trigger} = -3$ mV trigger criteria and at three levels of cathode inlet humidity: $T_{dew,cat,in} = 52, 55, 58$ °C.

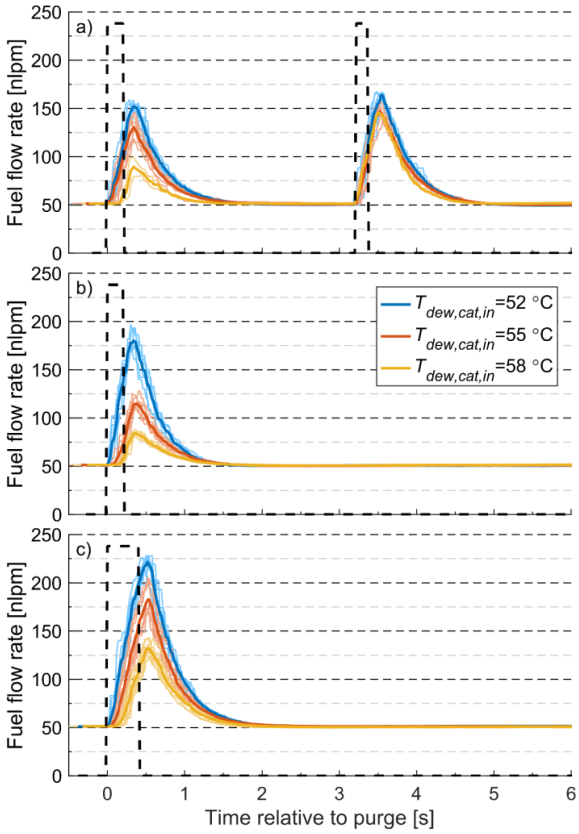

Figure 16. Fuel (hydrogen) feed flow rate profiles during a) double purge ($t_p = 200$ ms), b) single purge, ($t_p = 200$ ms) and c) single purge ($t_p = 400$ ms) performed with varying cathode inlet humidities ($T_{dew,cat,in} = 52, 55, 58$ °C) and with purge triggering criteria $E_{trigger} = -3$ mV. The dashed lines show the control signal of the purge valve (on/off). The averaged flow profiles are based on 6-9 (*) consecutive purge cycles (each plotted in lighter color) at each condition (see publication [II]). *The experiments with $T_{dew,cat,in} = 58$ °C in a)-figure were repeated only 2 times.

The effect of cathode inlet humidity on purge efficiency is clearly seen from the higher flow rates achieved at drier conditions. When a double purge is performed (Figure 16 a), the second flow rate peak is almost independent of the

cathode inlet humidity, which indicates that the first purge had flushed the liquid water from the gas channels. The double purge can be used to indicate purge efficiency [64].

Following the approach presented in Section 4.1.2, the amount and the composition of the purged gas can be determined based on hydrogen flow rate profile measurements (Figure 16) and changes in the hydrogen mole fraction. The results are shown in Figure 17.

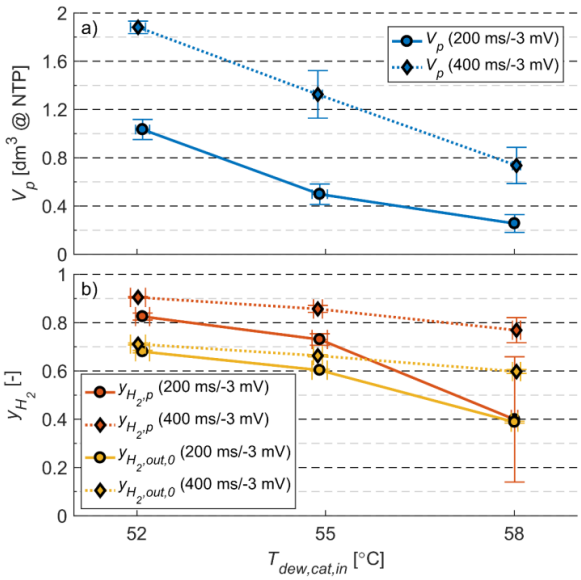

Figure 17. a) Volume of anode gas purged (V_p) and b) hydrogen mole fraction in purged gas ($y_{H_2,p}$) and hydrogen mole fraction at anode outlet before the purge ($y_{H_2,out,0}$) as a function of cathode inlet humidity ($T_{dew,cat,in}$). Operating parameters: $\Delta E_{trigger} = -3$ mV; $t_p = 200, 400$ ms. The error bars show the standard deviation of the measured values. Figure is a combination of two figures in publication [II]. The results are based on 6-9 consecutive purge cycles at each condition (see publication [II]).

As expected, the amount of purged gas decreased with an increase in cathode inlet humidity (Figure 17 a) due to a greater amount of condensed water and, consequently, an increase in flow resistance. Simultaneously, the composition of the purged gas approached that of the anode outlet before the purge (Figure 17 b), especially with $t_p = 200$ ms. This indicates that the change in flow rate during the purge became too sluggish for the temporary increase in fuel utilization per pass to affect the composition of the purged gas.

Figure 18 shows the fraction of fresh fuel in the purged gas ($n_{p,ff}/n_p$) as a function of cathode inlet humidity. At the most humid conditions ($T_{dew,cat,in} = 58$ °C) and with a short purge $t_p = 200$ ms, $n_{p,ff}/n_p$ essentially dropped to zero (Figure 18 a), which from a fuel efficiency point of view is optimal. Figure 18 b shows the amount of purged gas at this condition, $V_p = 0.26$ dm^3 @ NTP. This corresponds to the maximum volume that could be purged in this system with

minimum hydrogen concentration in the purged gas. For comparison, the total anode volume was ca 2.6 dm³.

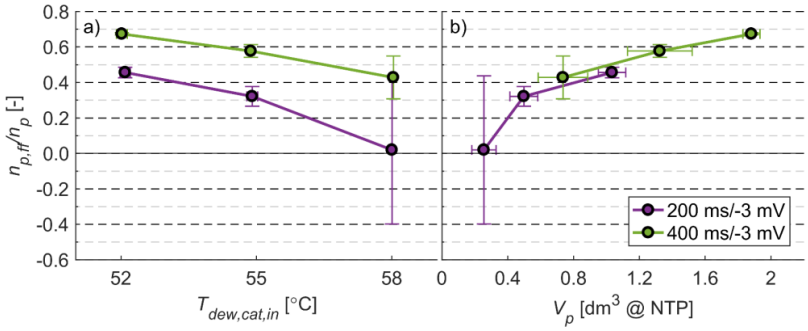

Figure 18. Fraction of fresh hydrogen in purged gas ($n_{p,ff}/n_p$) as a function of a) cathode inlet humidity ($T_{dew,cat,in}$) and b) purged volume (V_p). Operating parameters: $\Delta E_{trigger} = -3$ mV; $t_p = 200, 400$ ms. The error bars show the standard deviation of the measured values. Figure modified from publication [II]. The results are based on 6-9 consecutive purge cycles at each condition (see publication [II]).

4.3.3 Effect of inert buildup on concentration polarization [II]

The voltage drop that triggered the hydrogen purge ($\Delta E_{trigger} = -3, -6, -9$ mV) is related to the decrease in reactant concentration at catalyst sites. The Nernst equation (Eq. 9) relates reactant concentrations to cell voltage. Therefore, the theoretical voltage drop can be calculated with Eq. 27, which relates the measured hydrogen partial pressures at the anode ($p_{H_2,an}$) and the expected voltage drop. As the hydrogen partial pressure varies inside the cell, the hydrogen partial pressure is averaged between the cell inlet and outlet:

$$\overline{p_{H_2,an}} = \frac{p_{an,in} \cdot y_{H_2,in} + p_{an,out} \cdot y_{H_2,out}}{2} \tag{49}$$

The temperature (T) in Eq. 27 is the anode outlet temperature and is believed to represent well the conditions inside the stack.

Figure 19 shows the results. As seen, the calculated voltage drop as a result of dilution of the anode gas by the inert gases is roughly half of the measured voltage drop. This implies that the hydrogen partial pressure in the gas channel deviates remarkably from the catalyst site hydrogen partial pressure. In other words, the mass transfer resistance between the anode gas channels and the catalyst sites (i.e. in the GDL) can be notable and should be taken into account when designing the hydrogen supply and recirculation in PEMFC system.

The cathode inlet humidity does not seem to affect the ratio of theoretical to measured voltage drop even though the changes in water activity were disregarded when calculating the theoretical voltage drop. This can be due to the low operating temperature and that liquid water was present. The activity of liquid water is close to one and is independent of pressure.

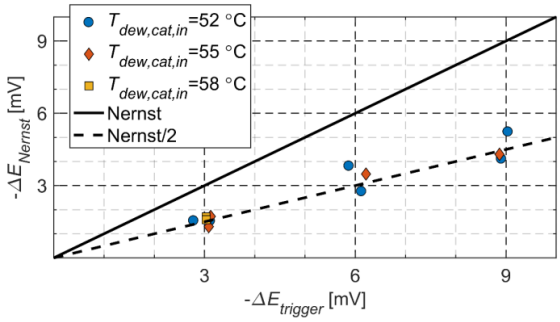

Figure 19. Measured voltage drop between purges ($\Delta E_{trigger}$) compared to the voltage drop calculated using measured hydrogen mole fractions and the Nernst equation (ΔE_{Nernst}). Operating parameters: $T_{dew,cat,in} = 52, 55, 58$ °C; $\Delta E_{trigger} = -3, -6, -9$ mV; $t_p = 200, 400$ ms; $p_{an,in} = 186 - 217$ mbarg; $u_{f,pp} = 54 - 79\%$. Figure modified from publication [II]. The results are based on 6-9 consecutive purge cycles at each condition (see publication [II]).

Strictly speaking, the Nernst equation holds only at OCV when no current is applied [6]. Therefore, when applying Eq. 27 in calculating the theoretical polarization caused by varying reactant concentration, one must assume that the reactant concentration does not influence any of the other polarization phenomena that take place in a PEMFC. For example, an increase in the concentration of oxygen at the cathode is known to reduce the cathode activation loss owing to higher catalyst site coverage [6]. In contrast, the anode activation loss is known to be negligible [6] and, thus, does not need to be considered here.

4.3.4 Effect of hydrogen purge on fuel and stack efficiencies [II]

The amount of hydrogen lost during hydrogen purges affects the total efficiency of the system through fuel efficiency. Figure 20 shows the measured fuel efficiency (η_f), stack efficiency (η_s), and their combined efficiency (η_c), all as a function of purge-triggering voltage and as a function of the cathode inlet humidity. The efficiencies are computed as follows:

$$\eta_f = \frac{\dot{n}_{H_2,s}}{\dot{n}_{H_2,s}+\dot{n}_{H_2,p}} = \frac{\dot{n}_{H_2,s}}{\dot{n}_f \cdot y_{H_2,f}} = 1 - f_p \tag{50}$$

$$\eta_s = \overline{\eta_{cell}} = \frac{E_{cell,avg}}{E^0} = \frac{2 \cdot F \cdot E_{cell,avg}}{\Delta H^0} \tag{51}$$

$$\eta_c = \eta_f \cdot \eta_s = \frac{\dot{n}_{H_2,s}}{\dot{n}_{H_2,s}+\dot{n}_{H_2,p}} \cdot \frac{2 \cdot F \cdot E_{cell,avg}}{\Delta H^0} = \frac{P_s}{(\dot{n}_{H_2,s}+\dot{n}_{H_2,p}) \cdot \Delta H^0} \tag{52}$$

where it has been recognized that stack efficiency equals average cell efficiency ($\overline{\eta_{cell}}$). The stack efficiency is calculated based on the LHV of hydrogen at standard conditions, $\Delta H^0 = -241830$ J/mol [16].

As shown in Figure 20 a, frequent purges ($\Delta E_{trigger} = -3$ mV) result in poorer fuel efficiency because more hydrogen is vented out. Nonetheless, the highest combined efficiency was achieved at these same conditions with the two tested purge lengths and with two different cathode inlet humidities (Figure 20 c). This underlines the importance of one of the main purposes of the hydrogen purge:

to prevent concentration polarization through the removal of impurities. In addition, a close to 100% fuel efficiency increases the risk of (local) fuel starvation, thus compromising stack lifetime.

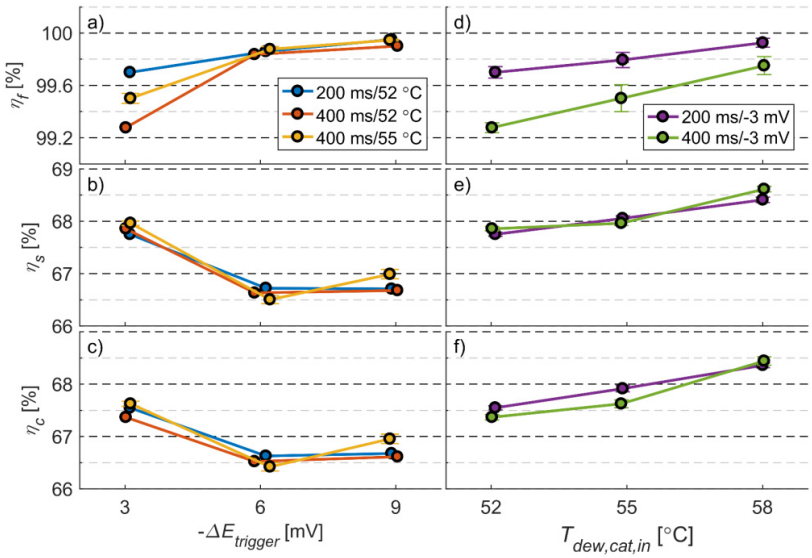

Figure 20. a) & d) Fuel efficiency (η_f, not including fuel crossover), b) & e) stack efficiency (η_s based on the LHV of hydrogen), and c) & f) combined efficiency (η_c) as function of purge-triggering criteria ($\Delta E_{trigger}$, a-c) and as function of cathode inlet dew point temperature ($T_{dew,cat,in}$, d-f). Operating parameters: $t_p = 200, 400$ ms; $T_{dew,cat,in} = 52, 55, 58$ °C. The error bars show the standard deviation of the measured values. Figure is a combination of two figures in publication [II]. The results are based on 6-9 consecutive purge cycles at each condition (see publication [II]).

The combined efficiency also increased with an increase in cathode inlet humidity, as shown in Figure 20 f. This is partly due to higher fuel efficiency (Figure 20 d) and partly due to higher stack efficiency (Figure 20 e). Compared to the short purge ($t_p = 200$ ms), the long purge ($t_p = 400$ ms) appears to improve stack efficiency and the combined efficiency at high-humidity conditions despite poorer fuel efficiency (Figure 20 f). This underlines the importance of the second main purpose of the hydrogen purge: to guarantee stable stack operation by the removal of condensed water from the gas channels.

5. Hydrogen Humidification

Even with hydrogen recirculation, the anode inlet humidity may be inadequate, as was discussed in Section 3. The work presented in publication [III] targeted designing and manufacturing a hydrogen humidifier for a 50 kW PEMFC system [27,65], which is shown in the schematic diagram in Figure 21. A bubble humidifier was regarded as most suitable for this purpose mainly because of its simple, gastight construction and its continued humidification after power failure.

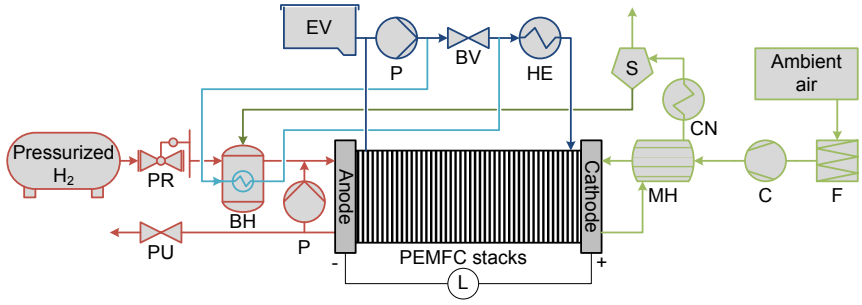

Figure 21. Simplified schematic diagram of the 50 kW PEMFC pilot plant. BH: bubble humidifier, BV: bypass valve, C: compressor, CN: condenser, EV: expansion vessel, F: filter, HE: heat Exchanger, L: load, MH: membrane humidifier, P: pump, PR: Pressure reducer, PU: Purge Valve, S: gas-liquid separator.

With a lack of references, the bubble humidifier was designed in-house with safe tolerances. Effort was put into characterizing the humidifier and validating the implemented model. The validated model was then employed for studying bubble humidifier control and for suggesting improvements in bubble humidifier design.

5.1 Bubble humidifier design and construction [III]

The design of the bubble humidifier is shown in Figure 22. The bubble column was a 1.525 m high DN 400 pipe. Both ends of the column were made of pipe caps; the bottom was welded to the pipe and the cover was removable and fastened with a flange fitting.

The gas inlet and outlet were located in the cover of the bubble column. The gas inlet was connected with a pipe to the sparger that was located at the bottom of the column. Two spargers were manufactured, one with 486 pieces of 1 mm

diameter laser-cut holes and the other with 65 pieces of 2 mm diameter holes. The sparger holes were sized to cause a gas pressure drop large enough to overcome the hydrostatic pressure inside the sparger and to push the water out through a hole drilled at the bottom. This enabled an even distribution of gas flow through the sparger holes. The humidifier gas outlet was open to the gas volume in the top part of the column.

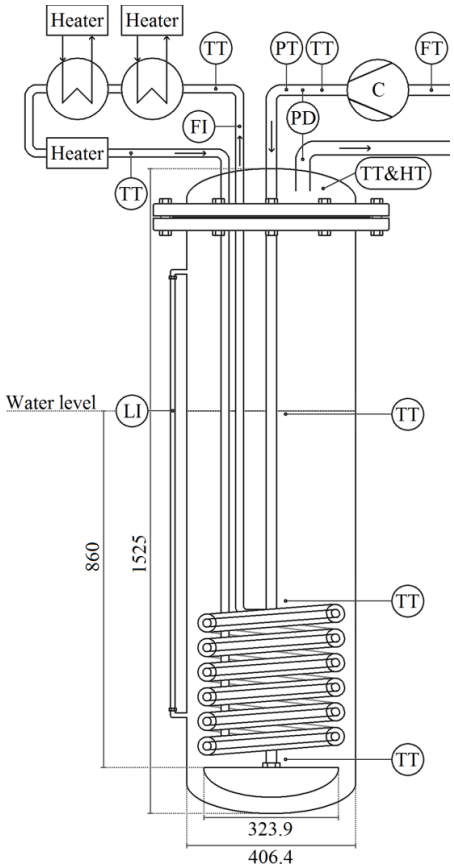

Figure 22. Bubble humidifier design and test setup. C: compressor, FI: flow rate indicator, FT: flow rate transmitter, HT: humidity transmitter, LI: level indicator, PD: differential pressure transmitter, PT: gauge pressure transmitter, TT: temperature transmitter. Dimensions are in mm. Figure from publication [III].

The heating water inlet and outlet were also located in the cover, and they were connected in a closed loop with the heat exchanger. The heat exchanger was made of 6 m long DN 15 finned pipe turned into a coil, and it had a total heat exchange area of ca 3.9 m^2. A fraction of the PEMFC system coolant water was circulated through the bubble column (controlled by a throttle) to supply the heat needed.

The water needed to replace the humidity leaving with the gas was supplied from the bottom of the column. The water supplied was condensed from the PEMFC stack cathode outlet and filtered through deionization filters. Therefore, the PEMFC system was completely self-contained with respect to water and heat

needed by the bubble humidifier. The water level was visible through a transparent tube located on side of the column. When operated in the power plant, capacitive water level sensors were mounted onto the transparent pipe to allow for automated water level control [27].

All bubble humidifier metal parts were made of corrosion-resistant steel (EN 1.4404), and the welds in contact with the water-gas mixture were passivated by pickling. In addition, the entire bubble humidifier was insulated with foamed plastic to minimize heat losses.

5.2 Bubble humidifier characterization [III]

The bubble humidifier was characterized using the setup illustrated in Figure 22. Ambient air was used instead of hydrogen, and it was supplied with a roots compressor (Ogura, TX12) at flow rates of 275, 550, and 840 nlpm. These flow rates correspond approximately to the hydrogen flow rates at low power (75 A), nominal power (150 A), and full power (230 A). The temperature and humidity of the humidifier outlet gas were measured with a Vaisala HMM-211 transmitter.

The heating water was supplied employing three heaters with a combined maximum heating power of 5.8 kW. The heating water was supplied at two flow rates (ca 8 lpm and 13.5 lpm) and three humidifier inlet temperatures (55 °C, 60 °C, and 65 °C). Both the heating water inlet and outlet temperatures were measured with K-type thermocouples.

During humidifier characterization, the water level was maintained at a constant 0.86 m above the sparger. Both of the spargers (the one with 1 mm holes and the one with 2 mm holes) were tested.

5.3 Bubble humidifier modelling [III]

The bubble humidifier model developed and presented in publication [III] can be divided into two parts: 1) heat transfer from heating water to bubble column, and 2) mass transfer of water (evaporation) from bubble column to bubbles. The principle is illustrated in Figure 23.

The heat transfer from heating water (subscript *h*) to bubble column media (subscript *l*) was modelled by solving the energy balance equations for two control volumes: 1) the bubble column (subscript *bc*) with all content including the gas (subscript *g*) and the heat exchanger with the exclusion of heating water, and 2) the heating water. The energy balances for these control volumes are:

$$\left(V_{liq} \cdot \rho_{liq}/M_{w,liq} \cdot C_{p,liq} + m_{bc} \cdot \underline{C_{bc}}\right) \cdot dT_{liq}/dt = \dot{Q} - \dot{n}_{gas} \cdot \int_{T_{gas,in}}^{T_{gas,out}} C_{p,gas} dT_{gas} - \dot{n}_{liq} \cdot \Delta H_{vap}(T_{liq}) \quad (53)$$

$$0 = \dot{Q} + \dot{n}_h \cdot \int_{T_{h,in}}^{T_{h,out}} C_{p,h} dT_h \quad (54)$$

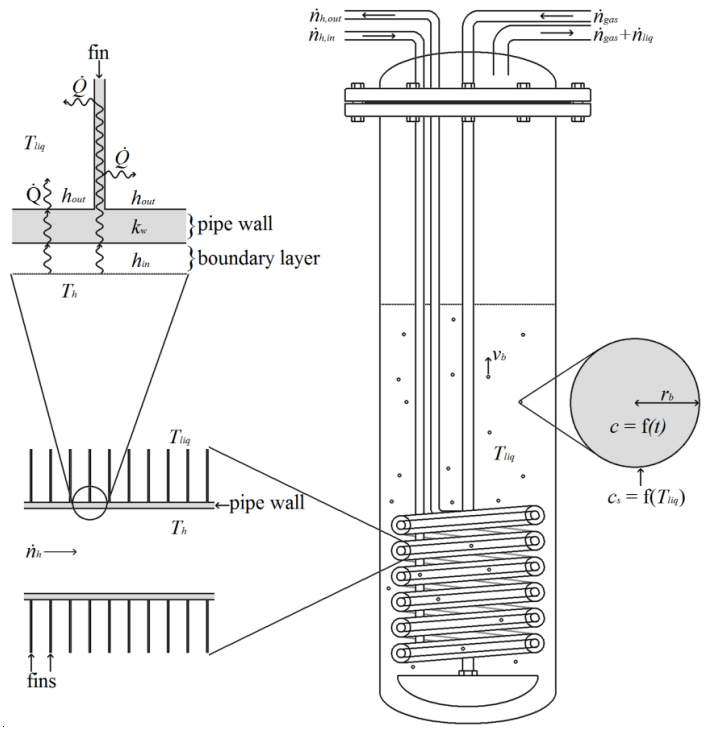

Figure 23. Humidifier model principle. $\dot{Q}$: heat transfer rate from heating water, T_{liq}: temperature of bubble column water, T_h: temperature of heating water, h_{out}: heat transfer coefficient outside the heat exchanger, h_{in}: heat transfer coefficient inside the heat exchanger, k_w: thermal conductivity of heat exchanger wall, $\dot{n}_h$: molar heating water flow rate, $\dot{n}_{gas}$: molar gas flow rate, $\dot{n}_{liq}$: evaporation rate of water in bubble column, v_b: bubble rise velocity, r_b: bubble radius, c: water concentration inside bubble, c_s: water concentration at the bubble surface, t: time. Figure modified from publication [III].

On the left hand side of Eq. 53, V_{liq} is the volume of (liquid) water in bubble column, ρ_{liq} is the density of (liquid) water in bubble column, $M_{w,liq}$ is the molar mass of water, $C_{p,liq}$ is the heat capacity of (liquid) water in bubble column, and T_{liq} is the temperature of bubble column content. On the right hand side of Eq. 53, $\dot{Q}$ is the heat transfer rate, $\dot{n}_{gas}$ is the molar flow rate of gas, T_{gas} is the gas temperature, $\dot{n}_{liq}$ is the molar evaporation rate of water in the bubble column, and ΔH_{vap} is the latent heat of water. In Eq. 54, $\dot{n}_h$ is the molar flow rate of heating water, $C_{p,h}$ is the heat capacity of heating water, and T_h is the temperature of heating water. The heat transfer rate ($\dot{Q}$) depends on the heat transfer resistance inside the heat exchanger pipe (R_{in}), through the pipe (R_{wall}), and outside the pipe (R_{out}):

$$\dot{Q} = \Delta T_{lm}/R_{tot} = \Delta T_{lm}/(R_{in} + R_{wall} + R_{out}) \quad (55)$$

where the logarithmic mean temperature difference (ΔT_{lm}) is computed from heating water inlet and outlet temperatures ($T_{h,in}$, $T_{h,out}$) and the temperature of bubble column content as follows:

$$\Delta T_{lm} = \left(T_{h,in} - T_{h,out}\right)/ln\left(\{T_{h,in} - T_{liq}\}/\{T_{h,out} - T_{liq}\}\right), \quad (56)$$

the heat transfer resistance inside the heat exchanger pipe depends on the convective heat transfer coefficient inside the heat exchanger (h_{in}) and the pipe inside area (A_{in}) as follows:

$$R_{in} = 1/(h_{in} \cdot A_{in}), \tag{57}$$

the heat transfer resistance through the pipe depends on the pipe inner and outer radius (r_{in}, r_{out}), the pipe inside area, and the thermal conductivity of heat exchanger wall (k_w) as follows:

$$R_{wall} = r_{in} \cdot ln\{r_{out}/r_{in}\}/(A_{in} \cdot k_w), \tag{58}$$

and the heat transfer resistance outside the pipe depends on the convective heat transfer coefficient outside the heat exchanger (h_{out}), the heat exchanger pipe outside area (A_{out}), the fin efficiency (η_{fin}), and the fin area (A_{fin}) as follows:

$$R_{out} = 1/\big(h_{out} \cdot \{A_{out} + \eta_{fin} \cdot A_{fin}\}\big) \tag{59}$$

In the bubble column energy balance equation (Eq. 53) and in calculating the logarithmic mean temperature difference (Eq. 56), uniform bubble column temperature was assumed.

The convective heat transfer coefficients (h_{in} and h_{out}) were calculated using correlations found in literature ([66,67] and [68,69], respectively). The fin efficiency in Eq. 59 accounts for a decline in fin temperature when approaching its tip, and is calculated as suggested in reference [70].

The mass transfer of water to the gas bubbles was assumed to occur solely by diffusion and can be thought to represent a worst-case scenario. First, the bubble surface was assumed to be saturated with water vapor at the temperature of the bubble column media. Assuming ideal gas behavior, the saturated water concentration is:

$$c_s = \frac{p_{vap}(T_{liq})}{R \cdot T_{liq}} \tag{60}$$

The volume-average water concentration inside the bubble ($\bar{c}$) was calculated as follows [71]:

$$\frac{\bar{c}}{c_s} = 1 - exp\{-1.5 \cdot Fo \cdot \overline{Sh}\} \tag{61}$$

where the time averaged Sherwood number ($\overline{Sh}$) and the Fourier number (Fo) are defined as follows:

$$\overline{Sh} = 4/\sqrt{\pi \cdot Fo} + \frac{63.237 \cdot \sqrt{Fo} + 71.892 \cdot Fo + \pi^2/1.5 \cdot 116.673 \cdot Fo^{1.5}}{1 + 33.616 \cdot \sqrt{Fo} + 45.628 \cdot Fo + 116.673 \cdot Fo^{1.5}} \tag{62}$$

$$Fo = \frac{D_{H_2O} \cdot \Delta t}{r_b^2} \tag{63}$$

where D_{H_2O} is the water diffusion coefficient, Δt is the bubble retention time, and r_b is the bubble radius. The radius of bubbles formed in the sparger was

calculated using correlations suggested by Bhavaraju et al. [72]. The bubble retention time was calculated based on the water level and the rise velocity, of which the latter was calculated using a correlation by Grace et al. [73].

5.4 Results and discussion [III]

A comparison of simulated and measured bubble column temperatures during characterization tests is shown in Figure 24. As can be seen, the match is good: the average deviation of bubble column temperature (T_{liq}) was less than 0.3 °C at all tested conditions.

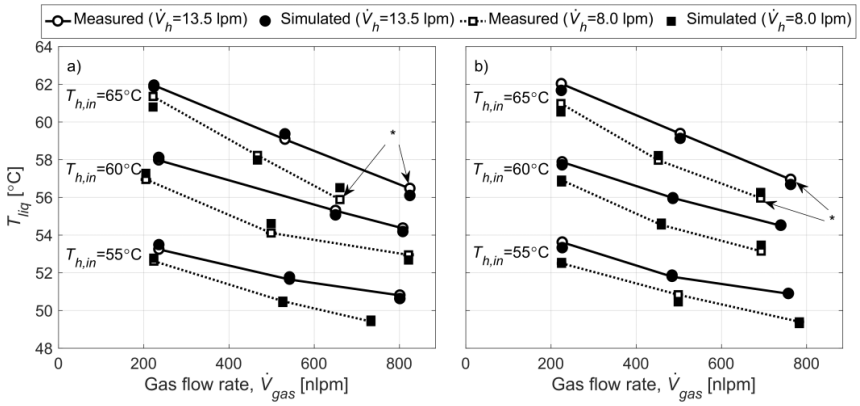

Figure 24. Time average bubble column temperature (T_{liq}) as a function of air flow rate ($\dot{V}_{gas}$). Sparger orifice size: a) 1 mm, b) 2 mm. *Measurements during which the setpoint temperature could not be maintained. Figure modified from in publication [III].

The measured approach dew point temperatures relative to heating water inlet temperatures were in the range of 1.8 to 8.7 °C. The corresponding relative humidities (RH) were in the range of 67% to 92% at heating water inlet temperature. At a gas flow rate corresponding to low system power, the approach dew point temperature was 3.1 °C when heating water was supplied at 65 °C and at a 13.5 lpm flow rate. At a gas flow rate corresponding to nominal and full power, the approach dew point increased to 5.9 °C and 8.5 °C, respectively.

The measurements with a 13.5 lpm heating water flow rate resulted in a 0.6-2.3 °C lower approach dew point temperature (2.4 to 7.7% higher RH) compared to measurements conducted with an 8 lpm heating water flow rate. The effect of heating water flow rate increased with increasing gas flow rate.

Using the sparger with larger holes resulted in a lower approach dew point temperature in most cases. However, the differences were small.

The approach dew point temperatures above were calculated from the heating water inlet temperature and the surface temperature of the bubble column water – not the gas outlet dew point temperature. This was due to the assumed condensation of water vapor from the gas phase during characterization tests and a resulting drop in dew point temperature.

Figure 25 shows the results of water mass transfer simulations when the mass transfer rate is assumed to be limited by the diffusion rate in the gas bubbles. In reality, some convection also occurs and, thus, the simulated mass transfer rates were interpreted as worst-case scenarios. The results show that bubbles with a ca 1 cm diameter (as in the present study) require roughly a 5 cm water bed to reach saturation. In practice, fitting a large enough heat exchanger in such a low water bed is challenging. Therefore, it is safe to say that the mass transfer rate does not limit the performance of the humidifier but the heat transfer rate does. In addition, it is justified to use the surface temperature of the bubble column water in calculating the approach dew point temperatures of the humidified gas.

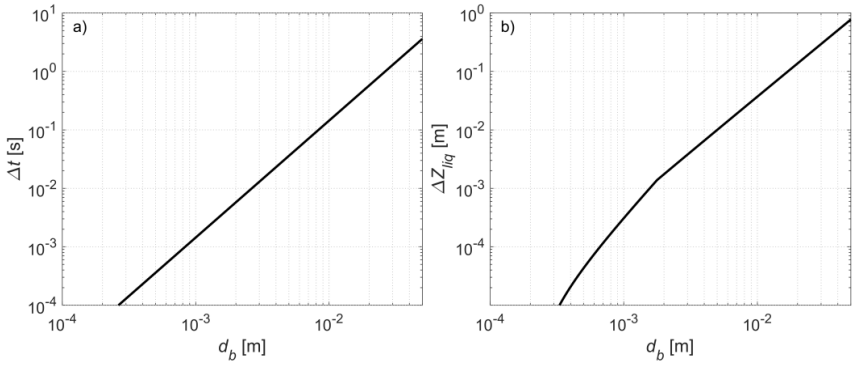

Figure 25. a) Time (Δt) and b) water bed height (ΔZ_{liq}) needed for water vapor to reach 99.9% of equilibrium concentration ($= c_s$) in spherical hydrogen bubbles due to pure diffusion at $T_{liq} = 60$ °C as a function of hydrogen bubble diameter ($d_b = 2 \cdot r_b$). Figure modified from publication [III].

The high gas pressure drop is one of the most cited disadvantages of a bubble humidifier (e.g. [47,49]). The results shown in Figure 25 suggest that this is not necessarily true. The 5 cm water bed height required to reach saturation is equivalent to a 5 mbar hydrostatic pressure drop. With the pressure drop introduced in the spargers (≤ 15 mbar [65]), the total pressure drop would be approximately 20 mbar – a figure comparable to many other humidifier types. However, as pointed out above, the heat exchanger needs careful design to accomplish this if placed inside a bubble humidifier. Another option is to heat the humidifier water in an external heat exchanger.

Since humidifier performance is not mass transfer limited according to the simulations, it must be heat transfer limited. Thus, humidifier performance can be improved by improving heat transfer. In practice, the means to improve humidifier performance are limited to increasing the heating water flow rate and the heat exchange area. The heat transfer rate also depends on the gas flow rate (through heat consumption and a change in temperature difference) and the heating water inlet temperature. However, these parameters are typically fixed by system design.

Figure 26 shows the simulated effect of the heating water flow rate and heat exchange area on the humidifier outlet dew point temperature reached. According to simulations, a 5.7 °C approach dew point temperature is reached at nominal system power (i.e. with 558 nlpm hydrogen gas flow rate), with 13.5 lpm heating water flow rate, and with 3.9 m² heat exchange area. Doubling the heating water flow rate to 27 lpm decreases the approach dew point temperature to 4.3 °C, whereas, doubling the heat exchange area to 7.8 m², decreases the approach dew point temperature to 4.1 °C. However, a high heating water flow rate translates into a high pressure drop and additional power consumption of the coolant pump. A large heat exchanger, on the other hand, is more expensive. Thus, sizing the bubble humidifier is a compromise between performance and cost.

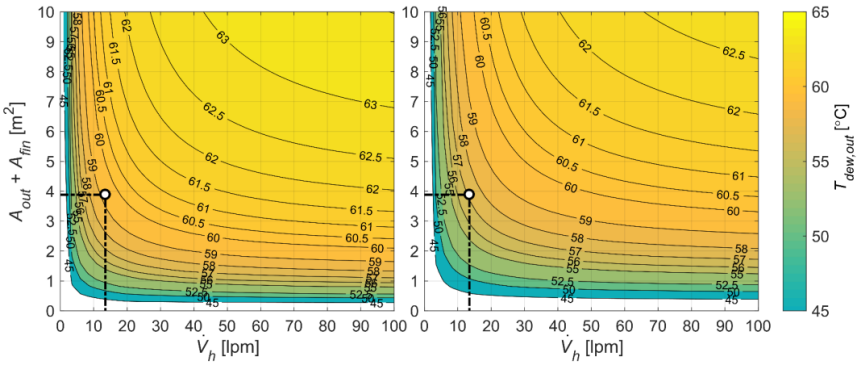

Figure 26. Simulated steady state bubble humidifier outlet dew point temperature ($T_{dew,out}$) as a function of heating water flow rate ($\dot{V}_h$) and heat exchange area ($A_{out} + A_{fin}$). Hydrogen gas flow rate ($\dot{V}_{gas}$) is 558 nlpm (left) and 856 nlpm (right). Heating water inlet temperature is $T_{h,in} = 65$ °C. The dew point temperature attained with 3.9 m² heat exchanger and 13.5 lpm heating water flow rate is marked in the figures. Figure modified from publication [III].

The membrane's proton conductivity, and, consequently, fuel cell performance, improves with increasing humidity level. However, operating conditions that are too humid cause unstable fuel cell performance because of water condensation in the gas channels. The water generation rate and, consequently, the humidity level in the fuel cell is proportional to the load current. Therefore, controlling the inlet gas humidity may be desired. With a bubble humidifier, the humidification can be controlled either by varying the heating water flow rate or by varying the heat transfer area, as shown in Figure 26. The heating water flow rate can be varied with a (proportional) valve or a pump. The heat transfer area can be varied, for example, by passing heating water either through one or several parallel heat exchangers all submerged in the bubble column.

5.5 Bubble humidifier in 50 kW power plant

The bubble humidifier was successfully operated for 4,400 hours and it provided sufficient humidification for the 50 kW PEMFC pilot plant [27]. The only problem encountered was the too efficient humidification at low gas flow rates, which caused stack flooding during system startup. In addition, minor corrosion

was observed in the heat exchanger welds after characterization experiments conducted with air.

A solution to the too efficient humidification at low gas flow rates could be a humidifier bypass [27] or controllable heat transfer, as discussed in Section 5.4. The rather slow humidifier control discussed in publication [III] could be speeded up with a decrease in the amount of water in the humidifier. This would allow more rapid changes in humidification, but it would also place more strict requirements on the humidifier control. The amount of water used in publication [III] was excessive due to the rapid mass transfer in evaporation.

6. Hydrogen Recirculation

One of the main challenges of mechanical hydrogen recirculation pumps is their wear and, ultimately, breakdown [27]. One option for a mechanical hydrogen recirculation pump is to use a single fixed geometry ejector and its discrete control in a PEMFC system. This hydrogen recirculation scheme operates without any moving parts apart from the solenoid valves for hydrogen supply and hydrogen purge. Thus, it provides a hydrogen supply and recirculation setup with ultimate simplicity and at a potentially very low price compared to mechanical hydrogen recirculation pumps. The downside of employing a single fixed geometry ejector with discrete control is, however, a more challenging system operation since the ejector operation is limited to discrete points.

This chapter discusses the application of a single, fixed geometry ejector and discrete flow control in PEMFC system. First, a 2D CFD modelling approach to the ejector is introduced and the modelling accuracy is discussed (publication [IV]). Second, the discrete control approach, its challenges, and management strategies are discussed (publication [V]). Finally, the capabilities of a system employing the ejector and discrete control method for rapid load changes are studied (publication [VI]).

6.1 Ejector design and manufacturing [IV]

The work presented in publications [IV-VI] is based on the same ejector, the design of which is shown in Figure 27. The primary nozzle was sized based on isentropic flow relations, assuming critical flow and ideal gas behavior. The rest of the ejector dimensions were chosen based on previous work found in the literature [74–76]. The ejector design targeted a wide operating range in a 5 kW PEMFC system.

The ejector was manufactured by 3D printing at AM Finland Oy with the direct metal laser-sintering technique. The critical ejector surfaces were polished at the Finnish School of Watchmaking.

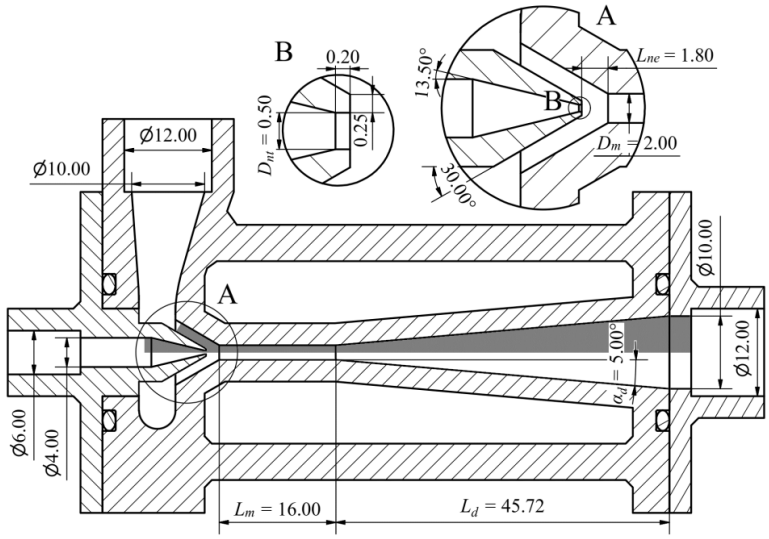

Figure 27. Geometry of ejector employed in publications [IV-VI]. Figure from publication [IV].

6.2 Ejector modelling [IV]

Modelling always involves assumptions and simplifications. Therefore, the modelling approach must be validated against experimental data before any conclusions are drawn based on the results.

The modelling work in publication [IV] aimed at validating a 2D axisymmetric CFD modelling approach. The differences in the accuracies of three turbulence models (SST k-ω, RNG k-ε, and Realizable k-ε) in predicting ejector performance were studied in particular.

The modelling was conducted with ANSYS Fluent v16.0 software installed on workstation with an 8-core CPU and 16 GB RAM. The flow was assumed compressible and steady. The fluid was treated as an ideal gas, and both gravity and phase transitions were neglected. The modelled domain (shaded area in Figure 27) was spatially discretized with structured quadrilateral meshes. Mesh-indepence tests were conducted. The smallest mesh tested had ca 48,000 cells and the finest had ca 753,000 cells. The balance equations were solved with a pressure-based solver. Second-order interpolation and upwind schemes were employed for the pressure and the balance equations, respectively. The ejector walls were assumed smooth and adiabatic, and the no-slip condition was applied.

6.3 Ejector characterization [IV]

Publication [IV] presents the characterization of two ejectors; the custom-made ejector and a commercially available ejector (SMC, ZH05S-X267) sold mainly for vacuum generation.

The characterization was conducted with the test setup shown in Figure 28. In the setup, the ejector primary and secondary inlets were fed with either air or

hydrogen. The pressure of both inlets could be varied independently with manual pressure regulators. The secondary inlet gas passed through a liquid-to-gas membrane humidifier before being fed to the ejector. The secondary inlet gas humidity could be controlled by varying the liquid temperature and flow rate. Ejector outlet pressure was controlled with a manual backpressure regulator.

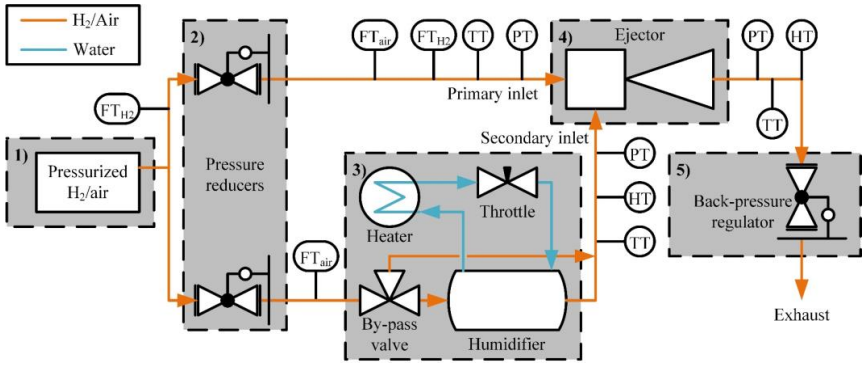

Figure 28. Ejector characterization test setup. TT: temperature transmitter, FT: flow rate transmitter, PT: gauge pressure transmitter, HT: humidity transmitter. Figure from publication [IV].

6.4 Ejector discrete control [V]

In publication [V], a discrete ejector-primary-gas-control system (EPC) based on three solenoid valves and flow restrictions was designed and implemented.

The principle of the discrete EPC is to fluidically connect two or more (in this case three) flow restrictions in parallel. By allowing flow either through one or several of these flow restrictions, discrete flow rate levels (corresponding to PEMFC stack load current levels) is achieved. The solenoid valves used for enabling/disabling flow through a restrictor can also act as the restrictors if suitable sizes are available. The principle of the discrete EPC is shown in Figure 29.

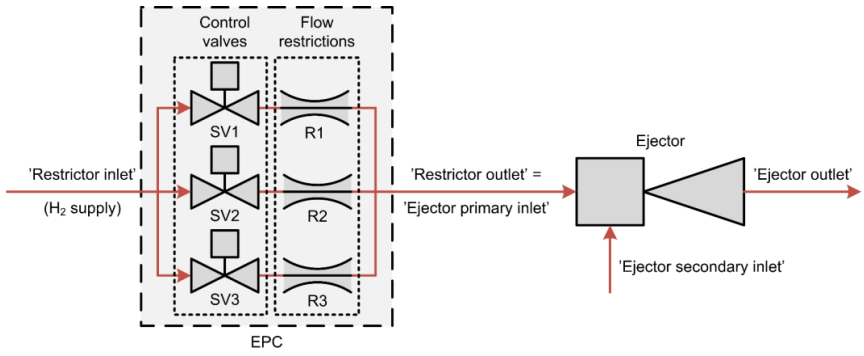

Figure 29. Principle of the discrete EPC. Figure from publication [V].

The sizing of flow restrictions can be done in various ways. One approach that results in evenly spaced flow rate levels is obtained when the smallest flow restrictor (or valve) is sized to pass a flow rate that equals the desired flow rate difference between two levels. The next restrictors should be sized to pass a flow

rate twice that of the previous restrictor. This sizing approach was employed in publication [V]. However, because of a hydrogen supply pressure that was too low (ca 16 barg was required while only ca 9 barg was applied), the evenly spaced flow rate levels could not be achieved throughout the operating range. Table 4 shows the stack currents achieved with the EPC sizing employed in the present work.

Table 4. Measured 50-cell stack load current levels achieved with the current fuel supply system operated at 8.5-8.7 barg restrictor inlet pressure and 0.05 to 0.1 barg anode pressure. Table reproduced from publication [V].

Load level [#]	*Control valve open*	*Restrictor inlet pressure [barg]*	*Ejector primary pressure [barg]*	*Stack current [A]*	*Stack current increment [A]*
0	-	8.7	-	0	-
1	1	8.6	0.5 (*)	29 (*)	29
2	2	8.6	1.6	56	28
3	1, 2	8.5	2.8	83	27
4	3	8.5	4.0	111	27
5	1, 3	8.5 (**)	5.0	133	22
6	2, 3	8.5 (**)	5.7	149	16
7	1, 2, 3	8.5 (**)	6.3	162	14

(*) Flow in ejector primary nozzle is subcritical, i.e. the primary flow rate (and the achievable stack current) depends on both ejector primary and outlet pressure.
(**) Flow in restrictors is subcritical, i.e. the current step increment size decreases.

One drawback of the discrete EPC is that the hydrogen supply rate cannot be adjusted from the levels fixed in the design stage. If the supply rate deviates from the consumption rate, anode pressure will vary. The rate of variation in anode pressure due to a mismatch between hydrogen supply and consumption rate is inversely proportional to the anode volume. Consequently, in anode volume-optimized systems, the anode pressure changes can be very fast (several bars per second).

During normal operation, a mismatch between hydrogen supply rates and the consumption rate can occur due to a load change, a hydrogen purge, or a variation in hydrogen supply pressure (e.g. because of temperature variation in a spring-loaded pressure reducer). When such a mismatch occurs, some action must be taken to prevent over- or under-pressure. A possible action in hybridized systems, for example, is variation of the load current.

If variation of the load current is not possible, the EPC can be sized and the PEMFC system can be operated in such a way that hydrogen is always delivered in excess. The excess hydrogen can be vented out with periodic or pressure triggered purges, continuous purge (=bleed), or by employing a backpressure regulator. In the work described in publication [V], both periodic purging and variation of load current were proven to work well.

6.5 Ejector-based system testing [V]

The characterized custom-made ejector and the discrete EPC were tested in a 5 kW PEMFC system with a 50-cell S2 stack by PowerCell Sweden AB. Other main components in the system were an air blower (Ametek Inc., Windjammer, 230 VAC), a cathode gas-to-gas membrane humidifier (Perma Pure LLC, FC300-1600-10HP), a coolant pump (EMP Inc., WP29), a coolant deionization filter (Spectrapure Inc., DI-MBHT-RT3-10L-25), and a liquid-to-liquid heat exchanger (Swep International AB, B5Hx20/1P-SC-S). The anode inlet was humidified only with the hydrogen recirculation achieved with the single ejector. A simplified system scheme is shown in Figure 30.

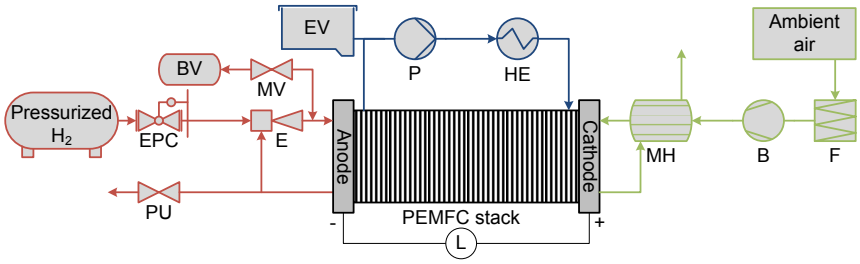

Figure 30. Simplified 5 kW PEMFC system scheme. B: blower, BV: buffer volume, E: ejector, EPC: ejector primary gas control system, EV: expansion vessel, F: filter, HE: heat exchanger, L: electronic load, MH: membrane humidifier, MV: manual valve, P: coolant pump, PU: purge valve.

A buffer volume of roughly 11 dm^3 was applied at the anode inlet, as shown in Figure 30. This was a safety precaution targeted at slower pressure changes that result from the mismatch between the hydrogen supply rate and consumption rate. The use of a buffer volume turned out to be useful in preventing an excessive pressure rise or drop and, thus, possible system damage, especially during the system testing phase. Later, with experience on system behavior, the buffer volume was disconnected from the anode loop with a manual valve.

After initial system testing, two sets of measurements were conducted. First, a polarization curve was measured to validate system and ejector performance at steady state operation. The polarization curve was measured by operating the system at load current levels 1 A to 3.5 A below those dictated by EPC sizing. Excessive anode pressure was avoided by periodic hydrogen purges. The system was operated at the load current levels shown in Table 4 in the following order: starting from load level 4, increasing the load up to level 7, then decreasing down to level 0, and finally increasing the load back to level 4. Each load current level (except load level zero) was maintained for 15 minutes.

Second, the effect of inert content on the recirculation rate was measured. The measurements were conducted by operating the system at constant load current and anode pressure levels with long purge cycles to allow inert gas buildup in the anode. The measurements were conducted with varying anode inlet pressure levels (20, 60, 150 mbarg) at load level 4 (each measurement repeated 2-5 times) and with varying load levels (1, 4, 7) and constant anode inlet pressure of 60 mbarg (each measurement repeated 5 times).

6.6 Load changes with discrete ejector control [VI]

During a load change, the fuel supply and consumption rates temporarily mismatch when discrete ejector control is used. This is because the load current changes almost instantaneously while the fuel supply rate develops more slowly. The mismatch can cause over- or under-pressure at the anode or, at worst, fuel starvation. One method to manage the mismatch is to optimize the timing of fuel supply with respect to the load change.

The effect of fuel supply timing was studied with the 5 kW PEMFC system. For these experiments, the control software was modified as follows. First, the data acquisition routine was improved to achieve continuous a 100 Hz data recording rate. Second, the timing of the hydrogen supply valve, air blower, and electronic load control was improved. In addition, mechanical relays employed for controlling the hydrogen supply valve were found unreliable during fast control sequences, and they were replaced with solid-state relays.

The experiments were conducted by letting the system stabilize on load level 2 (see Table 4), which resulted in ca 2 kW stack power. The anode pressure was maintained at 100 mbarg, air stoichiometry was maintained at 2.5, and the coolant inlet temperature was maintained at 70 °C. The buffer volume employed during system testing was disabled, and the anode pressure was controlled by fine-tuning the load current with a PI controller.

Prior to ramping up the power, the airflow rate was increased (ca 2 seconds before power ramp), and fine-tuning of the load current was disabled (ca 1 second before the power ramp). In addition, the data recording rate was increased to 100 Hz.

The power ramp-up was performed by ramping up the fuel supply and the load current to level 7 (≈ 4 kW). The load ramp-up timing (t_{lrf}) was relative to the fuel supply initiation. Five load ramp-up timings were tested: -50 ms, 0 ms, +50 ms, +100 ms, and +200 ms. The experiments with each load ramp-up timing were repeated at least six times. Approximately 1 second after the power ramp-up, load current fine-tuning was again enabled, and, approximately after 10 seconds, the recording rate was set to normal.

The anode pressure was observed to be a critical parameter in the initial tests because a pressure that is too high or low could damage the stack. Therefore, a model for predicting anode pressure during load changes was implemented. The simulation results were used for determining the safe load ramp-up timings listed in the previous paragraph. A description of the model can be found in publication [VI].

6.7 Results and discussion

6.7.1 Ejector modelling [IV]

The measured ejector entrainment ratios and those obtained with 2D CFD modelling were compared by calculating both the mean absolute deviation (AD) and the mean relative deviations (RD). The ADs and RDs were computed as follows:

$$\mathrm{AD} = \frac{1}{N_{tot}} \cdot \sum_{i=1\ldots N_{tot}} \left| \Omega_{meas,i} - \Omega_{sim,i} \right| \tag{64}$$

$$\mathrm{RD} = \frac{1}{N_{tot}} \cdot \sum_{i=1\ldots N_{tot}} \left| 1 - \frac{\Omega_{sim,i}}{\Omega_{meas,i}} \right| \tag{65}$$

where $\Omega_{meas,i}$ is the measured entrainment ratio, $\Omega_{sim,i}$ is the simulated entrainment ratio, i is the index of measurement, and N_{tot} is the total number of measurements. The entrainment ratio is the ratio of the ejector secondary inlet mass flow rate ($\dot{m}_{s,in}$) to the ejector primary inlet mass flow rate ($\dot{m}_{p,in}$):

$$\Omega = \frac{\dot{m}_{s,in}}{\dot{m}_{p,in}} \tag{66}$$

The ADs and RDs of modelled entrainment ratios compared to the measured entrainment ratio are shown in Table 5.

Table 5. ADs and RDs calculated separately for data points with low ($\Omega_{meas} < 1$) and high ($\Omega_{meas} > 1$) entrainment ratio, and for all data points. Working gas: H_2, $T_{dew,s,in} = 60$ °C, $p_{ej,out} = 250$ mbarg. Table reproduced from publication [IV].

	AD			***RD***		
Model	***Ω_{meas} < 1***	***Ω_{meas} > 1***	***All***	***Ω_{meas} < 1***	***Ω_{meas} > 1***	***All***
SST k-ω	0.78	0.72	0.73	227.2%	31.5%	68.2%
RNG k-ε	0.47	1.08	0.97	144.6%	41.5%	60.9%
Realizable k-ε	0.48	1.17	1.04	146.2%	44.5%	63.6%

Overall, the 2D axisymmetric CFD modelling gave relatively good predictions of the performance of the ejector considering the substantially lighter computation compared to 3D modelling. The 2D modelling overestimated the performance of the ejector for all turbulence models at nearly all conditions. The mean absolute deviations (ADs) of simulated ejector entrainment ratios were in the range 0.73 to 1.04 and the mean relative deviations (RDs) were in the range 60.9% to 68.2%, as shown in Table 5.

Simulations conducted with the SST k-ω model had the lowest AD while simulations conducted with the RNG k-ε model had the lowest RD. There was, however, notable variation in the accuracies of the turbulence models depending on the conditions, as seen in Figure 31. In a system with a low flow resistance (≤51.7 mbar, Δp_s: "low"), the SST k-ω model gave more accurate predictions of the ejector performance at high primary gas flow rates while the two k-ε models gave better predictions at low primary gas flow rates. In a system with a high flow resistance (≤206.9 mbar, Δp_s: "high"), all three turbulence models gave similar predictions, the maximum deviation in the predicted entrainment ratio being less than 9%.

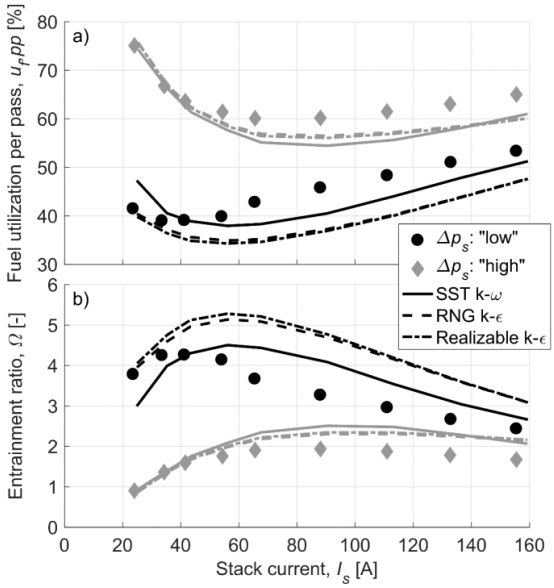

Figure 31. Comparison of a) fuel utilization per pass and b) entrainment ratio predictions obtained with the different turbulence models along the low-flow-resistance operating curve (≤51.7 mbar, Δp_s: "low") and the high-flow-resistance (≤206.9 mbar, Δp_s: "high") operating curve. Working gas = H_2, $T_{dew,s,in} = 60$ °C, $p_{ej,out} = 250$ mbarg. Figure modified from publication [IV].

Figure 32 shows the ejector exergetic efficiency as a function of stack pressure drop measured and modelled at three primary pressure levels. It can be seen that the maximum efficiency occurred at stack pressure drops close to half of their maximum at all primary pressure levels.

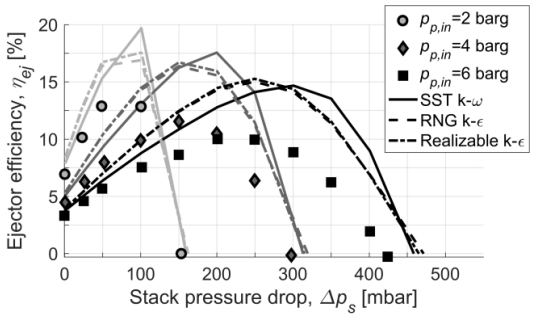

Figure 32. Measured and simulated ejector efficiency (η_{ej}) as function of stack pressure drop (Δp_s). Working gas = H_2, $p_{ej,out} = 250$ mbarg. Figure modified from publication [IV].

The ejector should operate at maximum efficiency for highest recirculation rate. The observation that maximum efficiency is reached at stack pressure drops half of their maximum can be useful in the first stage of dimensioning an ejector for a specified system because, in principle, only the maximum pressure difference for an ejector must be known for optimal sizing. However, the maximum efficiency of a certain ejector geometry does not necessarily mean that that ejector geometry, of all possible ejector geometries, gives the best performance.

Therefore, this method can only be used as a first approximation in the search for optimal ejector dimensions.

A comparison of the simulation results of the three models in Figure 32 shows that the two k-ε models accurately predict the position of maximum efficiency. Therefore, these models would be more useful in ejector optimization than the k-ω model, which tends to predict maximum efficiency at a pressure drop that is too high. None of the models predicted the value of the efficiency accurately.

6.7.2 Ejector characterization [IV]

The entrainment ratio and efficiency maps of the two ejectors measured with humid air and a 500 mbarg ejector outlet pressure are shown in Figure 33. The operating lines plotted on the maps represent the path along which an ejector operates when used in systems with low (≤51.7 mbar, Δp_s: "low"), moderate (≤103.4 mbar, Δp_s: "moderate"), or high flow resistance (≤206.9 mbar, Δp_s: "high"). The maximum efficiency curve, i.e. the curve along which maximum efficiency is achieved, is also plotted on the efficiency maps.

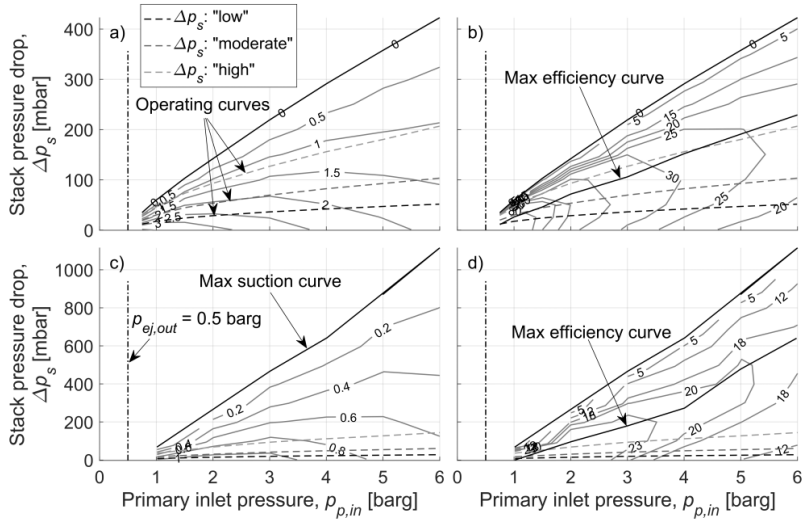

Figure 33. Custom-made ejector operating curves plotted on a) entrainment ratio map and b) efficiency map, and commercial ejector operating curves plotted on c) entrainment ratio map and d) efficiency map. Working gas = air, $T_{dew,s,in} = 60$ °C, $p_{ej,out} = 500$ mbarg. Figure modified from publication [IV].

The ejector operating maps in Figure 33 show that the recirculation rate achieved with the ejectors declined when system flow resistance increased, as expected. For the custom-made ejector, the best efficiency was achieved close to the high-flow-resistance operating curve. The commercial ejector operated mostly far from its maximum efficiency and, therefore, achieved a poor recirculation rate compared to the custom-made ejector.

Optimally, the ejector would operate close to maximum efficiency throughout its operating range. However, the ejector operating curve and the maximum efficiency curve might not be possible to match over the entire range. Either a

variable geometry ejector can be employed [74] or several differently sized ejectors can be operated in parallel [75] to address this issue.

Figure 34 shows the custom-made ejector operating curves plotted on the efficiency and fuel utilization per pass maps measured with humid hydrogen and a 250 mbarg outlet pressure. Again, the highest efficiency was mostly achieved in the high-flow-resistance system. Nonetheless, the highest recirculation rate was achieved in a system with low flow resistance for which the fuel utilization per pass was almost 50% at a primary pressure as high as 5 barg. This highlights the significance of anode subsystem flow resistance in the achieved recirculation rate, especially when ejectors are employed.

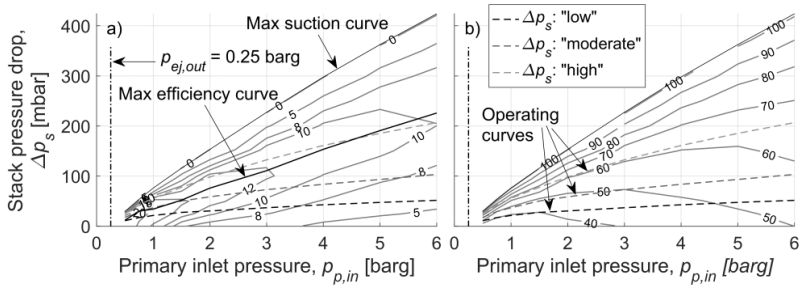

Figure 34. Custom-made ejector operating curves plotted on a) exergetic efficiency (η_{ej}) map and b) fuel utilization per pass ($u_{f,pp}$) map. Working gas = H_2, $T_{dew,s,in} = 60$ °C, $p_{ej,out} = 250$ mbarg. Figure modified from publication [IV].

6.7.3 System testing [V]

The measured ejector performance in the actual PEMFC system is shown in Figure 35. The time-averaged fuel utilization per pass ($u_{f,pp}$) varied between 40% (±7%) at 25 A stack current and 64% at 160 A stack current. Correspondingly, the time-averaged anode inlet hydrogen stoichiometry (λ_f) varied from 2.6 (±0.4) to 1.6 within the same stack current range.

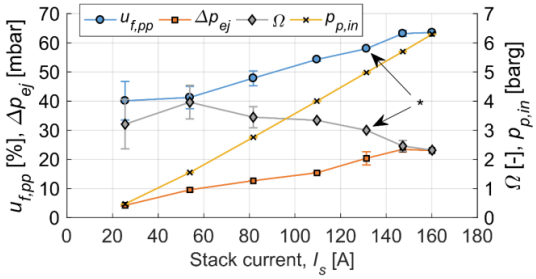

Figure 35. Ejector performance as function of stack current: fuel utilization per pass ($u_{f,pp}$), ejector secondary gas pressure lift (Δp_{ej}), entrainment ratio (Ω), and ejector primary pressure ($p_{p,in}$). The error bars show the variation in time-averaged values between upward and downward polarization curve measurements. *Only data from downward curve is available. Figure modified from publication [V].

The recirculation rate was lower than what could be expected from Figure 34. Possible reasons for this include the inert content of the recirculated gas (characterization was conducted with pure hydrogen) and the lower anode pressure. Both of these factors were found to affect the recirculation rate, and their effect will be addressed below. An additional cause for the observed lower recirculation rate is the poor efficiency of the ejector at these conditions. Because of the low efficiency, the effect of flow resistance of the system on the achieved recirculation rate is minor.

The effects of recirculated gas inert content and anode pressure are shown in Figure 36. The fuel utilization per pass, the ejector entrainment ratio, the ejector secondary inlet dew point temperature (which is close to the anode outlet dew point temperature), the ejector outlet dew point temperature (i.e. the anode inlet dew point temperature), and the ejector secondary gas pressure increase are plotted as functions of the inert mole fraction of the ejector secondary gas calculated on dry basis ($y_{N_2,dry,s,in}$).

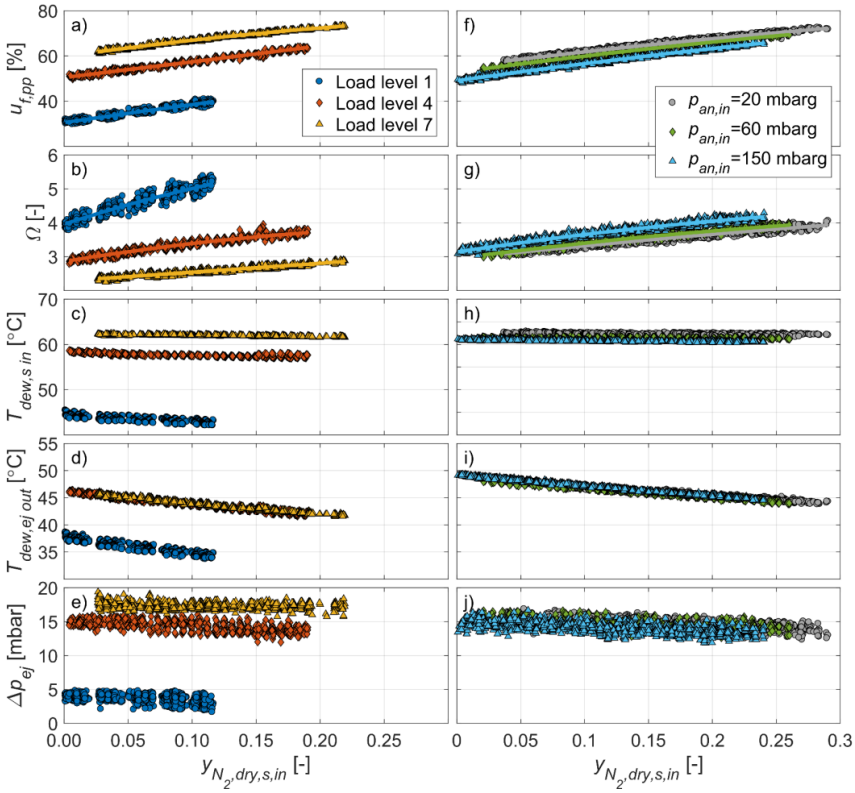

Figure 36. Effect of anode gas inert content on dry basis ($y_{N_2,dry,s,in}$) on fuel utilization per pass ($u_{f,pp}$), entrainment ratio (Ω), ejector secondary inlet dew point temperature ($T_{dew,s,in}$), ejector outlet dew point temperature ($T_{dew,ej,out}$), and ejector secondary gas pressure lift (Δp_{ej}) at load levels 1, 4, and 7 (a-e) and at anode pressure levels 20, 60, and 150 mbarg (f-j). Each experiment was repeated 2-5 times. Figure is a combination of two figures in publication [V].

The increase in the anode gas inert content reduced the anode inlet dew point temperature ($T_{dew,ej,out}$) roughly by 2 to 3 °C when the inert content of dry recirculated gas ($y_{N_2,dry,s,in}$) increased by 0.1 (Figure 36 d and i). The decrease in anode inlet humidity (Figure 36 c and h) was a result of the decrease in molar recirculation rate (increased fuel utilization per pass, Figure 36 a and f), which was a result of hydrogen being replaced with the heavier nitrogen. At the same time, the mass-based recirculation rate (i.e. the entrainment ratio) increased (Figure 36 b and g). The magnitude of the effect depended on the load level. These observations can explained with the added molar mass of recirculated gas, which leads to a lower recirculation rate since the ejector operation is based on momentum transfer.

The effect of the anode gas inert content on water management is twofold. On one hand, the added inert concentration decreases the recirculation rate (as noted in the previous paragraph) thus, depressing the removal of water droplets from gas channels. On the other hand, the added inert concentration increases both the mass flow rate and the anode gas viscosity, both of which enhance the removal of water droplets. Therefore, the net effect of added inert concentration on water management deserves additional study.

The increase of anode pressure level caused both the molar recirculation and the mass-based recirculation rate to increase, as seen in Figure 36 f and g. This can be explained by a higher gas density that allowed a higher flow rate through the fixed geometry ejector.

The anode inlet humidity appeared to be independent of the anode pressure level despite the greater recirculation rate (Figure 36 i). Instead, the anode outlet humidity decreased 1.4-1.7 °C with a 130 mbar (20 mbarg to 150 mbarg) increase in the anode pressure level. A possible explanation for this observation is a decreased water transport rate from cathode to anode as a result of the higher anode pressure. Another explanation is the drier operating conditions at higher anode pressures, which are a result of more efficient hydrogen purges.

6.7.4 Load changes with discrete ejector control [VI]

During rapid load changes with a PEMFC system, one of the main concerns is sufficient fuel supply and prevention of fuel starvation. In addition, the anode pressure variation is a concern in systems where the anode pressure is not autoregulated (e.g. by a pressure regulator). Figure 37 shows ejector primary pressure (which is proportional to the hydrogen supply rate), anode pressure, as well as stack current, voltage, and power measured during the experiments described in Section 6.6.

The hydrogen flow developed relative slowly; the final primary pressure level and, consequently, the final hydrogen flow rate was reached in ca 350 milliseconds, as seen in Figure 37 a. The time is proportional to the volume between the EPC and the ejector. Thus, by minimizing this volume, the time required to reach the final flow rate can be reduced. The opening times of the fuel supply valve also affect the time required to reach the final flow rate.

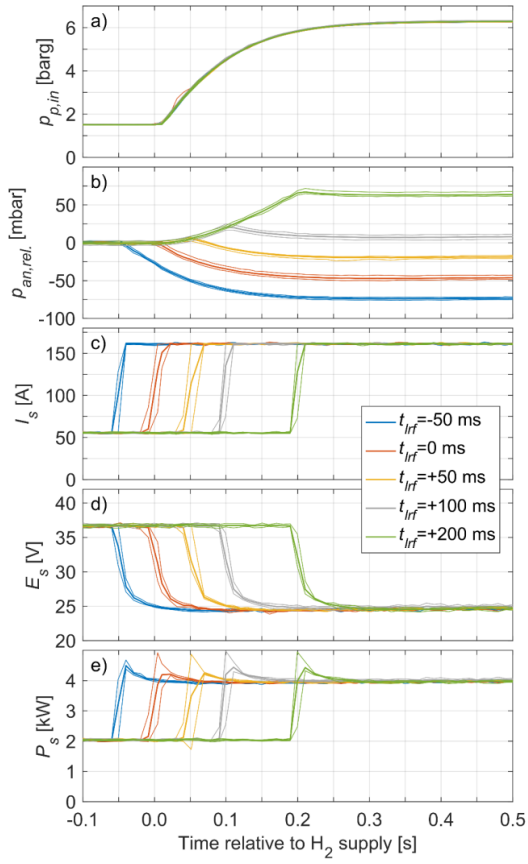

Figure 37. a) Ejector primary pressure ($p_{p,in}$), b) anode inlet pressure relative to set setpoint ($p_{an,rel.} = p_{an,in} - 100$ mbar), c) stack load current (I_s), d) stack voltage (E_s), and e) stack output power (P_s) as function of time relative to hydrogen supply ramp-up for five load ramp-up timings relative to fuel supply ramp-up ($t_{lrf} = -50, 0, +50, +100, +200$ ms). The experiments with each load ramp-up timing were repeated at least six times. The thin lines show the measurement variation. Figure modified from publication [VI].

The stack voltages (Figure 37 d) showed no depression, i.e. no sign of fuel shortage on the reaction sites despite the slowly developing fuel supply rate. In one case (i.e. $t_{lrf} = -50$ ms), the load current was increased even before the initiation of fuel supply, and still the stack voltage showed no depression. This can be explained by a sufficiently large hydrogen buffer in the anode volume. Therefore, this behavior might be different in anode-volume-optimized systems.

The pressure at the anode inlet (Figure 37 b) shows relatively modest variations, which supports the notion that the hydrogen buffer was sufficient. The measured variations in anode pressure are in line with the simulated ones (Figure 38 a) with the exception of the effect of load control, which was disabled in the measurements. Figure 38 b shows minimum and maximum anode pressures as functions of load ramp-up timing.

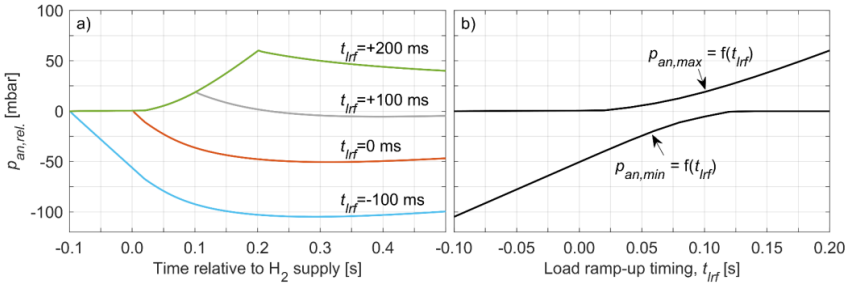

Figure 38. Simulated a) relative anode inlet pressure $(p_{an,rel.} = p_{an,in} - 100\ \text{mbar})$ as function of time relative to hydrogen supply ramp-up for four load ramp-up timings $(t_{lrf} = -100, 0, +100, +200\ \text{ms})$ and b) maximum and minimum anode pressure as a function of load ramp-up timing. Figure modified from publication [VI].

Optimally, the load ramp-up timing would be chosen to result in minimal variation in anode pressure. In publication [VI] it was found that minimal variation in pressure does not occur when the hydrogen supply is ramped up simultaneously with the load current (i.e. at $t_{lrf} = 0$ ms). Instead, variation in pressure depends on the time that the hydrogen flow requires to fully develop, and the optimal load ramp-up timing is, therefore, always positive (assuming that the load change occurs instantaneously). In the current case, it was ca 100 milliseconds and the resulting pressure variation was 20-25 mbar, as shown in Figure 39.

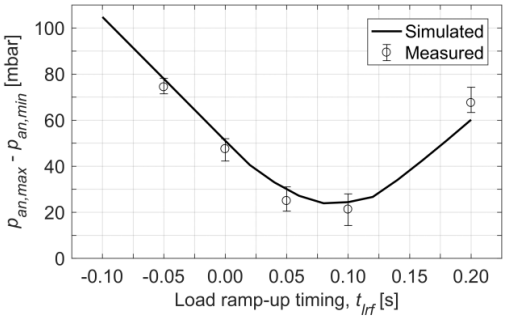

Figure 39. Simulated and measured anode pressure variation $(p_{an,max} - p_{an,min})$ during a power ramp-up as function of load ramp-up timings relative to fuel supply ramp-up (t_{lrf}). The error bars show measurement variations.

In the present system, where the anode volume was rather large (~1.5 dm³ or ~0.3 dm³/kW), the variation in anode pressure was only little higher than 100 mbar even when the load ramp-up time deviated 200 milliseconds from the optimum. Since the pressure variation is inversely proportional to the anode volume, the rate of pressure changes in anode-volume-optimized systems can be notably higher.

7. Summary and Conclusions

This work studied devices and methods for the hydrogen supply system in PEMFC systems both through modelling and experimental work. The studies concentrated on 1) inert buildup and hydrogen purge, 2) hydrogen humidification, and 3) hydrogen recirculation. A summary of key findings follows.

7.1 Hydrogen purge

Inert gas buildup and hydrogen purges were studied with a close to commercial PEMFC system with advanced instrumentation. Methods for determining membrane permeability, fuel purity, as well as the amount and composition of purged gas were developed. The effects of hydrogen purge on system performance were studied by varying the purge triggering criteria (average cell voltage drop 3 mV, 6 mV, or 9 mV), purge length (200 ms or 400 ms), purge type (single or double), and cathode inlet dew point temperature (52 °C, 55 °C, or 58 °C).

It was found that, even though fuel efficiency decreased with more frequent purging, the overall system efficiency increased. In other words, while very high fuel efficiencies (>99.9%) were easily attainable, the buildup of inert gases caused voltage polarization that outweighed the benefits of improved fuel efficiency.

At increasingly humid conditions, the primary function of a hydrogen purge shifted from the removal of inert gas towards the removal of water. While increasing the humidity level improved PEMFC performance, the operation also became more unstable because of accumulated liquid water in the gas channels. At high-humidity conditions, relatively long (400 ms) and frequent hydrogen purges resulted in the highest combined fuel and stack efficiency.

A double purge (two consecutive purges performed with a short interval) was also tested. The second purge resulted in higher flow rates because the first purge had flushed part of the liquid water from the gas channels. Thus, the second purge could serve as an indicator of the suitability of the purge parameters (length, frequency) employed. The double purge was not found to improve the removal of water compared to a longer single purge.

Finally, the concentration polarization measured between consecutive purges was compared to the voltage polarization predicted by the Nernst equation calculated with gas concentrations in anode gas channels. The measured voltage polarization was observed to be roughly twice that of the theoretical one. Thus,

it is important to account for mass transfer resistance when designing the PEMFC hydrogen supply system.

7.2 Hydrogen humidification

A bubble humidifier for a 50 kW_e PEMFC pilot plant was designed and characterized. The humidifier was powered with waste heat from the PEMFC system and supplied with water condensed from the cathode outlet gas.

The humidifier was characterized by supplying air at flow rates corresponding to hydrogen consumption rates at PEMFC system low (75 A), nominal (150 A), and full (230 A) power. The approach dew point temperatures achieved were 3.1 °C at low power, 5.9 °C at nominal power, and 8.5 °C at full power when the humidifier was supplied with heating water at 65 °C at a 13.5 lpm flow rate.

The bubble humidifier was modelled with correlations for heat and mass transfer found in literature. A comparison of experimental data and simulation results showed good agreement. Simulations revealed that the humidifier performance was heat transfer limited. According to the simulations, the approach dew point could be decreased from 5.7 °C to 4.3 °C or 4.1 °C at nominal power by doubling the heating water flow rate or the heat transfer area, respectively.

The bubble humidifier was successfully operated for 4,400 hours in a 50 kW_e pilot plant in Äetsä, Finland. During operation at low power, the bubble humidifier was found to provide humidification that was too efficient. Thus, humidification control would be needed. The easiest control methods would be letting part of the gas bypass the humidifier or letting part of the heating water bypass the humidifier.

7.3 Hydrogen recirculation

An ejector for a 5 kW PEMFC system was characterized, modelled, and verified in a PEMFC system. Moreover, a discrete ejector primary flow control system, based on three solenoid valves, was designed and verified in the PEMFC system. Finally, power ramp-rate capabilities of the PEMFC system employing the ejector and the discrete primary flow control system were studied.

A custom-made ejector was designed and manufactured from stainless steel with 3D printing. The ejector was characterized with dry and humid air and humid hydrogen, and its performance was compared to a commercial ejector. The custom-made ejector performed notably better than the commercial one.

Ejector performance maps visualized how close to optimum conditions the ejector operated. Optimum performance is achieved when the ejector operates close to maximum efficiency throughout its operating range. The maximum efficiency occurred close to pressure drops that were half of the maximum pressure differences against which the ejector could operate. This can be used as an initial sizing rule for ejectors.

It was found that an ejector can be sized for optimal operation either at high currents or at low currents, but not both. Sizing an ejector for high currents would inevitably compromise its performance at low currents, and vice versa. A

relatively high recirculation rate is usually required at low currents (compared to high high currents) for stable stack performance.

The custom-made ejector was modelled with CFD in 2D axisymmetric geometry, and three turbulence models were tested. It was found that, while none of the three turbulence models provided accurate results (ca 60-70% error in entrainment ratio), there were clear differences in accuracies. The SST k-ω turbulence model predicted ejector performance better at high primary and secondary gas flow rates, in general. The RNG k-ε and the Realizable k-ε turbulence models, on the other hand, more accurately predicted the position of maximum efficiency.

The custom-made ejector was installed in a 5 kW PEMFC system, and the system was characterized with stack currents ranging from 15% to 81% of maximum. The fuel utilization achieved per pass varied between 40% at lowest stack current and 64% at highest stack current. This high recirculation with a single ejector was possible because of 1) low stack flow resistance, and 2) ejector sizing that favored operation at low currents.

The effect of anode pressure and inert concentration on the recirculation rate achieved with the ejector was studied with the 5 kW PEMFC system. The recirculation rate increased with anode pressure level. A possible explanation for this is the increase in gas density. On the other hand, an increase in inert concentration resulted in an added mass-based recirculation rate but decreased the molar-based recirculation rate. This is explained by the high molar mass of nitrogen (compared to hydrogen), which is the main constituent of impurities that enter the anode. The net effect of added inert concentration on the removal of liquid water from gas channels was, however, unclear because of the added viscosity.

A discrete primary flow control setup was designed for a 5 kW PEMFC system. The control setup was based on three discrete solenoid valves, thereby enabling seven discrete open states (and one closed state). The setup was proven to function in practice.

The main benefits of the discrete ejector control setup are its robustness and the minimum requirement of moving parts. However, because operation is only possible at specified discrete states, some sort of balancing between hydrogen consumption and supply is necessary. For this reason, two methods were tested: 1) varying the load current, and 2) a hydrogen purge triggered by a pressure limit. Both methods were proven to work.

When using the discrete ejector primary flow control, the fuel supply and consumption rates temporarily mismatched during a load change, which resulted in variations in anode pressure. One method to manage the mismatch is to optimize the timing of fuel supply with respect to the load change. This was studied for the 5 kW PEMFC system.

It was found that, in this system (with ~0.3 dm^3/kW anode volume), the mismatch between fuel supply and consumption was relatively easy to manage. The anode pressure variation with optimal timing was 20-25 mbar. The optimal timing depends mainly on fuel supply valve opening times and the volume that is required to pressurize upstream of the ejector primary inlet.

When the load ramp-up timing relative to fuel ramp-up deviated 200 millisecond from the optimal, the pressure variation was little above 100 mbar, which is a modest variation. The pressure variation is inversely proportional to the anode volume and, thus, depending on tha node volume, the pressure variation might be several times that reported here.

7.4 Concluding remarks and future work

PEMFCs are regarded as an important part of a future carbon neutral energy supply. PEMFC technology is developing but still remains too expensive for commercialization in many applications. The total cost of a PEMFC system consists of two main parts: the stack and the BoP.

The design of a PEMFC BoP is application specific. PEMFC stacks are well suited for a wide range of applications, but limitations in BoP performance might constrain PEMFC system operation. A BoP design is intended to maximize PEMFC system lifetime and efficiency while minimizing cost and meeting the targets placed for the system.

This thesis contributes to this topic by presenting applied studies on the fuel supply subsystem. The results presented are useful when designing the fuel supply for cost-effective, efficient, and long-lasting PEMFC systems. Even though the focus of this work is on stationary systems, the findings are applicable to other applications as well.

Because of the wide variety of possible applications for PEMFCs, each one with its own specific requirements, the work with BoP design for PEMFC systems is far from finished. For example, the design and operation of a bubble humidifier with 5-10 cm water bed and either an internal or external heat exchanger is an interesting topic for future studies. In addition, questions related to hydrogen supply based on an ejector with discrete primary flow control during fast power transients deserves future study to avoid conditions that compromise stack lifetime.

One interesting topic for future work is the recirculation rate achieved with an ejector during fast power transients. When the stack current is abruptly increased, the anode pressure decreases, as was shown in Section 6. If the impurity content of anode gas is high, the hydrogen inside the cells might be temporarily consumed unless the ejector recirculates the hydrogen-richer anode gas from the anode loop. However, since the ejector operation relies on hydrogen feed, the recirculation rate will not increase until the hydrogen feed is ramped-up. Therefore, fuel starvation might occur during power transients unless the timing of a fuel ramp-up is optimized.

The ejector sizing deserves also further studies. There are numerous studies about ejector modelling with CFD in 3D. However, the ejectors designed for

PEMFC applications are with no exceptions (to the authors knowledge) modelled in 2D. Therefore, there is no information available of the 3D-modelling accuracy under operating conditions relevant to the PEMFC. Finally, there are only few studies regarding ejector dimensioning. How should the ejector dimensions be chosen to achieve the desired performance at specified conditions? How does the choice of dimension affect ejector performance at “off-design” conditions? What is the best approach to size a dual-ejector system (with two ejectors in parallel)? These questions all deserve further work.

References

[1] 2014 CODATA recommended values, NIST Ref. Constants, Units, Uncertainty. (2015). https://physics.nist.gov/cuu/Constants/ (accessed November 27, 2017).

[2] F. Zhang, P. Zhao, M. Niu, J. Maddy, The survey of key technologies in hydrogen energy storage, Int. J. Hydrogen Energy. 41 (2016) 14535–14552. doi:https://doi.org/10.1016/j.ijhydene.2016.05.293.

[3] REN21, Renewables 2014 Global Status Report, Paris, 2014. http://www.ren21.net/Portals/0/documents/Resources/GSR/2014/GSR2014_full report_low res.pdf.

[4] REN21, Renewables 2017 Global Status Report, Paris, 2017. http://www.ren21.net/wp-content/uploads/2017/06/17-8399_GSR_2017_Full_Report_0621_Opt.pdf.

[5] J.O.M. Bockris, The hydrogen economy: Its history, Int. J. Hydrogen Energy. 38 (2013) 2579–2588. doi:https://doi.org/10.1016/j.ijhydene.2012.12.026.

[6] J. Larminie, A. Dicks, Fuel cell systems explained, J. Wiley, 2003.

[7] Y. Wang, K.S. Chen, J. Mishler, S.C. Cho, X.C. Adroher, A review of polymer electrolyte membrane fuel cells: Technology, applications, and needs on fundamental research, Appl. Energy. 88 (2011) 981–1007. doi:10.1016/j.apenergy.2010.09.030.

[8] N. Guerrero Moreno, M. Cisneros Molina, D. Gervasio, J.F. Pérez Robles, Approaches to polymer electrolyte membrane fuel cells (PEMFCs) and their cost, Renew. Sustain. Energy Rev. 52 (2015) 897–906. doi:https://doi.org/10.1016/j.rser.2015.07.157.

[9] B.D. James, J.M. Huya-Kouadio, C. Houchins, D.A. DeSantis, Mass Production Cost Estimation of Direct H2 PEM Fuel Cell Systems for Transportation Applications: 2016 Update, Arlington VA, 2017. https://energy.gov/sites/prod/files/2017/06/f34/fcto_sa_2016_pemfc_transportation_cost_analysis.pdf.

[10] O. Himanen, Characterization of transport phenomena in small polymer electrolyte membrane fuel cells, Helsinki University of Technology, 2008. http://lib.tkk.fi/Diss/2008/isbn9789512291472/.

[11] K. Nikiforow, Optimization of polymer electrolyte membrane fuel cell systems - Applied study of hydrogen recirculation, Aalto University,

2010. http://lib.tkk.fi/Dipl/2010/urn100359.pdf.

[12] M. Seibert, S. Nieh, Comparison of hydrogen and hydrogen-rich reformate enrichment of JP-8 in an open flame, Fuel. 210 (2017) 91–97. doi:10.1016/J.FUEL.2017.08.056.

[13] R. Scenna, T.G. DuBois, S. Nieh, Autothermal reforming of synthetic JP-8 derived from a coal syngas stream, Fuel. 108 (2013) 731–739. doi:10.1016/J.FUEL.2013.02.022.

[14] P. Koski, V. Pulkkinen, S. Auvinen, J. Ihonen, H. Karimäki, T. Keränen, A. Ryden, T. Tingelöf, S. Limonta, D. Croci, P. Fracas, M. Wichert, G. Kolb, R. Magalhaes, F. Relvas, M. Boaventura, A. Mendes, Development of reformed ethanol fuel cell system for backup and off-grid applications — system design and integration, in: 2016 IEEE Int. Telecommun. Energy Conf., IEEE, 2016: pp. 1–8. doi:10.1109/INTLEC.2016.7749097.

[15] G.C. Bandlamudi, M. Saborni, P. Beckhaus, F. Mahlendorf, A. Heinzel, PBI/H3PO4 Gel Based Polymer Electrolyte Membrane Fuel Cells Under the Influence of Reformates, J. Fuel Cell Sci. Technol. 7 (2010) 14501. doi:10.1115/1.3119054.

[16] J.A. Dean, N.A. Lange, Lange's handbook of chemistry., Lange's Handb. Chem. (1973).

[17] S.A. Vilekar, R. Datta, The effect of hydrogen crossover on open-circuit voltage in polymer electrolyte membrane fuel cells, J. Power Sources. 195 (2010) 2241–2247. doi:https://doi.org/10.1016/j.jpowsour.2009.10.023.

[18] K. Jiao, X. Li, Water transport in polymer electrolyte membrane fuel cells, Prog. Energy Combust. Sci. 37 (2011) 221–291. doi:10.1016/j.pecs.2010.06.002.

[19] W. Dai, H. Wang, X.-Z. Yuan, J.J. Martin, D. Yang, J. Qiao, J. Ma, A review on water balance in the membrane electrode assembly of proton exchange membrane fuel cells, Int. J. Hydrogen Energy. 34 (2009) 9461–9478. doi:https://doi.org/10.1016/j.ijhydene.2009.09.017.

[20] T.A. Zawodzinski, T.E. Springer, J. Davey, R. Jestel, C. Lopez, J. Valerio, S. Gottesfeld, A Comparative Study of Water Uptake By and Transport Through Ionomeric Fuel Cell Membranes, J. Electrochem. Soc. 140 (1993) 1981–1985. doi:10.1149/1.2220749.

[21] M. Ji, Z. Wei, A Review of Water Management in Polymer Electrolyte Membrane Fuel Cells, Energies. 2 (2009) 1057–1106. doi:10.3390/en20401057.

[22] H. Li, Y. Tang, Z. Wang, Z. Shi, S. Wu, D. Song, J. Zhang, K. Fatih, J. Zhang, H. Wang, Z. Liu, R. Abouatallah, A. Mazza, A review of water flooding issues in the proton exchange membrane fuel cell, J. Power Sources. 178 (2008) 103–117. doi:DOI: 10.1016/j.jpowsour.2007.12.068.

[23] R. Borup, J. Meyers, B. Pivovar, Y.S. Kim, R. Mukundan, N. Garland, D. Myers, M. Wilson, F. Garzon, D. Wood, P. Zelenay, K. More, K. Stroh, T. Zawodzinski, J. Boncella, J.E. Mcgrath, M. Inaba, K. Miyatake, M. Hori, K. Ota, Z. Ogumi, S. Miyata, A. Nishikata, Z. Siroma, Y. Uchimoto, K.

Yasuda, K.-I. Kimijima, N. Iwashita, Scientific Aspects of Polymer Electrolyte Fuel Cell Durability and Degradation, Chem. Rev. 107 (2007) 3904–3951. doi:10.1021/cr050182l.

[24] F.N. Büchi, S. Srinivasan, Operating Proton Exchange Membrane Fuel Cells Without External Humidification of the Reactant Gases Fundamental Aspects, J. Electrochem. Soc. 144 (1997) 2767–2772. doi:10.1149/1.1837893.

[25] R.K. Ahluwalia, X. Wang, Fuel cell systems for transportation: Status and trends, J. Power Sources. 177 (2008) 167–176. doi:DOI: 10.1016/j.jpowsour.2007.10.026.

[26] J. Zhang, Y. Tang, C. Song, J. Zhang, H. Wang, PEM fuel cell open circuit voltage (OCV) in the temperature range of 23°C to 120°C, J. Power Sources. 163 (2006) 532–537. doi:https://doi.org/10.1016/j.jpowsour.2006.09.026.

[27] J. Ihonen, P. Koski, V. Pulkkinen, T. Keränen, H. Karimäki, S. Auvinen, K. Nikiforow, M. Kotisaari, H. Tuiskula, J. Viitakangas, Operational experiences of PEMFC pilot plant using low grade hydrogen from sodium chlorate production process, Int. J. Hydrogen Energy. 42 (2017) 27269–27283. doi:10.1016/J.IJHYDENE.2017.09.056.

[28] A.J.L. Verhage, J.F. Coolegem, M.J.J. Mulder, M.H. Yildirim, F.A. de Bruijn, 30,000 h operation of a 70 kW stationary PEM fuel cell system using hydrogen from a chlorine factory, Int. J. Hydrogen Energy. 38 (2013) 4714–4724. doi:10.1016/j.ijhydene.2013.01.152.

[29] N.-C. Shih, B.-J. Weng, J.-Y. Lee, Y.-C. Hsiao, Development of a small fuel cell underwater vehicle, Int. J. Hydrogen Energy. 38 (2013) 11138–11143. doi:https://doi.org/10.1016/j.ijhydene.2013.01.095.

[30] J. Renau, A. Lozano, J. Barroso, J. Miralles, J. Martín, F. Sánchez, F. Barreras, Use of fuel cell stacks to achieve high altitudes in light unmanned aerial vehicles, Int. J. Hydrogen Energy. 40 (2015) 14573–14583. doi:https://doi.org/10.1016/j.ijhydene.2015.02.071.

[31] X. Cheng, Z. Shi, N. Glass, L. Zhang, J. Zhang, D. Song, Z.-S. Liu, H. Wang, J. Shen, A review of PEM hydrogen fuel cell contamination: Impacts, mechanisms, and mitigation, IBA – HBC 2006 - Sel. Pap. from Int. Batter. Assoc. HAWAII Batter. Conf. 2006 Waikoloa, Hawaii, USA 9-12 January 2006. 165 (2007) 739–756. doi:DOI: 10.1016/j.jpowsour.2006.12.012.

[32] R.H. Perry, D.W. Green, Section 2 Physical and Chemical Data, in: Perry's Chem. Eng. Handb., 8th ed., McGraw-Hill, 2008. doi:10.1036/0071511253.

[33] R.K. Ahluwalia, X. Wang, Buildup of nitrogen in direct hydrogen polymer-electrolyte fuel cell stacks, J. Power Sources. 171 (2007) 63–71. doi:10.1016/J.JPOWSOUR.2007.01.032.

[34] C. Mittelsteadt, M. Umbrell, Gas Permeability in Perfluorinated Sulfonic Acid Polymer Electrolyte Membranes, in: Proc. 207th Electrochem. Soc. Meet. Gas Permeability Perfluorinated Sulfonic Acid Polym. Membr., Toronto, Canada, 2005. http://ma.ecsdl.org/content/MA2005-01/18/770.full.pdf.

[35] A. Rabbani, M. Rokni, Effect of nitrogen crossover on purging strategy in PEM fuel cell systems, Appl. Energy. 111 (2013) 1061–1070. doi:10.1016/j.apenergy.2013.06.057.

[36] K. Promislow, J. St-Pierre, B. Wetton, A simple, analytic model of polymer electrolyte membrane fuel cell anode recirculation at operating power including nitrogen crossover, J. Power Sources. 196 (2011) 10050–10056. doi:10.1016/j.jpowsour.2011.08.070.

[37] Y.-S. Chen, C.-W. Yang, J.-Y. Lee, Implementation and evaluation for anode purging of a fuel cell based on nitrogen concentration, Appl. Energy. 113 (2014) 1519–1524. doi:10.1016/j.apenergy.2013.09.028.

[38] M. Piffard, M. Gerard, E. Bideaux, R. Da Fonseca, P. Massioni, Control by state observer of PEMFC anodic purges in dead-end operating mode, IFAC-PapersOnLine. 48 (2015) 237–243. doi:10.1016/j.ifacol.2015.10.034.

[39] C.A. Reiser, L. Bregoli, T.W. Patterson, J.S. Yi, J.D. Yang, M.L. Perry, T.D. Jarvi, A Reverse-Current Decay Mechanism for Fuel Cells, Electrochem. Solid-State Lett. 8 (2005) A273–A276. doi:10.1149/1.1896466.

[40] Z. Hu, Y. Yu, G. Wang, X. Chen, P. Chen, J. Chen, S. Zhou, Anode purge strategy optimization of the polymer electrode membrane fuel cell system under the dead-end anode operation, J. Power Sources. 320 (2016) 68–77. doi:https://doi.org/10.1016/j.jpowsour.2016.04.023.

[41] Y. Yang, X. Zhang, L. Guo, H. Liu, Overall and local effects of operating conditions in PEM fuel cells with dead-ended anode, Int. J. Hydrogen Energy. 42 (2017) 4690–4698. doi:https://doi.org/10.1016/j.ijhydene.2016.08.091.

[42] L. Dumercy, M.-C. Péra, R. Glises, D. Hissel, S. Hamandi, F. Badin, J.-M. Kauffmann, PEFC Stack Operating in Anodic Dead End Mode, Fuel Cells. 4 (2004) 352–357. doi:10.1002/fuce.200400053.

[43] N. Bussayajarn, H. Ming, K.K. Hoong, W.Y. Ming Stephen, C.S. Hwa, Planar air breathing PEMFC with self-humidifying MEA and open cathode geometry design for portable applications, Int. J. Hydrogen Energy. 34 (2009) 7761–7767. doi:10.1016/j.ijhydene.2009.07.077.

[44] R. Eckl, W. Zehtner, C. Leu, U. Wagner, Experimental analysis of water management in a self-humidifying polymer electrolyte fuel cell stack, J. Power Sources. 138 (2004) 137–144. doi:10.1016/j.jpowsour.2004.06.042.

[45] P. Koski, L.C. Pérez, J. Ihonen, Comparing Anode Gas Recirculation with Hydrogen Purge and Bleed in a Novel PEMFC Laboratory Test Cell Configuration, Fuel Cells. 15 (2015) 494–504. doi:10.1002/fuce.201400102.

[46] L. Xingsheng, M. Shihu, Z. Juntao, Z. Hong, Z. Weilin, Z. Yangjun, Comparative Study of Membrane Humidifier and Enthalpy Wheel Humidifier for Large Power Fuel Cell System, J. Fuel Cell Sci. Technol. 6 (2008) 14501–14503. http://dx.doi.org/10.1115/1.2971175.

[47] A. Casalegno, S. De Antonellis, L. Colombo, F. Rinaldi, Design of an

innovative enthalpy wheel based humidification system for polymer electrolyte fuel cell, Int. J. Hydrogen Energy. 36 (2011) 5000–5009. doi:https://doi.org/10.1016/j.ijhydene.2011.01.012.

[48] S.H. Jung, S.L. Kim, M.S. Kim, Y. Park, T.W. Lim, Experimental study of gas humidification with injectors for automotive PEM fuel cell systems, J. Power Sources. 170 (2007) 324–333. doi:10.1016/j.jpowsour.2007.04.013.

[49] H. Zhang, Z. Qian, D. Yang, J. Ma, Design of an air humidifier for a 5 kW proton exchange membrane fuel cell stack operated at elevated temperatures, Int. J. Hydrogen Energy. 38 (2013) 12353–12362. doi:https://doi.org/10.1016/j.ijhydene.2013.07.050.

[50] C.-C. Sung, C.-Y. Bai, J.-H. Chen, S.-J. Chang, Controllable fuel cell humidification by ultrasonic atomization, J. Power Sources. 239 (2013) 151–156. doi:10.1016/j.jpowsour.2013.03.076.

[51] G. Vasu, A.K. Tangirala, B. Viswanathan, K.S. Dhathathreyan, Continuous bubble humidification and control of relative humidity of H2 for a PEMFC system, Int. J. Hydrogen Energy. 33 (2008) 4640–4648. doi:10.1016/j.ijhydene.2008.05.051.

[52] L. Zhang, S. Gao, H. Zhang, Experimental Researches of Factors Affecting Bubbling Humidification, in: D. Jin, S. Lin (Eds.), Adv. Comput. Sci. Intell. Syst. Environ., Springer Berlin Heidelberg, Berlin, Heidelberg, 2011: pp. 359–364. doi:10.1007/978-3-642-23753-9_57.

[53] D. Kadylak, W. Mérida, Experimental verification of a membrane humidifier model based on the effectiveness method, J. Power Sources. 195 (2010) 3166–3175. doi:https://doi.org/10.1016/j.jpowsour.2009.12.005.

[54] D.A. McKay, A.G. Stefanopoulou, J. Cook, A Controllable Membrane-Type Humidifier for Fuel Cell Applications—Part I: Operation, Modeling and Experimental Validation, J. Fuel Cell Sci. Technol. 7 (2010) 51006–51012. http://dx.doi.org/10.1115/1.4000997.

[55] D. Chen, W. Li, H. Peng, An experimental study and model validation of a membrane humidifier for PEM fuel cell humidification control, J. Power Sources. 180 (2008) 461–467. doi:DOI: 10.1016/j.jpowsour.2008.02.055.

[56] J.H. Keenan, E.P. Neumann, F. Lustwerk, An investigation of ejector design by analysis and experiment, J. App. Mech. 17 (1950) 299–309.

[57] B.J. Huang, J.M. Chang, C.P. Wang, V.A. Petrenko, A 1-D analysis of ejector performance, Int. J. Refrig. 22 (1999) 354–364. doi:https://doi.org/10.1016/S0140-7007(99)00004-3.

[58] Y. Zhu, Y. Li, New theoretical model for convergent nozzle ejector in the proton exchange membrane fuel cell system, J. Power Sources. 191 (2009) 510–519. doi:DOI: 10.1016/j.jpowsour.2009.02.014.

[59] Y. Bartosiewicz, Z. Aidoun, P. Desevaux, Y. Mercadier, Numerical and experimental investigations on supersonic ejectors, Int. J. Heat Fluid Flow. 26 (2005) 56–70. doi:http://dx.doi.org/10.1016/j.ijheatfluidflow.2004.07.003.

[60] J.-J. Hwang, C.-C. Cho, W. Wu, C.-H. Chiu, K.-C. Chiu, C.-H. Lin, Numerical and experimental investigation into passive hydrogen recovery scheme using vacuum ejector, J. Power Sources. 275 (2015) 539–546. doi:http://dx.doi.org/10.1016/j.jpowsour.2014.11.057.

[61] Y. Yin, M. Fan, K. Jiao, Q. Du, Y. Qin, Numerical investigation of an ejector for anode recirculation in proton exchange membrane fuel cell system, Energy Convers. Manag. 126 (2016) 1106–1117. doi:https://doi.org/10.1016/j.enconman.2016.09.024.

[62] J. Chen, H. Havtun, B. Palm, Investigation of ejectors in refrigeration system: Optimum performance evaluation and ejector area ratios perspectives, Appl. Therm. Eng. 64 (2014) 182–191. doi:https://doi.org/10.1016/j.applthermaleng.2013.12.034.

[63] K.D. Baik, M.S. Kim, Characterization of nitrogen gas crossover through the membrane in proton-exchange membrane fuel cells, 11th Int. Conf. "Hydrogen Mater. Sci. Chem. Carbon Nanomater. 36 (2011) 732–739. doi:DOI: 10.1016/j.ijhydene.2010.09.046.

[64] J. Ihonen, K. Nikiforow, H. Karimäki, T. Keränen, Methods relating to monitoring fuel cells, WO/2014/188061, 2014.

[65] T. Keränen, H. Karimäki, K. Nikiforow, S. Kukkonen, H. Uusalo, J. Viitakangas, J. Ihonen, A 50 kW PEMFC pilot plant operated with industry grade hydrogen - System design and site integration, in: Fuel Cells, John Wiley and Sons Ltd, 2014: pp. 701–708.

[66] E.N. Sieder, G.E. Tate, Heat Transfer and Pressure Drop of Liquids in Tubes, Ind. Eng. Chem. 28 (1936) 1429–1435. doi:10.1021/ie50324a027.

[67] V. Gnielinski, New equations for heat and mass transfer in turbulent pipe and channel flow, Int. Chem. Eng. 16 (1976) 359–368.

[68] W.-D. Deckwer, On the mechanism of heat transfer in bubble column reactors, Chem. Eng. Sci. 35 (1980) 1341–1346. doi:10.1016/0009-2509(80)85127-X.

[69] A. Mersmann, H. Noth, D. Ringer, R. Wunder, Maximum heat transfer in equipment with dispersed two-phase systems, Int. Chem. Eng. 22 (1982) 16–29.

[70] A.D. Kraus, A. Aziz, J. Welty, Convection with Simplified Constraints, in: Ext. Surf. Heat Transf., John Wiley & Sons, Inc., Hoboken, NJ, USA, n.d.: pp. 1–58. doi:10.1002/9780470172582.ch1.

[71] V. Alopaeus, Mass-transfer calculation methods for transient diffusion within particles, AIChE J. 46 (2000) 2369–2372. doi:10.1002/aic.690461205.

[72] S.M. Bhavaraju, T.W.F. Russell, H.W. Blanch, The design of gas sparged devices for viscous liquid systems, AIChE J. 24 (1978) 454–466. doi:10.1002/aic.690240310.

[73] J.R. Grace, T. Wairegi, T.H. Nguyen, Shapes and velocities of single drops and bubbles moving freely through immiscible liquids, Trans. Inst. Chem. Eng. 54 (1976) 167–173.

[74] D.A. Brunner, S. Marcks, M. Bajpai, A.K. Prasad, S.G. Advani, Design and characterization of an electronically controlled variable flow rate ejector for fuel cell applications, Int. J. Hydrogen Energy. 37 (2012) 4457–4466. doi:10.1016/J.IJHYDENE.2011.11.116.

[75] E. Hosseinzadeh, M. Rokni, M. Jabbari, H. Mortensen, Numerical analysis of transport phenomena for designing of ejector in PEM forklift system, Int. J. Hydrogen Energy. 39 (2014) 6664–6674. doi:http://dx.doi.org/10.1016/j.ijhydene.2014.02.061.

[76] A. Maghsoodi, E. Afshari, H. Ahmadikia, Optimization of geometric parameters for design a high-performance ejector in the proton exchange membrane fuel cell system using artificial neural network and genetic algorithm, Appl. Therm. Eng. 71 (2014) 410–418. doi:http://dx.doi.org/10.1016/j.applthermaleng.2014.06.067.

Appendix A: Purged gas amount and composition

This appendix presents the calculation of the amount and composition of purged gas assuming a perfectly mixed anode volume. All species are assumed to be in their gaseous phase ($y_{i,j} = z_{i,j}$). The schematic of such a system is shown in Figure A 1.

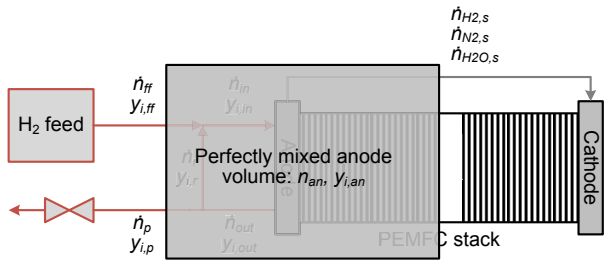

Figure A 1. Schematic of a PEMFC system with perfectly mixed anode volume and all species in their gaseous phase ($y_{i,j} = z_{i,j}$).

The total material balance and species balance equations for the perfectly mixed anode volume are:

$$\frac{dn_{an}}{dt} = \dot{n}_{ff} - \dot{n}_p - \dot{n}_s \tag{A1}$$

$$\frac{dn_{i,an}}{dt} = \frac{d(n_{an} \cdot y_{i,an})}{dt} = \dot{n}_{ff} \cdot y_{i,ff} - \dot{n}_p \cdot y_{i,an} - \dot{n}_s \cdot y_{i,s} \tag{A2}$$

where it has been recognized that the purged gas has the same composition as the perfectly mixed anode ($y_{i,an} = y_{i,p}$). Further, the correct way of expressing hydrogen consumption, inert gas permeation through the membrane, and water transport ($\dot{n}_{i,s}$) has been replaced with a more generic representation ($\dot{n}_s \cdot y_{i,s}$). In this representation, the $y_{i,s}$ represents the fraction and direction of, e.g. hydrogen consumption relative to $\dot{n}_s$, not the species mole fraction in a stream (there is no actual stream). This representation proves to be useful later.

The flow rates and, consequently, the amount of anode gas are assumed constant:

$$\frac{d(\dot{n}_{ff})}{dt} = \frac{d(\dot{n}_p)}{dt} = \frac{d(\dot{n}_s)}{dt} = 0 \tag{A3}$$

$$\dot{n}_{ff} = \dot{n}_p + \dot{n}_s \tag{A4}$$

Then, the species balance equation may be written as follows:

$$\frac{dy_{i,an}}{dt} = \frac{\dot{n}_p}{n_{an}} \cdot \left(y_{i,ff} - y_{i,an}\right) + \frac{\dot{n}_s}{n_{an}} \cdot \left(y_{i,ff} - y_{i,s}\right) \tag{A5}$$

Integrating this over an arbitrary time period from the time $t = 0$ to $t = t$ and from the initial composition $y_{i,\mathrm{an},0}$ to $y_{i,an}$, yields:

$$ln\left(\frac{\dot{n}_p \cdot (y_{i,ff} - y_{i,an,0}) - \dot{n}_s \cdot (y_{i,s} - y_{i,ff})}{\dot{n}_p \cdot (y_{i,ff} - y_{i,an}) - \dot{n}_s \cdot (y_{i,s} - y_{i,ff})}\right) = \frac{\dot{n}_p}{n_{an}} \cdot t \tag{A6}$$

This equation can be simplified by recognizing that the composition of the fresh fuel ($y_{i,ff}$) is typically close to $y_{i,s}$ (i.e. $y_{H_2,ff} \approx y_{H_2,s} \approx 1$). The simplified equation is:

$$ln\left(\frac{y_{i,ff} - y_{i,an,0}}{y_{i,ff} - y_{i,an}}\right) = \frac{\dot{n}_p}{n_{an}} \cdot t \tag{A7}$$

or

$$y_{i,an} = \left[1 - exp\left(-\frac{\dot{n}_p \cdot t}{n_{an}}\right)\right] \cdot y_{i,ff} + exp\left(-\frac{\dot{n}_p \cdot t}{n_{an}}\right) \cdot y_{i,an,0} \tag{A8}$$

This equation is valid when

$$\dot{n}_p \cdot \left(y_{i,ff} - y_{i,an,0}\right) \gg \dot{n}_s \cdot \left(y_{i,s} - y_{i,ff}\right) \tag{A9}$$

and

$$\dot{n}_p \cdot \left(y_{i,ff} - y_{i,an}\right) \gg \dot{n}_s \cdot \left(y_{i,s} - y_{i,ff}\right) \tag{A10}$$

This is true when the purge is not performed too frequently ($y_{i,ff} \gg y_{i,an,0}$) and when the purge is not too long ($y_{i,ff} \gg y_{i,an}$), or when the flow rate of the purged gas is high compared to the rate of hydrogen consumption ($\dot{n}_p \gg \dot{n}_s$). At least the first two requirements are generally true.

The total amount of gas purged (n_p) and species i purged ($n_{i,p}$) are obtained by integrating over one purge from the time $t = 0$ to $t = t_p$, as follows:

$$n_p = \int_0^{t_p} \dot{n}_p \, dt = \dot{n}_p \cdot t_p \tag{A11}$$

$$\begin{aligned} n_{i,p} &= \frac{1}{n_p} \int_0^{t_p} \left(\dot{n}_p \cdot y_{i,an}\right) dt \\ &= \left(\dot{n}_p \cdot t_p - \left[\frac{1 - exp\left(-\frac{\dot{n}_p \cdot t_p}{n_{an}}\right)}{1/n_{an}}\right]\right) \cdot y_{i,ff} + \left[\frac{1 - exp\left(-\frac{\dot{n}_p \cdot t_p}{n_{an}}\right)}{1/n_{an}}\right] \cdot y_{i,an,0} \\ &= \left(n_p - \left[\frac{1 - exp\left(-\frac{n_p}{n_{an}}\right)}{1/n_{an}}\right]\right) \cdot y_{i,ff} + \left[\frac{1 - exp\left(-\frac{n_p}{n_{an}}\right)}{1/n_{an}}\right] \cdot y_{i,an,0} \end{aligned} \tag{A12}$$

In other words, the purged gas can be thought as being a mixture of 1) fresh fuel and 2) gas present in the anode before the purge is executed ("old anode gas"). The amount of old anode gas purged ($n_{p,0}$) is:

$$n_{p,0} = \left[\frac{1-exp\left(-\frac{n_p}{n_{an}}\right)}{1/n_{an}}\right] \tag{A13}$$

as seen in Eq. A12. Consequently, the amount of fresh fuel purged ($n_{p,ff}$) is the remaining part:

$$n_{p,ff} = n_p - \left[\frac{1-exp\left(-\frac{n_p}{n_{an}}\right)}{1/n_{an}}\right] \tag{A14}$$

During long purges (n_p is large), the amount of old anode gas purged relative to the total amount of gas purged is small, and the composition of the purged gas approaches that of fresh fuel. During short purges, the opposite is true, and the composition of purged gas approaches that of the old anode gas.

The composition of the anode gas at any instance can be calculated from Eq. A8. In the beginning of a purge (at time $t = 0\ s$), it is $y_{i,an,0}$ and at the end of a purge (at time $t = t_p$):

$$\begin{aligned} y_{i,an,1} &= \left[1 - exp\left(-\frac{\dot{n}_p \cdot t_p}{n_{an}}\right)\right] \cdot y_{i,ff} + exp\left(-\frac{\dot{n}_p \cdot t_p}{n_{an}}\right) \cdot y_{i,an,0} \\ &= \left[1 - exp\left(-\frac{n_p}{n_{an}}\right)\right] \cdot y_{i,ff} + exp\left(-\frac{n_p}{n_{an}}\right) \cdot y_{i,an,0} \end{aligned} \tag{A15}$$

The average composition of purged gas ($\overline{y_{i,p}}$) can be calculated using Eq. A12:

$$\overline{y_{i,p}} = \frac{n_{i,p}}{n_p} = \left(1 - \left[\frac{1-exp\left(-\frac{n_p}{n_{an}}\right)}{n_p/n_{an}}\right]\right) \cdot y_{i,ff} + \left[\frac{1-exp\left(-\frac{n_p}{n_{an}}\right)}{n_p/n_{an}}\right] \cdot y_{i,an,0} \tag{A16}$$

which, using Eq. A15, can be rewritten in terms of the composition of anode gas before ($y_{i,an,0}$) and after ($y_{i,an,1}$) the purge, as follows:

$$\begin{aligned} \overline{y_{i,p}} &= y_{i,ff} - \frac{\left(\left[1-exp\left(-\frac{n_p}{n_{an}}\right)\right] \cdot y_{i,ff} + exp\left(-\frac{n_p}{n_{an}}\right) \cdot y_{i,an,0}\right) - y_{i,an,0}}{n_p/n_{an}} \\ &= y_{i,ff} - \frac{y_{i,an,1} - y_{i,an,0}}{n_p/n_{an}} \end{aligned} \tag{A17}$$

The above equations hold, strictly, only in case of a perfectly mixed anode volume when the assumptions made are true. In reality, the anode volume is not perfectly mixed. Neither are the flow rates constant and equal throughout the purge. Nonetheless, the purged gas can be represented with a mixture of fresh fuel and old anode gas as long as the assumptions in Eqs. A9 and A10 hold. In this case, the fractions of these gases are, however, not easily determined because the flow rates vary during a purge. On the other hand, if the assumptions in Eqs. A9 and A10 do not hold, the magnitude of stream "s" (primarily the hydrogen consumption rate) will affect the composition of purged gas.

Appendix B: Errata

This appendix lists the errors found in publications I-VI.

Publication II

Figure 11 in publication II contains erroneous values of calculated Nernst voltage drop. The erroneous values and corrected values are shown Table B 1.

Table B 1. Erroneous ($E_{Nernst,err}$) and correct ($E_{Nernst,cor}$) values of calculated Nernst voltage drop in publication II.

$T_{dew,cat,in}$ [°C]	t_p [ms]	$\Delta E_{trigger}$ [mV]	$\Delta E_{Nernst,err}$ [mV]	$\Delta E_{Nernst,cor}$ [mV]
52	200	-3	-1.5	-1.5
52	200	-6	-2.8	-2.8
52	200	-9	-4.1	-4.1
52	400	-3	-1.7	-1.5
52	400	-6	-3.1	-3.8
52	400	-9	-4.2	-5.2
55	200	-3	-1.3	-1.3
55	400	-3	-1.7	-1.7
55	400	-6	-3.5	-3.5
55	400	-9	-4.3	-4.3
58	200	-3	-1.7	-1.7
58	400	-3	-1.6	-1.6

The error does not change the conclusions drawn since most erroneous values of calculated Nernst voltage drop deviated only little from the correct values. Figure 19 in Section 4.3.3 is plotted with the correct values.

Equation 6 in publication II is erroneous. The correct definition of the stack efficiency (η_s) reads:

$$\eta_s = \frac{2 \cdot F \cdot E_{cell,avg}}{\Delta H^0} \tag{B1}$$

The correct form of stack efficiency is also shown in Eq. 51 in Section 4.3.4. Stack efficiency in publication II was calculated with the correct equation despite the erroneous equation in the written text.

Publication III

Equation 3 in publication III is erroneous. It should show the approximation of time-averaged Sheerwood number instead of the approximation of instantaneous Sherwood number. The approximation of time-averaged Sheerwood number ($\overline{Sh}$) reads [71]:

$$\overline{Sh} = 4/\sqrt{\pi \cdot Fo} + \frac{63.237 \cdot \sqrt{Fo} + 71.892 \cdot Fo + \pi^2/1.5 \cdot 116.673 \cdot Fo^{1.5}}{1 + 33.616 \cdot \sqrt{Fo} + 45.628 \cdot Fo + 116.673 \cdot Fo^{1.5}} \quad \text{(B2)}$$

The correct form of time-averaged Sheerwood number approximation is also shown in Eq. 62 in Section 5.3. The bubble humidifier in publication III was simulated with the correct equation despite the erroneous equation in the written text.

I

Karimäki H, Pérez LC, Nikiforow K, Keränen T, Viitakangas J, Ihonen J. The use of on-line hydrogen sensor for studying inert gas effects and nitrogen crossover in PEMFC system. Int J Hydrogen Energy 2011;36:10179–87. doi:10.1016/j.ijhydene.2011.04.230.

INTERNATIONAL JOURNAL OF HYDROGEN ENERGY 36 (2011) 10179–10187

Available at www.sciencedirect.com

ScienceDirect

journal homepage: www.elsevier.com/locate/he

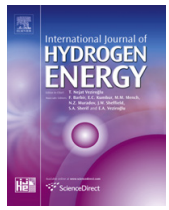

The use of on-line hydrogen sensor for studying inert gas effects and nitrogen crossover in PEMFC system

H. Karimäki [a,*], L.C. Pérez [a,b], K. Nikiforow [a], T.M. Keränen [a], J. Viitakangas [a], J. Ihonen [a]

[a] VTT-Technical Research Centre of Finland, Biologinkuja 3-5, 02044 Espoo, Finland

[b] LEPAE-Laboratório de Engenharia de Processos, Ambiente e Energia, Faculdade de Engenharia, Universidade do Porto, Rua Dr. Roberto Frias s/n, 4200-465 Porto, Portugal

ARTICLE INFO

Article history:
Received 10 February 2011
Received in revised form
27 April 2011
Accepted 30 April 2011
Available online 8 June 2011

Keywords:
PEMFC system
Inert build-up
Hydrogen quality
Hydrogen concentration sensor
Nitrogen crossover
Anode purge

ABSTRACT

The design and construction of a polymer electrolyte membrane fuel cell (PEMFC) system test bench suitable for investigating the effects of inert gas build-up and hydrogen quality on the performance of PEMFC systems is reported. Moreover, a new methodology to measure the inert gas crossover rate using an on-line hydrogen concentration sensor is introduced, and preliminary results are presented for an aged 8 kW PEMFC stack. The system test bench was also characterized using the same stack, whereupon its performance was observed to be close to commercial systems. The effect of inert gas accumulation and hence the quality of hydrogen on the performance of the system was studied by diluting hydrogen gas in the anode supply pipeline with nitrogen. During these experiments, uneven performance between cells was observed for the aged stack.

1. Introduction

General interest in clean-energy production is increasing and environmental concerns are a daily topic. In this context, emerging energy-conversion technologies such as polymer electrolyte membrane fuel cells (PEMFC) have attracted attention due to their high efficiency, low or null local greenhouse gas emissions, high power density, low operating temperature, lack of moving parts, quiet operation and fast start-up and shutdown [1].

Despite their advantages, PEMFC systems have not reached the full-scale commercial stage, as they face many technical challenges concerning balance of plant (BoP), durability and cost [2,3]. One way to reduce overall system costs is to simplify the BoP. However, this will compromise the systems' durability and reduce controllability.

To keep the hydrogen utilization rate high, PEMFC systems usually operate in dead-end mode with periodic opening of the exhaust valve (hydrogen purge) and gas recirculation [4,5]. Dead-end operation mode means that the anode compartment is closed, and anode gas and water are purged when necessary [6]. The cathode is usually fed with humidified air from the atmosphere at a stoichiometric ratio above 2.

Dead-end operation and the purging cycles are achieved using an electro-valve, usually a solenoid valve (SV), which is placed downstream from the anode exit. The purge can then be triggered based on pressure [7], current [8], voltage [9] or it can be time-dependent [10], or a combination of these.

* *Corresponding author*. Tel.: +358 20 722 6449; fax: +358 20 722 7048.
E-mail address: henri.karimaki@vtt.fi (H. Karimäki).

0360-3199/$ – see front matter
doi:10.1016/j.ijhydene.2011.04.230

Independently of the purging strategy, the most important parameters to optimize and control during the purging cycles are: i) the purge stop time, which is the time the SV is kept closed between purges; and ii) the purge time, which is the time the SV is kept open [11]. These parameters are always system-dependent.

Gas recirculation is carried out either by using a pump or an ejector or a combination of the two [12]. Since the recirculated anode gas contains water, the gas recirculation will provide some humidity to the anode gas entering the cell.

When the anode is operated in dead-end mode with gas recirculation, inert gases accumulate on the gas channels, diluting the fuel and increasing mass transfer resistance. Inert gases originate both from the cathode, via permeation through the membrane [13], and from hydrogen that is supplied to the system, especially if the hydrogen is produced from hydrocarbons [14]. If liquid water accumulates in the gas diffusion layers (GDL) and gas channels, mass transfer resistance is further increased. Water can condense and accumulate at the anode due to transport through the membrane from the cathode and since hydrogen is consumed [15].

Accumulation of nitrogen along the anode channel of a PEMFC stack has been modeled and experimentally validated by Müller et al. [16]. These authors observed a significant decline of stack voltage due to nitrogen accumulation, but the effect on cell voltage distribution was not reported. In their model, accumulation of liquid water was not taken into account.

Uneven liquid water accumulation can cause uneven current distribution in a cell and deviation between cell voltages in PEMFC stacks. Moçotéguy et al. [17] presented experimental results and simulations of the dynamic behavior of a stack operated in dead-end mode. According to these results, the performance of a single cell is affected by its relative position in the stack and further by aging of the stack. The results also stated that the cells near the inlet perform better due to higher partial pressure of the gases, while cells near the outlet perform worse due to water accumulation. Uneven cell voltage distribution due to flooding has been studied by ÓRourke et al. [18], who have developed a method to detect anode flooding in PEMFC stacks.

The effects of inert gases and water accumulation (flooding) have been studied using experimental set-ups that do not allow continuous monitoring [19–21] or control [16] of the relative humidity (RH) of the gas. Inert gas accumulation in the anode gas mixture and liquid water accumulation in GDLs and gas channels have a combined effect on mass transfer resistance.

Within this study, a PEMFC test bench to study system-level issues was designed and constructed. The test bench was designed and operated so as to correspond closely to a commercial PEMFC system. The test bench was equipped with both humidity sensors and an on-line hydrogen concentration sensor (H_2 CS) so that the water balance and the effect of hydrogen dilution on the system's performance could be studied.

In this article, the PEMFC system test bench is first described. The performance and characteristics of the system test bench are then presented. On-line monitoring of hydrogen concentration has been applied to determine nitrogen crossover and the hydrogen quality using an aged stack. On-line monitoring was also applied when the effect of inert gas content on system performance and deviation between cell voltages were studied.

2. Description of the fuel cell system test bench

The system test bench was built under a fume hood in such way that easy substitution of the stack, system components and instrumentation is possible. In this study, a commercial PEMFC stack (Nedstack P8) was used. The stack has a nominal output power of 8 kW and comprises 64 cells, each with 200 cm^2 of active area. The test bench was designed especially to study the inert (mainly N_2) build-up characteristics, optimization of BoP subsystems and performance of PEMFC systems.

The fuel cell system consisted of four subsystems, namely: fuel supply, oxidant supply, cooling and control. A simplified scheme of the experimental set-up is shown in Fig. 1. A brief description of the four subsystems is given below. A detailed description of the test bench and more details of the system components can be found in the M.Sc. theses of Viitakangas, Karimäki and Nikiforow [22–24].

The fuel supply subsystem fed hydrogen with an industrial purity of >99.9% and humidity of <20 ppm from a hydrogen pipeline to the anode of the stack. The gas was humidified by mixing humid hydrogen from the exhaust with the dry hydrogen using a recirculation pump. The effects of different fuel qualities on PEMFC system performance were analyzed by feeding N_2 into the hydrogen flow using a mass flow controller.

Hydrogen flow rate was measured using a mass flow meter (Bronkhorst EL-FLOW F-112AC), and the downstream pressure was controlled using a manual pressure regulator. The anode was operated in dead-end mode with gas recirculation executed by a double diaphragm hydrogen pump (GD Thomas 118ZC20/24) and programmed purging cycles.

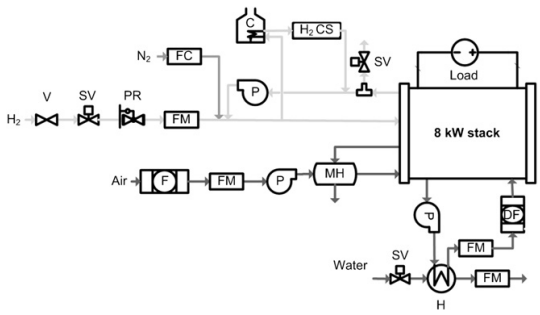

Fig. 1 – Simplified scheme of the system test bench. V: valve, SV: solenoid valve, PR: pressure regulator, FM: flow meter, FC: flow controller, P: pump/blower, C: condenser (ice bath), H_2 CS: hydrogen concentration sensor, F: filter, MH: membrane humidifier, DF: de-ionization filter and H: heat exchanger.

The hydrogen content of the anode gas was measured online using an H2scan HY-OPTIMA 740 hydrogen concentration sensor (H_2 CS). For the hydrogen concentration measurements, a small fraction of the anode exhaust gas, taken after the H_2 recirculation pump, was first dried by refrigerating it using an ice bath and then passed through the H_2 CS using a hydrogen sensor slipstream loop (H_2 SL), shown in Fig. 1. The pressure gradient between the inlet and outlet of the H_2 SL determined the gas flow rate in the loop. H_2 CS measured the partial pressure of hydrogen. Therefore, the absolute pressure in the location of the hydrogen sensor was also measured. Drying the gas reduced the vapor pressure down to approximately 10 mbar. Therefore, the measurement of humidity (water vapor pressure) at the location of the sensor was not needed.

The oxidant supply subsystem fed humidified air to the cathode. It consisted of a filter, a flow meter, a by-pass blower and a membrane humidifier, as in commercial fuel cell systems. The cathode blower was controlled to follow the current profile drawn from the stack so that $5 \geq \lambda O_2 \geq 2.5$ for most of the time. The control system has been documented in more detail by Keränen et al. [25].

The cooling subsystem regulated the temperature of the stack. De-ionized water was used as a coolant in the cooling subsystem's primary cooling loop. A mixed bed ion-exchange filter was implemented in the loop to extend the coolant replacement frequency. Heat from the stack was transferred to a secondary cooling loop (using cold tap water) through a liquid-to-liquid heat exchanger. Water flow in the secondary loop was controlled by using a solenoid valve.

The control subsystem was based on an embedded open-source control system developed mainly at Aalto University [25,26]. Additional data from different sensors was acquired through a data acquisition system developed in-house based on Fieldpoint/LabView by National Instruments.

All BoP components operated with a 24 V DC supply voltage. Therefore, a lead-acid battery pack with corresponding nominal voltage was used to power all the BoP components in order to mimic a commercial system. A programmable electronic DC load (AMREL PLW12K-120-1200) capable of loading up to 12 kW was used for the measurements. Fig. 2 shows the physical layout of the test bench used in this study.

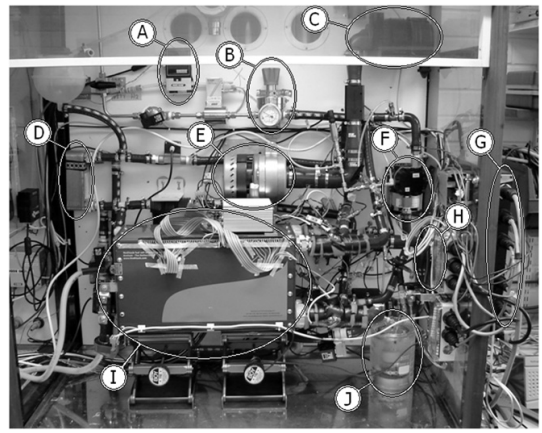

Fig. 2 – Physical layout of the test bench: A. N_2 mass flow controller, B. Pressure regulator, C. Air filter, D. Heat exchanger, E. Cathode blower, F. H_2 recirculation pump, G. Control system, H. H_2 concentration sensor, I. Fuel cell stack, J. Ice bath.

3. Experimental results and discussion

3.1. Test bench and PEMFC system characterization

The gross power, net power and BoP-associated parasitic losses of the system as a function of the stack current are presented in Fig. 3. The maximum gross power of the system was 6.5 kW, while the maximum net power delivered by the system was 5 kW at maximum stack current of 180 A. The performance was not measured at its full rated current (225 A) due to an insufficient flow rate of the recirculation pump that could not provide adequate hydrogen humidification at full power. Due to limited hydrogen humidification capability, the operation temperature was also kept 10 °C lower than specified maximum temperature (65 °C). Because of these safety measures, the nominal power of the stack (8 kW) was not reached. However, reaching the nominal power of the stack was not the main goal of this study.

Fig. 3 also shows that parasitic losses due to BoP components were in the range of 400 W at stand-by and low-current conditions. The system could not deliver net power below a stack current of 7 A. At the maximum current level, auxiliary power consumption was about 1.5 kW, almost 23% of gross power. This is slightly too high to be comparable with commercial systems. There are two main reasons for this poor system efficiency, in addition to the low operation temperature mentioned earlier. Firstly, the brushless DC blower used on the cathode side operates below 10% efficiency over a wide range of operating conditions [22]. This

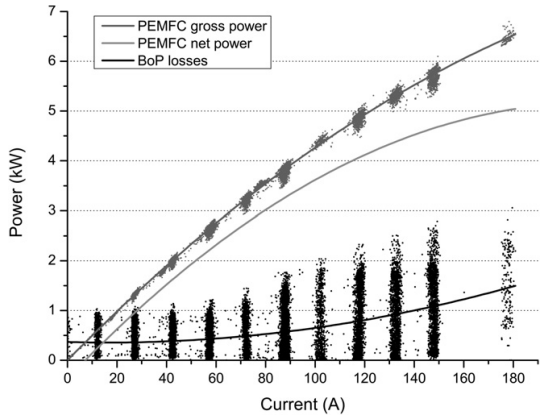

Fig. 3 – PEMFC system gross power, net power and BoP related losses as a function of stack current. Operating conditions: $T_{stack} = 55$ °C.

highlights the importance of selecting the correct blower and its control strategy. Secondly, during this measurement the cooling was provided by an underdimensioned radiator with power-consuming fans instead of a liquid-to-liquid heat exchanger used in later experiments [23].

The performance and controllability of the integrated system were characterized to ensure that its behavior was reasonably close to a commercial system. The polarization curve, along with stack and system efficiencies, is presented in Fig. 4. The stack efficiency, calculated using the higher heating value of hydrogen (HHV_{H_2}), includes losses due to hydrogen purge and hydrogen crossover (Eq. (A1) in Appendix). Therefore, the stack efficiency reached a maximum of 53% at a current level of 20 A. The system efficiency, which included the BoP related parasitic losses (Eq. (A2) in Appendix), reached a maximum of 43% when stack current was 60 A, which corresponded to a net power of 2.2 kW.

The control strategy of the cathode blower is very important for both system efficiency and ramp rate capability of the system. The blower control strategy followed in the present work is similar to the one recommended for dynamic operation of PEMFC stacks for automotive applications [27] and is further documented by Keränen et al. [25].

The small graph on the upper left corner of Fig. 5 shows that the oxygen stoichiometry (Eq. (A3) in Appendix) could be maintained between the desired values (between 2.5 and 5) during steady state measurements.

However, the measured cathode stoichiometric ratio during the transients was significantly lower. The cathode blower response to a current pulse is presented in Fig. 5. When the current was increased from 20 A to 120 A, the cathode stoichiometric ratio dropped temporarily to $\lambda O_2 \approx 1.5$ due to the blower control delay. As the system was also pressurized during the transient, the actual air flow rate in the stack at the beginning of the transient was even lower.

The hydrogen recirculation and humidification subsystem was characterized. The performance of the recirculation pump was measured at different control voltages (33%, 66% and 100% of maximum) at two stack currents (120 A and 160 A) and anode pressure levels (100 mbarg and 300 mbarg). The rate of recirculation was then calculated using the humidities of exhaust gas and mixed gas stream (Eq. (A7) in Appendix).

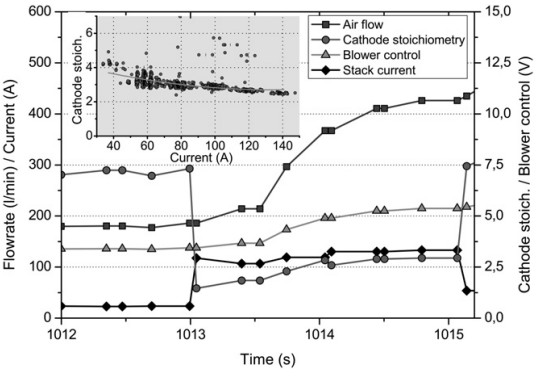

Fig. 5 – Cathode blower response during a stack current transient.

In Fig. 6 the achieved flow rates are shown. These flows were achieved using humid hydrogen (absolute humidity of about 15%). In these measurements a time-triggered hydrogen purge was used frequently to ensure that the amount of accumulated nitrogen in the measurement was kept very low. The maximum flow rate specified by the manufacturer (55 lpm for dry hydrogen) was not reached. This is probably due to the increased temperature, pressure head and humidity of the hydrogen. The limited accuracy (±5%) may also explain part of the discrepancy.

The results in Fig. 6 also show that when the anode side is pressurized, higher recirculation rates, leading to higher inlet humidity, can be obtained. On the other hand, higher pressure on the anode side increases hydrogen permeability, which may reduce the lifetime of the membrane [28].

The achieved flow rates, shown in Fig. 6, corresponded to a hydrogen stoichiometric ratio (Eq. (A4) in Appendix) between 1.19 and 1.73 assuming no inert gas accumulation. Since the

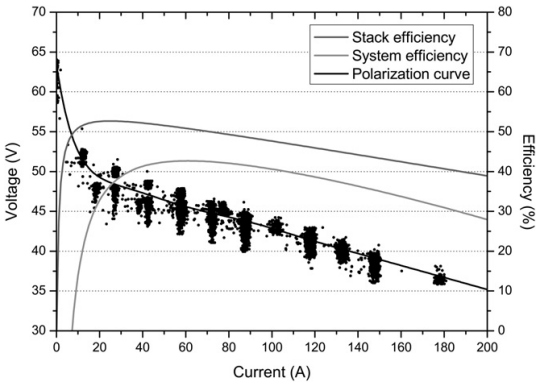

Fig. 4 – PEMFC stack efficiency (HHV_{H_2}), system efficiency and polarization curve. Operating conditions: T_{stack}: 55 °C.

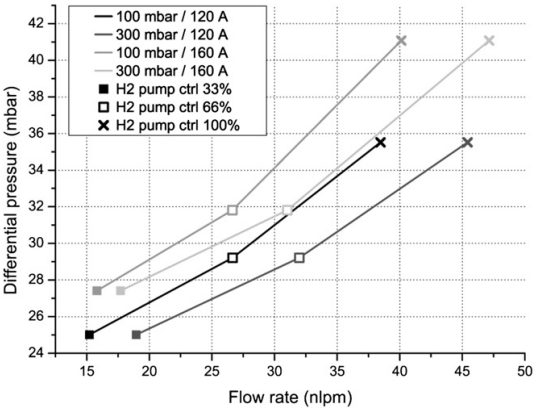

Fig. 6 – Differential pressure over anode as a function of anode gas flow rate at STP (IUPAC, 1 bar and 273.15 K) in different operating conditions.

humidification of the hydrogen in this system is based only on anode gas recirculation, these stoichiometric ratios do not provide adequate humidification (>RH 50%) at higher current levels, even if the recirculation pump is used at full power. Therefore, the control strategy for the hydrogen recirculation pump was to use it at maximum power at all times. This strategy also contributed to the measured low system efficiency.

3.2. *Measurement of nitrogen crossover rate in an aged stack*

The PEMFC system test bench was used for measuring nitrogen crossover in an aged stack. Before these experiments, the stack had been exposed to various experiments over a three-year period.

The N_2 permeation was measured at different currents ranging between 25 A and 175 A, with 25 A intervals. Hydrogen purge was deactivated during the measurements to enable sufficient measuring times. The temperature of the stack was now kept at 58 °C, slightly higher than in the measurements described in Section 3.1. The results for currents 25 A, 100 A and 175 A, presented in the Fig. 7, show how the increase of inert gas content is linear over time. At $t = 0$, the initial hydrogen concentration varied between 88.75% and 90.25%. In the measurements, the lowest hydrogen concentrations in the recirculated gas were between 79% and 86% at the end of the measurements. A constant flow rate was used on the cathode side to minimize the variation in differential pressure between anode and cathode. It has been shown that differential pressure has a significant influence on the crossover rate [28].

In these measurements, the time scale was several minutes, and changes in the hydrogen concentration were slow. Therefore, placing the hydrogen sensor in the slipstream did not introduce significant error in the measurements. The time required to replace the gas volume in the slipstream loop (0.15 dm^3) has been calculated as approximately 1.1 s, depending on the differential pressure over the anode side [24]. The replacement time can be decreased either by minimizing the gas volume of the loop or increasing the slipstream flow. In the former case, drying the gas becomes more difficult. In the latter case, the humidity balance of the fuel cell system is distorted at low stack currents.

The inert gas build-up rates were calculated as a function of current, using the slopes of the hydrogen mole fractions from Fig. 7 and assuming that all other gas in the gas mixture is accumulated nitrogen.

In Fig. 8 the inert build-up rates calculated from experimental data are converted to molar rates using the volume of the anode side (Eq. (A10) in Appendix) and plotted as a function of the current. The inert gas build-up rate is linearly dependent on the stack current, which can be expected since hydrogen consumption and, consequently, inert gas feed rate depend linearly on the current. A similar linear trend was observed in recent works at the single cell level [19], when the nitrogen content was at the level of 100 ppm. However, if membrane permeability were to change significantly in the measurements, this would distort the linear relationship.

From the results in Fig. 8, the inert build-up at zero current could be determined from the y-axis trend line interception (Eq. (A11) in Appendix). Using this rate and total membrane area (14400 cm^2), the average nitrogen flux in the stack can be calculated as 6.2×10^{-6} mol m^{-2} s^{-1}, which is about 5 times greater than what could be calculated using the data from Baik et al. [19]. The higher nitrogen flux values obtained here could probably be associated with the age of the stack. Hydrogen crossover has been shown to increase by more than one order of magnitude during a stack's lifetime [28]. Even if nitrogen permeability could also be assumed to increase, there have not been, to the authors' knowledge, any published results on the evolution of nitrogen permeability with aging membrane.

Hydrogen quality was calculated (Eq. (A12) in Appendix) by using the linear regression equation of Fig. 8. During the measurement it was determined to be 99.925%. Hydrogen quality should be frequently checked. Otherwise, the changes in hydrogen quality between different measurements can induce an error when determining the nitrogen permeation rate.

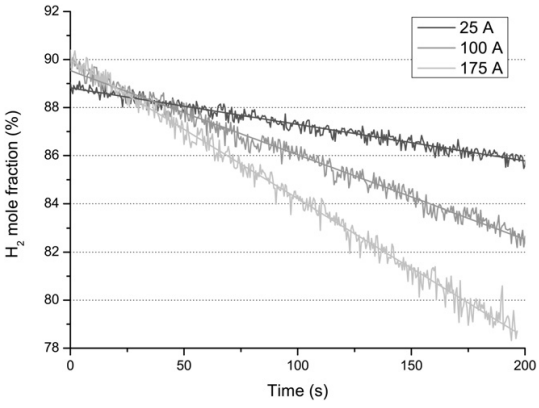

Fig. 7 – The measured hydrogen mole fraction as a function of time. Operating conditions: p_{anode} = 200 mbar(g), $p_{cathode}$ = 130 mbar(g), H_2 recirculation pump control = 100%, T_{stack} = 58 °C.

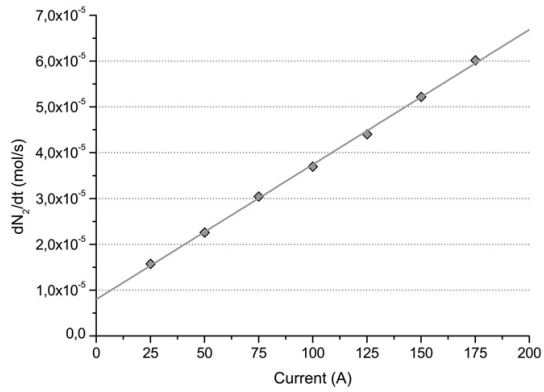

Fig. 8 – The calculated inert gas build-up rate as a function of current load.

The advantages of continuously measuring the hydrogen partial pressure on-line are: i) the concept can be easily applied to commercial fuel cell systems (e.g. vehicles); ii) the gas composition in the dead-end anode compartment does not change due to sampling extraction as in the case of other gas analysis techniques [16]; iii) the fuel quality evolution over a period of time can be analyzed more accurately; and iv) dried gas enables more accurate measurements of the hydrogen content. A clear disadvantage with placing the H_2 CS in the slipstream is that the response time becomes sluggish [24]. In addition, during the measurements it was noted that the hydrogen concentration sensor requires frequent calibration to maintain sufficient accuracy.

3.3. *PEMFC system performance with high inert gas content*

The effect of inert gas accumulation on the performance of the system was studied by diluting hydrogen gas on the anode side with nitrogen and monitoring the cell voltages while the stack current was held constant. Relatively high inert gas contents were used in the measurements. In this way the mass transfer problems on the anode side in different cells could be better identified. In these measurements the stack current was 120 A, and the hydrogen recirculation pump was used at full power.

The sequence of the measurement is shown in Fig. 9. First, nitrogen was fed into the incoming hydrogen stream at the rate of 300 sccm for 200 s. After that, the flow rate was decreased to 100 sccm for 25 s, after which the nitrogen flow was stopped. The level of dilution was chosen so that one of the cells would start falling rapidly within a reasonable time, thereby triggering the purge. Before the first purge was triggered, the hydrogen concentration was about 22.5%, and after the purge a maximum value of about 40% could be measured.

After the first purge, the nitrogen feed was reactivated and measurements were continued so that several purges could be measured. In these measurements the purge was triggered when hydrogen concentration was between 20% and 30%. The cell voltage necessary to trigger the 500 ms-purge was set to a very low value (500 mV).

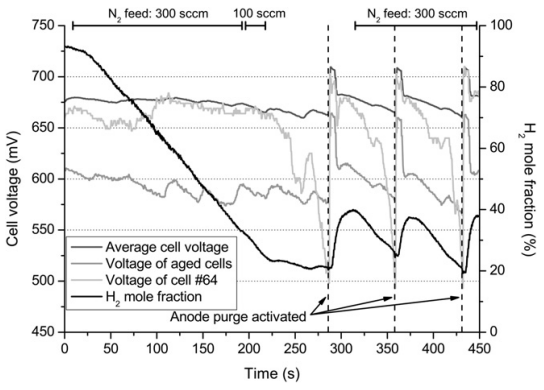

Fig. 9 – Drive cycle showing the cell voltage behavior, the inert feed rate, the hydrogen mole fraction and the purge sequences.

Because the volume of the hydrogen gas side is known, the volume of purged inert gas and hydrogen can be calculated from the measured change of hydrogen concentration. However, in this type of measurement the main drawback of slipstream arrangement (time delay) is demonstrated. There is a clear delay in the measurement signal of H_2 CS, and this limits the accuracy of the measurement. Therefore, at this point only a rough estimate of 0.2–0.4 dm^3 for the volume of the purged gas could be given.

Because the stack used was aged, there were already significant deviations in cell performances. While the less aged cells of the stack showed an average cell voltage of 690 mV, the four more aged cells (number 8, 9, 14 and 15) showed an average voltage of about 610 mV at the beginning of the measurement.

From Fig. 9 it can be seen that after 260 s there is a very steep decrease in the cell voltage of cell number 64, leading to the first purge cycle. This cell, which is the closest to the gas inlets and outlets, was responsible for activating all the purge cycles. The initial voltage of cell 64 was not far from the average cell voltage, but it clearly had the most pronounced response to the hydrogen dilution. However, the results show that the more aged cells recovered better after purges (i.e. their voltage increased) as compared to other cells. All the cells in the stack increased their voltage after the purge cycles, as can be seen from Fig. 9. The average recovery was 40 mV, while for the aged cells the recovery was 85 mV. From these results, it can be concluded that the lower cell voltage of the more aged cells is at least partially due to inadequate water management on the anode side.

Cell 64, which triggered the pulse, however, recovered 200 mV after the purge. This major recovery indicates significant water accumulation in cell 64, which causes significant mass transfer problems. The purge removes both water and inert gas, improving the mass transfer.

Increased water accumulation in the end cells has been observed experimentally by Manke et al. [29]. There can be several reasons for additional water accumulation. Firstly, the operation temperature of the outermost cell may be lower due to cooling effect of the end plates and current collectors. Secondly, the surface pressure distribution may be different in the end cells [30]. Because increased surface pressure causes GDL intrusion in the channels and decreases the hydraulic diameter of the channel, the water removal may become more difficult [31]. Finally, changes in the hydrophobic properties of both gas channels and GDL may affect the water management. However, it is difficult to clarify why the change in the cell 64 should be different from other cells.

When a PEMFC is operated in co-flow or counter-flow mode, inert build-up is not a factor that influences the performance since the small amounts of N_2 that permeate from the cathode to the anode are immediately removed [15]. However, in PEMFC systems operated in dead-end mode with purge and gas recirculation, the simultaneous effect of inert build-up and water accumulation in the anode affect the performance and stability of each cell of the stack to a different degree, as shown in Fig. 9.

As previously mentioned, in these measurements the hydrogen dilution was excessive. In fact, the hydrogen concentration was much lower than what is estimated to be optimal for maximum system efficiency [13]. There is still no consensus concerning what would be the optimal quality (inert gas content) for the hydrogen, when hydrogen production costs and fuel cell system efficiency are both considered. In the modeling work of Ahluwalia and Wang [13], the complex interrelation between hydrogen quality, purge rate, recirculation ratio, stack efficiency and system efficiency is demonstrated. In their simulations, the optimum purge rates and inert gas accumulation were determined for different combinations of fuel quality and recirculation ratio.

However, in real systems the question of optimum purge strategy becomes even more complex, including at least recirculation pump efficiency, the definition of acceptable stack degradation rate, system control and reliability issues as well as the costs of all components.

4. Conclusions

A PEMFC system test bench suitable for studying the effect of inert build-up and hydrogen quality on the performance of PEMFC systems was designed and constructed. The PEMFC system was integrated and characterized in the test bench, where its performance was observed to be close to commercial systems. The test bench was instrumented with flow, pressure and temperature transducers as well as with an on-line hydrogen concentration sensor. This instrumentation enables characterization of system components as well as different stacks at the beginning and end of lifetime.

The applicability of the on-line hydrogen concentration sensor has been confirmed in a system-level study. The use of the on-line hydrogen concentration sensor in a slipstream has been proven to be a feasible method in measurements where inert gas (nitrogen) permeability of the membrane and hydrogen quality were determined. Accurate use of hydrogen concentration monitoring requires the measurement of absolute pressure as well as hydrogen humidity.

On-line hydrogen concentration monitoring during the hydrogen purge sequence revealed the level of inert gases that triggered the purge. Using the concentration monitoring, the amount of purged hydrogen can also be determined. However, for accurate measurements, optimization of the sensor placement in the slipstream is needed due to the gas replacement time in the slipstream loop.

Acknowledgments

This research has been conducted under the “Fuel Cell 2007–2013” technology program of Tekes, the Finnish Funding Agency for Technology and Innovation. The authors would also like to acknowledge their TopDrive project partners.

Luis C. Pérez is grateful to FCT for his PhD grant reference SFRH/BD/44684/2008.

Appendix.

In this appendix some equations used in the study are presented.

Efficiencies

The stack efficiency, η_{stack}, can be calculated either as the ratio of stack electric power, P_{stack}, to theoretical maximum power, which is calculated from the reaction enthalpy, Δh_r, or as the stack electric power, P_{stack}, divided by the theoretical maximum energy content of the fuel consumed, $\dot{n}_{H_2\ consumed}$. The latter one is used here, i.e. the stack efficiency calculated from hydrogen consumption since this accounts for the hydrogen lost during purges and due to hydrogen crossover,

$$\eta_{stack} = P_{stack}/\left(\dot{n}_{H_2\ consumed} \cdot \Delta h_{r,HHV}\right) \tag{A1}$$

The system efficiency, η_{system}, on the other is calculated as the ratio of the system net power, P_{net}, i.e. the stack power, P_{stack}, subtracted with the power of BoP components, P_{BoP}, to the system gross power, P_{gross}, i.e. the stack power,

$$\eta_{system} = P_{net}/P_{gross} = (P_{stack} - P_{BoP}/P_{stack}) \tag{A2}$$

Stoichiometries

The reactant stoichiometry, λ_i, is defined as the ratio of reactant fed, $\dot{n}_{i,stack\ in}$ to reactant consumed, $\dot{n}_{i,consumed}$. The amount of reactants consumed can be calculated using Faraday's law using the stack current, I, and the number of cells, N_{cells}. The stoichiometric ratios of the reactants in this study, oxygen and hydrogen, are calculated as follows

$$\lambda_{O_2} = \dot{n}_{O_2,stack\ in}/\dot{n}_{O_2,consumed} = \dot{n}_{O_2,stack\ in} \cdot (4 \cdot F)/(N_{cells} \cdot I) \tag{A3}$$

$$\lambda_{H_2} = \dot{n}_{H_2,stack\ in}/\dot{n}_{H_2,consumed} = \dot{n}_{H_2,stack\ in} \cdot (2 \cdot F)/(N_{cells} \cdot I) \tag{A4}$$

Rate of hydrogen recirculation

The rate of hydrogen recirculation can be calculated by establishing an overall material balance and a water balance over the stack exhaust and inlet streams, as follows

$$\dot{n}_{exhaust} + \dot{n}_{H_2,feed} = \dot{n}_{in} \tag{A5}$$

$$\dot{n}_{exhaust} \cdot y_{H_2O,exhaust} = \dot{n}_{in} \cdot y_{H_2O,in} \tag{A6}$$

Combining Eqs. (A5) and (A6) gives

$$\dot{n}_{exhaust} = \dot{n}_{H_2,feed} \cdot y_{H_2O,in}/\left(y_{H_2O,exhaust} - y_{H_2O,in}\right) \tag{A7}$$

which equals the recirculation rate.

Rate of inert build-up

Taking the humidity of the recirculated gas to be constant, the molar rate of inert build-up is

$$\dot{n}_{inert\ build-up} = -dn_{H_2,anode}/dt = -n_{anode} \cdot dy_{H_2}/dt \tag{A8}$$

Assuming a perfect gas, the measured rate of change in hydrogen concentration can be converted into molar inert build-up rate as follows

$$\dot{n}_{\text{inert build-up}} = -P_{\text{anode}} \cdot V_{\text{anode}} / (R \cdot T_{\text{anode}}) \cdot dy_{H_2}/dt \quad \text{(A9)}$$

where p_{anode} and T_{anode} are the mean pressure and temperature, respectively, and V_{anode} is the total anode volume including the recirculation loop and the slipstream loop. However, a correction has to be introduced to Eq. (A9) that accounts for the volume taken by vapor since, in the present arrangement the concentration of dry hydrogen is measured and the anode compartment contains a substantial amount of water vapor. This is done by assuming the average water vapor partial pressure to equal saturated vapor in the temperature of gas entering the anode of the stack ($p_{H_2O} \approx p^s_{H_2O}(T_{\text{anode,in}})$). The corrected equation becomes

$$\dot{n}_{\text{inert built-up}} = \left(p^s_{H_2O}(T_{\text{anode,in}}) - p_{\text{anode}}\right) \cdot V_{\text{anode}} / (R \cdot T_{\text{anode}}) \cdot dy_{H_2}/dt \quad \text{(A10)}$$

By using linear regression between the rate of inert build-up and the stack current, the membrane permeability can be calculated using the y-axis intercept, as follows

$$\dot{n}_{\text{inert,membrane}} = \dot{n}_{\text{inert build-up}}(I = 0)/(N_{\text{cells}} \cdot A_{\text{cell}}) \quad \text{(A11)}$$

On the other hand, the hydrogen mole fraction of the feed gas can be solved using the slope, as follows

$$Y_{H_2,\text{feed}} = 1 - (2 \cdot F)/N_{\text{cells}} \cdot d\dot{n}_{\text{inert build-up}}/dI \quad \text{(A12)}$$

REFERENCES

[1] Mench MM. Fuel cell engines. 1st ed. New Jersey: John Wiley & Sons Inc.; 2008.

[2] Scholta J, Berg N, Wilde P, Jörissen L, Garche J. Development and performance of a 10 kW PEMFC stack. Journal of Power Sources 2004;127(1–2):206–12.

[3] Chang H-P, Chou C-L, Chen Y-S, Hou T-I, Weng B- J. The design and cost analysis of a portable PEMFC UPS system. International Journal of Hydrogen Energy 2007;32(3):316–22.

[4] Ferraro M, Sergi F, Brunaccini G, Dispenza G, Andaloro L, Antonucci V. Demonstration and development of a polymer electrolyte fuel cell system for residential use. Journal of Power Sources 2009;193(1):342–8.

[5] Gerbec M, Jovan V, Petrovcic J. Operational and safety analyses of a commercial PEMFC system. International Journal of Hydrogen Energy 2008;33(15):4147–60.

[6] Barbir F. PEM fuel cells: theory and practice. Burlington, MA: Elsevier Academic Press; 2005. p. 120.

[7] Hwang JJ, Zou ML. Development of a proton exchange membrane fuel cell cogeneration system. Journal of Power Sources; 195(9):2579–2585.

[8] Eckl R, Zehtner W, Leu C, Wagner U. Experimental analysis of water management in a self-humidifying polymer electrolyte fuel cell stack. Journal of Power Sources 2004;138(1–2):137–44.

[9] Dumercy L, Péra MC, Glises R, Hissel D, Hamandi S, Badin F, et al. PEFC stack operating in Anodic dead end mode. Fuel Cells 2004;4(4):352–7.

[10] Bussayajarn N, Ming H, Hoong KK, Ming Stephen WY, Hwa CS. Planar air breathing PEMFC with self-humidifying MEA and open cathode geometry design for portable applications. International Journal of Hydrogen Energy 2009; 34(18):7761–7.

[11] Mokmeli A, Asghari S. An investigation into the effect of anode purging on the fuel cell performance. International Journal of Hydrogen Energy 2010;35(17):9276–82.

[12] Ahluwalia RK, Wang X. Fuel cell systems for transportation: status and trends. Journal of Power Sources 2007;177(1): 167–76.

[13] Ahluwalia RK, Wang X. Buildup of nitrogen in direct hydrogen polymer-electrolyte fuel cell stacks. Journal of Power Sources 2007;171(1):63–71.

[14] Besancon BM, Hasanov V, Imbault-Lastapis R, Benesch R, Barrio M, Mølnvik MJ. Hydrogen quality from decarbonized fossil fuels to fuel cells. International Journal of Hydrogen Energy 2009;34(5):2350–60.

[15] Ge S, Wang CY. Liquid water formation and transport in the PEFC anode. Journal of the Electrochemical Society 2007; 154(10):B998–1005.

[16] Muller EA, Kolb F, Guzzella L, Stefanopoulou AG, McKay DA. Correlating nitrogen accumulation with temporal fuel cell performance. Journal of Fuel Cell Science and Technology 2010;7(2):1–11. 021013.

[17] Moçotéguy P, Druart F, Bultel Y, Besse S, Rakotondrainibe A. Monodimensional modeling and experimental study of the dynamic behavior of proton exchange membrane fuel cell stack operating in dead-end mode. Journal of Power Sources 2007;167(2):349–57.

[18] O'Rourke J, Ramani M, Arcak M. In situ detection of anode flooding of a PEM fuel cell. International Journal of Hydrogen Energy 2009;34(16):6765–70.

[19] Baik KD, Kim MS. Characterization of nitrogen gas crossover through the membrane in proton-exchange membrane fuel cells. International Journal of Hydrogen Energy 2011;36(1): 732–9.

[20] Boillot M, Bonnet C, Jatroudakis N, Carre P, Didierjean S, Lapicque F. Effect of gas dilution on PEM fuel cell performance and impedance response. Fuel Cells 2006;6(1): 31–7.

[21] Li H, Tang Y, Wang Z, Shi Z, Wu S, Song D, et al. A review of water flooding issues in the proton exchange membrane fuel cell. Journal of Power Sources 2008;178(1): 103–17.

[22] Viitakangas J. Theoretical and experimental study of a 10 kilowatt proton exchange membrane fuel cell's thermal and moisture system control. M.Sc. thesis. Helsinki University of Technology, 2008. URL: http://lib.tkk.fi/Dipl/2008/urn100393.pdf, last accessed 10.2.2011.

[23] Karimäki H. Fuel cell hybridization for vehicle applications – theoretical and experimental analysis. M.Sc. thesis. Tampere University of Technology, 2009. URL: http://URN.fi/URN:NBN:fitty-201011231370, last accessed 10.2.2011.

[24] Nikiforow K. Optimization of polymer electrolyte membrane fuel cell systems – applied study of hydrogen recirculation. M.Sc. thesis. Helsinki University of Technology, 2010. URL: http://lib.tkk.fi/Dipl/2010/urn100359.pdf, last accessed 10.2. 2011.

[25] Keränen TM, Karimäki H, Viitakangas J, Vallet J, Ihonen J, Hyötylä P, et al. Development of integrated fuel cell hybrid power source for electric forklift. Journal of Power Sources. in press, [Corrected proof].

[26] NutDAC Open source software package website, URL: http://autsys.tkk.fi/nutdac/, last accessed 10.2.2011.

[27] Corbo P, Migliardini F, Veneri O. Experimental analysis of a 20 kWe PEM fuel cell system in dynamic conditions representative of automotive applications. Energy Conversion and Management 2008;49(10):2688–97.

[28] Inaba M, Kinumoto T, Kiriake M, Umebayashi R, Tasaka A, Ogumi Z. Gas crossover and membrane degradation in

polymer electrolyte fuel cells. Electrochimica Acta 2006; 51(26):5746–53.
[29] Manke I, Hartnig Ch, Grünerbel M, Kaczerowski J, Lehnert W, Kardjilov N, et al. Quasi-in situ neutron tomography on polymer electrolyte membrane fuel cell stacks. Applied Physics Letters 2007;90(18):1–3. 184101.
[30] Karvonen S, Hottinen T, Ihonen J, Uusalo H. Modeling of polymer electrolyte membrane fuel stack end plates. Journal of Fuel Cell Science and Technology 2008;5(4):1–9. 041009.
[31] Inoue G, Matsukuma Y, Minemoto M. Evaluation of the optimal separator shape with reaction and flow analysis of polymer electrolyte fuel cell. Journal of Power Sources 2006;154(1):18–34.

II

K. Nikiforow, H. Karimäki, T. Keränen, J. Ihonen, Optimization study of purge cycle in proton exchange membrane fuel cell system, J. Power Sources. 238 (2013) 336–344. doi:10.1016/j.jpowsour.2012.11.153.

Journal of Power Sources 238 (2013) 336–344

Contents lists available at SciVerse ScienceDirect

Journal of Power Sources

journal homepage: www.elsevier.com/locate/jpowsour

Optimization study of purge cycle in proton exchange membrane fuel cell system

K. Nikiforow*, H. Karimäki, T.M. Keränen, J. Ihonen

VTT – Technical Research Centre of Finland, P.O. Box 1000, FIN-02044, Espoo, Finland

HIGHLIGHTS

- An advanced PEMFC system test bench for anode side studies was built.
- Anode purge gas volume and composition were measured accurately and reproducibly.
- Effect of cathode inlet gas humidification on system performance was studied.
- Mass transport resistance in GDL was found to cause significant voltage polarization.

ARTICLE INFO

Article history:
Received 15 July 2012
Accepted 16 November 2012
Available online 26 March 2013

Keywords:
PEMFC system
Purge cycle
Inert build-up
Hydrogen quality

ABSTRACT

In PEMFC (*proton exchange membrane fuel cell*) systems operating in dead-end mode, hydrogen purges are needed to remove accumulated inert gases and liquid water from the anode side of the fuel cell stack. Hydrogen purges were studied using different humidity levels, purge times, and purge triggering criteria. The purged gas volume and composition were accurately measured with fast data acquisition and an advanced experimental set-up. The experiments were done with constant current density with aim of keeping the anode gas recirculation rate constant. Fuel utilization per pass varied as the hydrogen content on the anode side changed. This study demonstrates how the optimized purge strategy changes with a changing humidity level. It also shows that high fuel efficiency (>99%) is easily reached and that with optimized purge strategy a very high fuel efficiency (99.9%) can be reached. It was also shown that concentration polarization due to accumulation of inert gases on the anode side is two times higher than values obtained by theoretical calculations. This result is significant for purge strategy and system design.

1. Introduction

Proton exchange membrane fuel cells (PEMFCs) are an attractive technology, as they provide zero local emissions, high efficiency and quiet operation. PEMFC technology may provide solutions both for the clean transport as well as stationary applications, such as grid balancing. PEMFC technology has, however, been commercialized only in a limited number of niche applications. Improvements are still required to reduce the cost and to increase the durability of the systems so that mass market applications can be reached.

The design and operation of the anode subsystem, as other PEMFC subsystems, is a sum of many compromises between fuel cell system cost, complexity, efficiency, life-time, and response time. On the other hand, maximization of hydrogen utilization is typically dominated by stack design and system control optimization. Finding energy-efficient system designs to minimize both energy losses due to balance of plant and purged hydrogen is a challenging task.

A common anode subsystem structure in hydrogen fueled PEMFC systems for material handling application and for automotive applications is dead-end operation and valve-controlled hydrogen purge, usually combined with recirculation of the anode gas [1,2]. The hydrogen purge serves two functions. Firstly, it removes some of the inert gases that accumulate in the anode due to permeable membrane and consumption of impure hydrogen [3,4]. Secondly, the purge removes excess water that has accumulated in the anode. Water might accumulate in the anode, even when dry hydrogen is used, due to back-diffusion from the cathode [5].

While the accumulation of inert gas is a relatively simple function of hydrogen quality and membrane permeability, the accumulation of water depends on the stack design and operation conditions [2]. Water accumulation is a major challenge on the

* Corresponding author. Tel.: +358 44 576 2033.
E-mail addresses: kaj.nikiforow@aalto.fi, kaj.nikiforow@vtt.fi (K. Nikiforow).

0378-7753/$ – see front matter © 2013 Elsevier B.V. All rights reserved.
http://dx.doi.org/10.1016/j.jpowsour.2012.11.153

Nomenclature

GDL	gas diffusion layer
LHV	lower heating value (kJ/mol)
PEMFC	proton exchange membrane fuel cell
NLPM	liters per minute of gas at NTP
NTP	normal temperature (0 °C) and pressure (1.013 bar)
E	voltage (V)
E^0	standard voltage, i.e. reversible open circuit voltage at standard state (V)
F	Faraday constant (96,485 C mol^{-1})
ΔH_{H_2}	molar enthalpy change in hydrogen combustion (J mol^{-1})
I	current (A)
n	amount of substance (mol)
p	pressure (bar), 1 bar = 10^5 Pa
Q	volumetric flow rate (NLPM), 1 NLPM = $1.67 \cdot 10^{-5}$ m^3 s^{-1}
R	universal gas constant (8.314 J K^{-1} mol^{-1})
T	temperature (°C), 0 °C = 273.15 K
T_{dew}	dew point temperature (°C)
t	time (s)
V	volume (dm^3 @ NTP)
y	hydrogen mole fraction (−)

Greek symbols

η	efficiency (%)
λ	stoichiometric ratio (−)
Φ_{H_2}	hydrogen utilization per pass (%)
ψ_{H_2O}	fraction of water leaving the system as liquid water through the anode (%)

Subscripts

a	after a purge
an	anode
b	before a purge
cat	cathode
cool	coolant
f	in the fresh hydrogen feed
in	anode/cathode/coolant inlet
out	anode/cathode/coolant outlet
p	purge/in the purged gas

cathode side, and there are numerous studies of the topic, most of which are included in Anderson's review [6].

System efficiency optimization as a function of purged hydrogen and fuel quality has been modeled by Ahluwalia and Wang [1]. In their study, the fuel quality and the membrane thickness determining the nitrogen flux from the cathode were varied. In this optimization study, the accumulation of liquid water was neglected, even if it is known to be a significant cause of inhomogeneity in fuel cell stacks [7].

Recently, Promislow et al. modeled the optimum bleed rate for anode gas [8]. While the work of Promislow et al. points out many important aspects, such as the time scale to reach the steady state nitrogen level and the importance of the dilution effect of anode nitrogen, it is based on several assumptions that are difficult to achieve in practical systems. As the authors point out, uniform current density is assumed and the effects of water management are neglected.

The accumulation of nitrogen and water and their effects have been studied both at the single cell [9–12] and the stack or system level [13–19]. Both of these approaches serve a certain purpose. While the studies that use a single cell give more accurate results for flow field geometry, the studies that use a stack bring out the problems due to uneven flow distribution between the cells.

While many of these studies provide valuable information for the stack design and for system design and operation, data is lacking of the amount of hydrogen purged when the system is operated with realistic control parameters. The amount of purged hydrogen is measured by Adegnon et al. [15], but the purge time is several seconds, while in practical systems it is a fraction of a second. It is also important to quantify how much of the water is actually removed from the anode channels by the purge in different operating conditions. Only the study by Dehn has measured this [2].

In this work, development of a novel experimental set-up enabling measurement of both the purged gas volume and the hydrogen content of the purged gas in a dead-end operated system is reported. Purged volume and fuel utilization were experimentally studied using different purge strategies and different humidity levels of cathode air. Water balance for the system operating in constant current conditions was measured, including the liquid water leaving the system through the anode during a purge. Concentration polarization due to liquid water and nitrogen accumulation was measured and compared to theoretical polarization due to simple gas dilution.

2. Experimental

2.1. Fuel cell system test bench

The PEMFC system test bench reported in a previous study [13] was modified to enable accurate recording of anode side system behavior during purges and also to enable control of the cathode humidity level.

A high data sampling rate during the purge was enabled using a trigger signal from the PEMFC control system just before the control system triggers the purge. The sampling rate during anode purge was increased from 2 Hz to 50 Hz not more than 1 s prior to opening the purge valve and was maintained until 10 s had elapsed since closing the purge valve. A hydrogen mass flow meter (Alicat MS-500SLPM) with fast response time (10 ms) was added to the fuel inlet line. The use of this mass flow meter enabled accurate measurement of the hydrogen flow rate during the purge. The hydrogen concentration sensor, placed in the slipstream in the previous study [13], was replaced with two more stable hydrogen concentration sensors (Applied Sensor HPS-100), which were placed at the inlet and outlet of the anode main line.

The humidification level of the cathode gas was controlled by adding a by-pass line, enabling only a fraction of the inlet air to flow through the humidifier. The by-passed air flow rate was measured with mass flow meter (TSI 42350101).

In addition to these changes in the instrumentation, the aged commercial Nedstack P8 stack used in the previous work was replaced with a latest generation Nedstack P8 stack. A scheme of the experimental set-up is shown in Fig. 1.

2.2. Test procedure and test matrix for purge measurements

The measurements were made using a constant current and constant cathode flow rate and pressure, as the cathode was not pressurized. The current level corresponded to a high efficiency point ($E_{cell,avg}$ = 660–690 mV) and the air stoichiometric ratio (λ_{air} = 2.5)

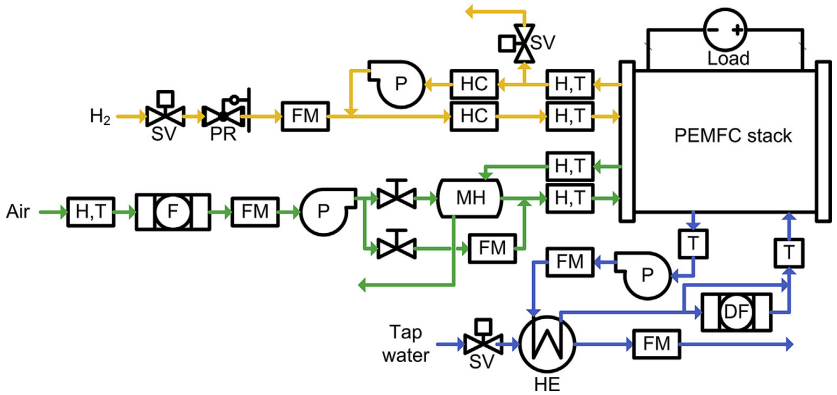

Fig. 1. Scheme of the system test bench. DF: de-ionization filter, F: filter, FM: flow meter, H: humidity measurement, HC: hydrogen concentration measurement, HE: heat exchanger, MH: membrane humidifier, P: pump/blower, PR: pressure regulator, SV: solenoid valve, T: temperature measurement.

was close to optimum from the system efficiency point of view. The hydrogen recirculation rate was maintained at its maximum to enable an even humidification on the anode side even under dry conditions. The anode inlet overpressure ($p_{an,in}$ = 200 mbar) was chosen based on previous experience and was a compromise between durability, fuel efficiency, and the ability of the purge gas to remove liquid water. The operating conditions are shown in Table 1.

Prior to conducting the measurements, the system was allowed to stabilize, i.e. it was operated until the hydrogen mole fractions in the anode line had reached a pseudo-steady state. Once the system had stabilized 10 consecutive purge cycles were recorded, during which the liquid water leaving system through purge valve was collected and measured. The length of one purge cycle varied between 3 and 22 min, depending mainly on the voltage drop allowed between purges. Using the humidity measurements and the measured amount of liquid water leaving the system through the anode purge valve, the total amount of water leaving the system could be determined by establishing a water balance. In Fig. 2 one complete measurement is presented and variations of the parameters are shown.

The measurement routine was repeated by varying (1) the cell-average voltage drop that triggers an anode purge ($\Delta E_{trigger}$ = 3, 6, 9 mV), (2) the cathode inlet dew point temperature ($T_{dew,cat,in}$ = 52, 55, 58 °C), and (3) the time the purge valve was kept open (t_p = 200, 400 ms).

The matrix of measurements performed in this work is shown in Table 2. Measurements performed in high humidity conditions and

Table 1
Measured time average operating conditions and parameters.

Parameter	Target	Measured time average
I_{stack}	120 A	119.9–120.0 A
$Q_{an,in}$ [a]	–	107–113 NLPM
$p_{an,in}$	200 mbarg	186–217 mbarg
$p_{an,out}$	–	146–180 mbarg
Fuel quality	–	99.9% H_2 [b], <20 ppm H_2O
$Q_{cat,in}$	319 NLPM	321–329 NLPM
λ_{O_2}	2.5	2.52–2.58
$p_{cat,in}$	–	75–84 mbarg
$p_{cat,out}$	–	10–15 mbarg
$T_{cool,in}$	60–60.5 °C	60.1–60.5 °C
ΔT_{cool}	–	2.8–4.1 °C

[a] Total anode gas flow rate including recirculation.
[b] The fuel quality was determined using the method described in Karimäki et al. [13].

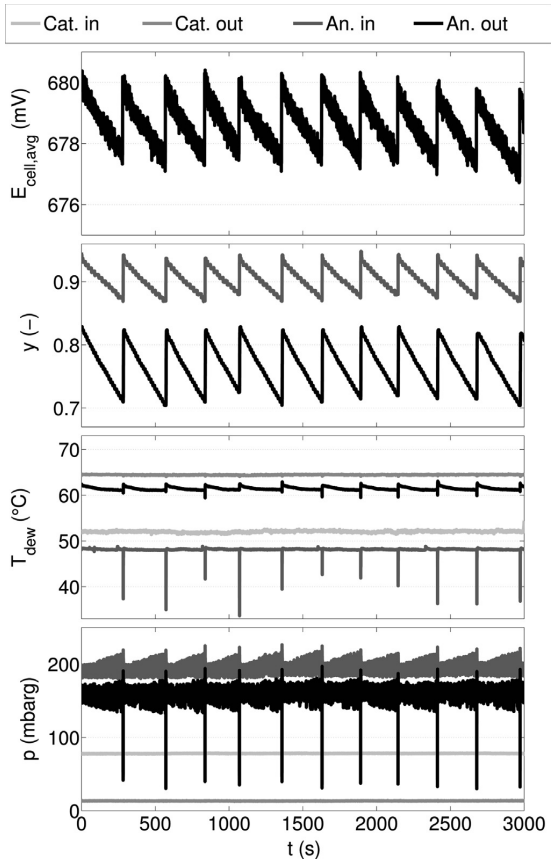

Fig. 2. Average cell voltage ($E_{cell,avg}$), hydrogen mole fractions (y), dew point temperatures (T_{dew}), and pressures (p) during one complete measurement. The cathode inlet dew point temperature is $T_{dew,cat,in}$ = 52 °C, the purge time is t_p = 400 ms, and the purge triggering criteria is $\Delta E_{trigger}$ = 3 mV.

Table 2
Test matrix and the number of successfully measured consecutive purge cycles. Three data sets are numbered and their ordinals are shown as superscripts.

↓ $\Delta E_{trigger}$ (mV)	The number of successfully measured consecutive purge cycles					
$T_{dew,cat,in}$ (°C)/t_p (ms) →	52/200	55/200	58/200	52/400	55/400	58/400
3	$6^{1,2,3}$	7^{1}	7^{1}	$9^{1,2}$	$9^{1,3}$	9^{1}
6	$7^{2,3}$	0	0	8^{2}	9^{3}	0
9	$7^{2,3}$	0	0	7^{2}	9^{3}	0

long purge intervals were shown to be challenging because of unstable performance of the stack due to extensive water accumulation. Reliable data from these measurements was not acquired. Instead, the results from the three data sets numbered in Table 2 are addressed.

2.3. Analysis of purged gas volume and composition

Analysis of the purged gas volume and the hydrogen mole fraction in the purged gas was performed using the measured flow rate profile of hydrogen entering the anode and the hydrogen concentration in the anode line before and after the anode purge.

Fig. 3 shows a typical hydrogen flow rate (Q) profile and anode inlet hydrogen mole fraction (y) change during an anode purge. As seen from the figure, there is a time lag between closing the purge valve and the measured maximum flow rate. The observed time lag is due to the opening and closing times of the valve, which result in anode gas being purged after giving the command to close the purge valve. Furthermore, the hydrogen flow rate profile is wider than the time the valve is kept open. This is explained with the principles of fluid dynamics in that a flow caused by a pressure gradient evens out the pressure gradient, thus resulting in a decreased fluid flow rate.

The volume of fresh hydrogen entering the anode during a purge is calculated by numerically integrating the hydrogen flow rate profile over time, as follows:

$$V = \int Q_{feed}\,dt \tag{1}$$

This volume equals the volume of anode gas purged (V_p) and can be converted into moles of gas purged (n_p) using the ideal gas law, as follows:

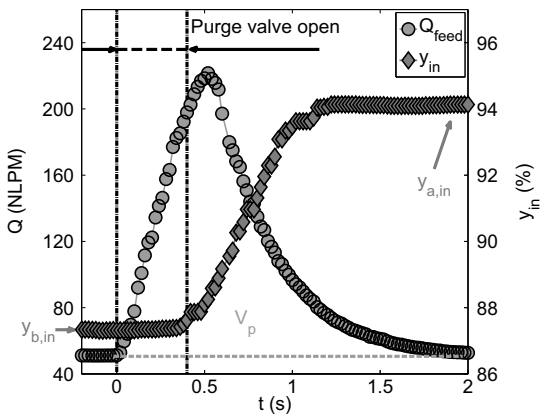

Fig. 3. Hydrogen flow rate (Q) and anode inlet hydrogen mole fraction (y_{in}) during anode purge. The cathode inlet dew point temperature is $T_{dew,cat,in}$ = 52 °C, the purge time is t_p = 400 ms, and the purge triggering criteria is $\Delta E_{trigger}$ = 3 mV.

$$n_p = \frac{p \cdot V_p}{R \cdot T} \tag{2}$$

The purged gas is a mixture of hydrogen, nitrogen, and water and the mole fraction of hydrogen (y_p) can be determined by establishing a mole balance for the purge process by using Eqs. (1) and (2), the measured hydrogen mole fractions in the anode line ($y_{b,in}$, $y_{a,in}$, $y_{b,out}$, $y_{a,out}$), and the mole fraction of hydrogen in the feed (y_f), as follows:

$$y_p = y_f - \frac{n_{an}}{n_p} \cdot (y_a - y_b) \tag{3}$$

In Eq. (3), y_b and y_a are the average hydrogen mole fractions in the anode line before and after the purge, respectively. They are calculated using $y_{b,in}$, $y_{b,out}$, $y_{a,in}$, $y_{a,out}$, and fractional volumes of anode gas at inlet and outlet concentrations. The fractional volumes of anode gas at different concentrations were determined by measuring the anode volume as described by Nikiforow [20]. n_{an} in Eq. (3), represents the moles of gas in the anode line and is calculated based on the anode line volume, temperature, and pressure using the ideal gas law (Eq. (2)). Eq. (3) is valid when it can be assumed that the temperature and pressure of the purged gas equal the temperature and pressure of the fresh hydrogen and that all compounds in the anode gas behave like an ideal gas.

When losing as little hydrogen as possible during an anode purge, y_p should equal $y_{b,out}$. In practice, however, this is seldom true because part of the excess fresh hydrogen entering the anode during a purge and mixing with the recirculated anode gas often makes it to the purge valve while it is still open. In this case, the purged gas can be thought of as a mixture of (1) fresh hydrogen and (2) anode outlet gas, and the fraction of fresh hydrogen (n_f) purged to the purged gas (n_p) can be expressed as follows:

$$\frac{n_f}{n_p} = \frac{y_p - y_{b,out}}{y_f - y_{b,out}} \tag{4}$$

Using Eq. (4), the amount of additional hydrogen compared to $y_{b,out}$ lost during a purged can be determined.

3. Experimental results and discussion

3.1. Effect of humidity level on purged volume and gas composition

During the experiments, the humidity level used was found to have a significant effect on the purged gas volume and composition. As discussed in Section 2.2, the measurements with the highest humidity level were troublesome to perform. Therefore, only measurements with lowest trigger voltage (3 mV) are used in this analysis.

In Table 3, the measured time average reactant dew point temperatures in both stack inlet and outlet, as well as the hydrogen mole fractions in both stack inlet and outlet, are shown. In Table 4, the calculated volume of anode gas purged, anode gas recirculation rate at the anode inlet, average hydrogen utilization per pass, and fraction of water leaving the system as liquid water through the

Table 3
The measured time average reactant dew point temperatures (T_{dew}) and average hydrogen mole fractions in anode loop before and after a purge (y). The purge triggering criteria was $\Delta E_{trigger} = 3$ mV.

↓ $T_{dew,cat,in}$ (°C)	$T_{dew,cat,in}$ (°C)		$T_{dew,cat,out}$ (°C)		$T_{dew,an,in}$ (°C)		$T_{dew,an,out}$ (°C)		y_b (−)		y_a (−)	
t_p (ms) →	200	400	200	400	200	400	200	400	200	400	200	400
52	52.1	52.0	64.7	64.4	47.6	48.1	60.4	61.4	0.78	0.80	0.85	0.88
55	54.9	54.9	64.9	64.9	49.5	49.7	62.5	62.9	0.73	0.77	0.79	0.85
58	58.0	58.0	65.4	65.5	50.3	51.1	64.0	64.1	0.59	0.73	0.65	0.80

Table 4
The calculated volume of anode gas purged (V_p), anode gas recirculation rate at anode inlet ($Q_{an,in}$), average hydrogen utilization per pass ($\Phi_{H_2,average}$), and fraction of water leaving the stack as liquid water on the anode side (ψ_{H_2O}). The purge triggering voltage drop was $\Delta E_{trigger} = 3$ mV.

↓ $T_{dew,cat,in}$ (°C)	V_p (dm³ @ NTP)		$Q_{an,in}$ (NLPM)		$\Phi_{H_2,average}$ (%)		ψ_{H_2O} (%)	
t_p (ms) →	200	400	200	400	200	400	200	400
52	1.03	1.88	112.5	109.7	55.8	55.9	0.1	0.3
55	0.50	1.32	111.5	110.8	59.4	56.9	3.1	3.6
58	0.26	0.74	108.2	112.4	70.3	58.4	6.5	7.3

anode are shown. All data presented in Tables 3 and 4 are averaged from the number of successfully measured consecutive purge cycles shown in Table 2. The anode gas recirculation rate at anode inlet presented in Table 4 is determined as described by Nikiforow [20].

The hydrogen flow rate profiles averaged from all successfully measured consecutive purge cycles are shown in Fig. 4. As seen from these figures, the higher the humidity level, the lower the peak flow rate and the longer it takes for the flow rate to respond to the opened purge valve. These observations suggest that flow resistance increases significantly with increasing the humidity level, i.e. with increasing liquid water accumulation in the flow channels. The increased flow resistance, in turn, results in less gas being purged. This is seen in Fig. 5, where the volume of gas purged as a function of humidity level is shown.

The mole fraction of hydrogen in the purged gas (y_p) as a function of humidity level and n_f/n_p as a function of humidity level and purged volume are shown in Figs. 6 and 7, respectively. Fig. 6 suggests that y_p approaches the hydrogen mole fraction at the anode outlet before the purge ($y_{b,out}$) when increasing the humidity level. This is quite intuitive because when the humidity level increases, the purged volume decreases (Fig. 5) and, thus, less fresh hydrogen entering the anode during purge reaches the purge valve. With the increasing humidity level and, thus, with the increasing flow resistance, a condition is eventually encountered where the fresh hydrogen entering the anode during the purge does not reach the purge valve. In this condition, the purged gas has the same composition as the anode outlet gas before the purge ($y_p = y_{b,out}$), the fuel efficiency reaches its maximum, and the fraction of fresh hydrogen in the purged gas is zero. This condition is approached, as shown in Fig. 7a. Assuming plug flow and no back flow from the recirculated gas, the volume of anode gas purged equals the volume between anode outlet and the purge valve (Fig. 7b).

When increasing the humidity level and decreasing the purge time, measurements become increasingly inaccurate because of the unsteady and unreliable behavior of the stack under these conditions. This means that while maintaining the purged volume below the limit when $y_p = y_{b,out}$ is desirable from the fuel efficiency point of view (because the maximum dilution of the purged gas is achieved), it may result in inefficient liquid water removal. Thus, minimizing the amount of hydrogen lost in a purge might not be the optimal solution for system performance, especially if the system is operated in high humidity conditions.

The measurements in the current set-up show that the fuel efficiency (η_{fuel}) does not play a very central role in the total efficiency ($\eta_{total} = \eta_{fuel} \cdot \eta_{stack}$) but instead the stack efficiency (η_{stack}), dominated by the stack humidity level, is the controlling factor. The efficiencies are calculated as follows:

$$\eta_{fuel} = \frac{n_{H_2,consumed}}{n_{H_2,consumed} + n_{H_2,purged}} \quad (5)$$

$$\eta_{stack} = \frac{2 \cdot F \cdot E_{stack}}{-\Delta H_{H_2,LHV}} \quad (6)$$

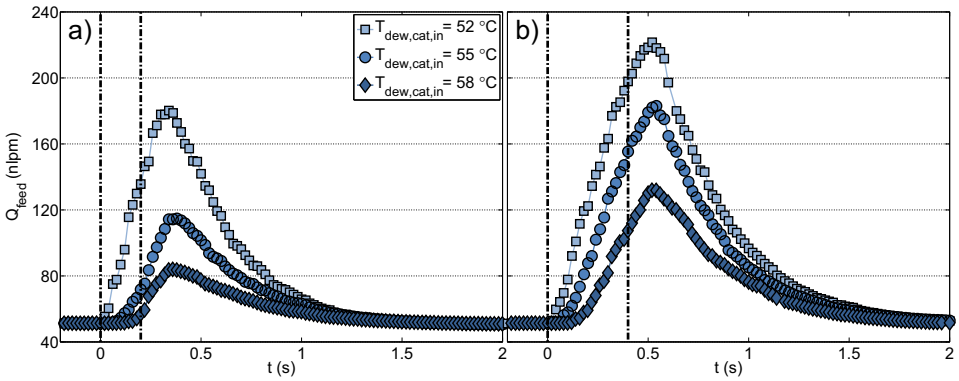

Fig. 4. The hydrogen flow rate profiles averaged from all successfully measured consecutive purge cycles. The cathode inlet dew point temperature was $T_{dew,cat,in} = 52, 55, 58$ °C, the purge time was (a) $t_p = 200$ ms and (b) $t_p = 400$ ms, and the purge triggering criteria was $\Delta E_{trigger} = 3$ mV.

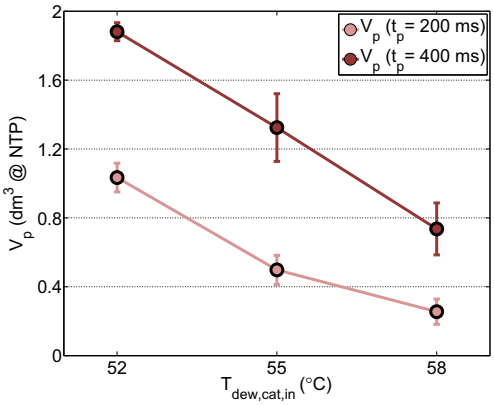

Fig. 5. The volume of anode gas purged (V_p) as a function of humidity level ($T_{dew,cat,in}$). The purge time was t_p = 200, 400 ms and the purge triggering criteria was $\Delta E_{trigger}$ = 3 mV. The error bars show the standard deviation of the measured values.

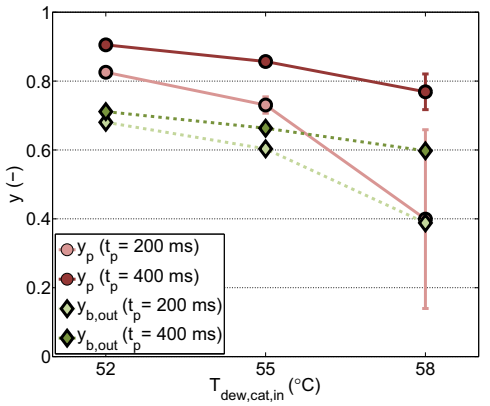

Fig. 6. The hydrogen mole fraction in the purged gas (y_p) and the hydrogen mole fraction at the anode outlet before the purge ($y_{b,out}$) as a function of humidity level ($T_{dew,cat,in}$). The purge time was t_p = 200, 400 ms and the purge triggering criteria was $\Delta E_{trigger}$ = 3 mV. The error bars show the standard deviation of the measured values.

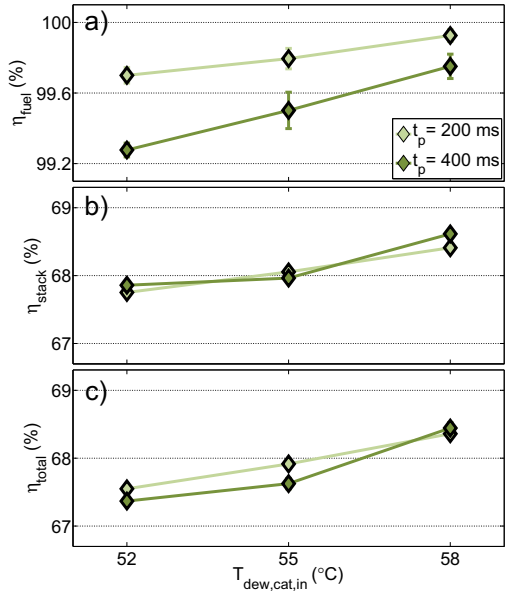

Fig. 8. (a) The fuel efficiency (η_{fuel}, not including fuel cross-over), (b) the stack efficiency (η_{stack}, based on the LHV of hydrogen), and (c) the total efficiency (η_{total}) as a function of humidity level ($T_{dew,cat,in}$). The purge time was t_p = 200, 400 ms and the purge triggering criteria was $\Delta E_{trigger}$ = 3 mV. The error bars show the standard deviation of the measured values.

$$\eta_{total} = \eta_{fuel} \cdot \eta_{stack} \tag{7}$$

As seen in Fig. 8, the stack efficiency accounts for approximately 0.8% of the increase in system efficiency when comparing humid conditions to dry conditions with t_p = 400 ms, while the fuel efficiency accounts for approximately 0.3% although the volume of purged gas changed by a factor of 2.5. The highest system efficiency is achieved when operating the system at the highest humidity level, $T_{dew,cat,in}$ = 58 °C. While it can be concluded that the purged volume might not have a prominent impact on the system total

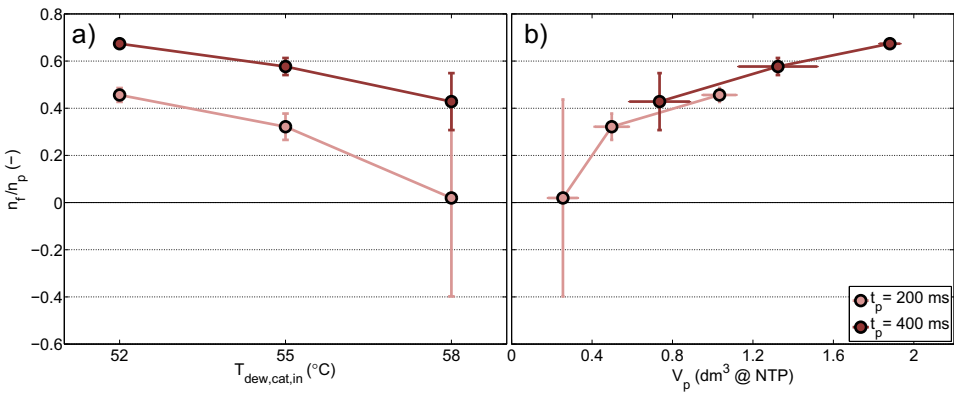

Fig. 7. The fraction of fresh hydrogen in the purged gas (n_f/n_p) (a) as a function of humidity level ($T_{dew,cat,in}$) and (b) as a function of volume purged (V_p). The purge time was t_p = 200, 400 ms and the purge triggering criteria was $\Delta E_{trigger}$ = 3 mV. The error bars show the standard deviation of the measured values.

Table 5
The measured time average reactant dew point temperatures (T_{dew}) and average hydrogen mole fractions in anode loop before and after a purge (y).

↓ $\Delta E_{trigger}$ (mV)	$T_{dew,cat,in}$ (°C)			$T_{dew,cat,out}$ (°C)			$T_{dew,an,in}$ (°C)			$T_{dew,an,out}$ (°C)			y_b (−)			y_a (−)		
$T_{dew,cat,in}$ (°C)/t_p (ms) →	52/200	52/400	55/400	52/200	52/400	55/400	52/200	52/400	55/400	52/200	52/400	55/400	52/200	52/400	55/400	52/200	52/400	55/400
52	52.1	52.0	54.9	64.7	64.4	64.9	47.6	48.1	49.7	60.4	61.4	62.9	0.78	0.80	0.77	0.85	0.88	0.85
55	52.1	52.3	55.0	64.5	65.1	65.9	47.6	48.0	50.2	60.7	60.9	63.7	0.66	0.64	0.62	0.78	0.80	0.76
58	52.0	52.1	54.9	64.8	64.5	65.4	46.1	46.2	49.5	59.5	59.7	63.1	0.56	0.58	0.51	0.70	0.78	0.65

Table 6
The calculated volume of anode gas purged (V_p), anode gas recirculation rate at anode inlet ($Q_{an,in}$), average hydrogen utilization per pass ($\Phi_{H_2,average}$), and fraction of water leaving the stack as liquid water on the anode side (ψ_{H_2O}).

↓ $\Delta E_{trigger}$ (mV)	V_p (dm^3 @ NTP)			$Q_{an,in}$ (NLPM)			$\Phi_{H_2,average}$ (%)			ψ_{H_2O} (%)		
$T_{dew,cat,in}$ (°C)/t_p (ms) →	52/200	52/400	55/400	52/200	52/400	55/400	52/200	52/400	55/400	52/200	52/400	55/400
3	1.03	1.88	1.32	112.5	109.7	110.8	55.8	55.9	56.9	0.1	0.3	3.6
6	0.81	1.33	0.89	109.9	111.2	109.1	62.5	61.4	64.7	0.4	0.5	2.5
9	0.75	1.49	0.58	107.8	107.1	108.0	69.0	65.9	72.9	0.0	0.0	2.9

efficiency, it is important in fuel cell system exhaust gas treatment, as discussed by Dehn et al. [2].

The fraction of liquid water leaving the system through the anode purge valve to the total amount of water leaving the system (water entering + water generation) at high humidity levels is substantial, as seen in Table 4, reaching a value of 7.3% under the most humid conditions. This should be taken into account when estimating the water balance and sizing the cathode humidifier in similar system configurations.

3.2. Effect of purge triggering criteria on system efficiency

One of the goals of this study was to determine the optimum trigger criteria from system efficiency point of view. However, as discussed above, a very high fuel efficiency (>99%) can easily be reached even when purge time and trigger voltage are not optimized.

The effect of purge triggering voltage drop on the efficiency and the purged volume can be studied using data from measurements with cathode inlet dew point temperature $T_{dew,cat,in} = 52$ °C and $T_{dew,cat,in} = 55$ °C. However, with $T_{dew,cat,in} = 55$ °C, data could be recorded only with the longer purge ($t_p = 400$ ms). The measured data is shown in Tables 5 and 6, which are organized in the same way as Tables 3 and 4, respectively.

Comparing the average hydrogen flow rate profiles measured using different purge triggering voltage drops in Fig. 9a and b, it is seen that the flow rate profiles with $\Delta E_{trigger} = 6$ mV and $\Delta E_{trigger} = 9$ mV are similar under dry conditions ($T_{dew,cat,in} = 52$ °C). This is true for measurements with both $t_p = 200$ ms and $t_p = 400$ ms. In contrast, under more humid conditions ($T_{dew,cat,in} = 55$ °C), increasing the $\Delta E_{trigger}$ (Fig. 9c) creates a similar effect on the average flow rate profiles as increasing the humidity level (Fig. 4). Since the interval between purges increases with increasing $\Delta E_{trigger}$, these observations suggest that the water accumulation in the flow channels has had time to reach equilibrium when operating the system at $T_{dew,cat,in} = 52$ °C and $\Delta E_{trigger} = 6$ mV.

The suggested equilibrium condition in water accumulation is also observed when comparing the stack efficiencies, i.e. stack voltages, as a function of $\Delta E_{trigger}$ in Fig. 10b. The stack efficiency seems to be constant in the range $\Delta E_{trigger} = 6$–9 mV in dry conditions.

However, in more humid conditions, the stack efficiency is not constant in this range of $\Delta E_{trigger}$. In fact, the stack efficiency seems

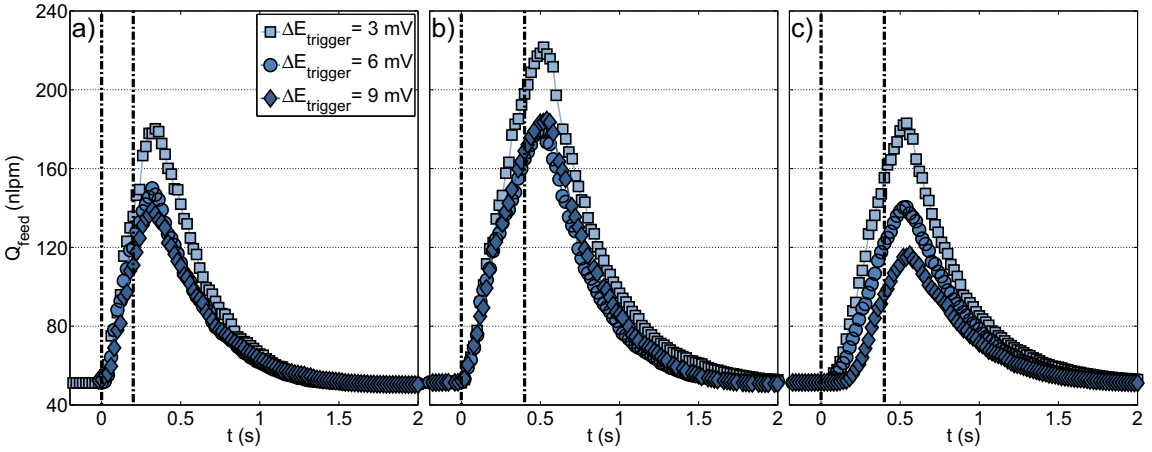

Fig. 9. The hydrogen flow rate profiles averaged from all successfully measured consecutive purge cycles. The cathode inlet dew point temperature and the purge time was (a) $T_{dew,cat,in} = 52$ °C, $t_p = 200$ ms, (b) $T_{dew,cat,in} = 52$ °C, $t_p = 400$ ms, (c) $T_{dew,cat,in} = 55$ °C, $t_p = 400$ ms, and the purge triggering criteria was $\Delta E_{trigger} = 3, 6, 9$ mV.

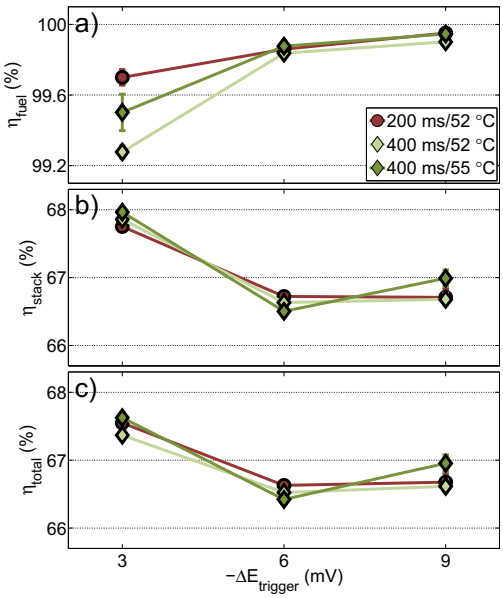

Fig. 10. (a) The fuel efficiency (η_{fuel}, not including fuel cross-over), (b) the stack efficiency (η_{stack}, based on the LHV of hydrogen), and (c) the total efficiency (η_{total}) as a function of purge triggering criteria ($\Delta E_{trigger}$). The purge time was t_p = 200, 400 ms and the humidity level was $T_{dew,cat,in}$ = 52, 55 °C. The error bars show the standard deviation of the measured values.

to increase in the range $\Delta E_{trigger}$ = 6–9 mV. This might be an erroneous result, caused by the stack voltage being very sensitive to the operating conditions, especially to the humidity level inside the stack and to the water accumulation in the flow channels, which were found to reach equilibrium very slowly.

In all measurements, the stack efficiency is found to reach its maximum at $\Delta E_{trigger}$ = 3 mV (Fig. 10b), which is expected because the average voltage drop is the smallest drop used in these experiments. Similarly, in all measurements, the highest fuel efficiency was reached at $\Delta E_{trigger}$ = 9 mV (Fig. 10a), which is due the longest purge interval and the smaller volume purged. The highest total efficiency, however, is reached at $\Delta E_{trigger}$ = 3 mV (Fig. 10c), implying that the stack efficiency through the water balance is the single most important factor in total efficiency, as concluded above.

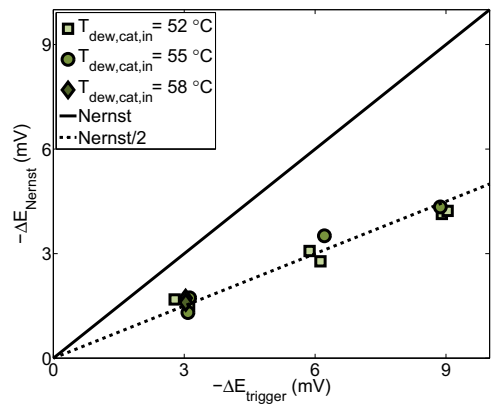

Fig. 11. The measured voltage drop between purges compared to the voltage drop calculated using the measured hydrogen mole fractions and the Nernst equation. The cathode inlet dew point temperature is $T_{dew,cat,in}$ = 52, 55, 58 °C, the purge time is t_p = 200, 400 ms, and the purge triggering criteria is $\Delta E_{trigger}$ = 3, 6, 9 mV.

3.3. Concentration polarization due to N_2 build-up

An important issue in optimizing the design and operation of a PEMFC system is to understand how much voltage loss N_2 build-up is causing on the anode side. In an ideal situation, the dilution is homogeneous throughout the stack. In practice, however, there will be hydrogen concentration gradients between the inlet and outlet as well as between the channel and rib area. In addition, there will be differences between the channels and cells, as flow resistance will be different due to tolerance errors and water accumulation during operation.

Since the hydrogen mole fraction at both the anode inlet and outlet are measured, the theoretical voltage drop due to hydrogen dilution can be calculated using the average hydrogen mole fraction in the Nernst equation. The Nernst equation for a fuel cell using hydrogen as fuel is:

$$E = E^0 - \frac{RT}{2F} \cdot \ln\left(\frac{p_{H_2O}}{p_{H_2} \cdot p_{O_2}^{1/2}}\right) \quad (8)$$

The voltage drop caused by concentration polarization, assuming constant oxygen and water partial pressures, is:

$$\Delta E_{Nernst} = E_2 - E_1 = \frac{RT}{2F} \cdot \ln\left(\frac{p_{H_2,2}}{p_{H_2,1}}\right) \quad (9)$$

As seen in Fig. 11, the voltage drop calculated using the Nernst equation is roughly half of the measured voltage drop and seems to be independent of the humidity level, which indicates that the water accumulation is not highly uneven.

This result suggests that the mass transport resistance for the hydrogen in the gas diffusion layer (GDL) cannot be ignored. Therefore, it can be concluded that mathematical models [21,22], in which the voltage drop is due to simple N_2 build-up and mass transfer resistance is not taken into account, give erroneous estimates of the concentration polarization.

4. Conclusions

In this work, a methodology of reproducibly measuring the purged gas volume and composition was verified and the hydrogen purge was studied as a function of humidity, purge time and purge triggering criteria. The results show that the operating conditions (humidity) are a significant factor for defining the optimum purge strategy. Consequently, in the models for the purge optimization, water accumulation should be taken into account if the stack is operated under such conditions that water accumulation in the flow channels is possible.

It was found that the highest system efficiency is achieved when operating the system under humid conditions and with quite frequent purges, corresponding to low voltage drop allowed between purges.

It could be observed that operating the system in humid conditions, and hence close to conditions where flooding occurs, makes the determination of stack efficiency challenging due to unstable stack performance and long stabilizing times. However, this was also the point of highest system efficiency.

The fuel efficiency, and hence the purge time, in turn, does not affect the system efficiency very much, since the impact of water balance on system efficiency dominates over fuel efficiency. Instead, it is concluded that the purge time should be justified to efficiently

remove the liquid water built-up in the flow channels. Moreover, when operating the system in humid conditions, the amount of water leaving the system as liquid through the anode was found to be significant, thus affecting the humidification of the cathode inlet air.

Furthermore, the theoretical concentration polarization, calculated using the average hydrogen concentration in the flow channels, was found to be roughly half of the measured polarization, indicating a significant mass transport resistance in GDL. However, the mass transport resistance was independent of the humidity level for the stack studied in this work.

The results presented in this paper using the developed methodology are specific to the stack and the system used in this study. In addition, only one current density level and air stoichiometry were studied.

Acknowledgments

This research has been conducted under the “Fuel Cell 2007-2013” technology program of Tekes, the Finnish Funding Agency for Technology and Innovation. The authors would also like to acknowledge their TopDrive project partners.

References

[1] R.K. Ahluwalia, X. Wang, J. Power Sources 171 (2007) 63–71.
[2] S. Dehn, M. Woehr, A. Heinzel, in: 2011 IEEE Vehicle Power and Propulsion Conference, VPPC 2011 (2011).
[3] K.D. Baik, M.S. Kim, Int. J. Hydrogen Energy 36 (2011) 732–739.
[4] A. Mokmeli, S. Asghari, Int. J. Hydrogen Energy 35 (2010) 9276–9282.
[5] J.B. Siegel, A.G. Stefanopoulou, in: American Control Conference (ACC), 2010 (2010), pp. 6606–6611.
[6] R. Anderson, L. Zhang, Y. Ding, M. Blanco, X. Bi, D.P. Wilkinson, J. Power Sources 195 (2010) 4531–4553.
[7] F.N. Büchi, Heterogeneous cell ageing in polymer electrolyte fuel cell stacks, in: F.N. Büchi, M. Inaba, T.J. Schmidt (Eds.), Polymer Electrolyte Fuel Cell Durability, Springer, New York, 2009, pp. 431–439.
[8] K. Promislow, J. St-Pierre, B. Wetton, J. Power Sources 196 (2011) 10050–10056.
[9] J.B. Siegel, D.A. McKay, A.G. Stefanopoulou, in: Proceedings of the 6th International Conference on Fuel Cell Science, Engineering, and Technology, 2008, pp. 757–768.
[10] J.B. Siegel, S.V. Bohac, A.G. Stefanopoulou, S. Yesilyurt, J. Electrochem. Soc. 157 (2010) B1081–B1093.
[11] J.W. Choi, Y. Hwang, S.W. Cha, M.S. Kim, Int. J. Hydrogen Energy 35 (2010) 12469–12479.
[12] A. Manokaran, S. Pushpavanam, P. Sridhar, S. Pitchumani, J. Power Sources 196 (2011) 9931–9938.
[13] H. Karimäki, L.C. Pérez, K. Nikiforow, T.M. Keränen, J. Viitakangas, J. Ihonen, Int. J. Hydrogen Energy 36 (2011) 10179–10187.
[14] L. Dumercy, M.C. Péra, R. Glises, D. Hissel, S. Hamandi, F. Badin, J.M. Kauffmann, Fuel Cells 4 (2004) 352–357.
[15] K.M. Adegnon, Y. Dube, K. Agbossou, Canadian Conference on Electrical and Computer Engineering (2009) 716–719.
[16] D.A. McKay, J.B. Siegel, W. Ott, A.G. Stefanopoulou, J. Power Sources 178 (2008) 207–222.
[17] M. Minutillo, A. Perna, Int. J. Energy Res. 32 (2008) 1297–1308.
[18] E.A. Müller, F. Kolb, L. Guzzella, A.G. Stefanopoulou, D.A. McKay, J. Fuel Cell Sci. Technol. 7 (2010) 0210131–02101311.
[19] T. Pokphet, W. Khan-ngern, J. Charoensuk, International Conference on Electrical Engineering/Electronics Computer Telecommunications and Information Technology (2010) 88–92.
[20] K. Nikiforow, M.Sc. Thesis. Helsinki University of Technology (2010), URL: http://lib.tkk.fi/Dipl/2010/urn100359.pdf, [last accessed 05.07.2012].
[21] J.P. Torreglosa, F. Jurado, P. García, L.M. Fernández, Int. J. Hydrogen Energy 36 (2011) 7628–7640.
[22] R. Seyezhai, B.L. Mathur, Int. J. Hydrogen Energy 36 (2011) 15029–15043.

III

K. Nikiforow, J. Ihonen, T. Keränen, H. Karimäki, V. Alopaeus, Modeling and experimental validation of H2 gas bubble humidifier for a 50 kW stationary PEMFC system, Int. J. Hydrogen Energy. 39 (2014) 9768–9781. doi:10.1016/j.ijhydene.2014.04.058.

INTERNATIONAL JOURNAL OF HYDROGEN ENERGY 39 (2014) 9768–9781

Available online at www.sciencedirect.com

ScienceDirect

journal homepage: www.elsevier.com/locate/he

Modeling and experimental validation of H_2 gas bubble humidifier for a 50 kW stationary PEMFC system

K. Nikiforow [a,*], J. Ihonen [b], T. Keränen [b], H. Karimäki [b], V. Alopaeus [a]

[a] Aalto University, Department of Biotechnology and Chemical Technology, P.O. Box 16100, 00076 Aalto, Finland
[b] VTT Technical Research Centre of Finland, P.O. Box 1000, 02044 VTT, Finland

ARTICLE INFO

Article history:
Received 19 December 2013
Received in revised form
2 April 2014
Accepted 7 April 2014
Available online 9 May 2014

Keywords:
PEMFC
Hydrogen
Humidity
Bubble humidifier

ABSTRACT

Ensuring uniform membrane hydration in a PEMFC (Proton Exchange Membrane Fuel Cell) is important for its performance and durability. In this study, a bubble humidifier for humidifying hydrogen in a 50 kW PEMFC pilot plant was designed, built, and modeled. Initial tests, carried out by humidifying air, show that a dew point temperature of higher than 59 °C is attained when operating the PEMFC plant at nominal power at 65 °C. The model simulation results show good agreement with experimental data and the model is used for studying humidifier performance at other conditions. Steady state simulation results suggest that by increasing the heating water flow rate, the humidifier outlet dew point temperature can be increased by several degrees because of improved heat transfer. Finally, dynamic simulation results suggest that the humidity of the hydrogen can be controlled by manipulating the heat supply to the humidifier.

Introduction

Hydrogen-fueled stationary PEMFC (Proton Exchange Membrane Fuel Cell) power plants are being considered for micro-CHP (Combined Heat and Power), grid-balancing, and telecommunications backup power applications. Properties of PEMFCs that support choosing them over other alternatives are, among other things, their rapid start-up and high efficiency.

In order to achieve high performance and good durability, the membrane in PEMFC must be hydrated, which partially is realized by water transport inside the fuel cell. Water transport alone, however, results in an uneven water distribution. Therefore, to guarantee uniform membrane hydration, the reactant gases can be humidified prior to feeding them into the fuel cell. Using water and heat produced by the fuel cell in humidifying the reactant gases, the fuel cell system can be made self-contained in this respect.

To increase hydrogen utilization in PEMFC, the unused hydrogen that is fed in excess to avoid fuel starvation can be recirculated. The recirculated anode gas also contains water and, thus, serves the purpose of humidifying the hydrogen. However, especially at high current loads, the recirculation of anode gas alone results in inadequate anode humidification, and additional humidification is necessary. Common methods to realize humidification in PEMFC systems include using bubble humidifiers [1], spray towers [2], membrane humidifiers, enthalpy wheels [3], and spray nozzles [4].

* *Corresponding author*. Tel.: +358 50 434 9070.
E-mail addresses: kaj.nikiforow@gmail.com, kaj.nikiforow@aalto.fi (K. Nikiforow).
http://dx.doi.org/10.1016/j.ijhydene.2014.04.058

In spray nozzle humidifiers, the water is atomized and mixed with gas to form an aerosol. The water droplets in the aerosol must then be evaporated so as not to cause flooding in the fuel cell. This is done either by heating the water prior to entering the nozzle or heating the aerosol. Because water has a rather high latent heat, heating the water prior to atomizing requires temperatures well above the desired dew point temperature. On the other hand, heating the aerosol is less efficient than heating liquid and also causes a pressure drop. Therefore, this technique cannot be considered suitable for stationary PEMFC applications where the humidifier is supplied with fuel cell excess heat. Nonetheless, transportation applications can benefit from the relatively small size and ease of control.

Membrane humidifier and enthalpy wheel are equivalent in that both even out the temperature and concentration differences between two gases without mixing them. In a PEMFC, the source of humidity can either be the exhaust hydrogen or the exhaust air. When hydrogen gas is being recirculated, only exhaust air can be considered as the humidity source. This, however, leads to a safety risk because in both membrane humidifiers and enthalpy wheels, leakages can occur. The membrane humidifier can also be operated in liquid-to-gas mode with the consequence, however, that impurities in the water will eventually block the pores in the membrane [4]. When the membrane humidifier is also relatively expensive, it is only used in applications where simplicity and size are critical factors.

Both in bubble humidifiers and in spray towers, the gas and liquid water are brought into contact and the gas is allowed to saturate with water vapor. These two humidifier types, in addition to the liquid-to-gas membrane humidifier, are therefore ideal for use in PEMFC applications where fuel cell excess heat is used for humidifying gases. These three humidifiers differ in acquisition cost, the membrane humidifier being the most expensive due to the high cost of the membrane. Another difference is in operating costs, the bubble humidifier being the most expensive due to the hydrostatic pressure exerted on the gas. The third difference is operation during an emergency shutdown. When the power is shut-off, both the spray tower and the membrane humidifier lose their humidifying capacity dramatically. However, the outlet humidity of a bubble humidifier decreases more slowly because of the thermal mass of the water bed. Hence, correctly dimensioning the bubble humidifier water content prevents mechanical stresses inside the MEA even when power is lost, thus protecting the fuel cell against aging [2].

Both a low gas pressure drop and an adequate humidification during emergency shutdown can be achieved by using a hybrid of a bubble humidifier and a spray tower. The hybrid humidifier works as a spray tower during normal operating and as a bubble humidifier when power is lost. Because of the low gas pressure drop, the hybrid humidifier can also be used for humidifying air.

The present work is about designing, building, and modeling a humidifier suitable for humidifying hydrogen gas in a 50 kW PEMFC power plant. With the aforementioned factors in mind, a bubble humidifier is regarded as the most suitable humidifier type for this purpose at this stage. The experience gained and the model developed in this work can be used in designing gas humidification for multi-MW PEMFC systems.

Experimental

Bubble humidifier design

The bubble humidifier built and tested in this work is designed for a PEMFC pilot plant with nominal power of 50 kW, shown in Fig. 1. The fuel cell module comprises seven Nedstack P9.6 XXL stacks each having 75 cells and a maximum power output of 9.6 kWe. More details about the pilot plant are found elsewhere [5].

The bubble humidifier is heated using PEMFC system excess heat from the system coolant water. This setup not only is energy efficient, but also ensures that the dew point temperature of the gas never exceeds the operating temperature of the fuel cells. The fraction of coolant water flowing

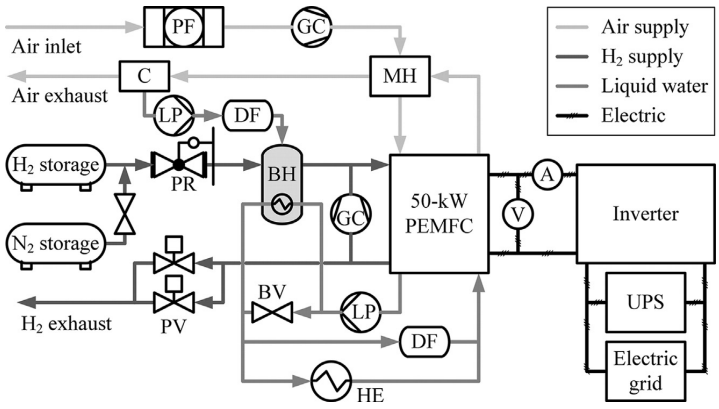

Fig. 1 – Schematic diagram of the 50 kW PEMFC pilot plant. PF: particle filter, GC: gas compressor, C: condenser, MF: membrane humidifier, LP: liquid pump, DF: de-ionizing filter, PR: pressure reducer, BH: bubble humidifier, PV: purge valve, BV: by-pass valve, HE: heat exchanger, UPS: uninterruptible power supply.

through the humidifier is controlled by a manual by-pass valve. By replacing the manual valve with an electronic one, it is possible to control the humidifier temperature and, hence, the outlet humidity on-line.

The de-ionized water supplied to the bubble humidifier is condensed from the cathode outlet air and passed through a de-ionizing filter. The water level in the bubble humidifier is automatically controlled and is maintained between two limits registered by capacitive level transmitters (Omron, E2K-L). The lower level transmitter triggers water feed from an intermediate storage and the higher level transmitter stop the feed. Additionally, a level switch (Cynergy3, RSF44H100RF) is hard-wired to the water feed pump, ensuring that the bubble humidifier cannot be overfilled.

The bubble humidifier (Fig. 2) is built in-house using DN 400 pipe with a pipe cap as the bottom and a removable flange cover. The total height of the bubble column (1.525 m) is chosen based on available space in the fuel cell pilot plant and to guarantee sufficient residence time for bubbles to reach saturation. All gas and heating water ducts and most of the instrumentation are placed in the removable cover.

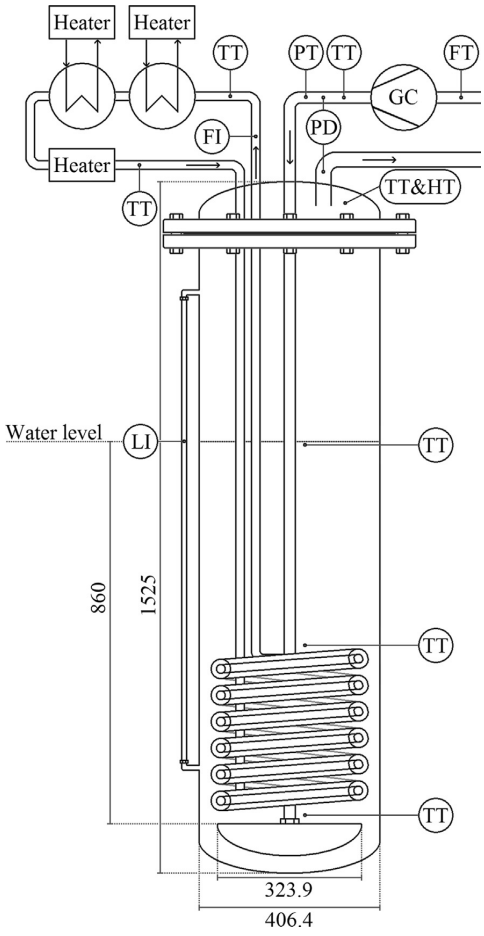

Fig. 2 – Bubble humidifier test setup. TT: temperature transmitter, FT: flow rate transmitter, FI: flow rate indicator, PT: gauge pressure transmitter, PD: differential pressure transmitter, HT: humidity transmitter, LI: level indicator, and GC: gas compressor.

Heat is supplied to the bubble humidifier through a heat exchanger made of a 6 m long DN 15 finned pipe turned into a coil of six turns, resulting in a total height of 0.34 m. The heat exchanger is placed at the bottom of the bubble column, allowing wide water level range (approximately 0.4 m–1.0 m from the sparger). The fins of the heat exchanger pipe are 12 mm in height and placed 222 pieces per meter. The resulting heat exchange area is approximately 3.9 m^2.

The gas sparger is attached to the gas inlet line and located below the heat exchanger. Two spargers were manufactured, each made of a steel plate with laser-cut holes welded onto a pipe cap. The diameter of the holes (1 mm/2 mm) and number of holes (486 pcs/65 pcs, respectively) are dimensioned to result in a gas pressure drop high enough to push the water through a small hole drilled at the bottom of the spargers. This ensures that water does not block any of the sparger holes.

All metal parts used in the bubble humidifier are made of corrosion-resistant steel (EN 1.4404), and all welds in contact with the water-gas mixture are passivated by pickling. Finally, the entire bubble humidifier is insulated using foamed plastic in order to minimize heat losses.

Bubble humidifier test setup

The initial testing of the bubble humidifier was carried out by humidifying air with the setup shown in Fig. 2. Parameters affecting the gas outlet dew point temperature are (1) heating water flow rate, (2) heating water temperature, (3) gas flow rate, and (4) water level. The effects of the first three parameters on air outlet humidity were studied keeping the water level constant at 0.86 m above the sparger. Both of the spargers were tested.

Air outlet temperature and dew point temperature were measured (Vaisala HMM-211) in the gas phase inside the bubble column. Additionally, the temperature of the water was measured (thermocouples) at three levels, namely below the heat exchanger, above the heat exchanger, and at the water surface.

The heating water was heated and recirculated in a closed loop through the bubble humidifier by a programmable electric heater (Huber CC-202C, 2 kW). The effect of heating water flow rate was studied at 13.5 lpm and 8 lpm, the former being the maximum flow rate obtained with this setup. The flow rate was measured using a rotameter (Parker).

Two additional heaters (VWR 1130-1S, 2.2 kW and Lauda Ecoline E-100, 1.6 kW), each in their own closed loops, were used in order to increase the maximum heating power. The effect of heating water inlet temperature on outlet humidity was studied with inlet temperatures being 55 °C, 60 °C, and 65 °C. Both the inlet and outlet heating water temperatures were measured (thermocouples).

The effect of gas flow rate on humidifier outlet humidity was studied by supplying air (Ogura TX12) at three flow rates (Bosch, HFM-5), namely 300 slpm, 600 slpm, and 900 slpm. These flow rates correspond approximately to hydrogen consumption rate in the pilot plant at low power (75 A),

nominal power (150 A), and full power (230 A), respectively. The gas inlet and outlet pressures (Sensortechnics CTE8001GY4 and Omega PX2300-5DI) and inlet temperature (thermocouple) were also measured.

Bubble humidifier model

Two phenomena are considered in this bubble humidifier model. One is the mass transfer of water vapor into gas bubbles, and the other is the heat transfer from heating water to the water through which gas is bubbled. Fig. 3 shows the principle of the model.

The mass transfer is assumed to be purely due to diffusion and the bubble surface is assumed to be saturated with water vapor at all times. Using the ideal gas law, the water concentration at the bubble surface (c_s) is:

$$c_s = p_{vap}(T_l)/(R \cdot T_l), \tag{1}$$

where the water vapor pressure (p_{vap}) is a function of bubble column content temperature (T_l) and R is the universal gas constant. The time dependent volume-average water concentration inside the bubble ($\bar{c}$) is calculated using an approach by Alopaeus [6]:

$$\bar{c}/c_s = 1 - exp\{-1.5 \cdot Fo \cdot Sh_{ave}\}, \tag{2}$$

where the time average Sherwood number (Sh_{ave}) and the Fourier number (Fo) are defined as follows:

$$Sh_{ave} = 2/(\pi \cdot Fo)^{1/2} + (117.346 \cdot Fo^{0.5} + 39.596 \cdot Fo + 1.5 \cdot \pi^2 \cdot 337.258 \cdot Fo^{1.5})/(1 + 62.166 \cdot Fo^{0.5} + 31.169 \cdot Fo + 337.258 \cdot Fo^{1.5}), \tag{3}$$

$$Fo = D_{H2O} \cdot t_r / r_b^2. \tag{4}$$

D_{H2O} is the diffusion coefficient of water in the gas, t_r is the bubble retention time in water, and r_b is radius of a bubble.

All the bubbles being produced at the sparger are assumed to be of the same size and to be constant in size the entire time they are in the water bed. That is, bubble break-up and coalescence is assumed not to occur. The diameter of the bubbles (d_b) produced at the sparger is calculated using a correlation suggested by Bhavaraju et al. [7], which without bubble break-up and coalescence is:

$$d_b = 2 \cdot r_b = \left(6 \cdot d_{or}/g \Big/ \left\{\rho_{l,or} - \rho_{g,or}\right\}\right)^{1/3} \quad \dot{V}_{g,or} < \dot{V}_{g,or,T} \tag{5a}$$

$$d_b = 3.23 \cdot Re_{or}^{-0.1} \cdot Fr_{or}^{0.21} \quad \dot{V}_{g,or} \geq \dot{V}_{g,or,T} \tag{5b}$$

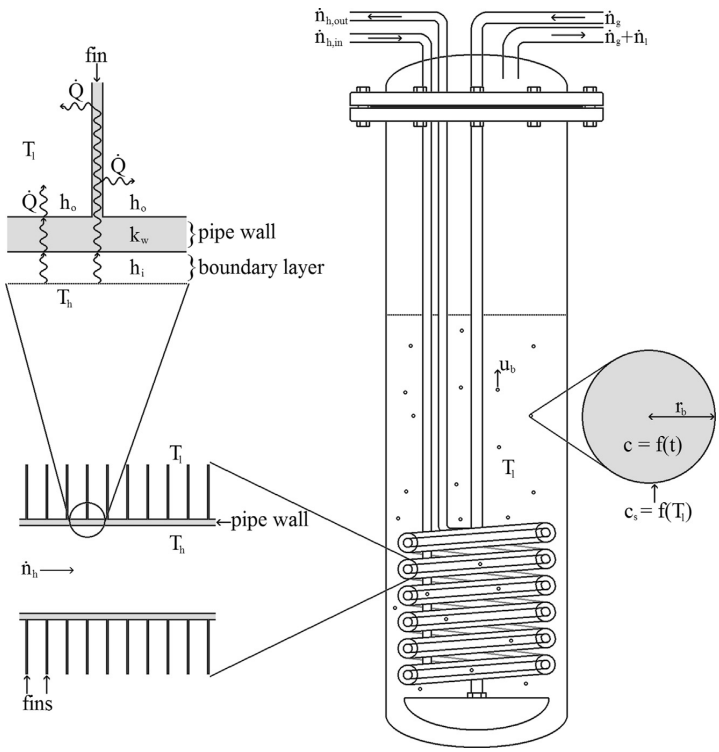

Fig. 3 – Humidifier model principle. $\dot{Q}$: heat transfer rate from heating water, T_l: temperature of bubble column content, T_h: temperature of heating water, h_o: heat transfer coefficient outside the heat exchanger, h_i: heat transfer coefficient inside the heat exchanger, k_w: thermal conductivity of heat exchanger wall, $\dot{n}_h$: molar heating water flow rate, $\dot{n}_g$: molar gas flow rate, $\dot{n}_l$: evaporation rate of water in bubble column, u_b: bubble rise velocity, r_b: bubble radius, c: water concentration inside bubble, c_s: water concentration at the bubble surface, and t: time.

where the modified orifice Reynolds number (Re_{or}) is defined as follows [7]:

$$Re_{or} = 4\cdot\rho_{l,or}\cdot\dot{V}_{g,or}/\pi/\mu_{l,or}/d_{or}, \tag{6}$$

the Froude number at the orifice (Fr_{or}) is defined as follows:

$$Fr_{or} = \dot{V}_{g,or}^2/d_{or}^2/g, \tag{7}$$

the transition volumetric gas flow rate at the orifice ($\dot{V}_{g,or,T}$) is defined as follows:

$$\dot{V}_{g,or,T} = 0.38\cdot g^{1/2}\cdot\left(6\cdot s_{l,or}\cdot d_{or}/g/\left(\rho_{l,or}-\rho_{g,or}\right)\right)^{5/6}, \quad Re_b \gg 1 \tag{8}$$

the Reynolds number for a bubble (Re_b) is defined as follows:

$$Re_b = u_b\cdot d_b\cdot\rho_l/\mu_l, \tag{9}$$

and d_{or} is the diameter of sparger orifice, g is the gravitational acceleration, ρ_l is the liquid density, ρ_g is the gas density, $\dot{V}_g$ is the volumetric gas flow rate, μ_l is the liquid dynamic viscosity, s_l is the surface tension of water in contact with gas being bubbled, and u_b is the bubble rise velocity. The subscript *or* refers to conditions at the orifice. The bubble size is calculated using humidifier inlet gas pressure and average bubble column temperature. In conditions used in current experiments, the predicted bubble size varies in the range $d_b = 7.4\cdot10^{-3}$ m–$14.6\cdot10^{-3}$ m resulting in bubble Reynolds numbers much larger than unity (Re_b » 1).

The bubble retention time in Eq. (4) is calculated by dividing the water level (Δy_l) with the bubble rise velocity:

$$t_r = \Delta y_l/u_b, \tag{10}$$

where the bubble rise velocity is calculated using a correlation suggested by Grace et al. [8]:

$$u_b = \mu_l/(\rho_l\cdot d_b)\cdot M^{-0.149}\cdot(J-0.857). \quad Re_b > 0.1, M < 10^{-3}, Eo < 40 \tag{11}$$

In this equation, the dimensionless groups J and H, Eötvös number (Eo), and Morton number (M) are defined as follows:

$$J = 0.94\cdot H^{0.757} \quad 2 < H \le 59.3 \tag{12a}$$

$$J = 3.42\cdot H^{0.441} \quad H > 59.3 \tag{12b}$$

$$H = 4/3\cdot Eo\cdot M^{-0.149}(0.00009\ Pa\ s/\mu_l)^{0.14} \tag{13}$$

$$Eo = g\cdot\left(\rho_l-\rho_g\right)\cdot d_b^2/s_l \tag{14}$$

$$M = g\cdot\mu_l^4\cdot\left(\rho_l-\rho_g\right)/\rho_l^2\cdot s_l^3. \tag{15}$$

Using the volume-average water concentration inside the bubbles leaving the water bed (Eq. (2)), the water evaporation rate ($\dot{n}_l$) can be calculated as follows:

$$\dot{n}_l = \dot{V}_g\cdot\bar{c}. \tag{16}$$

In the bubble humidifier, two control volumes are considered: (1) the bubble column with content (i.e., the bubble column, the water bed, and heat exchanger) and (2) the content of the heat exchanger. Assuming that the bubble humidifier does not have heat losses to surrounding and that the water evaporated in the bubble humidifier is replaced by water at the same temperature, the energy balance for the bubble column control volume is:

$$\left(V_l\cdot\rho_l/M_l\cdot C_{p,l}+m_{bc}\cdot\underline{C}_{bc}\right)\cdot dT_l/dt = \dot{Q}-\dot{n}_g\cdot\int C_{p,g}dT_g-\dot{n}_l\cdot\Delta_{vap}H_l(T_l), \tag{17}$$

and the energy balance for the heat exchanger content control volume is:

$$0 = \dot{Q}+\dot{n}_h\cdot\int C_{p,h}dT_h, \tag{18}$$

where V_l is the volume of water in the bubble column, M_l is the molar weight of water, $C_{p,l}$ is the heat capacity of the water in bubble column, m_{bc} is the mass of bubble column, $\underline{C}_{bc}$ is the specific heat of bubble column, $\dot{Q}$ is the rate of heat leaving the heating water, $\dot{n}_g$ is the gas molar flow rate, T_g is the gas temperature, $\Delta_{vap}H_l$ is the latent heat of water, $\dot{n}_h$ is the heating water molar flow rate, $C_{p,h}$ is the isobaric heat capacity of heating water, and T_h is the heating water temperature. The integrations of the isobaric heat capacity in Eqs. (17) and (18) are carried out between the inlet and the outlet temperatures.

The heat transfer occurs from heating water flowing inside the pipes to the pipe inner wall and through the pipe wall. From here on, heat transfer occurs through two parallel paths: (1) from pipe outer wall to surrounding water and (2) from pipe outer wall, through the fins to the surrounding water. The heat transfer rate at any point along the heat exchanger is therefore

$$\dot{Q} = (T_h-T_l)/\Big(1/\{h_i\cdot A_i\}+r_i\cdot ln\{r_o/r_i\}/\{A_i\cdot k_w\} + 1/\left\{h_o\cdot\left(A_o+\eta_f\cdot A_f\right)\right\}\Big), \tag{19}$$

where h_i is the heat transfer coefficient inside the heat exchanger, h_o is the heat transfer coefficient outside the heat exchanger, r_i is the heat exchanger pipe inner radius, r_o is the heat exchanger pipe outer radius, k_w is the thermal conductivity of the heat exchanger wall, A_i is heat exchanger inside area in contact with heating water, A_o is the heat exchanger outside area excluding fins, A_f is the heat exchanger fin area, and η_f is the fin efficiency.

The heat transfer coefficient inside the heat exchanger in laminar flow is calculated using a correlation suggested by Sieder and Tate [9]:

$$h_i = k_h/r_i\cdot0.93\cdot(Re_i\cdot Pr\cdot2\cdot r_i/L)^{1/3}\cdot\left(\mu_h/\mu_{h,w}\right)^{0.14}, \quad Re_t \le 2100 \tag{20}$$

and in turbulent flow using a correlation suggested by Gnielinski [10]:

$$h_i = k_h/r_i\cdot f/16\cdot(Re_i-1000)\cdot Pr/\left(1+12.7\cdot(f/8)^{1/2}\cdot\left(Pr^{2/3}-1\right)\right)\cdot\left[1+(2\cdot r_i/L)^{2/3}\right]\cdot(Pr/Pr_w)^{0.11}\cdot2300 < Re_i < 10^6, 0.6 < Pr < 10^5, 0.05 < Pr/Pr_w < 20 \tag{21}$$

In Eqs. (20) and (21), the Reynolds number for flow inside heat exchanger pipe (Re_i) and the Prandtl number (Pr) are defined as follows:

$$Re_i = 2\cdot r_i\cdot u_h\cdot\rho_h/\mu_h, \tag{22}$$

$$Pr = \mu_h\cdot C_{p,h}/k_h. \tag{23}$$

k_h is the thermal conductivity of the heating water, L is the heat exchanger pipe length, μ_h is the dynamic viscosity of bulk heating water, $\mu_{h,w}$ is the dynamic viscosity of heating water close to the pipe wall, f is the Darcy friction factor, Pr_w is the Prandtl number close to the wall, u_h is the mean heating water velocity, and ρ_h is the heating water density. In the transient region ($2100 < Re < 2300$) where neither Eq. (20) nor Eq. (21) is valid, the heat transfer coefficient inside the heat exchanger is assumed to be a linear function of the Reynolds number.

The heat transfer coefficient outside the heat exchanger is calculated using a correlation by Deckwer [11]:

$$St = 0.1\cdot\left(Re_b\cdot Fr\cdot Pr^2\right)^{-0.25}, \quad u_g < 0.1 \text{ m/s} \tag{24}$$

where the Stanton number (St) and the Froude number (Fr) are defined as follows:

$$St = h_o/\left(\rho_l\cdot C_{p,l}\cdot u_g\right) \tag{25}$$

$$Fr = u_g^2/(g\cdot d_b), \tag{26}$$

and u_g is the superficial gas velocity. Pr is defined as in Eq. (23) except that the properties are now those of the liquid in the bubble column. According to measurements carried out by Saxena et al. [12], the heat transfer coefficient is at maximum at $u_g \geq 0.25$ m/s. The maximum heat transfer coefficient ($h_{o,max}$) is given by Ref. [13]:

$$h_{o,max} = 0.12\cdot\left(g^2\cdot\rho_l/\mu_l\right)^{1/6}\cdot\left(\left(\rho_l-\rho_g\right)/\rho_l\right)^{1/3}\cdot\left(k_l\cdot\rho_l\cdot C_{p,l}\right)^{1/2}, \quad Ar\cdot Pr > 10^6 \tag{27}$$

where the Archimedes number (Ar) is defined as follows:

$$Ar = d_b^3\cdot\left(\rho_l-\rho_g\right)\cdot g\cdot\rho_l/\mu_l^2, \tag{28}$$

and k_l is the thermal conductivity of water in the bubble column. The heat transfer coefficient is assumed to be a linear function of superficial gas velocity in the range from 0.1 m/s to 0.25 m/s and at most $h_{o,max}$ at any superficial gas velocity.

The convective heat transfer coefficient near the fins is assumed to equal that heat exchanger pipes (h_o). However, because the fin temperature decreases when moving away from the heat exchanger wall, the heat transfer declines. This is accounted for by using the fin efficiency (η_f), which for the current fin geometry is [14]:

$$\eta_f = 2\cdot r_o/m\left(\left(r_o+\Delta y_f\right)^2 - r_o^2\right)\cdot\left(I_1\left(m\left(r_o+\Delta y_f\right)\right)\cdot K_1(m\cdot r_o) - K_1\left(m\left(r_o+\Delta y_f\right)\right)\cdot I_1(m\cdot r_o)\right)\Big/\left(K_1\left(m\left(r_o+\Delta y_f\right)\right)\cdot I_0(m\cdot r_o) + I_1\left(m\left(r_o+\Delta y_f\right)\right)\cdot K_0(m\cdot r_o)\right), \tag{29}$$

where the fin parameter (m) is defined as follows:

$$m = 2\cdot\Delta y_f/\left(k_w\cdot\Delta z_f\right)^{1/2}, \tag{30}$$

and Δy_f is the fin height (base to tip), $I_n(x)$ is the modified Bessel function of first kind, $K_n(x)$ is the modified Bessel function of second kind, and Δz_f is the fin thickness.

When calculating the average heat transfer rate in the bubble humidifier, the temperature difference in Eq. (19) has to be replaced by the logarithmic mean temperature difference (ΔT_{lm}) [15], which assuming a uniform bubble column temperature ($T_{l,in} = T_{l,out}$), becomes

$$\Delta T_{lm} = \left(T_{h,in} - T_{h,out}\right)/ln\left(\left\{T_{h,in} - T_l\right\}/\left\{T_{h,out} - T_l\right\}\right). \tag{31}$$

The pressure drop of heating water (Δp_h) is calculated as follows:

$$\Delta p_h = \rho_h\cdot f\cdot L/4/r_i\cdot u_h^2. \tag{32}$$

The physical properties of the gas, the water in the bubble column, and the heating water depend on temperatures that are not initially known. Therefore, the model is solved by trial-and-error. First, T_l is guessed and the heat transfer rate is calculated form Eq. (17). Then $T_{h,out}$ is solved using Eqs. (19) and (31). Finally, a check is made whether Eq. (18) is satisfied – if not, a new guess of T_l is made.

The parameters for the model are presented in Table 1. The properties of water and air are considered to be functions of temperature [16].

Results and discussion

Experimental and simulation results

The results of initial tests are plotted in Figs. 4 and 5, and the measured time average value ($\bar{x}$;) and the standard deviation (σ) are listed in Appendix A. The rather high standard deviation of the air flow rate is due to the pulsating flow generated by the roots type air compressor. The standard deviations of the temperature measurements are, however, very low.

The bubble humidifier gas phase temperature (not shown) is systematically 1.1–2.3 °C lower than the bubble humidifier water temperature at the surface. Also, the gas phase is systematically saturated with water vapor. This is believed to be due to heat losses affecting the gas phase temperature measurement. Therefore, in this study, the gas phase temperature measurements are disregarded. Instead, the surface water temperature is assumed to better represent the true dew point of gas leaving the water bed.

Table 1 – The parameters for the model.

Parameter	Value	T (°C)	Ref
Δy_l	0.86 m		
k_w	15, 16 W/m K[a]	20, 100	[17]
r_i	$9.15\cdot10^{-3}$ m		
r_o	$10.65\cdot10^{-3}$ m		
Δy_f	$12\cdot10^{-3}$ m		
Δz_f	$0.5\cdot10^{-3}$ m		
A_i	0.421 m^2		
A_o	0.445 m^2		
A_f	3.439 m^2		
m_{bc}	100 kg		
C_{bc}	500 J/kg K	0–100	[17]

[a] Assumed to be a linear function of temperature in the range 20 °C–100 °C.

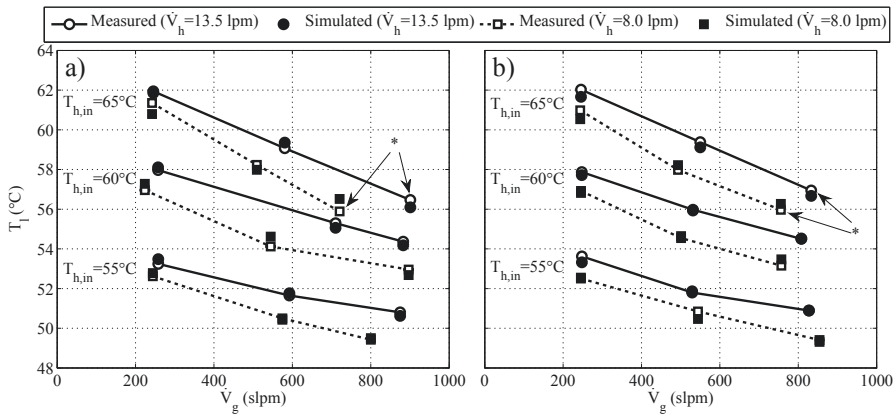

Fig. 4 – Time average bubble column temperature (T_l) as a function of air flow rate ($\dot{V}_g$). Sparger orifice size (d_{or}): a) 1 mm and b) 2 mm *Measurement points in which the set-point temperature could not be maintained.

The results show that the humidifier outlet dew point temperature increases when heating water temperature and flow rate are increased, and also increases with decreasing gas flow rate (Fig. 4). These trends are explained with (1) the higher temperature difference due to the higher operating temperature, (2) the increased heat transfer rate due to the increased heating water flow rate, and (3) the added heat consumption due to the increased gas flow rate. The choice of sparger was not found to have any notable effect on dew point temperature (Fig. 5).

Increasing the operating temperature from 55 °C to 60 °C–65 °C at nominal PEMFC power levels and using a heating water flow rate of 8 lpm, the dew point temperature increases from approximately 50.5 °C–54 °C to 57 °C, respectively. These correspond to relative humidities of 80%, 75%, and 69%, respectively. The decrease in relative humidity is because of the added heat consumption, which is a consequence of the higher dew point temperature.

If instead using a heating water flow rate of 13.5 lpm and increasing the operating temperature from 55 °C to 60 °C–65 °C at nominal PEMFC power levels, the dew point temperature increases from approximately 52 °C–56 °C to 59 °C, respectively. These correspond to relative humidities of 86%, 83%, and 76%, respectively. So, there is a notable increase in humidity with increasing the heating water flow rate. With the anode gas recirculation, somewhat higher anode inlet humidities are reached.

At high gas flow rate, the heating water inlet temperature could not be maintained at 65 °C because of inadequate heating power. These measurements are indicated with asterisks in Figs. 4 and 5.

The simulated humidifier outlet temperatures with the corresponding measured ones are listed in Appendix B. Additionally, the simulated bubble humidifier temperatures are plotted in Figs. 4 and 5. As seen, the simulation results agree well with measured data. The highest deviation in bubble column temperature is 0.9 °C and on average the deviation is 0.2 °C, while for the outlet heating water temperature the highest deviation is 1.0 °C and the average deviation is 0.3 °C.

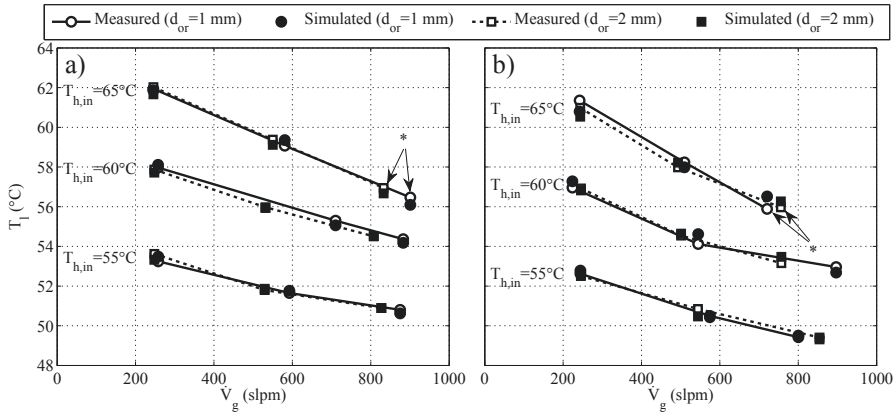

Fig. 5 – Time average bubble column temperature (T_l) as a function of air flow rate ($\dot{V}_g$). Heating water flow rate ($\dot{V}_h$): a) 13.5 lpm and b) 8 lpm. *Measurement points in which the set-point temperature could not be maintained.

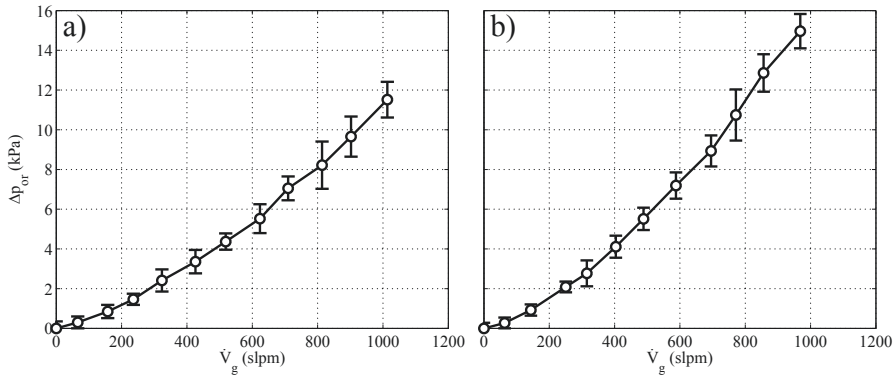

Fig. 6 – Time average gas pressure drop across sparger (Δp_{or}) as a function of gas flow rate ($\dot{V}_g$). a) Spager with 486 holes á d_{or} = 1 mm, b) spager with 65 holes á d_{or} = 2 mm. The error bars show the standard deviation of the measured values.

The gas pressure drop in spargers (Δp_{or}) as a function gas flow rate is plotted in Fig. 6. The pressure drop was determined by measuring the total pressure drop of gas in the bubble humidifier and subtracting the hydrostatic pressure drop. As seen, at nominal gas flow rate (599 slpm), the gas pressure drop is by far high enough to push the water out of the 0.072 m high spargers (<0.7 kPa pressure drop is needed). This relatively high pressure drop guarantees that the spargers function as intended. On the other hand, the high pressure drop causes unnecessary high parasitic losses.

Mass transfer limitation

As the mass transfer rate is finite, the bubbles being formed at the bottom of the humidifier need some time to reach saturation. The mass transfer rate together with bubble rise velocity determines the water level required for the gas to reach a certain degree of saturation.

The time and water level needed for water vapor to reach 99.9% of equilibrium concentration in spherical hydrogen bubbles due to pure diffusion at $T_l = 60°C$ are calculated using Eqs. (2), (4) and (10). The results are shown in Fig. 7 as a function of hydrogen bubble diameter. As can be seen, the water level required to (nearly) saturate the gas bubbles is approximately $\Delta y_l \approx 0.02–0.08$ m in the current study ($d_b = 7.4\cdot10^{-3}$ m–$14.6\cdot10^{-3}$ m). In practice, the water level needs to be somewhat higher to fit the heat exchanger in water and to guarantee that occasional larger bubbles also get saturated. Also, the more water the bubble humidifier contains, the better the humidification during an emergency shutdown.

In the current study, the size of the heat exchanger limits the minimum water level to $\Delta y_l = 0.4$ m. Therefore, it is safe to assume that mass transfer does not limit the humidifier outlet humidity. Efforts to increase the dew point temperature should instead be focused on enhancing the heat transfer rate.

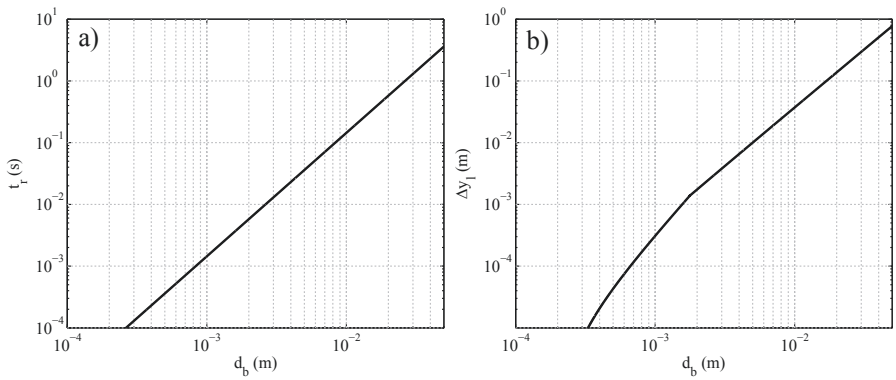

Fig. 7 – a) Retention time (t_r) needed for water vapor to reach 99.9% of equilibrium concentration ($=c_s$) in spherical hydrogen bubbles due to pure diffusion at $T_l = 60\ ^\circ C$ as a function of hydrogen bubble diameter (d_b). b) Water level (Δy_l) needed to reach 99.9% of equilibrium concentration ($=c_s$) in spherical hydrogen bubbles due to pure diffusion at $T_l = 60\ ^\circ C$ as a function of hydrogen bubble diameter (d_b).

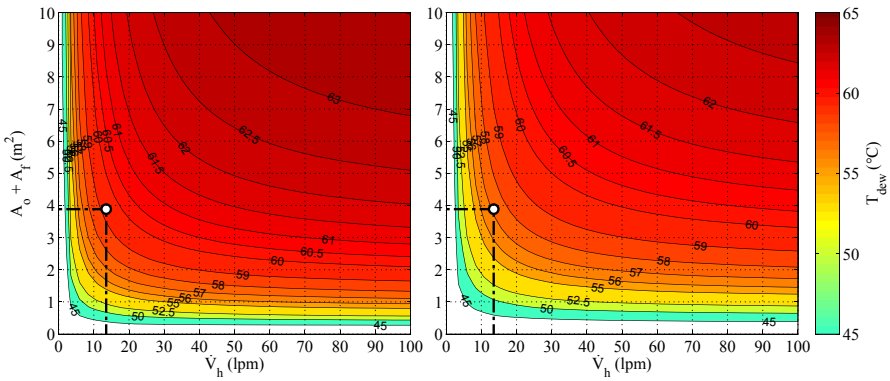

Fig. 8 – Steady state bubble humidifier outlet dew point temperature (T_{dew}) as a function of heating water flow rate ($\dot{V}_h$) and heat exchange area ($A_o + A_f$). Gas flow rate ($\dot{V}_g$) corresponds to nominal power (left) and full power (right). The dew point temperature attained with 3.9 m^2 heat exchanger and 13.5 lpm heating water flow rate is marked in the figures.

Heat transfer limitation

Because the mass transfer does not limit the humidifier outlet humidity, as concluded above, the humidifier outlet humidity is limited by the heat transfer rate. The parameters affecting the heat transfer rate (besides physical properties of the gas, the heating water, and the heat exchanger) are (1) the heating water flow rate ($\dot{V}_h$), (2) the heating water temperature, (3) the gas flow rate, and (4) the heat exchanger area.

The heating water temperature and gas flow rate are set by the operating point of the fuel cell system. However, the heating water flow rate and heat exchange area can be set in the humidifier design phase. To investigate the effect of these design parameters on humidifier steady state performance, the model is simulated with parameters shown in Table 2.

The simulations results for the two gas flow rates are shown in Fig. 8. The approach dew point temperature is defined as the difference between the attained dew point temperature and the theoretical maximum dew point temperature. With a heating water flow rate of 13.5 lpm and a heat exchange area of 3.9 m^2 (as in the present study), the predicted approach dew point temperature is 5.6 °C at nominal power and 7.8 °C at full power. These points are marked in the figures.

Increasing the heating water flow rate to 27 lpm decreases the approach dew point temperature at nominal power to 4.3 °C and at full power to 6.0 °C. However, the heating water pressure drop also increases from 3.2 kPa at 13.5 lpm to 11.9 kPa at 27 lpm. If instead the heat transfer area (i.e., the length of the finned pipe) is increased from 3.9 m^2 to 7.8 m^2, the approach dew point temperature decreases at nominal power to 4.1 °C and at full power to 5.7 °C but the heating water pressure drop increases to 6.4 kPa. Using a 7.8 m^2 heat exchanger and a heating water flow rate of 27 lpm, the resulting approach dew point temperature is 2.8 °C at nominal power and 4.1 °C at full power but the heating water pressure drop is 23.9 kPa.

Based on these simulations, the approach dew point temperature can be decreased notably by increasing the heat exchange area and heating water flow rate. These factors, however, also affect the heating water pressure drop. The heating water flow rate limitation caused by the pressure drop can be overcome by reducing the flow resistance in the heat exchanger or by using a heating water pump.

Humidity control

Depending on the fuel cell water balance, limiting the hydrogen humidity may be desired. Fig. 9, being projections of Fig. 8, shows the steady state dew point temperatures (T_{dew}) as a function of heating water flow rate. Based on this, the dew point temperature can be varied on a wide range by controlling the heating water flow rate. At low heating water flow rates, however, the dew point temperature becomes very sensitive to the flow rate.

In order to find out the dynamic behavior of the bubble column temperature, the model is simulated with parameters shown in Table 3. In the simulation, the humidifier is assumed to be initially in steady state with a heating water flow rate of 13.5 lpm. After 10 s, the heating water flow rate is turned off while still humidifying hydrogen at a rate corresponding to PEMFC system nominal power. After 1 min without heating, the bubble column temperature has decreased 0.8 °C. At this point two different control strategies are employed to restore the initial bubble column temperature.

Table 2 – Parameters for the model in steady state.

Parameter	Value
Gas	H_2
$T_{h,in}$	65 °C
Δy_l	0.4 m
$A_o + A_f$	0–10 m^2
$\dot{V}_h$	0–100 lpm[a]
$\dot{V}_g$	599/919 slpm[b]

[a] A coolant water flow rate of approximately 140 lpm is needed to maintain the temperature difference across the PEMFCs at 5 °C at nominal power.
[b] Nominal power/full power (150/230 A).

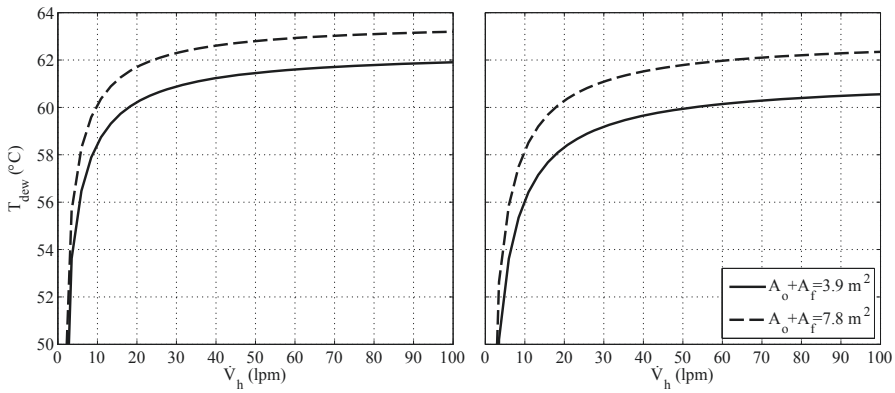

Fig. 9 – Steady state bubble humidifier outlet dew point temperature (T_{dew}) as a function of heating water flow rate ($\dot{V}_h$) with two different heat exchange areas ($A_o + A_f$): 3.9 m² and 7.8 m². Gas flow rate ($\dot{V}_g$) corresponds to nominal power (left) and full power (right).

Table 3 – Parameters for the dynamic model.

Parameter	Value
Gas	H_2
$T_{h,in}$	65 °C
Δy_l	0.4 m
$A_o + A_f$	3.9 m²
$\dot{V}_h$	0/13.5/27 lpm
$\dot{V}_g$	599 slpm

In the first control strategy (Fig. 10a), the initial heating water flow rate is restored. This results in a temperature increase achieving the steady state (with a precision of one decimal) after approximately 15.5 min. The closer the temperature to the steady state temperature, the slower the approach. Therefore, this strategy results in a relatively slow approach towards the steady state.

In the second control strategy (Fig. 10b), a heating water flow rate of 27 lpm is applied until the steady state temperature is reached after 81 s. The faster temperature recovery is partly due to a higher heat transfer coefficient ($h_i = 12.7$ kW/m² K vs. $h_i = 6.6$ kW/m² K at $t = 70$ s) and partly due to a higher temperature difference between bubble column content and heating water ($\Delta T_{lm} = 5.4$ °C vs. $\Delta T_{lm} = 4.5$ °C at $t = 70$ s). These same factors enable the higher steady state temperature.

As seen in theses simulations, the rate of temperature change is at maximum in the order 1 °C/min. Therefore, even though the steady state dew point temperature is sensitive to heating water flow rate at low flow rates (Fig. 9), the dew point temperature is easily maintained close to the set-point value even with a simple on/off-control of the heating water flow.

Summary

In this work, a hydrogen gas bubble humidifier for a 50 kW PEMFC pilot plant was designed, built, and validated experimentally. The humidifier utilizes water and heat produced in a PEMFC plant for humidifying hydrogen gas.

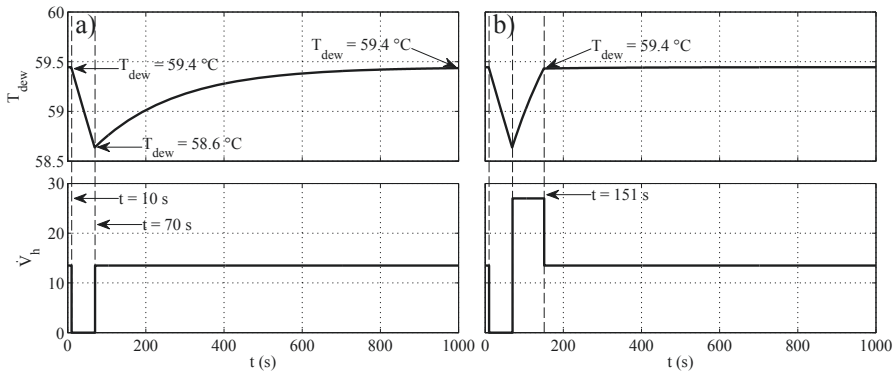

Fig. 10 – Effect of heating water flow rate ($\dot{V}_h$) on dew point temperature (T_{dew}) dynamics of the bubble humidifier containing approximately 50 dm³ water. Heating water flow rate is varied as follows: a) 13.5/0/13.5 lpm and b) 13.5/0/27/13.5 lpm.

Experimental validation of the humidifier was carried out by humidifying air and by varying the heating water flow rate, the heating water temperature, and the gas flow rate. Using a heating water flow rate of 13.5 lpm and a heating water temperature of 65 °C, a dew point temperature of 59 °C was attained at gas flow corresponding to nominal power of the PEMFC plant. At the same conditions but with a gas flow rate corresponding to full power, a dew point temperature of 56 °C was attained. Experimental results suggest that the dew point temperatures can be increased by increasing the heating water flow rate.

A model of the bubble humidifier taking into account heat and mass transfer was implemented. The simulation results show good agreement with experimental results.

Simulating the model in steady state suggests that the mass transfer does not limit the performance of the bubble humidifier in the present setup. Additionally, simulation results suggest that increasing the heating water flow rate from 13.5 lpm, which was the maximum flow rate in the present study, to 27 lpm, an approach dew point temperature can be decreased from 5.6 °C to 4.2 °C at nominal power and from 7.8 °C to 6.0 °C at full power.

Additionally, steady state simulations show that the humidifier outlet dew point temperature is very sensitive to heating water flow rate, especially at low flow rates. However, dynamic simulations show that the changes in humidifier temperature are relatively slow, in the order of 1 °C/min at maximum. Therefore, accurate, although relatively slow, control of the humidifier outlet humidity is possible by simple means.

Acknowledgments

This research was conducted under the "Fuel Cell 2007–2013" technology program of Tekes, the Finnish Funding Agency for Technology and Innovation, and was partly funded by the Graduate School in Chemical Engineering. The authors would also like to acknowledge their DuraDemo project partners.

Appendix A. Experimental results

Table A.1 – Humidifier initial test results. $\bar{x}$ is the time averaged measured value and σ is the standard deviation of the measured value during 5 min of steady state operation.

#	d_{or} (mm)	$\dot{V}_h$ (lpm)	$\dot{V}_g$ (slpm)		$T_{h,in}$ (°C)		$T_{h,out}$ (°C)		$T_{l,top}$ (°C)		$T_{l,middle}$ (°C)		$T_{l,bottom}$ (°C)	
			$\bar{x}$	σ	$\bar{x}$	σ	$\bar{x}$	σ	$\bar{x}$	σ	$\bar{x}$	σ	$\bar{x}$	σ
1	1	13.5	245.2	46.0	64.99	0.05	62.78	0.03	61.94	0.02	61.75	0.02	61.37	0.04
2	1	13.5	580.7	104.4	65.15	0.06	60.55	0.06	59.07	0.06	58.78	0.05	58.69	0.06
3	1	13.5	900.9	247.3	62.84[a]	0.05	58.21	0.03	56.47	0.02	56.15	0.03	55.85	0.06
4	1	13.5	257.5	47.2	60.69	0.02	58.77	0.04	57.97	0.02	57.62	0.02	57.39	0.02
5	1	13.5	710.2	234.9	60.48	0.44	56.59	0.05	55.29	0.13	54.93	0.14	54.86	0.14
6	1	13.5	882.9	241.3	60.18	0.03	55.98	0.05	54.37	0.03	54.09	0.04	53.77	0.03
7	1	13.5	257.8	50.5	55.49	0.03	53.96	0.02	53.24	0.02	52.92	0.02	52.77	0.03
8	1	13.5	592.6	112.3	55.67	0.02	52.71	0.02	51.65	0.03	51.32	0.02	51.21	0.07
9	1	13.5	875.1	243.2	55.47	0.01	52.10	0.01	50.80	0.04	50.51	0.05	50.31	0.07
10	1	8.0	242.2	42.5	65.07	0.03	61.98	0.02	61.35	0.02	61.10	0.02	60.85	0.02
11	1	8.0	509.6	93.9	65.17	0.02	59.44	0.06	58.23	0.05	57.98	0.05	57.59	0.06
12	1	8.0	720.7	189.0	64.31[a]	0.04	57.28	0.03	55.89	0.02	55.58	0.03	55.38	0.09
13	1	8.0	223.7	45.2	60.38	0.04	57.58	0.03	56.96	0.02	56.64	0.02	56.39	0.03
14	1	8.0	544.7	101.7	60.53	0.05	55.35	0.03	54.12	0.01	53.83	0.02	53.52	0.04
15	1	8.0	896.6	259.1	60.57	0.02	54.40	0.02	52.96	0.02	52.73	0.03	52.41	0.04
16	1	8.0	244.0	46.7	55.44	0.06	53.24	0.03	52.62	0.02	52.34	0.02	52.08	0.02
17	1	8.0	574.5	109.1	55.48	0.08	51.49	0.02	50.50	0.01	50.21	0.02	49.88	0.03
18	1	8.0	800.3	232.2	55.44	0.04	50.59	0.03	49.42	0.02	49.14	0.02	48.89	0.02
19	2	13.5	245.6	47.9	64.75	0.03	62.44	0.04	62.02	0.04	61.74	0.02	61.81	0.03
20	2	13.5	550.0	108.9	64.52	0.05	60.44	0.04	59.38	0.01	59.06	0.03	59.07	0.02
21	2	13.5	833.0	246.2	62.87[a]	0.09	58.12	0.06	56.95	0.02	56.59	0.02	56.61	0.04
22	2	13.5	247.7	48.9	60.14	0.03	58.22	0.01	57.87	0.03	57.51	0.01	57.56	0.02
23	2	13.5	531.4	97.2	60.34	0.05	56.79	0.06	55.97	0.06	55.60	0.03	55.65	0.05
24	2	13.5	807.8	251.0	59.92	0.05	55.53	0.03	54.50	0.02	54.16	0.03	54.15	0.02
25	2	13.5	247.9	44.9	55.25	0.03	53.85	0.02	53.62	0.02	53.30	0.03	53.35	0.02
26	2	13.5	529.3	96.5	55.39	0.03	52.47	0.03	51.80	0.02	51.41	0.02	51.49	0.03
27	2	13.5	827.2	248.4	55.38	0.14	51.78	0.11	50.89	0.03	50.53	0.03	50.57	0.02
28	2	8.0	243.6	48.2	64.72	0.02	61.33	0.02	60.98	0.01	60.72	0.01	60.78	0.01
29	2	8.0	493.3	90.8	64.93	0.02	58.85	0.01	57.98	0.02	57.75	0.01	57.77	0.02
30	2	8.0	755.5	221.6	64.24[a]	0.02	56.93	0.01	55.97	0.01	55.66	0.02	55.66	0.02
31	2	8.0	245.5	43.7	60.22	0.02	57.28	0.02	56.92	0.01	56.62	0.01	56.64	0.02
32	2	8.0	501.0	90.8	60.23	0.03	55.21	0.02	54.54	0.01	54.24	0.01	54.27	0.02
33	2	8.0	756.8	226.5	60.36	0.05	53.96	0.02	53.15	0.01	52.79	0.01	52.79	0.03
34	2	8.0	245.3	46.0	55.21	0.04	52.70	0.01	52.51	0.03	52.16	0.02	52.20	0.03
35	2	8.0	544.2	104.0	55.36	0.02	51.28	0.03	50.85	0.02	50.45	0.01	50.53	0.02
36	2	8.0	854.4	247.5	55.53	0.04	50.09	0.02	49.41	0.02	49.06	0.02	49.06	0.01

[a] In experiments with high heat consumption rate, the heaters used were unable to maintain the heating water temperature at set-point.

Appendix B. Experimental and simulation results compared

Table B.1 – Humidifier initial tests: comparison between experimental and simulated results.

#	T_l (°C)		$T_{h,out}$ (°C)		$T_{app,dew}$ (°C)		RH[b] (%)	
	Measured[a]	Simulated	Measured	Simulated	Measured	Simulated	Measured	Simulated
1	61.69	61.86	62.78	62.82	3.31	3.14	86.1	86.8
2	58.85	59.35	60.55	61.16	6.31	5.80	75.0	76.8
3	56.16	56.09	58.21	58.22	6.69	6.75	73.3	73.1
4	57.66	58.11	58.77	58.92	3.03	2.59	86.8	88.7
5	55.03	55.06	56.59	56.78	5.46	5.42	77.4	77.5
6	54.08	54.18	55.98	56.09	6.11	6.01	75.0	75.3
7	52.98	53.48	53.96	54.13	2.52	2.01	88.6	90.8
8	51.39	51.76	52.71	53.03	4.28	3.90	81.3	82.8
9	50.54	50.62	52.10	52.20	4.93	4.85	78.7	79.0
10	61.10	60.80	61.98	61.66	3.97	4.28	83.5	82.4
11	57.93	57.98	59.44	59.46	7.24	7.19	71.8	72.0
12	55.62	56.52	57.28	58.14	8.69	7.79	66.9	69.8
13	56.66	57.28	57.58	57.94	3.72	3.11	84.0	86.5
14	53.82	54.62	55.35	55.88	6.71	5.91	72.9	75.7
15	52.70	52.68	54.40	54.38	7.87	7.89	68.9	68.8
16	52.35	52.78	53.24	53.37	3.09	2.65	86.1	88.0
17	50.20	50.43	51.49	51.55	5.28	5.05	77.3	78.2
18	49.15	49.50	50.59	50.82	6.29	5.94	73.6	74.9
19	61.86	61.66	62.44	62.61	2.89	3.09	87.8	87.0
20	59.17	59.11	60.44	60.80	5.35	5.41	78.3	78.1
21	56.72	56.67	58.12	58.62	6.15	6.19	75.2	75.1
22	57.65	57.72	58.22	58.48	2.50	2.43	89.0	89.3
23	55.74	55.93	56.79	57.33	4.60	4.41	80.6	81.3
24	54.27	54.52	55.53	56.24	5.64	5.39	76.6	77.5
25	53.42	53.32	53.85	53.95	1.83	1.93	91.6	91.1
26	51.57	51.86	52.47	53.01	3.82	3.53	83.1	84.3
27	50.66	50.89	51.78	52.35	4.71	4.49	79.5	80.4
28	60.83	60.54	61.33	61.39	3.90	4.19	83.8	82.7
29	57.83	58.22	58.85	59.60	7.09	6.71	72.3	73.6
30	55.76	56.27	56.93	57.93	8.48	7.97	67.6	69.2
31	56.73	56.82	57.28	57.54	3.49	3.40	85.0	85.3
32	54.35	54.64	55.21	55.83	5.88	5.59	75.8	76.9
33	52.91	53.47	53.96	54.95	7.45	6.89	70.3	72.2
34	52.29	52.55	52.70	53.14	2.92	2.66	86.8	88.0
35	50.61	50.47	51.28	51.55	4.75	4.89	79.4	78.8
36	49.18	49.31	50.09	50.70	6.35	6.22	73.4	73.8

[a] Average of all three bubble column temperature sensors.
[b] Humidifier outlet humidity relative to PEMFC operating temperature.

Nomenclature

Abbreviations

CHP	combined heat and power
lpm	liters (liquid) per minute
PEMFC	proton exchange membrane fuel cell
RH	relative humidity
slpm	liters (gas) per minute at standard conditions, $T = 25$ °C, $p = 101{,}325$ Pa

Subscripts

b	bubble
bc	bubble column
h	heating water
i	inside
in	inlet
l	liquid in bubble column
o	outside
or	orifice
out	outlet
f	fin
w	heat exchanger wall

Latin letters

A_i	heat exchanger inside area, m^2
A_o	heat exchanger outside area excluding fins, m^2
A_f	fin area, m^2
Ar	Archimedes number, –, Eq. (28)
C_{bc}	specific heat capacity of bubble column, J/kg °C
$C_{p,g}$	heat capacity of ideal gas, J/mol °C

$C_{p,h}$	heat capacity of heating water, J/mol °C
$C_{p,l}$	heat capacity of liquid, J/mol °C
c	water concentration inside bubble, mol/m^3
c_s	water concentration at the bubble surface, mol/m^3
$\bar{c}$	volume-average concentration of water inside bubble, mol/m^3
D_{H2O}	diffusion coefficient of water in the gas, m^2/s
d_b	bubble diameter, m
d_{or}	Sparger orifice diameter, m
Eo	Eötvös number, –, Eq. (14)
f	Darcy friction factor, –
Fo	Fourier number, –, Eq. (4)
Fr	Froude number, –, Eq. (26)
Fr_{or}	Froude number at an orifice, – Eq. (7)
g	gravitational acceleration, 9.80665 m/s^2
H	dimensionless group,–, Eq. (13)
$\Delta_{vap}H_l$	latent heat of water in bubble column, J/mol
Δy_f	fin height, m
h_i	heat transfer coefficient inside the heat exchanger, W/m^2 °C
h_o	heat transfer coefficient outside the heat exchanger, W/m^2 °C
$h_{o,max}$	maximum heat transfer coefficient outside the heat exchanger, W/m^2 °C
$I_n(x)$	modified Bessel function of first kind
J	dimensionless group, –, Eq. (12)
$K_n(x)$	modified Bessel function of second kind
k_h	thermal conductivity of the heating water, W/m °C
k_l	thermal conductivity of water in bubble column, W/m °C
k_w	thermal conductivity of heat exchanger wall, W/m °C
L	length, m
M	Morton number, –, Eq. (15)
M_l	molar weight of water, kg/mol
m	fin parameter, (W/m K)$^{-1/2}$, Eq. (30)
m_{bc}	mass of bubble column, kg
$\dot{n}_g$	molar gas flow rate, mol/s
$\dot{n}_h$	molar heating water flow rate, mol/s
$\dot{n}_l$	evaporation rate of water in bubble column, mol/s
Pr	Prandtl number, –, Eq. (23)
Pr_w	Prandtl number close to pipe wall, –, Eq. (23)
p_{vap}	water vapor pressure, Pa
Δp_h	pressure drop of heating water, Pa
Δp_{or}	pressure drop across sparger, Pa
$\dot{Q}$	heat transfer rate from heating water, W
R	universal gas constant, 8.3145 J/mol K
Re_b	Reynolds number for bubble, –, Eq. (9)
Re_i	Reynolds number for flow in pipe, –, Eq. (22)
Re_{or}	modified orifice Reynolds number, –, Eq. (6)
r_b	bubble radius, m
r_i	heat exchanger pipe inner radius, m
r_o	heat exchanger pipe outer radius, m
Sh_{ave}	time average Sherwood number, –, Eq. (3)
St	Stanton number, –, Eq. (25)
s_l	surface tension of water in contact with the gas being bubbled, N/m
$T_{app,dew}$	approach dew point temperature, °C
T_{dew}	dew point temperature, °C
T_g	temperature of gas, °C
T_h	temperature of heating water, °C
T_l	temperature of bubble column content, °C, K
ΔT_{lm}	logarithmic mean temperature difference, °C
t	Time, s
t_r	bubble retention time in water bed, s
u_b	bubble rise velocity, m/s
u_g	superficial gas velocity, m/s
u_h	mean heating water velocity, m/s
$\dot{V}_g$	volumetric gas flow rate, m^3/s, slpm
$\dot{V}_{g,or,T}$	transition volumetric gas flow rate at an orifice, m^3/s
$\dot{V}_h$	volumetric heating water flow rate, lpm
V_l	volume of water in bubble column, m^3
$\bar{x}$	measured time average value
Δy_l	water level, m
Δz_f	fin thickness, m

Greek letters

μ_h	dynamic viscosity of bulk heating water, Pa s
$\mu_{h,w}$	dynamic viscosity of heating water close to wall, Pa s
μ_l	dynamic viscosity of liquid, Pa s
ρ_g	density of gas, kg/m^3
ρ_h	density of heating water, kg/m^3
ρ_l	density of liquid, kg/m^3
σ	standard deviation
η_f	fin efficiency, –

REFERENCES

[1] Vasu G, Tangirala AK, Viswanathan B, Dhathathreyan KS. Continuous bubble humidification and control of relative humidity of H2 for a PEMFC system. Int J Hydrogen Energy 2008;33:4640–8.

[2] Verhage AJL, Coolegem JF, Mulder MJJ, Yildirim MH, de Bruijn FA. 30,000 h operation of a 70 kW stationary PEM fuel cell system using hydrogen from a chlorine factory. Int J Hydrogen Energy 2013;38:4714–24.

[3] Xingsheng L, Weilin Z, Yangjun Z, Shihu M, Juntao Z, Hong Z. Comparative study of membrane humidifier and enthalpy wheel humidifier for Large power fuel cell system. J Fuel Cell Sci Tech 2009;6:014501.1–3.

[4] Sung C, Bai C, Chen J, Chang S. Controllable fuel cell humidification by ultrasonic atomization. J Power Sources 2013;239:151–6.

[5] Keränen T, Karimäki H, Nikiforow K, Kukkonen S, Uusalo H, Viitakangas J, et al. A 50 kW PEMFC pilot plant operated with industry grade hydrogen system design and site integration. In: Proceedings of 4th European PEFC and H2 Forum, vol. 13; 2013. pp. 23–31.

[6] Alopaeus V. Mass-transfer calculation methods for transient diffusion within particles. AIChE J 2000;46:2369–72.

[7] Bhavaraju SM, Russell TWF, Blanch HW. The design of gas sparged devices for viscous liquid systems. AIChE J 1978;24:454–66.

[8] Grace JR, Wairegi T, Nguyen TH. Shapes and velocities of single drops and bubbles moving freely through immiscible liquids. Trans Inst Chem Eng 1976;54:167–73.

[9] Sieder EN, Tate GE. Heat transfer and pressure drop of liquids in tubes. Ind Eng Chem 1936;28:1429–35.

[10] Gnielinski V. New equations for heat and mass transfer in turbulent pipe and channel flow. Int Chem Eng 1976;16:359–68.

[11] Deckwer WD. On the mechanism of heat transfer in bubble column reactors. Chem Eng Sci 1980;35:1341–6.

[12] Saxena SC. Heat transfer from a cylindrical probe immersed in a bubble column. Chem Eng J 1989;41:25–39.
[13] Mersmann A, Noth H, Ringer D, Wunder R. Maximum heat transfer in equipment with dispersed two-phase systems. Int Chem Eng 1982;22:16–29.
[14] Kraus AD, Aziz A, Welty J. Convection with simplified constraints. In: Anonymous extended surface heat transfer. John Wiley Sons, Inc.; 2000. pp. 1–58.
[15] Geankoplis CJ. Principles of steady-state heat transfer. In: Anonymous transport processes and separation process principles. 4th ed. New Jersey: Pearson Education, Inc.; 2003. pp. 235–356.
[16] Design Institute for Physical Properties, Sponsored, by AIChE, DIPPR Project 801-Full Version.
[17] Cverna F. ASM ready reference: thermal properties of metals. Materials Park, Ohio: ASM International; 2002.

IV

K. Nikiforow, P. Koski, H. Karimäki, J. Ihonen, V. Alopaeus, Designing a hydrogen gas ejector for 5 kW stationary PEMFC system – CFD-modeling and experimental validation, Int. J. Hydrogen Energy. 41 (2016) 14952–14970. doi:10.1016/j.ijhydene.2016.06.122.

INTERNATIONAL JOURNAL OF HYDROGEN ENERGY 41 (2016) 14952–14970

Available online at www.sciencedirect.com

ScienceDirect

journal homepage: www.elsevier.com/locate/he

Designing a hydrogen gas ejector for 5 kW stationary PEMFC system – CFD-modeling and experimental validation

K. Nikiforow [a,*], P. Koski [b], H. Karimäki [b], J. Ihonen [b], V. Alopaeus [a]

[a] Aalto University, School of Chemical Technology, P.O. Box 16100, 00076 Aalto, Finland
[b] VTT Technical Research Centre of Finland, P.O. Box 1000, 02044 VTT, Finland

ARTICLE INFO

Article history:
Received 8 April 2016
Received in revised form
29 May 2016
Accepted 9 June 2016
Available online 29 June 2016

Keywords:
PEMFC
Ejector
Hydrogen recirculation
CFD
Turbulence models

ABSTRACT

Ejectors are durable and inexpensive equipment for realizing hydrogen recirculation in proton exchange membrane fuel cell (PEMFC) systems. In the present work, a hydrogen recirculation ejector targeted for high turndown ratio operation in a 5 kW_e PEMFC system was designed, manufactured with 3D-printing, and characterized experimentally with both air and humid hydrogen.

The ejector was modeled at the experimental conditions with computational fluid dynamics (CFD) assuming 2D axisymmetric flow and with three turbulence models. A systematic comparison of experimental and simulation results was conducted with humid hydrogen at conditions covering the entire operating map up to 6 bar gauge primary pressure. The simulation results deviate on average 60%–70% from the experimental results, the deviation being less pronounced at conditions relevant in PEMFC applications.

The SST k-ω turbulence model was identified to agree best overall with the experimental data while the RNG and Realizable k-ε turbulence models were observed to accurately predict the position of maximum ejector efficiency. Hence, the SST k-ω model is more useful for predicting ejector performance while one of the two k-ε models should be adopted when optimizing ejector design.

Introduction

Hydrogen recirculation is regularly applied in automotive proton exchange membrane fuel cell (PEMFC) systems. Hydrogen recirculation humidifies the otherwise dry fuel feed, thus improving PEMFC performance and durability. Hydrogen recirculation also distributes accumulated inert gases, mostly nitrogen, more evenly, thus increasing the fuel cell efficiency. Recent results demonstrate that when nitrogen accumulates at the end of a cell, it can cause reverse current decay conditions, thereby damaging the cathode catalyst layer [1].

While hydrogen recirculation has obvious benefits, it also introduces challenges. Recirculation with a mechanical compressor increase cost and reliability issues [2,3], for example. The tradeoffs in hydrogen recirculation are summarized as follows: with a higher recirculation rate, more uniform hydrogen and water concentrations inside the fuel cell are achieved, leading to better fuel cell performance and durability [4], but with the cost of higher power consumption.

* *Corresponding author*. Tel.: +358 40 164 8478.
E-mail addresses: kaj.nikiforow@aalto.fi, kaj.nikiforow@gmail.com (K. Nikiforow).
http://dx.doi.org/10.1016/j.ijhydene.2016.06.122

In contrast to mechanical compressors, ejectors lack moving parts and are therefore more durable and less expensive to manufacture. However, ejectors are known for their limited operating range [5], which complicates their dimensioning. In applications with a low operating temperature and only small transients in the power load, recirculation is generally not applied because the present-day membrane electrode assemblies tolerate operation without humidification. However, also in these applications, even the relatively low recirculation rate achievable with an ejector at low cost could be beneficial for system durability and efficiency.

An ejector is a compressor employing the Venturi effect [6]. It operates by accelerating a high-pressure primary gas to high velocity in a nozzle. Downstream of the nozzle, the high-velocity primary gas creates a low pressure region, which entrains the secondary gas. The two gases mix and exit the ejector. In PEMFC applications, the primary gas equals the consumed fuel and the secondary gas equals the recirculated gas, as illustrated in Fig. 1a.

Ejector dimensioning is a complex task. Due to its rigid construction, achieving an adequate recirculation rate is challenging over the entire PEMFC operating range. The recirculation rate is particularly poor at low hydrogen consumption rates because of the low primary pressure [7]. To overcome this problem, three solutions have been suggested: two or more different-sized ejectors in parallel [7], a variable geometry ejector [3], and a hybrid system comprising an ejector and a mechanical compressor in parallel [4]. In stationary applications, a single ejector optimized for wide operating range offers potentially the best solution regarding the system complexity, durability, and efficiency.

The ejector design process (Fig. 1b) comprises four steps: modeling, ejector testing with air, ejector testing with hydrogen, and system level testing. A wide variety of ejector geometries and operating conditions can be investigated by mathematical modeling with relatively little effort. However, modeling always involves assumptions and simplifications. Therefore, the modeling approach must be validated against experimental data. The ejector design and manufacturing quality can be verified with air. This is because the ejector operation is primarily characterized by the sonic limit of the working gas. Ejector testing with hydrogen is also required but can be limited to the most interesting range of conditions. Ultimately, the ejector operation in a PEMFC system should be validated.

Several studies have been conducted on optimizing ejector design for PEMFC systems. Kim et al. [8] adopted an analytical modeling approach in determining nozzle throat and mixing section diameters and experimentally verified the ejector operation. They noted that an optimally designed ejector achieves an acceptable performance on a wide PEMFC operating range. Dadvar and Afsari [9] also adopted an analytical ejector model and studied the effect of stack design parameters and ejector design parameters on the overall system performance. They proposed two dimensionless parameters that can be employed in system optimization. Hwang et al. [10] characterized an ejector with dry air and modeled it with computational fluid dynamics (CFD). They obtained a relatively close match between experimental and simulation results. Brunner et al. [3], Hosseinzadeh et al. [7], and Maghsoodi et al. [11] put effort into optimizing the ejector design for PEMFC applications with CFD. They identified several geometry parameters that affect the ejector performance and help dimension an ejector. Brunner et al. compared their simulation results to experimental data obtained with the ejector operated in an actual PEMFC system. The authors assumed a 100% relative humidity at the ejector secondary inlet. Maghsoodi et al. validated their modeling approach against experimental data obtained with refrigerant R142b as the working fluid. Hosseinzadeh et al. compared the results obtained with their modeling approach against those obtained with an analytical model.

The modeling stage in ejector design procedure should be conducted employing CFD due to the complex flow in ejectors. The CFD prediction accuracy has been reported to primarily depend on two factors: 1) the application of the 2D flow assumption and 2) the adopted turbulence model. 2D axisymmetric flow is commonly assumed [3,7,11] because it greatly reduces the computational effort compared to a 3D representation. However, a notably better agreement between simulations and experimental data has been reported with simulations conducted in 3D geometry [12,13]. This is true especially at conditions without double choking, which are of interest, for example, in PEMFC applications where ejectors operate at a wide range. Turbulence models commonly adopted in ejector modeling include Shear Stress Transport (SST) k-ω [3,7,13–15] and Re-Normalization Group (RNG) k-ε [11,14]. Although several studies [13–15] have reported better prediction accuracy of the SST k-ω model relative to others, no turbulence model has an established position in ejector modeling.

Experimental validation of modeling results is critical for a reliable ejector design procedure. Despite the recognized shortcomings of the 2D axisymmetric assumption in CFD modeling, no previous study has presented a systematic experimental validation of modeling results at conditions relevant to PEMFC applications and with humid hydrogen. In this work, the results of CFD modeling conducted with the 2D axisymmetric flow assumption and with three turbulence models are experimentally validated with humid hydrogen

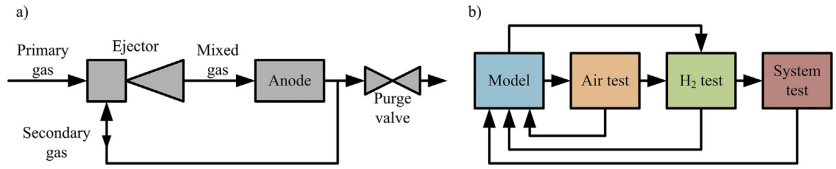

Fig. 1 – a) Simplified PEMFC system anode gas recirculation scheme. b) Ejector design process chart.

and at a wide range of conditions. The design, manufacturing, and experimental characterization of the ejector employed in this study are described in detail. Based on the experimental validation, recommendations are provided concerning the choice of turbulence model in designing ejectors for PEMFC systems.

Experimental

Ejector design and manufacturing

The nozzle throat is the most important dimension in an ejector. Together with the primary pressure, it determines the primary gas flow rate and, hence, the achievable PEMFC current level. The nozzle throat can be sized based on the maximum fuel consumption rate ($\dot{n}_{p,in}$) and the maximum primary pressure ($p_{p,in}$). The nozzle sizing equation for critical flow condition and an ideal gas is [6]:

$$\dot{n}_{p,in} \times M_{w,p} = C \times \pi \left(\frac{D_{nt}}{2}\right)^2 \times p_{p,in}[bara] \times 10^5 \times \sqrt{\gamma \times \frac{M_{w,p}}{R \times (T_{p,in} + 273.15)} \times \left(\frac{2}{\gamma+1}\right)^{\frac{\gamma+1}{\gamma-1}}} \quad (1)$$

where the fuel consumption rate depends on the stack current (I) and number of cells in stack (N_{cell}):

$$\dot{n}_{p,in} = \frac{N_{cell} \times I}{2 \times F} \quad (2)$$

A 5 kW PEMFC ($N_{cell} \times I = 50 \times 160$ A) consumes approximately 0.041 mol/s. A suitable nozzle throat diameter for 6 barg maximum primary pressure is therefore 0.5 mm according to Eq. (1). Table 1 lists the parameters used in Eq. (1). The discharge coefficient C is reported to vary primarily with Reynolds number in the range 0.95–0.99 [6]. With $C = 0.97$, the flow rates computed with Eq. (1) deviate less than 0.3% at 6 barg primary pressure compared to the CFD simulations conducted in this study.

Rest of the ejector dimensions were chosen based on previous studies [3,7,11]. The most important of these are the mixing section diameter (D_m) and length (L_m), the nozzle position relative to the mixing section (L_{ne}), as well as the diffuser length (L_d) and divergence angle (α_d).

Table 1 – Parameters used in Eq. (1) for determining nozzle throat diameter.

Variable	Value	Explanation
$\dot{n}_{p,in}$	0.041 mol/s	Maximum hydrogen consumption
$p_{p,in}$	7.01325 bara = 6 barg	Maximum primary inlet pressure
F	96,485 C/mol	Faraday constant
R	8.3145 J/(K × mol)	Universal gas constant
$T_{p,in}$	20 °C	Primary inlet temperature
M_w	2.016×10^{-3} kg/mol	Molar weight
γ	1.4	Isentropic expansion factor
C	0.97	Nozzle discharge coefficient

In choosing these dimensions, special attention was given to ejector performance on wide range of primary gas flow rates as the target was to achieve wide operating range with a single ejector. The mixing section diameter was set to 2 mm (=4 × D_{nt}) because relatively small values enhance performance at low primary gas consumption rates [7]. The mixing section length was set to 16 mm (=8 × D_m), which is above the optimum (6 × D_m [11]), to ensure fully developed flow before the diffuser. The nozzle position relative to mixing section was set to 1.8 mm (=0.9 × D_m) to avoid a too small gap between primary nozzle and wall that could restrict the secondary flow and decrease ejector performance. The diffuser length 45.7 mm (=22.9 × D_m) was determined by choosing a 10 mm outlet diameter and 5° diffuser divergence angle which is more than optimum (~2.5° [11]) but works better on a wider range [7]. All ejector dimensions are presented in Fig. 2.

The ejector was 3D printed at AM Finland Oy from stainless steel powder (EN 1.4404) by direct metal laser sintering (DMLS) method in three parts due to limited printing volume. The three parts, comprising the primary inlet, the ejector body, and the outlet (see Fig. 3), were interconnected with flanges. The flanges with suitable grooves in the main body were sealed with O-rings (16.3 mm × 2.4 mm, FPM). The DMLS printing accuracy is between 0.02 and 0.06 mm but due to lack of support against gravity, this accuracy was not met in some regions, especially in the suction chamber.

After 3D printing, the ejector was finalized at The Finnish School of Watchmaking. The walls highlighted in Fig. 2 were polished. The nozzle flange face was also polished to meet the intended nozzle position: L_{ne} was measured to be 1.80 + 0.05–0.05 mm. The suction chamber was not polished as it would have required excessive tooling effort. The ejector nozzle diameter was drilled from the printed value of 0.4 mm to the final 0.50 + 0.03–0.00 mm value. D_m was matched to 2.0 + 0.02–0.00 mm with a custom made file. The tolerances are estimates provided by the watchmaking school and are based on measured tolerances.

Finally, stainless steel pipes with 4 mm, 10 mm, and 10 mm inner diameters were brazed to the primary inlet, secondary inlet and ejector outlet, respectively. 6 and 12 mm Swagelok fittings were connected to the pipes, the ejector was assembled and pressure tested at 10 barg.

Experimental setup and measurements

The experimental setup (Fig. 4) comprise five main components: 1) a high pressure (~15 bara) gas supply, 2) two manual pressure reducers for adjusting the primary and secondary inlet pressures, 3) a membrane humidifier for humidifying the secondary gas, 4) an ejector, and 5) a manual back-pressure regulator for adjusting the ejector outlet pressure. In addition, temperatures, pressures, flow rates, and humidities were recorded at locations indicated in Fig. 4. In the experiments with hydrogen as the working gas, the secondary gas flow rate was determined as the difference between total gas flow rate and primary gas flow rate. The experimental setup main components are listed in Table 2.

The experiments were conducted with two ejectors: the custom-made ejector and a commercial ejector. The commercial ZH05S-X267 ejector was purchased from SMC. Both

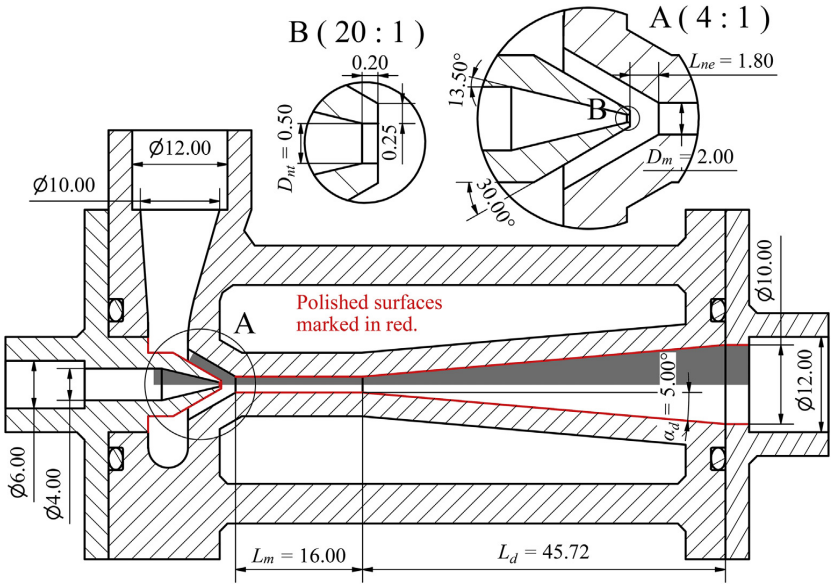

Fig. 2 – Custom-made ejector geometry with dimensions in mm. Area shaded in gray indicates the 2D axisymmetric computational domain.

ejectors have a 0.5 mm nozzle diameter but the SMC ejector is sold mainly for vacuum generation applications with air as the motive gas. Compared to mechanical compressors, the SMC ejector is an inexpensive (~100 €), mass produced device and, thus, an interesting option for hydrogen recirculation in PEMFC applications.

The measurements were conducted by fixing the ejector primary inlet pressure, the outlet pressure, and the secondary inlet dew point temperature and then reducing the secondary inlet pressure stepwise until minimum secondary inlet pressure was achieved. At minimum secondary inlet pressure, the ejector entrains no secondary fluid. The measurements were conducted at conditions listed in Table 3.

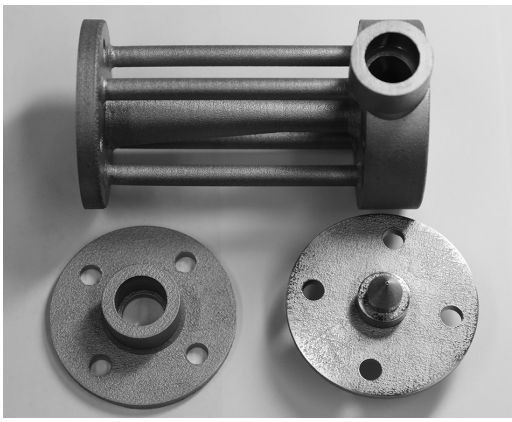

Fig. 3 – The ready 3D printed and polished ejector body with nozzle and outlet flanges.

The secondary inlet dew point temperature was controlled by regulating the heating water throttling valve and by adjusting the heating circuit pump speed and water bath temperature. The secondary inlet dew point temperature ($T_{dew,s,in}$) was calculated as follows:

$$T_{dew,s,in} = \frac{1435.264}{4.6543 - \log_{10}\left(p_{s,in}^{vap} \times RH_s\right)} - 208.302 \quad (3)$$

where the vapor pressure (p^{vap}) is calculated from Ref. [16].

$$p^{vap} = 10^{4.6543 - \frac{1435.264}{T + 208.302}} \quad (4)$$

A measurement was considered successful when all four quantities controlled remained close to target values for at least 60 consecutive data points recorded with 0.5 s intervals. Table 3 lists the observed maximum standard deviation (σ_{max}) of the four quantities. The experimental results for the custom-ejector are tabulated in Appendix B.

Ejector performance measures

In the literature, entrainment ratio is a commonly employed ejector performance measure. In PEMFC applications, fuel utilization per pass is an established measure of anode gas recirculation rate. From the ejector optimization perspective, the ejector efficiency is a central performance measure. In this work, all these three measures are employed in analyzing ejector performance.

The entrainment ratio (Ω) is defined as the ratio of the secondary stream mass flow rate ($\dot{m}_s$) to the primary stream mass flow rate ($\dot{m}_p$):

$$\Omega = \dot{m}_s / \dot{m}_p \quad (5)$$

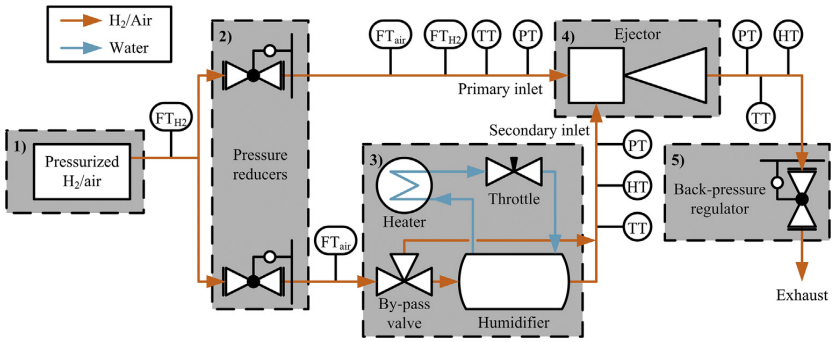

Fig. 4 – Experimental setup. TT: temperature transmitter, FT: flow rate transmitter, PT: gauge pressure transmitter, HT: humidity transmitter.

Table 2 – Experimental setup main components.

Component	Location	Manufacturer/model
Pressure reducer	Primary inlet	Swagelok KPR1FJL412A
Pressure reducer	Secondary inlet	RHPS LRSN4-02-1-VTV/S-02275
Back-pressure regulator	Outlet	Kenmac KBP1A1A5DA4
Humidifier	Secondary inlet	Permapure FC100-80-6MSS
Flow rate transmitter, hydrogen	Primary inlet	Bronkhorst EL-FLOW F-111AC
Flow rate transmitter, hydrogen	Total inlet flow	Bronkhorst EL-FLOW F-112AC
Flow rate transmitter, air	Both inlets	Sensortechnics WTA L050DUP
Pressure transmitter	Primary inlet	Sensortechnics CTE 9010 G
Pressure transmitter	Secondary inlet	Sensortechnics CTE 9N01 G
Pressure transmitter	Outlet	Sensortechnics CTE 9001 G
Temperature transmitter	Primary inlet	K-type thermocouple
Temperature and humidity transmitter	Secondary inlet	Vaisala HMT337
Temperature and humidity transmitter	Outlet	Vaisala HMT337

The primary stream mass flow rate is calculated from the measured dry primary gas volumetric flow rate ($\dot{V}_{p,n}$) at normal conditions ($T_n = 0\,^{\circ}C$, $p_n = 1.01325$ bara) assuming ideal gas behavior:

$$\dot{m}_p = \dot{n}_p \times M_{w,p} = \frac{(p_n \times 10^5 + 101325) \times \dot{V}_{p,dry\ gas,n}}{R \times (T_n + 273.15)} \times M_{w,p} \tag{6}$$

The secondary stream mass flow rate is computed in a similar fashion with the exception of the considering the effect of humidity:

$$\dot{m}_s = \frac{(p_n \times 10^5 + 101325) \times \dot{V}_{s,dry\ gas,n}}{R \times (T_n + 273.15)} \times \left(M_{w,s,dry\ gas} + M_{w,H_2O} \times \frac{y_{H_2O,s,in}}{1 - y_{H_2O,s,in}} \right) \tag{7}$$

The water mole fraction at the secondary inlet ($y_{H_2O,s,in}$) is calculated from the measured temperature (through water vapor pressure), relative humidity, and absolute pressure as follows:

$$y_{H_2O,s,in} = \frac{p_{s,in}^{vap} \times RH_{s,in}}{p_{s,in}} \tag{8}$$

where the water vapor pressure is calculated with Eq. (4).

In PEMFC applications, the fuel utilization per pass (u_f) is a common measure of anode gas recirculation rate. It is defined as the percentage of fuel (here hydrogen) consumed per one pass through the fuel cell stack and, hence, equals the

Table 3 – Controlled quantities in experiments: range and maximum standard deviation.

Quantity	Ejector	Target value		σ_{max}
		Working gas: hydrogen	Working gas: air	
$p_{p,in}$ [barg]	Custom-made	0.50, 0.75, 1.0, 1.5, 2.0, 3.0, 4.0, 5.0, 6.0	0.50, 0.75, 1.0, 1.5, 2.0, 3.0, 4.0, 5.0, 6.0 ($p_{p,in} > p_{out}$)	0.010
	SMC ZH05S-X267	–	1.0, 2.0, 3.0, 4.0, 5.0, 6.0	0.016
p_{out} [barg]	Custom-made	0.25	0.00, 0.25, 0.50	0.004
	SMC ZH05S-X267	–	0.50	0.003
$p_{s,in}$ [barg]	Custom-made	p_{out} – (0.000, 0.025, 0.050, 0.100, 0.150, …)	p_{out}–(0.000, 0.025, 0.050, 0.100, 0.150, …)	0.005
	SMC ZH05S-X267	–	p_{out}–(0.000, 0.100, 0.200, …)	0.009
$T_{dew,s,in}$ [°C]	Custom-made	60	Dry, 60, 75	0.22
	SMC ZH05S-X267	–	Dry, 60, 75	0.12

reciprocal of hydrogen stoichiometry per one pass (λ). As the primary gas flow rate equals the fuel consumption rate at constant pressure operation (neglecting any impurities in the primary gas), the fuel utilization per pass can be calculated directly from dry inlet gas flow rates. Alternatively, it can be calculated from the entrainment ratio.

$$u_f = \frac{100\%}{1+\frac{\dot{V}_{s,dry\ gas,n}}{\dot{V}_{p,dry\ gas,n}}} = \frac{100\%}{1+\frac{\Omega}{1+\frac{M_{w,H_2O}}{M_{w,H_2}}\times\frac{y_{H_2O,s,in}}{1-y_{H_2O,s,in}}}} = \frac{100\%}{\lambda} \tag{9}$$

At low current levels, the fuel consumption rate, and hence, the gas linear velocity inside the stack gas channels are low. The low gas velocity allows liquid water accumulation in the gas channels. Therefore, lower fuel utilization per pass is generally required at low currents than at high currents for stable PEMFC operation.

Efficiency is a performance measure related to ideal performance, which depends on the chosen definition. Out of the many different ejector efficiencies presented by McGovern et al. [17], the exergetic efficiency is adopted in this work. The exergetic efficiency (η) is defined as the ratio of secondary stream exergy increase to the primary stream exergy decrease. Neglecting any changes in kinetic and potential energy, the exergetic efficiency is [17,18]:

$$\eta = \frac{(e_{s,out} - e_{s,in}) \times \dot{n}_s}{(e_{p,in} - e_{p,out}) \times \dot{n}_p} = \frac{(h_{s,out} - h_{s,in} - T_0 \times [s_{s,out} - s_{s,in}]) \times \dot{n}_s}{(h_{p,in} - h_{p,out} - T_0 \times [s_{p,in} - s_{p,out}]) \times \dot{n}_p} \tag{10}$$

where e_j [J/mol] is the molar flow exergy of stream j, h_j [J/mol] is the molar enthalpy of stream j, s_j [J/(K × mol)] is the molar entropy of stream j, $\dot{n}_j$ is the molar flow rate of stream j, and T_0 is the dead state temperature following from the exergy analysis.

In case the ejector inlet streams have the same composition, Eq. (10) can be applied as it stands because the molar outlet quantities (enthalpy and entropy) are equal for the two streams at the outlet conditions. The situation becomes more complex when the ejector inlet streams differ in composition, as in the current case, because the contribution of each inlet stream on the molar outlet quantities must be considered.

By definition, the ejector outlet molar enthalpy and entropy are mole fraction weighted sums of the partial molar quantities:

$$h_{out} = \sum\left(y_{i,out} \times \overline{h}_{i,out}\right) \tag{11}$$

$$s_{out} = \sum\left(y_{i,out} \times \overline{s}_{i,out}\right) \tag{12}$$

where $y_{i,out}$ is the outlet stream mole fraction of compound i, $\overline{h}_{i,out}$ is the outlet stream partial molar enthalpy of compound i, and $\overline{s}_{i,out}$ is the outlet stream partial molar entropy of compound i. For ideal gases, the partial molar enthalpy equals the molar enthalpy but the partial molar entropy is

$$\overline{s}_{i,out} = s_{i,out} - R \times \ln\left(y_{i,out}\right) \tag{13}$$

Applying the material balance, the ejector outlet mole fraction can be written as the sum of the contributions from each inlet stream:

$$y_{i,out} = \frac{y_{i,p} \times \dot{n}_p + y_{i,s} \times \dot{n}_s}{\dot{n}_{out}} = y_{i,p} \times \frac{\dot{n}_p}{\dot{n}_{out}} + y_{i,s} \times \frac{\dot{n}_s}{\dot{n}_{out}} \tag{14}$$

Applying Eq. (14) in Eq. (11) and Eq. (12), yield:

$$h_{out} = \sum\left(y_{i,p} \times \frac{\dot{n}_p}{\dot{n}_{out}} \times \overline{h}_{i,out}\right) + \sum\left(y_{i,s} \times \frac{\dot{n}_s}{\dot{n}_{out}} \times \overline{h}_{i,out}\right) = h_{p,out} + h_{s,out} \tag{15}$$

$$s_{out} = \sum\left(y_{i,p} \times \frac{\dot{n}_p}{\dot{n}_{out}} \times \overline{s}_{i,out}\right) + \sum\left(y_{i,s} \times \frac{\dot{n}_s}{\dot{n}_{out}} \times \overline{s}_{i,out}\right) = s_{p,out} + s_{s,out} \tag{16}$$

where $h_{p,out}$, $h_{s,out}$, $s_{p,out}$, and $s_{s,out}$ are the contributions of the inlet streams to the outlet stream molar quantities, which enable correct determination of exergetic efficiency in Eq. (10).

Modeling

The simulations were conducted with CFD employing ANSYS Fluent v16.0 software which is based on the finite volume method. 2D axisymmetric, compressible, and steady flow was assumed. Furthermore, the fluid was assumed to obey the ideal gas equation of state. Both gravity and phase transitions were neglected.

The ejector axisymmetric computational domain (the area shaded in gray in Fig. 2) was discretized with a structured meshes refined at walls and created with ANSYS ICEM CFD 16.0 software. Several meshes with cell count ranging from 45 k to 753 k were tested at conditions corresponding to the experimental data. Four meshes with approximately 45 k, 159 k, 237 k, and 424 k cells were tested more thoroughly at every experimental point. The mesh with approximately 159 k cells was observed to be dense enough for mesh independent results and was therefore employed in subsequent simulations.

Because of compressibility, the flow was governed by Favre-averaged Navier–Stokes equations. The momentum balance equation is:

$$\frac{\partial(\rho v_i v_j)}{\partial x_j} = -\frac{\partial p}{\partial x_i} + \frac{\partial}{\partial x_j}\left[\mu\left(\frac{\partial v_i}{\partial x_j} + \frac{\partial v_j}{\partial x_i} - \frac{2}{3}\delta_{ij}\frac{\partial v_i}{\partial x_i}\right)\right] + \frac{\partial}{\partial x_j}\left[-\rho\overline{v_i' v_j'}\right] \tag{17}$$

where $-\rho\overline{v_i' v_j'}$ are the Reynolds stresses. These were modeled applying the Boussinesq approximation of the eddy viscosity:

$$-\rho\overline{v_i' v_j'} = \mu_t\left(\frac{\partial v_i}{\partial x_j} + \frac{\partial v_j}{\partial x_i}\right) - \frac{2}{3}\delta_{ij}\left(\rho k + \mu_t\frac{\partial v_k}{\partial x_k}\right) \tag{18}$$

where k is the turbulence kinetic energy and μ_t is the eddy viscosity, both solved from a turbulence transport equation. The three turbulence models tested in this work were:

- Shear Stress Transport (SST) k-ω with low-Reynolds number correction and viscous heating enabled
- Re-Normalization Group (RNG) k-ε with enhanced wall treatment and viscous heating enabled
- Realizable k-ε with enhanced wall treatment and viscous heating enabled

These models were chosen because the SST k-ω model has proved its accuracy on a wide operation range in several studies [13–15] and the k-ε models have been found to perform well at some conditions [13,14]. The enhanced wall treatment is adopted with the k-ε models as recommended by the Fluent Theory Guide [19] for meshes refined at walls.

The momentum balance equations and pressure based continuity equation were solved in a coupled manner and the remaining equations (energy conservation, species conservation, and turbulence transport) were solved in a segregated manner. A 2nd order pressure interpolation scheme was employed and all the equations were spatially discretized with 2nd order upwind schemes.

The temperatures, pressures, and secondary inlet fluid composition measured experimentally were employed as boundary conditions for the inlets. An experimentally determined mass flow rate based pressure correction was applied for the pressure readings to account for the pressure drop between pressure probes and the ejector. This correction turned out to be meaningful only at the primary inlet but in most cases negligible also there. The ejector walls were assumed smooth and adiabatic and the no-slip condition was adopted. The physical properties (heat capacity, diffusion coefficients, viscosity, and thermal conductivity) were computed with correlations presented in Appendix A.

Flow normal to ejector inlets with 5% turbulence intensity (I_T) was assumed. This turbulence intensity value corresponds to a Reynolds number of approximately 11,000 according to the following equation [20]:

$$I_t = 0.16 \times \left(Re_{D_h}\right)^{-\frac{1}{8}} \tag{19}$$

Reynolds number based on hydraulic diameter and calculated from experimental data (assuming inlet conditions) varied in the range of 400–3000 at primary inlet, 0 to 1600 at secondary inlet, 200 to 6900 at ejector outlet, 3.5×10^6 to 45×10^6 at the nozzle throat, and 0.9×10^6 to 35×10^6 at the mixing section.

The simulations results were checked to satisfy the energy balance with a tolerance of $\pm 10^{-2}$ W and the mass balance with a tolerance of $\pm 10^{-8}$ kg/s. The simulations were first repeated for each experimental point with hydrogen as the working gas and with each of the three turbulence models. After this, ejector performance sensitivity relative to the manufacturing tolerances (D_{nt}, L_{ne}, D_m and smoothness of the unpolished wall at secondary inlet), the assumed boundary conditions (turbulent intensities and secondary inlet flow direction), and the measured boundary conditions ($p_{p,in}$, $p_{s,in}$, p_{out}, $y_{H_2,s,in}$) was tested with a subset of data points highlighted in Table B.1.

Results and discussion

Custom-made ejector performance at discrete points covering the entire ejector *operating map* (range of primary and secondary pressures) for a given ejector outlet pressure are tabulated in Appendix B. The ejector performance in a PEMFC system with a specified stack flow resistance is not easily perceived from these data.

To investigate the ejector performance in PEMFC systems, linear interpolation is employed to match the pressure increase achieved by the ejector (Δp_E):

$$\Delta p_E = p_{out} - p_{s,in} \tag{20}$$

with the PEMFC stack pressure drop (Δp_{FC}):

$$\Delta p_{FC} = b \times \dot{m}_{out} \tag{21}$$

where b is a coefficient and $\dot{m}_{out}$ is the ejector outlet mass flow rate. Matching these two pressure differences essentially determines the ejector *operating curve*, $\Delta p_{FC} = f(p_{p,in})$, which is the path an ejector takes on its operating map. The ejector operating curve depends on ejector performance (and hence its geometry) and on the system flow resistance.

In this work, ejector performance is studied in three PEMFC systems by varying the coefficient b (see Table 4). The values are chosen to result in maximum pressure drop of 51.7 mbar (0.75 psi), 103.4 mbar (1.5 psi), and 206.9 mbar (3 psi) when the custom-made ejector is operated with the secondary gas saturated at 60 °C and with a 0.25 barg outlet pressure.

Ejector characterization with air

The custom-made ejector and the commercial ejector operating curves are plotted on entrainment ratio and efficiency maps for air in Fig. 5. The figure illustrates the effect of system flow resistance on the achieved entrainment ratio and on the ejector efficiency along the operating range. The higher the system flow resistance, the lower is the entrainment ratio. The maximum system flow resistance is limited by the *maximum suction curve* (labeled in Fig. 5c). Above this curve, at least part of the primary gas exits the ejector through the secondary inlet and the flow is reversed.

The maximum efficiency as a function of primary pressure is called the *maximum efficiency curve* and is labeled in Fig. 5b and d. In this work, the maximum efficiency curves are obtained by interpolating efficiency data (see Fig. 10) with max 4th order polynomials and taking their maximum value. The maximum efficiency (along the primary pressure range) occurs approximately at suction pressures half of the maximum with both of the ejectors.

For an optimal ejector performance in a PEMFC system, the operating curve should match the maximum efficiency curve. The custom-made ejector achieves high efficiency in low-flow-resistance systems at low primary pressures and in high-flow-resistance systems at high primary pressures (Fig. 5b). The commercial ejector, on the other hand, achieves high efficiency in systems with considerably higher flow resistances than those considered here (Fig. 5d, notice the different 'Stack pressure drop'-scale). This is expected considering the intended application of the ejectors.

The ejector performance in an actual PEMFC system is more conveniently illustrated by plotting the achieved entrainment ratios along each operating curve. Fig. 6 shows that high recirculation rate is achieved on a wide range in the low-flow-resistance system. In particular, the maximum entrainment ratio is obtained at primary pressure as low as 0.75–1.0 barg. The high recirculation rate at low primary pressures is beneficial for PEMFC operation at low currents

Table 4 – The pressure drop coefficient in Eq. (21).

Coefficient	Value with air	Value with hydrogen	Maximum pressure drop, $\Delta p_{FC,max}$	Dry hydrogen flow rate at $\Delta p_{FC,max}$	Explanation
b_1	61.8 $\frac{bar}{kg/s}$	194.3 $\frac{bar}{kg/s}$	51.7 mbar (0.75 psi)	$\dot{n}_{H_2,out} = 0.0755 \frac{mol}{s}$	Low-flow-resistance
b_2	134.4 $\frac{bar}{kg/s}$	427.5 $\frac{bar}{kg/s}$	103.4 mbar (1.5 psi)	$\dot{n}_{H_2,out} = 0.0701 \frac{mol}{s}$	Moderate-flow-resistance
b_3	323.9 $\frac{bar}{kg/s}$	1005.0 $\frac{bar}{kg/s}$	206.9 mbar (3 psi)	$\dot{n}_{H_2,out} = 0.0619 \frac{mol}{s}$	High-flow-resistance

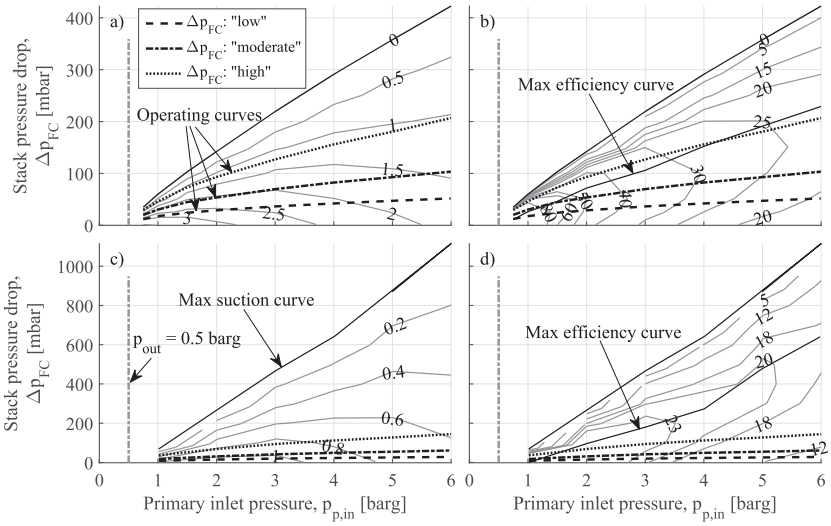

Fig. 5 – Custom-made ejector operating curves plotted on a) entrainment ratio map and b) efficiency map, and commercial ejector operating curves plotted on c) entrainment ratio map and d) efficiency map. Working gas: air, $T_{dew,s,in}$: 60 °C, p_{out}: 0.5 barg.

due to enhanced inert gas mixing and liquid water removal from flow field channels. Decreasing the primary pressure eventually results in a rapid decrease in entrainment ratio (ejector performance collapses).

The maximum entrainment ratio in moderate- and high-flow-resistance systems is achieved at higher primary pressures due to the lower efficiency at low primary pressures. High efficiency throughout the primary pressure range is apparently not achievable. This is not a problem in low-flow-resistance systems because satisfactory recirculation rate is achieved at high pressures despite the lower efficiency. In systems with higher flow resistance, covering the entire range with a single ejector becomes increasingly challenging.

The entrainment ratio achieved with the commercial ejector is considerably lower at all conditions compared to that achieved with the custom-made ejector, as shown in Fig. 6 (notice the different 'Entrainment ratio'-scales). Nonetheless, the low entrainment ratio achieved with the commercial ejector may be high enough in some applications.

Ejector performance with humid hydrogen

The operating curves for the custom-made ejector operated with hydrogen are plotted on efficiency and fuel utilization per pass maps in Fig. 7. As when operated with air, the maximum efficiency curve is located approximately at suction pressures half of the maximum. A high efficiency point is achieved along all three operating curves but none achieves high efficiency throughout the operating range, like with air. The achieved recirculation rate in terms of fuel utilization per pass strongly depends on system flow resistance.

Fig. 8a displays the fuel utilization per pass (u_f [%]) along each operating curve as a function of fuel cell stack current. The fuel cell stack current (I [A]) is calculated from the ejector primary gas flow rate assuming a 50 cell stack. Fig. 8b and c show the entrainment ratio and the stack pressure drop along the operating curves, respectively, and Fig. 8d shows the stack polarization curve. Simulation results are also displayed. The stack voltage (U [V]) is computed as follows:

$$I < 30\ A: \quad U = 0.00024 \times I^2 - 0.0155 \times I + 1 \tag{22}$$

$$I \geq 30\ A: \quad U = \frac{0.75 - 0.60}{30 - 160} \times (I - 30) + 0.75 \tag{23}$$

According to this polarization curve, at 6 barg primary pressure, the ejector delivers hydrogen at a rate enough for 4.7 kW of electric power.

Satisfactory recirculation rate ($\Omega \geq 2.1$, $u_f \leq 57.5\%$) is achieved in low- and moderate-flow-resistance systems down to low current levels, as illustrated in Fig. 8a and b. Particularly in the low-flow-resistance system, a minimum fuel utilization

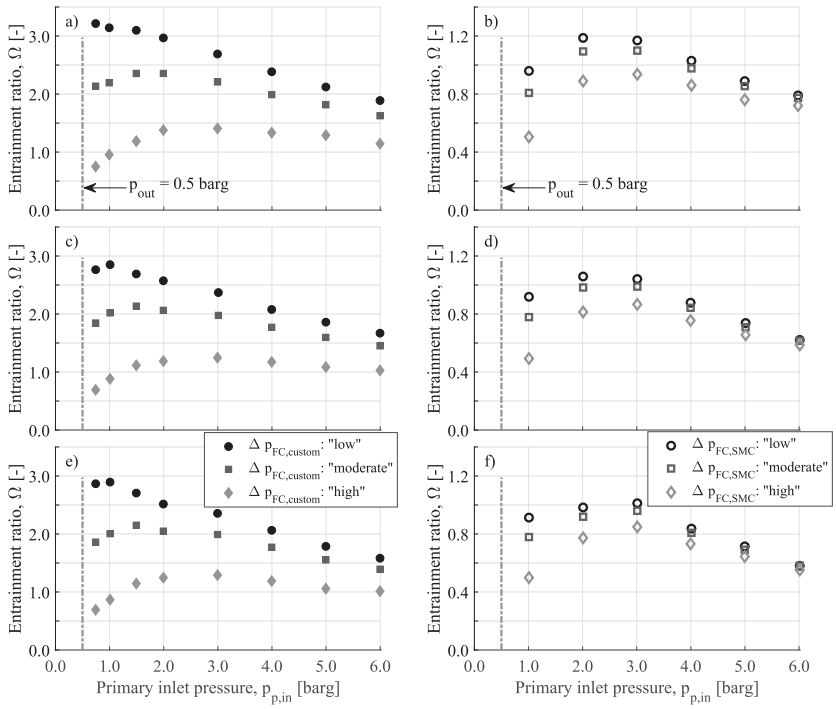

Fig. 6 – Entrainment ratio along the operating curves as function of primary pressure. Working gas: air, p_{out}: 0.5 barg, a) custom-made ejector, dry secondary inlet, b) commercial ejector, dry secondary inlet, c) custom-made ejector, $T_{dew,s,in}$: 60 °C, d) commercial ejector, $T_{dew,s,in}$: 60 °C, e) custom-made ejector, $T_{dew,s,in}$: 75 °C, f) commercial ejector, $T_{dew,s,in}$: 75 °C.

per pass ($u_f = 39\%$) is achieved at current level as low as 40 A. Thus, provided a reasonably low stack flow resistance, a single ejector achieves satisfactory recirculation rate on a wide range.

In high-flow-resistance systems, the ejector achieves satisfactory recirculation rate ($\Omega \geq 1.7$, $u_f \leq 65.0\%$) at high primary pressures (3–6 barg), i.e. where high efficiency is achieved. The maximum entrainment ratio ($\Omega = 1.9$) and the minimum fuel utilization per pass ($u_f = 60.1\%$) are achieved between 70 and 80 A current level. At lower current levels, the recirculation rate diminishes due to low efficiency.

The simulation results obtained with the SST k-ω turbulence model and the experimental data are in acceptable agreement, as illustrated in Fig. 8. The model correctly predicts the general trends in the achieved recirculation rate but the entrainment ratio is generally over-estimated. In addition, the model predicts the position of maximum entrainment ratio at higher current levels than observed in experiments, particularly for low- and moderate-flow-resistance systems. A more thorough comparison of simulation results and experimental data will follow in the next section.

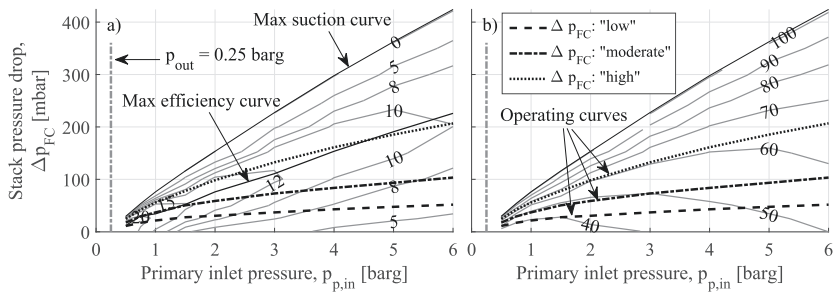

Fig. 7 – Custom-made ejector operating curves plotted on a) efficiency (η) map and b) fuel utilization per pass (u_f) map. Working gas: hydrogen, $T_{dew,s,in}$: 60 °C, p_{out}: 0.25 barg.

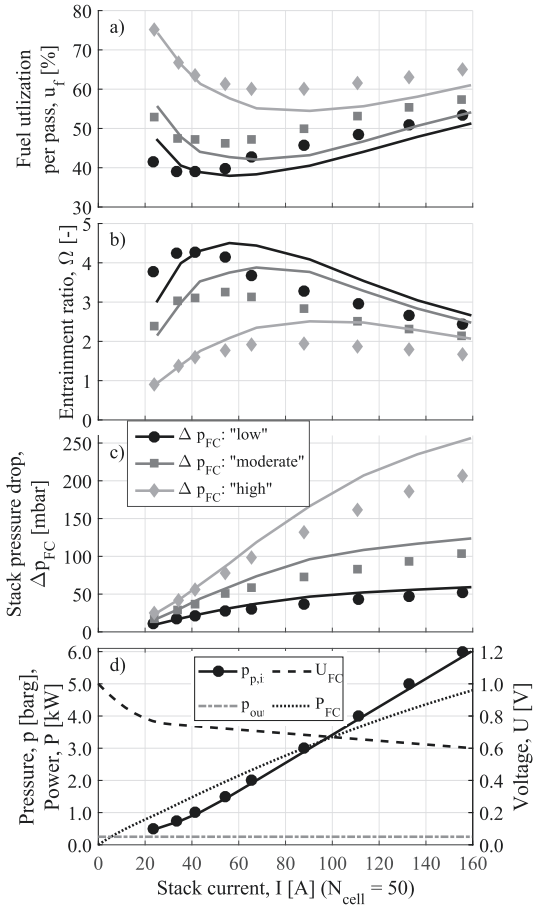

Fig. 8 – Experimental data (markers) and simulation results (SST k-ω, solid lines) along the operating curves as function of 50 cell stack current. a) Fuel utilization per pass, b) entrainment ratio, c) stack pressure drop, d) primary gas pressure and stack polarization curve. Working gas: hydrogen, p_{out}: 0.25 barg, $T_{dew,s,in}$: 60 °C.

Model validation

The simulated and experimental ejector performance comparison is made based on the entrainment ratio (Ω) applying mean absolute deviations (ADs):

$$AD = \frac{1}{n} \times \sum_{i=1\ldots n} \left| \Omega_{meas,i} - \Omega_{sim,i} \right| \quad (24)$$

and mean relative deviations (RDs):

$$RD = \frac{1}{n} \times \sum_{i=1\ldots n} \left| 1 - \frac{\Omega_{sim,i}}{\Omega_{meas,i}} \right| \quad (25)$$

Based on the experimental data measured with hydrogen as working gas (Table B.1), Table 5 compares the ADs and RDs for the three turbulence models considered.

The simulations conducted with k-ε models have lower overall RD while the simulations conducted with SST k-ω model have lower overall AD, as shown in Table 5. This is because the two k-ε models, which provide almost identical results, predict ejector performance better at conditions with low entrainment ratios ($\Omega_{meas} < 1$) while the SST k-ω model predicts ejector performance better at conditions with high entrainment ratios ($\Omega_{meas} > 1$). Therefore, in systems with low flow resistance and high recirculation rate, the SST k-ω model provides better predictions except for the lowest current levels, as illustrated in Fig. 9. In high-flow-resistance systems and at low recirculation rate, all the turbulence models provide similar predictions on ejector performance. Hence, the SST k-ω turbulence model is preferred over the k-ε models when accurate predictions are prioritized.

Concerning ejector performance optimization, the position of simulated maximum performance is more important than the simulated absolute performance. Fig. 10 displays the measured and simulated ejector efficiencies as function of secondary pressure increase for three primary pressures. As observed, the k-ε models predict the position of maximum efficiency very accurately while the SST k-ω model predicts maximum efficiency at a higher secondary pressure increase. This suggests that ejectors can accurately be optimized with CFD simulation conducted in 2D geometry with either of the k-ε turbulence models even though the predicted absolute performance might be inaccurate.

All the turbulence models over-estimate the entrainment ratio at all tested conditions except the SST k-ω model at conditions with low primary pressure and high entrainment ratio (see Fig. 9). This is caused by an over-estimation of the secondary gas flow rate. The primary gas flow rate deviates from +1.7% to +5.7%, and thus, actually decreases the entrainment ratio over-estimation.

In a previous work [13], the 2D flow assumption was observed to result in a relatively high secondary flow over-estimation (~46%–48% on average) for a rectangular ejector operated with air, but only at conditions without double choking (i.e. at critical operational mode). In the present study, double choking was not predicted at any conditions with the SST k-ω model, suggesting that the 2D assumption might be responsible for the deviations also in this study. With both of the k-ε models, double choking was predicted only at conditions with high primary pressure (5 and 6 barg) and high entrainment ratio, i.e. at conditions where the SST k-ω model provided more accurate predictions. Fig. 11 displays the Mach contour predictions of the three turbulence models at the highest applied secondary flow rate. The white color indicates the areas where supersonic flow occurs.

Other possible explanations for the deviations between experimental and simulated ejector performance include ejector manufacturing tolerances and inaccurate boundary conditions. Therefore, the ejector performance sensitivity with respect to these parameters was studied by conducting simulations with the SST k-ω turbulence model on a subset of the experimental points.

Table 6 lists the parameters included in the sensitivity test, their variation, and the resulting performance deviation (AD and RD) compared to the experimentally observed values. The AD and the RD for the reference case (calculated for a subset of

Table 5 – ADs and RDs calculated separately for data points with low ($\Omega_{meas} < 1$) and high ($\Omega_{meas} > 1$) entrainment ratio, and for all data points. Working gas: H_2, $T_{dew,s,in}$: 60 °C, p_{out}: 0.25 barg.

Model	AD			RD		
	$\Omega_{meas} < 1$	$\Omega_{meas} > 1$	All	$\Omega_{meas} < 1$	$\Omega_{meas} > 1$	All
SST k-ω	0.78	0.72	**0.73**	227.2%	31.5%	**68.2%**
RNG k-ε	0.47	1.08	**0.97**	144.6%	41.5%	**60.9%**
Realizable k-ε	0.48	1.17	**1.04**	146.2%	44.5%	**63.6%**

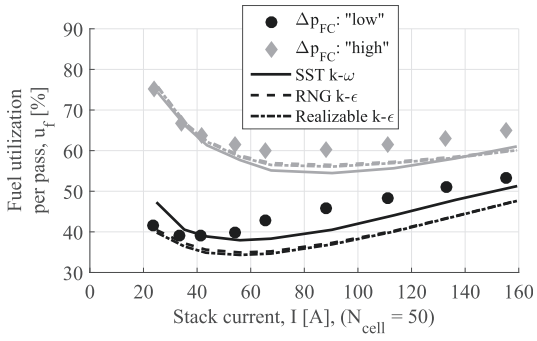

Fig. 9 – Comparison of fuel utilization predictions obtained with the different turbulence models along the low-flow-resistance (black) and high-flow-resistance (gray) operating curves. Working gas: hydrogen, $T_{dew,s,in}$: 60 °C, p_{out}: 0.25 barg.

data points highlighted in Table B.1.) is shown uppermost. The variations in ejector dimensions are the manufacturing tolerances presented in Section 2.1. The ejector performance sensitivity to the unpolished secondary inlet wall roughness (see Fig. 2) was tested by applying a visually approximated wall roughness height ($K_{s,s,in}$). The change in secondary inlet flow direction was varied from −30° to +10° relative to ejector center axis. Because the ejector secondary gas inlet boundary normal has a 30° angle with ejector axis, a −30° change results in horizontal flow and a +10° change results in a flow with 40° angle relative to the ejector axis. The primary and secondary inlet flow turbulence intensities are calculated for each data point separately with Eq. (19). The values employed for measured boundary conditions are computed from the transmitter uncertainties provided by the manufacturers.

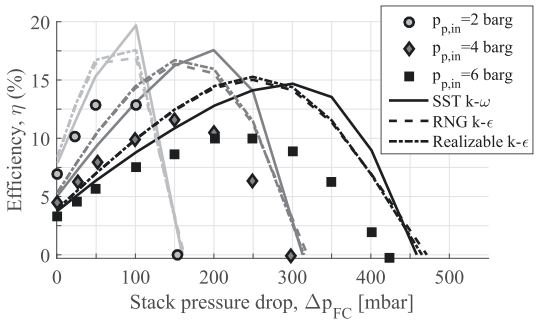

Fig. 10 – Measured and simulated ejector efficiency as function of secondary pressure increase for primary pressures 2 barg (light gray), 4 barg (dark gray), and 6 barg (black). Working gas: hydrogen, $T_{dew,s,in}$: 60 °C, p_{out}: 0.25 barg.

The tolerance of nozzle throat diameter (D_{nt}) has the most notable effect on ejector performance, as shown in Table 6. However, comparing simulated and experimental primary gas mass flow rates (simulation results deviate from +1.7% to +5.7%, as mentioned above) demonstrates that the actual D_{nt} is very close to the intended value of 0.5 mm. The other ejector geometry parameters (L_{ne} and D_m) have only a very minor effect on ejector performance within their tolerances, indicating a reasonable manufacturing accuracy. Also the unpolished secondary inlet wall roughness has only a small effect on ejector performance.

Considering the assumed boundary conditions, both the secondary inlet flow direction and the turbulence intensities affect ejector performance mainly at conditions with high entrainment ratio. The results suggest that the effect of the secondary inlet flow direction can be significant but the effects of turbulence intensities are minor.

Considering the measured boundary conditions, the ejector performance is most sensitive to the secondary inlet pressure, the outlet pressure, and the secondary inlet composition within the transmitter accuracy reported by the manufacturers. Ejector performance sensitivity to the primary pressure is minor. The secondary inlet pressure and outlet pressure appear to be the most critical measurements when comparing the observed experimental standard deviations (σ_{meas}, listed in Table 6), and the simulated ejector performance sensitivity. However, neither of these parameters alone can explain the observed deviation between simulated and measured ejector performance.

Conclusions

In this work, a custom-made ejector was studied experimentally and modeled with CFD. Experimental results indicate that the ejector achieves satisfactory performance on a wide operating range. In particular, high recirculation rate at low primary pressure was achieved in systems with low flow resistance. This suggests that hydrogen recirculation can be realized with a single ejector in PEMFC systems with low enough flow resistance. Satisfactory recirculation was also achieved in a system with high flow resistance but only at high primary pressures, i.e. at conditions with high ejector efficiency.

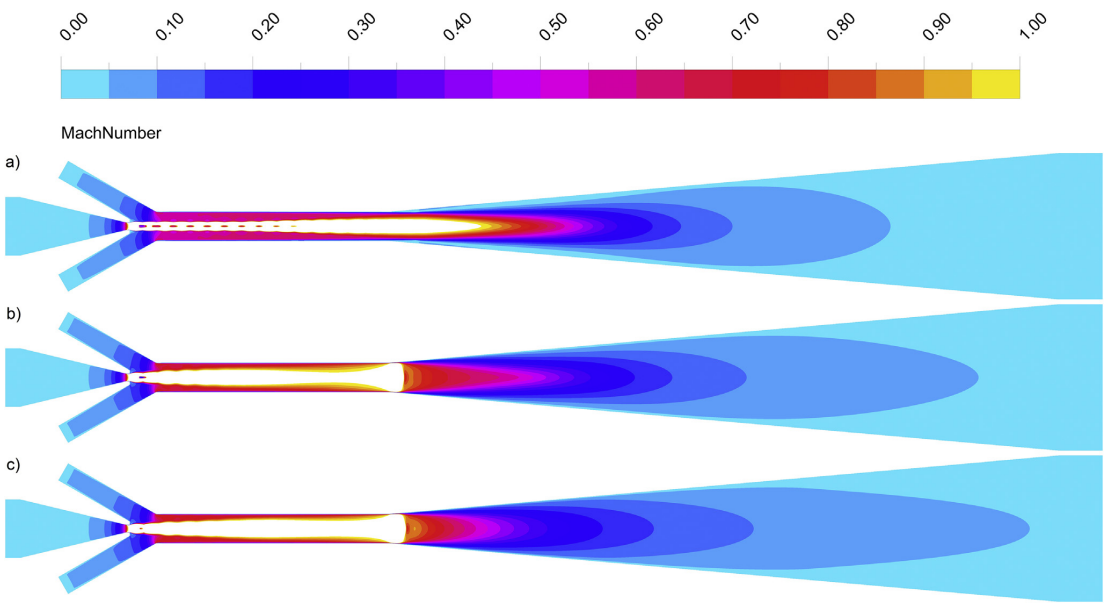

Fig. 11 – Mach number contours predicted by CFD modeling with a) SST k-ω, b) RNG k-ε, and c) Realizable k-ε turbulence models. Working gas: hydrogen, $T_{dew,s,in}$: 60 °C, $p_{p,in}$: 6 barg, $p_{s,in}$: 0.25 barg, p_{out}: 0.25 barg.

The simulation results agreed reasonably well with experimental data (average deviation 60%–70% overall), especially at conditions relevant in PEMFC applications. The best agreement was generally obtained with the SST k-ω turbulence model. However, the tested k-ε models were observed to predict the position of maximum efficiency along the primary pressure range more accurately. This knowledge is useful in designing ejectors for specified PEMFC systems.

The secondary inlet boundary conditions and ejector outlet pressure were recognized as the modeling parameters with most notable influence on ejector performance, particularly at low primary pressures. However, none of the tested parameters alone explain the observed deviation between experiments and simulations.

The markedly lower recirculation rate achieved with the commercial ejector highlights the significance of customized ejector design.

Table 6 – ADs and RDs of simulation conducted with varied ejector dimensions and boundary conditions.

Case	Parameter varied	Change	AD	RD
Reference	None	–	0.72	96.4%
Ejector geometry	D_{nt}	+0.03 mm	0.72	146.4%
	L_{ne}	+0.05 mm	0.73	96.6%
		−0.05 mm	0.71	96.3%
	D_m	+0.01 mm	0.72	91.2%
		+0.02 mm	0.72	85.9%
	$K_{s,s,in}$ (see Fig. 2)	0.5 mm	0.73	97.0%
Boundary conditions based on assumptions	Secondary inlet flow direction relative to boundary	+10°	0.71	96.3%
		−10°	0.73	96.7%
		−30°	0.77	98.0%
	$I_{t,p,in}$	0.9% … 2.0%	0.75	97.0%
	$I_{t,s,in}$	1.9% … 5.4%		
Measured boundary conditions	$p_{p,in}$ (σ_{meas} = 1.8 … 4.1 mbar)	+20 mbar	0.73	99.2%
		−20 mbar	0.71	93.6%
	$p_{s,in}$ (σ_{meas} = 0.5 … 1.9 *mbar*)	+4 mbar	0.77	106.8%
		−4 mbar	0.66	86.0%
	p_{out} (σ_{meas} = 0.4 … 1.5 mbar)	+2 mbar	0.69	91.2%
		−2 mbar	0.75	101.7%
	$y_{H_2,s,in}$ (σ_{meas} = 0.001 … 0.002)	+0.008 … +0.011	0.65	92.8%
		−0.012 … −0.008	0.78	100.0%

Acknowledgments

This research has received funding from the Finnish Graduate School in Chemical Engineering (GSCE), the European Union's Seventh Framework Programme (FP7/2007-2013) for the Fuel Cells and Hydrogen Joint Technology Initiative under grant agreement n° 621218, and the Walter Ahlström foundation.

Nomenclature

Latin

b	pressure drop coefficient, bar/(kg/s)
C	discharge coefficient, –
C_p	ideal gas heat capacity, J/(K × mol)
D	diameter, m
D_{ab}	binary diffusion coefficient, m^2/s
e	molar flow exergy, J/mol
F	Faraday constant, 96,485 C/mol
h	molar enthalpy, J/mol
$\overline{h}$	partial molar enthalpy, J/mol
I	current, A
I_T	turbulence intensity, %
K_s	wall roughness height, mm
k	turbulence kinetic energy, m^2/s^2
L	length, m
M_w	molar weight, kg/mol
$\dot{m}$	mass flow rate, kg/s
N_{cells}	number of cells in PEMFC stack
$\dot{n}$	molar flow rate, mol/s
P	power, W
p	pressure, bar = 10^5 Pa, 0 barg (gauge) = 1.01325 bara (absolute)
p^{vap}	vapor pressure, bar = 10^5 Pa
Δp	PRESSURE difference, bar = 10^5 Pa
R	universal gas constant, 8.3145 J/(K × mol)
Re	Reynolds number, –
RH	relative humidity, %
s	molar entropy, J/(K × mol)
$\overline{s}$	partial molar entropy, J/(K × mol)
T	temperature, °C, 0 °C = 273.15 K
U	stack voltage, V
u_f	fuel utilization per pass, %
$\dot{V}$	volumetric flow rate, m^3/s
v	velocity, m/s
x	coordinate
y	mole fraction, –

Greek

α	angle, °
γ	isentropic expansion factor, –
ε	turbulent dissipation rate, m^2/s^3
η	efficiency, %
κ	thermal conductivity, W/m/K
λ	stoichiometry, –
μ	dynamic viscosity, Pa × s
μ_t	turbulent viscosity, Pa × s
ρ	density, kg/m^3
σ	standard deviation
Ω	entrainment ratio, –
ω	specific turbulent dissipation rate, 1/s

Subscripts

0	stagnant state/dead state
d	ejector diffuser
dew	dew point
E	ejector
FC	fuel cell
in	ejector inlet
m	ejector mixing section
max	maximum
meas	measured value
n	normal conditions (T = 0 °C, p = 1.01325 bara)
ne	ejector nozzle exit
nt	ejector nozzle throat
out	ejector outlet
p	ejector primary stream
s	ejector secondary stream
sim	simulated value

Abbreviations

AD	mean absolute deviation
RD	mean relative deviation
CFD	computational fluid dynamics
DMLS	direct metal laser sintering
PEMFC	proton exchange membrane fuel cell
RNG	Re-Normalization Group
SST	Shear Stress Transport

Appendix A

The physical properties applied in CFD simulations (heat capacity, diffusion coefficients, viscosity, and thermal conductivity) were computed with correlations found in literature. The gas mixture heat capacity (C_p [J/(K × mol)]) was calculated with a mole-weighted mixing law and the following equation for each compound

$$C_{p,i} = a_1 + a_2 \times \left[\frac{a_3}{[T+273.15] \times \sinh(a_3/[T+273.15])}\right]^2 + a_4 \times \left[\frac{a_5}{[T+273.15] \times \cosh(a_5/[T+273.15])}\right]^2 \quad (A.1)$$

where T is the temperature [°C] and the parameters $a_1 - a_5$ are fitted against values found in literature [21–23] in temperatures ranging from 60 K to 300 K and from 300 K to 1000 K.

The binary diffusion coefficients (D_{ab} [m^2/s]) were calculated with the method by Fuller et al. [24].

$$D_{ij} = \frac{0.0101325}{\sqrt{1000}} \times [T+273.15]^{1.75} \times \frac{\sqrt{1/M_{w,i} + 1/M_{w,j}}}{(p \times 10^5 + 101325) \times \left(V_i^{1/3} + V_j^{1/3}\right)^2} \quad (A.2)$$

where $M_{w,i}$ is the mole weight [kg/mol] of component i, p is pressure [barg], and V_i is the so called diffusion volume of component i: $V_{H_2} = 7.07$, $V_{N2} = 17.9$, $V_{H_2O} = 12.7$.

The dynamic viscosity of the gas mixture (μ [Pa × s]) was calculated with the method proposed by Wilke [25]:

$$\mu = \sum_{i=1\ldots n}\left(\frac{\mu_i}{\frac{1}{y_i}\times\sum_{j=1\ldots n}\left[y_j\times\varphi_{ij}\right]}\right) \quad (A.3)$$

where μ_i is pure component i viscosity [Pa × s] calculated with equation from DIPPR Project [26], y_i is the component i mole fraction, and φ_{ij} is calculated as follows:

$$\varphi_{ij} = \frac{\left[1+\left(\mu_i/\mu_j\right)^{\frac{1}{2}}\times\left(M_{w,j}/M_{w,i}\right)^{\frac{1}{4}}\right]^2}{\frac{4}{\sqrt{2}}\times\left(1+M_{w,i}/M_{w,j}\right)^{\frac{1}{2}}} \quad (A.4)$$

The thermal conductivity for the gas mixture (κ [W/m/K]) was calculated with the method proposed by Lindsay and Bromley [27]:

$$\kappa = \sum_{i=1\ldots n}\left(\frac{\kappa_i}{\frac{1}{y_i}\times\sum_{j=1\ldots n}\left[y_j\times A_{ij}\right]}\right) \quad (A.5)$$

where κ_i is pure component i thermal conductivity [W/m/K] calculated with equation from DIPPR Project [26] and A_{ij} is calculated as follows:

$$A_{ij} = \frac{1}{4}\times\left\{1+\left[\frac{\mu_i}{\mu_j}\times\left(\frac{M_{w,j}}{M_{w,i}}\right)^{\frac{3}{4}}\times\frac{\left(1+S_i/[T+273.15]\right)}{\left(1+S_j/[T+273.15]\right)}\right]^{\frac{1}{2}}\right\}^2 \times\frac{\left(1+S_{ij}/[T+273.15]\right)}{\left(1+S_i/[T+273.15]\right)} \quad (A.6)$$

where $S_{ij} = (S_i \times S_j)^{1/2}$ except when one of the components is water (or some other strongly polar compound). In that case $S_{ij} = 0.733 \times (S_i \times S_j)^{1/2}$.

Appendix B

Table B.1 – Time averaged experimental results of hydrogen-operated custom-made ejector. Experiments considered in the sensitivity tests are bolded and highlighted with gray background.

$p_{p,in}$ Barg	$p_{s,in}$ Barg	p_{out} Barg	$T_{dew,s,in}$ °C	$\dot{m}_p$ 10^{-6} kg/s	$\dot{m}_s$ 10^{-6} kg/s
$T_{dew,s,in}$ = 60 °C, p_{out} = 0.25 barg					
0.50	0.249	0.251	59.7	12.1	70.5
0.50	0.225	0.250	60.0	12.6	10.6
0.50	0.221	0.250	–	0.0	–
0.75	0.250	0.250	59.9	17.3	101.6
0.75	0.225	0.251	60.0	17.6	59.6
0.75	0.200	0.250	59.9	18.0	5.7
0.75	0.197	0.250	–	17.8	–
1.00	**0.250**	**0.250**	**60.0**	**21.5**	**119.9**
1.00	**0.225**	**0.251**	**60.0**	**21.5**	**85.6**
1.00	**0.200**	**0.250**	**60.1**	**21.6**	**44.7**
1.00	0.173	0.250	–	21.9	–
1.50	0.249	0.249	59.9	28.3	152.7
1.50	0.225	0.251	60.0	28.2	118.5
1.50	0.200	0.250	60.1	28.2	92.6
1.50	0.149	0.250	60.0	28.5	13.2
1.50	0.135	0.251	–	28.4	–
2.00	**0.249**	**0.249**	**60.0**	**34.2**	**156.6**
2.00	0.225	0.249	60.0	34.2	128.5
2.00	**0.201**	**0.250**	**59.9**	**34.2**	**117.4**
2.00	0.150	0.250	60.1	34.2	62.7
2.00	**0.096**	**0.250**	–	**34.3**	–
3.00	**0.249**	**0.250**	**60.0**	**46.0**	**181.8**
2.99	0.224	0.251	60.0	46.0	157.2
3.00	0.200	0.250	60.1	46.0	141.5
2.99	**0.150**	**0.250**	**60.0**	**45.9**	**117.6**
3.00	0.099	0.251	60.0	46.0	71.6
3.00	0.050	0.251	60.1	46.1	18.5
3.00	**0.023**	**0.250**	–	**46.1**	–
4.00	**0.249**	**0.249**	**59.9**	**58.0**	**197.3**
4.00	0.224	0.250	60.0	58.0	181.6
4.00	0.199	0.251	60.0	58.0	166.1
4.00	0.150	0.250	59.9	57.9	134.6
4.00	**0.100**	**0.250**	**60.0**	**57.9**	**117.2**
4.00	0.050	0.250	60.1	58.0	79.6
4.00	0.000	0.250	60.0	58.0	35.8
4.00	**−0.047**	**0.251**	–	**57.8**	–
5.00	**0.250**	**0.251**	**60.0**	**69.4**	**208.7**
5.00	0.225	0.250	60.1	69.9	197.8
5.01	0.200	0.249	60.0	69.4	184.4
5.00	0.149	0.250	60.0	69.2	155.4
5.00	0.099	0.250	60.0	69.2	144.1
5.00	**0.049**	**0.250**	**59.9**	**69.3**	**114.7**
5.00	0.000	0.251	59.9	69.2	82.0
5.00	−0.049	0.250	60.1	69.2	45.7
5.00	−0.101	0.249	60.0	69.8	8.3
5.00	**−0.112**	**0.250**	–	**69.7**	–
6.00	**0.250**	**0.250**	**60.0**	**81.2**	**218.7**
6.00	0.225	0.250	60.0	81.2	210.0
6.00	0.200	0.250	60.0	81.2	198.9
6.00	0.149	0.250	60.0	81.2	174.2
6.01	0.100	0.250	60.0	81.2	148.6
6.00	0.050	0.250	60.1	81.2	139.1
6.00	**0.000**	**0.249**	**60.0**	**81.2**	**113.2**
6.00	−0.050	0.250	60.2	81.2	83.2
6.00	−0.100	0.250	60.1	81.3	48.5
5.99	−0.151	0.250	60.0	81.7	12.3
6.00	**−0.174**	**0.250**	–	**81.8**	–

Table B.2 – Time averaged experimental results of air-operated custom-made ejector.

$p_{p.in}$ Barg	$p_{s.in}$ Barg	p_{out} Barg	$T_{dew.s.in}$ °C	$\dot{m}_p$ 10^{-6} kg/s	$\dot{m}_s$ 10^{-6} kg/s
Dry, p_{out} = 0.00 barg					
0.25	0.000	0.001	–	43.0	171.0
0.25	−0.025	0.001	–	44.2	13.5
0.25	−0.028	0.001	–	45.1	–
0.51	0.000	0.001	–	61.1	235.2
0.50	−0.026	0.001	–	62.1	138.7
0.50	−0.050	0.001	–	62.1	–
0.75	0.000	0.001	–	75.3	274.3
0.75	−0.026	0.001	–	75.4	187.1
0.75	−0.050	0.001	–	76.0	103.2
0.75	−0.071	0.001	–	76.1	–
1.00	−0.001	0.001	–	88.0	304.9
1.00	−0.024	0.001	–	88.1	234.9
1.00	−0.049	0.001	–	88.1	165.4
1.00	−0.091	0.001	–	88.2	–

(continued on next page)

Table B.2 – (continued)

$p_{p.in}$ Barg	$p_{s.in}$ Barg	p_{out} Barg	$T_{dew.s.in}$ °C	$\dot{m}_p$ 10^{-6} kg/s	$\dot{m}_s$ 10^{-6} kg/s
1.50	0.000	0.001	–	109.3	352.9
1.50	−0.025	0.001	–	109.4	293.4
1.50	−0.050	0.001	–	109.4	223.5
1.50	−0.100	0.001	–	109.5	98.6
1.50	−0.130	0.001	–	109.6	–
2.01	0.001	0.001	–	130.8	389.0
2.00	−0.025	0.001	–	130.9	337.9
2.01	−0.050	0.001	–	130.9	272.1
2.00	−0.100	0.001	–	130.8	176.3
2.00	−0.149	0.001	–	130.7	40.2
2.00	−0.167	0.001	–	130.6	–
3.00	0.001	0.002	–	174.2	432.0
3.00	−0.025	0.001	–	173.7	393.1
3.00	−0.049	0.001	–	173.9	348.0
3.00	−0.101	0.001	–	174.3	271.3
3.00	−0.150	0.001	–	174.0	184.9
3.00	−0.200	0.001	–	174.4	90.0
3.00	−0.235	0.001	–	174.4	–
4.00	0.000	0.002	–	222.9	459.0
4.00	−0.025	0.002	–	223.2	424.1
4.00	−0.050	0.002	–	222.4	388.8
4.00	−0.099	0.001	–	222.8	321.7
4.00	−0.151	0.001	–	223.2	254.6
4.00	−0.200	0.001	–	222.7	178.1
4.00	−0.250	0.001	–	222.5	108.5
4.00	−0.299	0.001	–	223.1	–
5.00	0.000	0.003	–	270.0	473.3
5.00	−0.026	0.002	–	269.9	443.7
5.00	−0.051	0.002	–	271.1	412.8
5.00	−0.100	0.002	–	269.9	350.1
5.00	−0.150	0.001	–	269.7	296.5
5.00	−0.201	0.001	–	270.0	236.3
5.00	−0.249	0.001	–	270.7	177.1
5.00	−0.299	0.001	–	269.6	113.6
5.00	−0.350	0.001	–	270.5	18.0
5.00	−0.361	0.001	–	270.8	–
6.00	0.000	0.003	–	321.9	480.1
6.00	−0.025	0.003	–	321.8	457.1
6.00	−0.050	0.003	–	320.5	431.8
6.00	−0.100	0.002	–	321.3	374.3
6.00	−0.150	0.002	–	321.9	325.2
6.00	−0.201	0.002	–	321.5	272.4
6.00	−0.250	0.001	–	321.2	222.3
6.00	−0.298	0.001	–	320.8	175.6
6.00	−0.350	0.001	–	322.5	111.2
6.00	−0.400	0.001	–	322.9	23.0
6.00	−0.418	0.001	–	321.6	–
Dry, p_{out} = 0.25 barg					
0.50	0.250	0.251	–	48.3	212.9
0.49	0.220	0.250	–	50.3	–
0.75	0.250	0.250	–	68.7	283.8
0.75	0.225	0.250	–	69.6	177.6
0.75	0.200	0.249	–	70.2	31.7
0.75	0.195	0.250	–	70.2	–
1.01	0.250	0.250	–	84.6	330.8
1.01	0.224	0.250	–	84.9	235.6
1.01	0.199	0.249	–	84.9	147.5
1.00	0.173	0.250	–	85.2	–
1.50	0.250	0.250	–	108.8	391.7
1.50	0.225	0.250	–	108.9	322.5
1.50	0.200	0.250	–	108.8	242.1
1.50	0.149	0.250	–	109.1	58.9
1.50	0.135	0.250	–	109.0	–

Table B.2 – (continued)

$p_{p.in}$ Barg	$p_{s.in}$ Barg	p_{out} Barg	$T_{dew.s.in}$ °C	$\dot{m}_p$ 10^{-6} kg/s	$\dot{m}_s$ 10^{-6} kg/s
2.00	0.249	0.250	–	130.3	434.9
2.00	0.225	0.250	–	130.1	373.4
2.00	0.200	0.250	–	130.2	306.6
2.01	0.150	0.250	–	130.6	183.8
2.01	0.100	0.250	–	130.6	12.7
2.00	0.094	0.250	–	130.5	–
3.00	0.249	0.250	–	174.1	496.1
3.00	0.225	0.249	–	173.5	452.9
2.99	0.201	0.250	–	173.9	401.7
3.00	0.150	0.250	–	173.6	300.9
3.00	0.100	0.250	–	173.7	199.9
3.00	0.050	0.250	–	173.8	80.6
3.00	0.022	0.251	–	173.8	–
4.00	0.250	0.250	–	222.3	542.2
4.00	0.224	0.250	–	222.9	505.4
4.00	0.199	0.250	–	222.0	460.6
4.00	0.150	0.249	–	222.7	381.0
4.00	0.099	0.250	–	222.4	309.3
4.00	0.050	0.250	–	222.6	213.3
3.99	0.000	0.250	–	222.1	116.0
4.00	−0.046	0.251	–	222.6	–
5.00	0.249	0.251	–	269.9	567.5
5.00	0.224	0.251	–	270.6	538.0
5.00	0.200	0.250	–	269.7	504.4
5.00	0.151	0.250	–	269.7	428.3
5.00	0.101	0.250	–	270.1	361.9
5.00	0.051	0.250	–	270.4	294.5
5.00	−0.001	0.250	–	269.5	209.5
5.00	−0.050	0.249	–	270.5	136.8
5.00	−0.100	0.250	–	270.0	20.9
5.00	−0.111	0.250	–	270.3	–
6.00	0.249	0.250	–	320.7	583.8
6.01	0.224	0.250	–	322.1	558.6
6.01	0.199	0.251	–	322.2	532.2
6.00	0.149	0.250	–	321.4	461.1
6.00	0.100	0.250	–	320.8	397.4
6.00	0.049	0.250	–	321.3	343.8
5.99	0.000	0.250	–	321.8	278.1
5.99	−0.050	0.250	–	321.2	209.9
6.00	−0.100	0.250	–	321.9	142.2
6.00	−0.151	0.250	–	322.4	39.3
6.00	−0.174	0.250	–	322.2	–
Dry, p_{out} = 0.50 barg					
0.75	0.500	0.501	–	53.2	257.4
0.75	0.475	0.500	–	54.2	101.3
0.75	0.465	0.500	–	55.2	–
1.00	0.500	0.500	–	75.4	333.6
1.00	0.475	0.500	–	76.1	210.0
1.00	0.450	0.500	–	77.1	68.5
1.00	0.440	0.500	–	77.2	–
1.50	0.501	0.500	–	105.8	415.3
1.50	0.475	0.500	–	106.1	334.6
1.50	0.450	0.500	–	106.4	244.7
1.50	0.397	0.500	–	107.4	–
2.00	0.499	0.500	–	129.9	473.9
2.00	0.475	0.500	–	130.0	405.5
2.00	0.450	0.501	–	130.1	330.8
2.00	0.400	0.500	–	130.0	180.2
2.00	0.358	0.500	–	130.3	–
3.00	0.498	0.500	–	173.8	550.0
3.00	0.475	0.499	–	174.4	501.1
3.00	0.449	0.500	–	173.4	442.2
3.00	0.399	0.500	–	173.3	320.6

Table B.2 – (continued)

$p_{p.in}$ Barg	$p_{s.in}$ Barg	p_{out} Barg	$T_{dew.s.in}$ °C	$\dot{m}_p$ 10^{-6} kg/s	$\dot{m}_s$ 10^{-6} kg/s
3.00	0.350	0.500	–	173.8	210.3
3.00	0.300	0.500	–	174.1	44.5
3.00	0.282	0.501	–	174.5	–
4.00	0.498	0.499	–	221.7	604.4
4.00	0.473	0.499	–	222.7	565.2
4.00	0.449	0.500	–	222.2	522.4
4.00	0.400	0.500	–	221.9	417.0
4.00	0.350	0.500	–	222.4	334.1
4.00	0.300	0.499	–	222.6	227.1
4.01	0.250	0.500	–	222.8	116.4
4.01	0.208	0.500	–	223.4	–
5.00	0.498	0.500	–	268.0	645.2
5.00	0.475	0.500	–	268.5	609.0
5.00	0.449	0.499	–	267.8	570.9
5.00	0.399	0.501	–	267.4	484.7
5.00	0.349	0.500	–	267.6	411.5
5.00	0.300	0.500	–	267.3	339.7
5.01	0.249	0.500	–	268.7	238.2
5.00	0.200	0.500	–	267.4	143.2
5.01	0.150	0.500	–	268.0	20.0
5.00	0.142	0.499	–	268.2	–
6.00	0.499	0.500	–	318.8	671.4
6.00	0.474	0.500	–	318.1	640.9
6.00	0.449	0.500	–	317.6	609.4
6.00	0.400	0.500	–	320.0	538.9
6.01	0.350	0.500	–	320.9	461.4
6.00	0.299	0.499	–	317.9	397.3
6.00	0.250	0.500	–	319.5	325.2
6.00	0.200	0.500	–	318.0	238.1
6.00	0.150	0.500	–	317.2	161.9
6.00	0.100	0.500	–	319.3	45.5
6.00	0.077	0.500	–	318.6	–
$T_{dew.s.in}$ = 60 °C, p_{out} = 0.00 barg					
0.25	−0.001	0.001	60.1	42.2	145.8
0.25	−0.025	0.001	59.9	43.2	10.0
0.25	−0.028	0.001	–	45.1	–
0.50	0.000	0.001	60.0	60.1	200.6
0.50	−0.026	0.001	60.1	60.5	114.6
0.50	−0.050	0.001	–	62.1	–
0.75	0.000	0.001	60.0	74.4	236.1
0.75	−0.025	0.001	60.2	75.1	160.5
0.75	−0.050	0.001	59.8	75.1	72.5
0.75	−0.071	0.001	–	76.1	–
1.00	0.001	0.001	60.0	87.5	265.5
1.00	−0.026	0.001	59.8	88.0	191.3
1.00	−0.050	0.001	59.9	88.1	131.2
1.00	−0.091	0.001	–	88.2	–
1.50	−0.001	0.001	60.1	111.4	297.1
1.50	−0.025	0.001	60.2	111.5	248.3
1.50	−0.050	0.001	60.3	111.6	189.8
1.50	−0.100	0.001	60.1	111.6	69.3
1.50	−0.130	0.001	–	109.6	–
2.00	0.000	0.002	59.8	133.8	331.1
2.00	−0.024	0.001	59.9	133.8	287.5
2.00	−0.049	0.001	59.9	133.8	236.7
2.00	−0.100	0.001	60.1	134.0	143.5
2.00	−0.150	0.001	59.8	134.0	27.2
2.00	−0.167	0.001	–	130.6	–
3.00	−0.001	0.002	59.8	177.9	363.4
3.00	−0.025	0.002	59.9	177.5	331.7
3.00	−0.048	0.002	60.1	178.2	289.8
3.00	−0.101	0.001	60.0	178.4	211.5
3.00	−0.150	0.001	60.1	178.2	139.9
3.00	−0.201	0.001	60.1	178.6	57.2

Table B.2 – (continued)

$p_{p.in}$ Barg	$p_{s.in}$ Barg	p_{out} Barg	$T_{dew.s.in}$ °C	$\dot{m}_p$ 10^{-6} kg/s	$\dot{m}_s$ 10^{-6} kg/s
3.00	−0.235	0.001	–	174.4	–
4.00	0.000	0.003	60.0	224.3	389.2
4.00	−0.025	0.003	59.8	224.3	361.1
4.00	−0.050	0.002	59.9	224.2	330.7
4.01	−0.099	0.002	60.0	225.1	272.3
4.00	−0.150	0.001	60.0	224.8	209.4
4.00	−0.200	0.001	60.0	224.4	143.4
4.00	−0.251	0.001	60.0	225.1	70.2
4.00	−0.299	0.001	–	223.1	–
5.00	0.000	0.004	60.0	269.4	405.0
5.00	−0.024	0.003	60.0	269.4	384.9
5.00	−0.049	0.003	60.0	269.4	359.0
5.00	−0.101	0.002	60.2	269.1	304.7
5.00	−0.150	0.002	59.9	269.4	253.0
5.00	−0.199	0.001	60.0	269.7	191.9
5.00	−0.251	0.001	60.2	269.6	139.3
5.00	−0.300	0.001	59.9	270.1	73.0
4.99	−0.349	0.001	59.9	270.5	9.6
5.00	−0.361	0.001	–	270.8	–
6.00	0.000	0.004	59.7	316.6	411.8
6.00	−0.026	0.004	59.9	316.7	394.1
6.00	−0.050	0.004	60.0	317.1	371.8
6.00	−0.100	0.003	60.0	318.1	326.8
6.00	−0.150	0.003	59.9	316.5	280.3
6.00	−0.200	0.002	60.1	319.0	221.9
6.00	−0.250	0.002	60.1	318.8	171.6
6.00	−0.299	0.001	60.0	317.2	127.5
6.00	−0.349	0.001	60.0	319.0	70.1
6.00	−0.400	0.001	60.2	319.2	11.5
6.00	−0.418	0.001	–	321.6	–
$T_{dew.s.in}$ = 60 °C, p_{out} = 0.25 barg					
0.50	0.249	0.250	60.1	47.4	178.6
0.49	0.220	0.250	–	50.3	–
0.75	0.250	0.250	60.0	67.3	249.0
0.75	0.225	0.250	60.1	68.3	146.3
0.75	0.200	0.250	60.0	70.2	14.2
0.75	0.195	0.250	–	70.2	–
1.00	0.250	0.251	59.7	83.0	287.2
1.00	0.224	0.250	59.9	83.8	191.4
1.00	0.200	0.250	60.2	84.2	104.5
1.00	0.173	0.250	–	85.2	–
1.50	0.250	0.250	60.1	108.9	337.1
1.50	0.225	0.250	60.2	109.0	263.8
1.50	0.199	0.250	60.1	109.2	199.7
1.50	0.150	0.250	59.9	109.7	48.3
1.50	0.135	0.250	–	109.0	–
2.00	0.250	0.251	59.9	131.4	379.3
2.00	0.225	0.250	59.9	131.7	324.8
2.00	0.200	0.251	59.8	131.7	260.2
2.00	0.150	0.250	60.2	132.0	145.1
2.00	0.100	0.250	60.2	132.5	8.8
2.00	0.094	0.250	–	130.5	–
3.00	0.250	0.251	60.0	175.8	427.2
3.00	0.223	0.251	60.1	175.4	386.3
3.00	0.200	0.250	60.1	175.5	345.6
3.00	0.150	0.250	60.2	175.6	248.4
3.00	0.100	0.250	60.0	175.5	159.5
3.00	0.050	0.250	60.0	175.7	50.0
3.00	0.022	0.251	–	173.8	–
4.00	0.250	0.250	60.0	223.4	483.7
4.00	0.225	0.250	60.0	222.7	445.4
4.00	0.200	0.250	60.1	223.2	397.8
4.00	0.151	0.250	60.0	222.3	309.8

(continued on next page)

Table B.2 – (continued)

$p_{p.in}$ Barg	$p_{s.in}$ Barg	p_{out} Barg	$T_{dew.s.in}$ °C	$\dot{m}_p$ 10^{-6} kg/s	$\dot{m}_s$ 10^{-6} kg/s
4.00	0.100	0.250	60.0	223.3	235.0
3.99	0.051	0.250	60.1	223.2	161.3
4.00	0.000	0.249	60.1	223.6	79.4
4.00	−0.046	0.251	–	222.6	–
5.00	0.249	0.251	59.8	268.8	479.9
5.00	0.225	0.250	59.8	267.7	452.0
5.00	0.200	0.250	59.8	268.3	420.1
5.00	0.148	0.251	60.0	268.6	362.3
5.00	0.099	0.250	59.8	268.8	300.0
5.00	0.051	0.250	59.8	268.2	237.7
5.00	0.000	0.251	60.1	269.0	165.2
5.00	−0.050	0.249	59.9	269.3	94.0
5.00	−0.100	0.249	59.9	270.7	16.3
5.00	−0.111	0.250	–	270.3	–
6.00	0.251	0.250	59.8	316.9	508.9
6.00	0.224	0.250	60.0	315.8	481.0
6.00	0.201	0.251	60.1	317.3	452.4
6.00	0.150	0.250	60.3	316.7	398.4
6.00	0.100	0.499	60.0	319.5	35.8
6.00	0.099	0.250	60.0	316.7	347.3
6.00	0.051	0.250	60.2	317.3	284.7
6.00	0.000	0.250	60.0	317.3	220.9
6.00	−0.051	0.251	60.1	317.6	164.9
6.00	−0.099	0.251	60.1	316.3	100.8
6.00	−0.150	0.250	60.1	319.8	28.1
6.00	−0.174	0.250	–	322.2	–
$T_{dew.s.in}$ = 60 °C, p_{out} = 0.50 barg					
0.75	0.500	0.501	60.0	52.2	215.0
0.75	0.475	0.500	60.2	53.3	66.9
0.75	0.465	0.500	–	55.2	–
1.00	0.501	0.500	60.1	74.2	294.7
1.00	0.474	0.500	60.2	75.3	173.1
1.00	0.450	0.500	60.1	76.2	50.2
1.00	0.440	0.500	–	77.2	–
1.50	0.499	0.500	59.9	106.0	372.6
1.50	0.475	0.500	60.0	106.5	282.6
1.50	0.450	0.501	60.0	106.9	211.4
1.50	0.397	0.500	–	107.4	–
2.00	0.499	0.500	59.9	131.3	410.4
2.00	0.475	0.501	59.8	131.2	345.5
2.00	0.450	0.500	60.1	131.3	280.4
2.00	0.400	0.500	60.2	131.3	137.1
2.00	0.358	0.500	–	130.3	–
3.01	0.499	0.500	59.9	176.0	483.9
3.00	0.476	0.500	60.2	175.8	438.9
3.00	0.449	0.500	60.1	175.4	387.2
3.00	0.400	0.500	60.0	175.9	281.4
3.00	0.350	0.500	59.9	176.1	165.3
3.00	0.300	0.500	59.9	177.0	33.9
3.00	0.282	0.501	–	174.5	–
4.00	0.499	0.500	60.0	222.6	532.7
4.00	0.475	0.500	60.1	221.9	487.0
4.00	0.449	0.500	60.0	223.1	448.3
3.99	0.400	0.500	59.8	222.4	365.8
4.00	0.350	0.501	60.1	223.1	272.9
4.00	0.300	0.500	60.0	223.1	182.4
4.00	0.250	0.500	60.0	223.5	73.4
4.01	0.208	0.500	–	223.4	–
5.00	0.499	0.500	60.1	268.1	568.7
5.00	0.474	0.500	60.1	268.9	533.1
5.00	0.448	0.500	60.1	268.1	491.3
5.00	0.400	0.501	60.0	267.7	413.6
5.00	0.350	0.500	60.0	268.3	338.1

Table B.2 – (continued)

$p_{p.in}$ Barg	$p_{s.in}$ Barg	p_{out} Barg	$T_{dew.s.in}$ °C	$\dot{m}_p$ 10^{-6} kg/s	$\dot{m}_s$ 10^{-6} kg/s
5.00	0.300	0.500	60.1	268.2	260.2
5.00	0.250	0.500	59.9	267.9	184.1
5.00	0.202	0.500	60.0	268.2	109.4
5.00	0.151	0.500	59.9	270.3	16.1
5.00	0.142	0.499	–	268.2	–
6.00	0.499	0.500	60.0	316.1	593.3
6.00	0.474	0.501	59.9	316.2	564.9
5.99	0.450	0.501	59.7	315.6	526.8
6.00	0.400	0.501	60.1	316.6	460.9
6.00	0.350	0.501	59.9	316.6	400.0
6.00	0.300	0.501	60.0	316.7	335.4
6.00	0.249	0.500	60.0	316.7	260.6
6.00	0.200	0.500	59.9	317.2	194.0
6.00	0.149	0.501	59.8	317.1	116.8
6.00	0.077	0.500	–	318.6	–
$T_{dew.s.in}$ = 75 °C, p_{out} = 0.00 barg					
0.25	0.001	0.001	74.9	39.4	134.9
0.25	−0.025	0.001	75.0	41.8	0.6
0.25	−0.028	0.001	–	45.1	–
0.50	0.001	0.001	75.0	58.2	186.5
0.50	−0.026	0.001	74.9	59.2	102.8
0.50	−0.050	0.001	–	62.1	–
0.75	0.000	0.001	75.0	73.4	217.9
0.75	−0.025	0.001	75.0	74.2	148.1
0.75	−0.050	0.001	75.0	74.2	67.8
0.75	−0.071	0.001	–	76.1	–
1.00	0.000	0.001	74.9	86.6	235.8
0.99	−0.025	0.001	75.1	86.7	179.8
1.00	−0.050	0.001	75.0	87.0	119.4
1.00	−0.091	0.001	–	88.2	–
1.50	0.000	0.001	75.2	110.4	269.5
1.50	−0.026	0.001	75.0	110.5	221.3
1.50	−0.050	0.001	75.0	110.5	177.5
1.51	−0.100	0.001	75.0	111.2	62.8
1.50	−0.130	0.001	–	109.6	–
2.00	−0.001	0.001	75.0	133.1	300.6
2.00	−0.025	0.001	74.9	132.6	261.3
2.00	−0.050	0.001	75.0	132.8	211.5
2.00	−0.101	0.001	74.9	132.8	130.8
2.00	−0.150	0.001	74.8	133.8	22.0
2.00	−0.167	0.001	–	130.6	–
3.00	0.001	0.002	74.9	176.2	335.3
3.00	−0.025	0.002	75.1	176.6	303.9
3.00	−0.049	0.001	75.2	176.3	262.7
3.00	−0.100	0.001	75.0	176.5	193.4
3.00	−0.150	0.001	75.1	176.4	129.8
3.00	−0.201	0.001	75.0	176.5	53.8
3.00	−0.235	0.001	–	174.4	–
4.00	0.000	0.002	75.1	219.7	350.3
4.00	−0.024	0.002	74.8	220.9	323.9
4.00	−0.050	0.002	74.9	220.9	300.6
4.00	−0.100	0.002	75.0	221.0	242.0
4.00	−0.149	0.001	75.0	223.2	195.3
4.00	−0.199	0.001	75.0	223.2	132.5
4.00	−0.250	0.001	75.0	223.9	68.1
4.00	−0.299	0.001	–	223.1	–
5.00	−0.001	0.003	75.0	266.1	367.4
5.00	−0.025	0.002	75.0	265.5	345.0
5.00	−0.049	0.002	75.1	265.9	321.2
5.00	−0.100	0.002	75.0	266.5	277.0
5.00	−0.150	0.002	75.0	265.8	222.2
5.00	−0.200	0.001	74.8	265.8	169.8
5.00	−0.250	0.001	74.9	265.7	124.7

Table B.2 – (continued)

$p_{p.in}$ Barg	$p_{s.in}$ Barg	p_{out} Barg	$T_{dew.s.in}$ °C	$\dot{m}_p$ 10^{-6} kg/s	$\dot{m}_s$ 10^{-6} kg/s
5.00	−0.299	0.001	75.0	265.8	67.3
5.00	−0.349	0.001	75.1	269.1	8.2
5.00	−0.361	0.001	–	270.8	–
6.00	−0.001	0.003	75.0	313.5	374.7
6.00	−0.025	0.003	74.9	313.5	356.3
6.00	−0.049	0.003	74.8	313.8	339.6
6.00	−0.099	0.002	74.9	313.4	300.5
6.00	−0.149	0.002	74.9	314.8	251.1
6.00	−0.199	0.002	74.9	312.6	199.3
6.00	−0.249	0.002	75.1	313.3	153.8
6.00	−0.299	0.001	75.0	314.9	113.5
6.00	−0.349	0.001	75.0	313.9	61.9
6.00	−0.400	0.001	75.0	317.1	9.0
6.00	−0.418	0.001	–	321.6	–
$T_{dew.s.in}$ = 75 °C, p_{out} = 0.25 barg					
0.50	0.249	0.250	74.9	42.3	166.9
0.49	0.220	0.250	–	50.3	–
0.75	0.250	0.251	75.1	64.1	244.7
0.75	0.224	0.250	75.1	65.1	127.5
0.76	0.200	0.250	75.0	68.2	5.3
0.75	0.195	0.250	–	70.2	–
1.00	0.250	0.250	75.1	80.2	292.2
1.00	0.225	0.250	75.1	81.0	185.7
1.00	0.200	0.250	75.0	81.3	104.8
1.00	0.173	0.250	–	85.2	–
1.50	0.249	0.249	74.9	105.0	317.2
1.50	0.224	0.250	75.2	105.0	244.8
1.50	0.200	0.250	75.1	105.2	189.2
1.50	0.150	0.250	75.1	105.7	31.0
1.50	0.135	0.250	–	109.0	–
2.00	0.251	0.251	74.9	126.4	348.7
2.00	0.225	0.251	74.9	126.7	298.8
2.00	0.200	0.249	75.1	126.7	249.7
2.00	0.150	0.250	75.1	127.1	139.4
2.00	0.094	0.250	–	130.5	–
3.00	0.251	0.250	75.0	168.4	407.6
3.00	0.224	0.249	74.9	168.9	368.6
3.00	0.202	0.250	75.2	168.5	326.4
3.00	0.151	0.251	74.9	168.6	237.6
3.01	0.099	0.250	74.9	168.9	151.5
3.01	0.050	0.250	75.1	169.4	42.6
3.00	0.022	0.251	–	173.8	–
4.00	0.250	0.250	74.9	216.1	439.8
4.00	0.225	0.250	75.0	215.9	403.1
4.00	0.201	0.250	74.8	216.8	364.2
4.00	0.150	0.250	75.0	216.1	291.2
4.00	0.101	0.251	74.8	216.4	216.4
4.00	0.050	0.251	74.9	216.4	148.2
4.00	0.000	0.250	75.2	216.6	74.8
4.00	−0.046	0.251	–	222.6	–
4.99	0.249	0.249	75.2	261.8	457.9
5.00	0.225	0.250	75.2	262.0	434.6
5.00	0.200	0.250	75.1	262.3	399.7
5.00	0.151	0.250	74.9	262.9	341.4
5.00	0.099	0.250	75.0	262.9	280.3
5.00	0.049	0.251	75.1	261.5	214.8
5.00	0.001	0.249	75.0	262.6	159.5
5.01	−0.049	0.249	75.1	263.5	88.4
5.00	−0.100	0.250	74.9	266.4	10.3
5.00	−0.111	0.250	–	270.3	–
6.00	0.249	0.250	75.0	313.4	482.3
6.00	0.225	0.249	75.0	313.0	461.7
6.00	0.199	0.249	74.8	313.0	447.1

Table B.2 – (continued)

$p_{p.in}$ Barg	$p_{s.in}$ Barg	p_{out} Barg	$T_{dew.s.in}$ °C	$\dot{m}_p$ 10^{-6} kg/s	$\dot{m}_s$ 10^{-6} kg/s
6.00	0.150	0.250	75.1	310.8	377.6
5.99	0.100	0.251	75.1	310.7	324.1
6.00	0.051	0.251	75.0	311.2	273.5
6.00	0.000	0.251	75.1	311.6	205.3
6.00	−0.052	0.251	75.0	312.1	153.3
6.01	−0.098	0.250	75.0	312.6	97.5
6.00	−0.150	0.250	74.9	314.3	21.7
6.00	−0.174	0.250	–	322.2	–
$T_{dew.s.in}$ = 75 °C, p_{out} = 0.50 barg					
0.75	0.500	0.500	74.9	51.4	231.1
0.75	0.474	0.500	75.1	54.3	63.5
0.75	0.465	0.500	–	55.2	–
1.00	0.500	0.500	74.9	74.4	311.6
1.00	0.474	0.500	75.0	75.5	170.0
1.01	0.450	0.500	75.1	77.1	40.7
1.00	0.440	0.500	–	77.2	–
1.49	0.501	0.501	75.1	104.4	376.2
1.50	0.475	0.499	75.1	105.1	281.1
1.50	0.450	0.500	75.0	105.2	208.3
1.50	0.397	0.500	–	107.4	–
1.99	0.501	0.500	74.8	127.9	404.1
2.00	0.474	0.501	75.1	128.3	324.6
2.00	0.449	0.500	75.0	128.7	264.4
2.00	0.400	0.499	74.9	128.9	141.8
2.00	0.358	0.500	–	130.3	–
3.00	0.500	0.501	74.8	170.6	457.6
3.00	0.475	0.501	74.9	170.8	418.4
3.00	0.449	0.501	75.0	171.0	373.4
3.00	0.400	0.500	75.0	171.2	273.3
3.00	0.349	0.501	75.0	170.9	161.6
3.00	0.299	0.500	75.0	171.5	27.8
3.00	0.282	0.501	–	174.5	–
4.00	0.500	0.501	75.1	218.6	507.5
4.00	0.476	0.500	75.0	219.2	480.0
4.00	0.450	0.500	75.2	218.7	437.4
4.00	0.400	0.501	74.9	218.7	350.8
4.00	0.350	0.500	74.9	218.6	262.6
4.00	0.300	0.499	75.0	218.6	177.3
4.00	0.250	0.501	74.8	218.5	67.4
4.01	0.208	0.500	–	223.4	–
5.00	0.498	0.500	74.9	265.2	535.9
5.00	0.476	0.499	75.1	265.1	502.9
5.00	0.450	0.499	75.1	265.0	469.1
5.00	0.399	0.500	75.0	264.9	393.7
5.00	0.350	0.500	75.0	265.1	318.3
5.00	0.300	0.499	75.1	265.9	246.9
5.00	0.250	0.499	75.1	266.2	178.2
5.00	0.201	0.499	75.0	265.3	101.6
5.00	0.150	0.501	74.9	267.8	10.3
5.00	0.142	0.499	–	268.2	–
6.00	0.498	0.501	75.0	313.9	556.2
6.00	0.475	0.500	75.1	314.2	527.0
6.00	0.449	0.501	75.1	314.2	495.9
6.00	0.399	0.500	75.1	314.6	438.8
6.00	0.350	0.501	74.9	314.5	379.5
6.00	0.301	0.500	74.9	314.4	318.2
6.00	0.251	0.500	74.9	314.5	249.5
6.00	0.201	0.501	75.1	314.6	186.0
6.00	0.149	0.499	75.0	314.6	113.0
6.00	0.101	0.501	75.1	317.6	28.5
6.00	0.077	0.500	–	318.6	–

REFERENCES

[1] de Bruijn FA, Dam VAT, Janssen GJM. Review: durability and degradation issues of PEM fuel cell components. Fuel Cells 2008;8:3–22.

[2] Karimäki H, Keränen T, Koski P, Pulkkinen V, Kotisaari M, Ihonen J, et al. A 50kW PEMFC system durability study at industrial site operated with industry grade hydrogen, Manuscript in preparation.

[3] Brunner DA, Marcks S, Bajpai M, Prasad AK, Advani SG. Design and characterization of an electronically controlled variable flow rate ejector for fuel cell applications. Int J Hydrogen Energy 2012;37:4457–66.

[4] He J, Choe SY, Hong CO. Analysis and control of a hybrid fuel delivery system for a polymer electrolyte membrane fuel cell. J Power Sources 2008;185:973–84.

[5] Zhu Y, Li Y. New theoretical model for convergent nozzle ejector in the proton exchange membrane fuel cell system. J Power Sources 2009;191:510–9.

[6] Green DW, Perry RH. Perry's chemical engineers' handbook. 2008.

[7] Hosseinzadeh E, Rokni M, Jabbari M, Mortensen H. Numerical analysis of transport phenomena for designing of ejector in PEM forklift system. Int J Hydrogen Energy 2014;39:6664–74.

[8] Kim M, Sohn Y, Cho C, Lee W, Kim C. Customized design for the ejector to recirculate a humidified hydrogen fuel in a submarine PEMFC. J Power Sources 2008;176:529–33.

[9] Dadvar M, Afshari E. Analysis of design parameters in anodic recirculation system based on ejector technology for PEM fuel cells: a new approach in designing. Int J Hydrogen Energy 2014;39:12061–73.

[10] Hwang J, Cho C, Wu W, Chiu C, Chiu K, Lin C. Numerical and experimental investigation into passive hydrogen recovery scheme using vacuum ejector. J Power Sources 2015;275:539–46.

[11] Maghsoodi A, Afshari E, Ahmadikia H. Optimization of geometric parameters for design a high-performance ejector in the proton exchange membrane fuel cell system using artificial neural network and genetic algorithm. Appl Therm Eng 2014;71:410–8.

[12] Smolka J, Bulinski Z, Fic A, Nowak AJ, Banasiak K, Hafner A. A computational model of a transcritical R744 ejector based on a homogeneous real fluid approach. Appl Math Model 2013;37:1208–24.

[13] Mazzelli F, Little AB, Garimella S, Bartosiewicz Y. Computational and experimental analysis of supersonic air ejector: turbulence modeling and assessment of 3D effects. Int J Heat Fluid Fl 2015;56:305–16.

[14] Bartosiewicz Y, Aidoun Z, Desevaux P, Mercadier Y. Numerical and experimental investigations on supersonic ejectors. Int J Heat Fluid Fl 2005;26:56–70.

[15] Croquer S, Poncet S, Aidoun Z. Turbulence modeling of a single-phase R134a supersonic ejector. Part 1: numerical benchmark. Int J Refrig 2016;61:140–52.

[16] Thermodynamics Research Center, NIST Boulder Laboratories, M. Frenkel director, "Thermodynamics Source Database", in: P.J. Linstrom and W.G. Mallard (Ed.), NIST Chemistry WebBook, NIST Standard Reference Database Number 69, National Institute of Standards and Technology, Gaithersburg MD, 20899, http://webbook.nist.gov, (retrieved February 5, 2016).

[17] McGovern RK, Prakash Narayan G, Lienhard V JH. Analysis of reversible ejectors and definition of an ejector efficiency. Int J Therm Sci 2012;54:153–66.

[18] Moran MJ, Shapiro HN. Fundamentals of engineering thermodynamics. 5th ed. John Wiley & Sons, Inc; 2006.

[19] Fluent 16.0 theory guide. ANSYS, Inc; 2014.

[20] Fluent 16.0 user's guide. ANSYS, Inc; 2014.

[21] Woolley HW, Scott RB, Brickwedde FG. Compilation of thermal properties of hydrogen in its various isotopic and ortho-para modifications. J Res Natl Bur Stand 1948;41:379–475.

[22] Jacobsen RT, Stewart RB. Thermodynamic properties of nitrogen including liquid and vapor phases from 63 K to 2000 K with pressures to 10,000 bar. J Phys Chem Ref Data 1973;2:757–922.

[23] Friedman AS, Haar L. High-speed machine computation of ideal gas thermodynamic functions. I. Isotopic water molecules. J Chem Phys 1954;22:2051–8.

[24] Fuller EN, Schettler PD, Giddings JC. A new method for prediction of binary gas-phase diffusion coefficients. Ind Eng Chem 1966;58:19–27.

[25] Wilke CR. A viscosity equation for gas mixtures. J Chem Phys 1950;18:517–9.

[26] Design Institute for Physical Properties, Sponsored by AIChE, DIPPR Project 801-Full Version. Design Institute for Physical Property Research/AIChE. Online version available at: http://app.knovel.com/hotlink/toc/id:kpDIPPRPF7/dippr-project-801-full/dippr-project-801-full.

[27] Lindsay AL, Bromley LA. Thermal conductivity of gas mixtures. Ind Eng Chem 1950;42:1508–11.

V

K. Nikiforow, P. Koski, J. Ihonen, Discrete ejector control solution design, characterization, and verification in a 5 kW PEMFC system, Int. J. Hydrogen Energy. 42 (2017) 16760–16772. doi:10.1016/j.ijhydene.2017.05.151.

Available online at www.sciencedirect.com

ScienceDirect

journal homepage: www.elsevier.com/locate/he

Discrete ejector control solution design, characterization, and verification in a 5 kW PEMFC system

K. Nikiforow[*], *P. Koski*, *J. Ihonen*

VTT Technical Research Centre of Finland, P.O. Box 1000, VTT, 02044 Finland

ARTICLE INFO

Article history:
Received 24 March 2017
Received in revised form
18 May 2017
Accepted 20 May 2017
Available online 10 June 2017

Keywords:
PEMFC
Anode gas recirculation
Ejector
Ejector control
Inert build-up
Power ramp-up

ABSTRACT

An ejector primary gas flow control solution based on three solenoid valves is designed, implemented and tested in a 5 kW proton exchange membrane fuel cell (PEMFC) system with ejector-based anode gas recirculation. The robust and cost effective combination of the tested flow control method and a single ejector is shown to achieve adequate anode gas recirculation rate on a wide PEMFC load range.

In addition, the effect of anode gas inert content on ejector performance in the 5 kW PEMFC system is studied at varying load and anode pressure levels. Results show that increasing the inert content increases recirculated anode gas mass flow rate but decreases both the molar flow rate and the anode inlet humidity.

Finally, the PEMFC power ramp-rate limitations are studied using two fuel supply strategies: 1) advancing fuel supply and venting out extra fuel and 2) not advancing fuel supply but instead using a large anode volume. Results indicate that the power of the present PEMFC system can be ramped from 1 kW to 4.2 kW within few hundred milliseconds using either of these strategies.

Introduction

In proton exchange membrane fuel cell (PEMFC) systems, anode gas recirculation is typically applied for humidification of the otherwise dry anode inlet gas. Another important benefit of anode gas recirculation is the increased linear gas velocity inside the stack, which prevents liquid water build-up and blockage of catalyst sites [1,2]. Flooding of anode channels can cause local fuel starvation leading to reverse current decay conditions, which are detrimental for the cathode catalyst carbon support [3,4].

When anode gas recirculation is applied, impurities and inert gases accumulate in the anode gas recirculation loop, especially with high fuel utilization [5–7]. The limiting impurity is typically nitrogen, and the rate of accumulation is dependent on fuel cell membrane nitrogen permeability, nitrogen concentration in the hydrogen fuel, and anode gas purge rate [5]. The nitrogen content in the anode recirculation can reach tens of per cents [5,8]. This high nitrogen content should be taken into account in design and operation of anode gas recirculation systems.

Anode gas recirculation is achieved either with a mechanical pump or with an ejector. Recently ejectors have received an increasing attention because their durability, cost,

* *Corresponding author.*
E-mail address: kaj.nikiforow@vtt.fi (K. Nikiforow).
http://dx.doi.org/10.1016/j.ijhydene.2017.05.151

and energy efficiency are superior compared to mechanical pumps. A major challenge with ejectors is, however, their sizing to achieve sufficient performance over the entire PEMFC power range [9].

Another challenge with ejectors is the primary gas inflow (or equivalently the primary gas pressure) control which is required to match the fuel supply and the fuel consumption rates. Despite the several PEMFC- and ejector-related studies conducted in the recent years [9–23], studies addressing the practical implementation of an ejector-primary-gas-control-system (EPC) are scarce. Nonetheless, a range of possible EPCs exists. One option is to employ a mass flow or pressure controller. They are available for several flow rate ranges and provide accurate control over wide range. However, the price of a mass flow or pressure controller compared to an ejector is high.

One EPC not requiring active control is to use a dome loaded pressure regulator with an external pressure sensing port. The essential difference to a common dome loaded pressure regulator is that the primary inlet pressure of the ejector is controlled via its outlet pressure. This type of regulators have been used by Vasquez et al. [10] and Lyndon [15] without any reported problems. Unfortunately, a distributor for this type of regulators was not found in the current work.

The alternative to the passive control approach is an active EPC. Brunner et al. [17] developed a variable flow ejector where a mobile needle varies the primary nozzle flow area. Besides being able to vary the primary flow rate, this approach also maintains high primary gas velocity in the nozzle at low primary gas flow rates, which results in better ejector performance. Brunner et al. successfully demonstrated this control approach in an operational bus. However, the need for moving parts at elevated pressures and the requirement of high needle precision raise questions about the durability, safety, and price of the system.

A verified and a less expensive EPC is to employ a proportional valve. Kim et al. [13] and Hwang et al. [21] employed a proportional valve for controlling the primary gas flow rate of the ejector in their test setup. Hwang [18] employed a proportional valve and a solenoid valve in parallel. They covered the moderate and high primary gas flow rates with the proportional valve. At low primary gas flow rates, the ejector performance dropped and the solenoid valve was employed in pulsating mode. This approach was demonstrated to work well although, judging from the results, with relatively large anode volume.

In stationary applications, there is typically no need to cover the complete fuel cell power range in a continuous manner when sizing the fuel cell stack properly or if hybridizing the system with a battery or a supercapacitor. Instead, being able to operate at specific discrete load levels is often sufficient. A few properly sized solenoid valves can function as a discrete EPC at very low cost and with minimum moving parts.

One important application for PEMFCs is backup power. A characteristic requirement in these applications is a fast response to the increased power demand. The discrete EPC lacks any intermediate states between two set points and provides, therefore, flow control with ultimate speed and accuracy. In large back-up applications, the level of battery hybridization should be kept minimal for reducing costs. A PEMFC system with sufficient fast power ramp-up capability can reduce or even eliminate the need of battery hybridization.

The concept of discrete EPC is studied in this work. Design and sizing considerations of the flow control approach are addressed. The EPC is tested with a custom-made ejector [24] mounted into a 5 kW PEMFC system, with the design aimed for commercial operation in back-up applications. Both the ejector performance and the system performance are verified. In addition, the effect of anode gas inert content on ejector performance is studied by operating the system with long anode purge intervals. Finally, the dynamic limitations of the discrete EPC- and ejector-based fuel supply system are investigated under rapid PEMFC power ramp-ups both with and without an advance in fuel supply.

Experimental

Fuel cell system

Fig. 1 shows the schematic of the PEMFC system used in this study. A 50-cell S2 stack by PowerCell Sweden AB with a maximum power output of ca 5 kW is employed. Similar unpressurized systems were built in our previous studies [25,8] with the major difference that a mechanical anode gas recirculation pump was used instead of the ejector employed in the present system. The current PEMFC system design and the components selected are intended for commercial production, excluding the cathode blower, to be replaced with DC version. In addition, in commercial system, the majority of the sensors can be omitted. Table 1 lists the main components of the present system.

Fuel supply

The ejector (*E*) is custom-made and its design and characterization is described in a previous paper [24], while the EPC is described in Section Ejector primary gas flow control Hydrogen is supplied to the EPC through a pressure reducer (*PR*, reduces pressure to ca 9 barg), an excess flow valve (*EV*), and an inline filter (*FL*). The hydrogen flow rate is measured (*FT*, Bronkhorst HI-TEC F-112AC) upstream of the EPC. Downstream of the ejector and upstream of the stack, there is a pipe-branch leading to a burst disc (*BD*), a pressure relief valve (*RV*), and the extra volume. The purpose of the extra volume is to slow down possible changes in the anode pressure and it can be fluidly connected or disconnected with a manual valve (*MV*). The stack outlet gas passes a custom-made water separator (*S*, to remove liquid water) before entering the ejector secondary inlet. The purge valve (*SV*), connected to the water separator, is opened intermittently in order to remove liquid water and inert gases accumulated in the anode compartment. The measurement of pressure, temperature, humidity, and hydrogen concentration enables the determination of anode gas recirculation rate and inert gas content. The continuous measurement of pressure is also needed for safety reasons. Fig. 2 shows photos of the EPC, the ejector, and the complete PEMFC system.

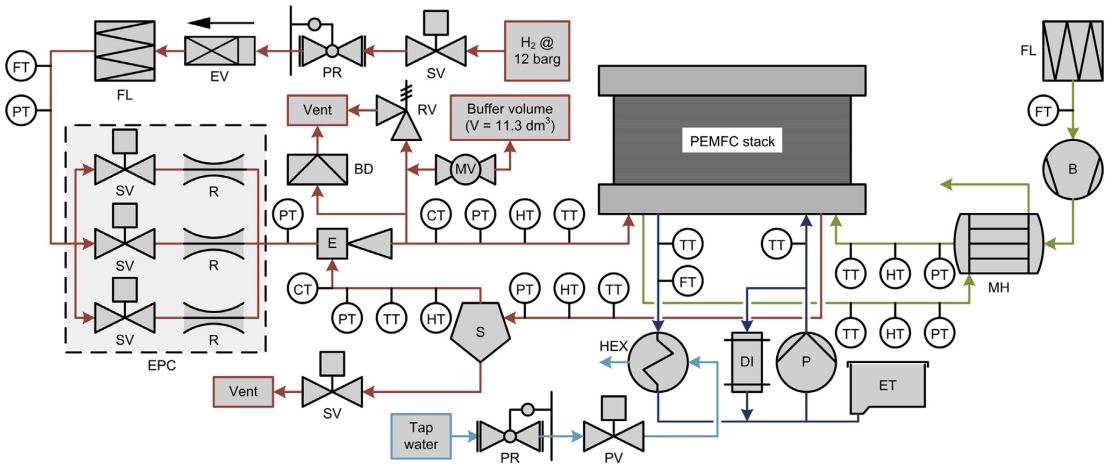

Fig. 1 – PEMFC system scheme. B: air blower, BD: burst disc, CT: H_2 concentration transmitter, DI: de-ionization filter, E: ejector, EPC: ejector primary gas control system, ET: expansion tank, EV: excess flow valve, FL: particle filter, FT: flow transmitter, HEX: heat exchanger, HT: humidity transmitter, MH: membrane humidifier,MV: manual valve, P: coolant pump, PR: pressure reducer, PT: gauge pressure transmitter, PV: proportional valve, R: flow restriction, RV: relief valve, S: water separator, SV: solenoid valve, TT: temperature transmitter.

Table 1 – PEMFC system main components.

Component	Manufacturer	Model
PEMFC stack	PowerCell Sweden AB	S2/50 cells
Ejector	Custom-made	
Air blower	Ametek DFS	Windjammer 230 VAC
Air humidifier	Perma Pure LLC	FC300-1600-10HP
Coolant pump	EMP, Inc.	WP29
Coolant de-ionizing filter	SpectraPure, Inc	DI-MBHT-RT3-10L-25
Coolant heat exchanger	SWEP International AB	B5Hx20/1P-SC-S

Air supply

On the cathode side, air is supplied to the fuel cell stack with a blower (*B*) and humidified with a membrane humidifier (*MH*). The temperatures, humidities, and pressures are measured both at the cathode inlet and outlet. The flow rate of dry air is measured (*FT*) upstream of the blower.

Cooling system

The cooling system consists of a controllable recirculation pump (*P*), a high temperature de-ionization filter (*DI*), and a liquid-to-liquid heat exchanger (*HEX*). The flow rate of tap water on the cold side of the heat exchanger is controlled with

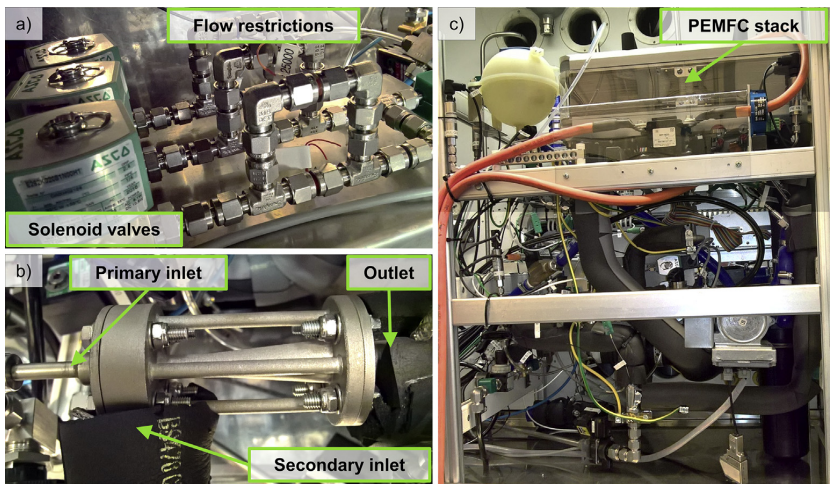

Fig. 2 – The PEMFC system assembled onto a rack. a) The EPC, b) the ejector, and c) the complete PEMFC system (the EPC, the ejector, and the air blower are located behind other components).

a proportional valve (PV) placed downstream of a pressure reducer (PR). The stack inlet and outlet temperatures as well as the stack outlet coolant flow rate are measured.

Control system

In systems employing ejectors, a proper control system is crucial because a failure in the control routine can at worst result in a pressure increase rate of several bars per second and, ultimately, in severe system damage and danger for other materials and personnel. In the current system, control and data acquisition is accomplished with National Instruments CompactRIO hardware which is programmed with Labview software.

The minimum data sampling interval with this system is 1 ms (max 1000 Hz) according to the manufacturer. However, due to CPU limitations and considerably slower response times of most transmitters and actuators, the minimum data sampling interval applied in this study is 50 ms (20 Hz). With optimized software, faster data sampling is possible.

The control software routines run at different speeds depending on their priority. For example, the fastest routine, the safety routine, run at 10 ms (100 Hz) loop interval. For reference, the response time (10–90%) of pressure transmitters, which are the most important transmitters monitored in the safety routine, is 5 ms according to the manufacturer (First Sensor AG).

The EPC studied in the current work requires fast and almost simultaneous control of four solenoid valves – three fuel supply control valves and one anode purge valve. Initially the valves were controlled with electromechanical relays. However, this approach was observed to cause overcurrent fault in the control hardware when frequently switching the valves. Replacing the electromechanical relays with solid-state relays solved this problem and made the valve control more reliable.

Ejector primary gas flow control

Principle

The principle of EPC studied in this work is as follows. The fuel supply line, delivering fuel to the fuel cell system at constant pressure, is split into a number of branches (in this case three, see Fig. 3). Each branch has a 2/2 solenoid valve (Asco 262-series) for controlling the flow through that branch in on/off manner. Downstream from each of the control valves, there is a static flow restriction (Lee Ihm RIGF5553-series restrictor) that is sized to pass a specified fuel flow rate. In the present case, each of the flow restrictions consist of two parallel restrictors to enable an accurate fuel flow rate with the fixed restrictor sizes available. In larger PEMFC systems, properly sized control valves can restrict the fuel flow rate and, thus, no additional restrictors are necessarily needed. Downstream of the restrictions, the three branches are combined and connected to the ejector primary inlet.

The number of possible PEMFC stack current load levels ($N_{load\ levels}$) achievable with the discrete EPC depends on the number of branches ($N_{branches}$) into which the fuel supply is split as follows:

$$N_{load\ levels} = 2 \wedge N_{branches} - 1 \tag{1}$$

Thus, adding more branches rapidly increases the number of achievable load levels, however, at the expense of added cost. The three branches in the present setup result in 7 load levels, which is regarded to be enough for most stationary applications. The price for the 3-branch setup presented here is approximately 900 € of which 3 × 90 € = 270 € is for the valves and less than 33 € is for the six restrictors used, with the rest amounting from pipe fittings. With careful design, the price could be considerably lowered.

Flow restrictor sizing

The flow rate through a restrictor ($\dot{V}$) can be calculated with the widely used valve and restrictor sizing equations, which in their general form can be written as follows [26,27]:

$$\text{Subcritical flow}\left(p_{r,in} < 1.9 \cdot p_{r,out}\right): \quad \dot{V} = C \cdot 2 \cdot \left\{\left(p_{r,in} - p_{r,out}\right) \cdot p_{r,out} \Big/ T_{r,in}\right\} \wedge (1/2) \tag{2}$$

$$\text{Critical flow}\left(p_{r,in} \geq 1.9 \cdot p_{r,out}\right): \quad \dot{V} = C \cdot p_{r,in} \Big/ T_{r,in} \wedge (1/2) \tag{3}$$

where the constant C accounts for the restrictor characteristics (orifice size, flow resistance, K_v-value), the gas properties, as well as the conversion factors to desired units of flow rate. $p_{r,in}$ is the restrictor (absolute) inlet pressure, $p_{r,out}$ is the restrictor (absolute) outlet pressure (i.e. the ejector primary pressure), and $T_{r,in}$ is the restrictor inlet (absolute) temperature.

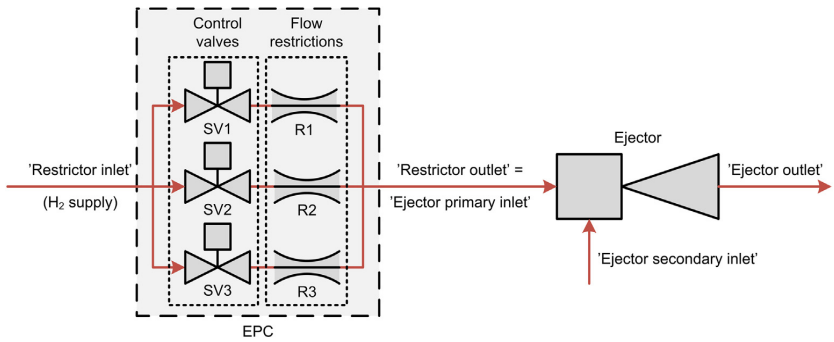

Fig. 3 – Principle of the discrete EPC.

To achieve discrete load current levels spread evenly over the current range, one should size the flow restrictions as follows:

1) choose a high enough fuel supply pressure, i.e. restrictor inlet pressure $p_{r,in}$ (will be clarified below)
2) choose a stack current increment (ΔI_{stack}) between two load levels (the maximum achievable stack current is $I_{stack,max} = N_{load\ levels} \cdot \Delta I_{stack}$)
3) size the smallest restrictor to pass a flow rate corresponding to ΔI_{stack} (given the $p_{r,in}$)
4) size each of the remaining restrictors to pass a flow rate twice that of the previous restrictor

This approach spreads the load current levels evenly over the range only if the flow through the restrictors remains critical at every operating point. This condition is met when $p_{r,in} \geq 1.9 \cdot p_{r,out}$ at the maximum load current level. For example, to operate the present system at 200 A stack current, the ejector should be supplied with approximately 8 barg (≈9 bara) primary pressure. Hence, the required restrictor inlet pressure for critical flow would be approximately 16 barg (≈1.9·9 bara).

If the flow in the restrictions becomes subcritical, the achieved current increment decreases. In the present study, we use a restrictor inlet pressure of $p_{r,in} \approx 9$ barg and restriction sizing that results in current increments of $\Delta I_{stack} = 27–29$ A in the low end of the stack current range. Table 2 lists the load current levels achieved with this approach during a system test. Starting from the load level 5, when the restrictor outlet (i.e. ejector inlet) pressure exceeds 4.2 barg (=9 barg divide by 1.9), the flow in the restrictor becomes subcritical and the current increment starts to decrease. The last current increment is only 14 A, i.e. roughly half of initial current increment.

The adopted stack current on each load level depends on the restrictor inlet pressure and the anode pressure control approach. Therefore, the load current levels vary between measurements and those listed in Table 2 do not hold for all measurements presented in this paper. The variation in current level is, however, in practice limited to a few amps.

Table 2 – Measured 50-cell stack load current levels achieved with the current fuel supply system operated at 8.5 to 8.7 barg restrictor inlet pressure and 0.05 to 0.1 barg anode pressure.

Load level [#]	Control valve open	$p_{r,in}$ [barg]	$p_{r,out}$ (=$p_{p,in}$) [barg]	I_{stack} [A]	ΔI_{stack} [A]
0	–	8.7	–	0	–
1	1	8.6	0.5[a]	29[a]	29
2	2	8.6	1.6	56	28
3	1, 2	8.5	2.8	83	27
4	3	8.5	4.0	111	27
5	1, 3	8.5[b]	5.0	133	22
6	2, 3	8.5[b]	5.7	149	16
7	1, 2, 3	8.5[b]	6.3	162	14

[a] Flow in ejector primary nozzle is subcritical, i.e. the primary flow rate (and achievable stack current) depends on both ejector primary and outlet pressure.
[b] Flow in restrictors is subcritical, i.e. the current step increment size is decreasing.

Anode pressure management

In order to maintain constant anode pressure during operation, the fuel consumption rate must match with the fuel supply rate. In ejector-based systems, the fuel supply rate depends mainly on ejector primary pressure and is almost independent of anode pressure level. Therefore, active control of ejector primary pressure is needed.

In the present system, where anode volume is roughly 1.5 dm^3, for example a 10 A mismatch in fuel supply and consumption rates leads to approximately 40 mbar/s pressure change rate. Thus, actions on mismatched fuel supply rate must be taken typically within seconds. With increasing mismatch between fuel consumption rate and supply rate (e.g. during load changes), the rate of pressure change can be notably higher and actions must be taken within a fraction of a second. A way to limit the pressure change rate is to increase the anode volume. This approach was employed during the initial system testing (see Fig. 1).

Exact match between the fuel consumption and the supply rates is difficult to achieve at all times despite the almost fixed flow rate achieved with the EPC presented in the this study. Reasons for this include load changes, intermittent anode purges, and small variation in fuel feed pressure (e.g. due to varying temperature). When there is a mismatch between the fuel consumption and the supply rate, there are three alternative control measures for maintaining a constant anode pressure in the current system: 1) vent out excessive fuel by periodic or intermittent purges, 2) vary fuel consumption rate, or 3) a hybrid of the first two. The first two approaches have been used in this work.

The first control measure obviously requires that fuel is supplied in excess. In that case, a pressure triggered purge or continuous (and controlled) bleed can be applied. This approach maintains a constant current load but consumes some excess fuel, thus lowering the fuel efficiency. However, the impact of this approach on fuel efficiency can be small, as inert gas removal by purges is needed in any case.

The second approach to prevent excessive pressure change relies on varying the fuel consumption rate. This means in practice that the stack current is varied to maintain approximately constant anode inlet pressure. This approach results in good fuel efficiency and is especially suited for hybridized fuel cell systems. However, constantly changing the load current might be problematic or even impossible in some applications.

During a load change, both the fuel supply and consumption rate vary rapidly, especially if the load change is large. Therefore, there is a risk of fuel starvation and over- or under-pressurizing the anode. A safe control measure is to let the flow rates develop by venting the excess hydrogen through the purge valve prior to the load increase. During a load decrease, one would proceed in the reverse order. If venting extra hydrogen during the load change is not an option, the timing of control valve and load control becomes critical. Large load changes both with and without an associated anode purge are tested in this work.

Measurements

The following measurements are conducted with the system:

1) polarization curve measurement to characterize the system,
2) inert build-up measurements to study the effect of anode gas inert content on ejector performance, and
3) load ramp-up measurements to investigate the dynamic limitations mainly in fuel supply but also in air supply.

The inert build-up measurements are conducted both varying the stack load current and varying the anode inlet pressure. The load ramp-up measurements are repeated both with and without the extra anode volume. Table 3 lists the parameters used in the measurements. In all measurements, the coolant pump is operated at constant power that resulted in a roughly 20 L per minute (lpm) flow rate and the coolant temperature at stack inlet is maintained at 70 °C. The heaters, applied for preventing condensation in the anode and cathode piping, are set to 75 °C temperatures.

The polarization curve measurements are conducted according to parameters and the load level list shown in Table 3. First, operation is initiated at load level 4 where the system is allowed to stabilize for more than 30 min. After this, the load level is ramped stepwise up to load level 7, down to load level 0, and again back to load level 4. Each step is maintained for 15 min (15 anode purge and air pulse cycles) and the results are calculated as time-averaged values from the last three purge cycles (=3 min). An exception is the load level 0 that is maintained less than 5 min and time-averaged results are calculated from a time period of 50 s. Ramping the polarization curve both upwards and downwards allows comparison between these two.

The inert build-up measurements are conducted to investigate how the inert gas (mainly nitrogen) concentration in the recirculated anode gas affects the ejector performance. To allow inert gas accumulation, the system is operated at a constant load and at constant anode pressure with long (5–7 min) purge cycles or until the weakest cell voltage deviated more than a threshold value from the average cell voltage (whichever comes first). Air pulses are performed periodically in a similar fashion as in the polarization curve measurements. In the beginning of each purge cycle, an excessively long anode purge (10 s) is performed to remove all the inert gases. The experiments are conducted both at constant load (level 4) and varying anode inlet pressure (20, 60, and 150 mbarg) and with constant anode inlet pressure (60 mbarg) and varying the load level (1, 4, and 7).

The transient tests are conducted to investigate the limitations of rapidly increasing stack load. In backup power applications, the PEMFC system ramp rate limitations needs to be compensated by energy storage and, in a vehicle application, by limiting the current by traction motor controller.

The transient tests are conducted by first operating the system at load level 1. When a power increase request is registered, one of the procedures listed in Table 4 is applied. First, the air blower control is changed and the blower is given 2 s to ramp up. The control of fuel supply depends on the procedure employed. Two different approaches are tested.

In the first approach, the system is operated without the extra anode volume. In this case, the fuel supply reacts on a power request as follows:

1) wait for some time (0 s, 1 s, or 1.5 s),
2) open the purge valve and apply the correct combination of control valves,
3) wait for some time ($\Delta t_{fuel,adv}$: 2 s, 1 s, or 0.5 s), and
4) close purge valve and apply the new current load.

The last step is synchronized with the 2 s ramp up time given for the air blower so that the load increase (which takes few milliseconds) always occurs 2 s after the power increase request. The drawback of this approach is extra fuel consumption as well as depressurizing anode side, which may lead to high differential pressure between the anode and cathode.

In the other fuel supply control strategy, extra anode volume is employed but the anode purge valve is kept closed during the load change procedure. In this case, the correct combination of control valves is applied simultaneously with increasing the load. The load change still occurs 2 s after the initial request because of the time needed to ramp up the air

Table 3 – Parameters employed during experiments.

Parameter	Polarization curve	Inert build-up		Load ramp-up	
Anode pressure control strategy	Periodic purges	Manual load control	Automatic load control	Automatic load control	Automatic load control
Anode pressure [mbarg]	0–170	20 (±7) 60 (±5) 150 (±13)	60 (±1.1)	60	60
Anode purge length [s]	0.5	10	10	0.5	0.5
Anode purge interval [min]	1	5–7 (max.)	5–7 (max.)	1	1
Air stoichiometry [–]	2	2	2	2.5	2.5
Air pulse length [s]	2	2	2	–	–
Air pulse interval [min]	1	1	1	–	–
Extra anode volume employed	Yes	Yes	Yes	No	Yes
Data acquisition interval [s]	1	1	1	0.05	0.05
Load levels [#]	4, 5, 6, 7, 6, 5, 4, 3, 2, 1, 0, 1, 2, 3, 4	4	1, 4, 7	1→7	1→7

Table 4 – Load increase procedure with and without advance in fuel supply.

Time elapsed from load request [s]	Advance in fuel supply ($\Delta t_{fuel,adv}$) [s]			
	2	1	0.5	0
0	1 Change blower ctrl 2 Open purge valve 3 Apply new control valve combination	1 Change blower ctrl	1 Change blower ctrl	1 Change blower ctrl
1	–	2 Open purge valve 3 Apply new control valve combination	–	–
1.5	–	–	2 Open purge valve 3 Apply new control valve combination	–
2	4 Close purge valve 5 Apply load change	4 Close purge valve 5 Apply load change	4 Close purge valve 5 Apply load change	2 Apply new control valve combination 3 Apply load change

blower. The drawback of this approach is a large anode volume, which may lead to additional degradation during a start-up as the degradation is dependent on the gas exchange time [28].

Results and discussion

System characterization

Fig. 4 shows the results as mean values of the upward and the downward polarization curves and the variation between these as error bars. Only the variation of dew point temperatures is notable. The dew point temperatures (T_{dew} [°C]) are calculated as in Ref. [24]. Table 5 lists the variation in time-averaged operating conditions during polarization curve measurements.

The measured stack polarization curve is almost identical with the reference from stack manufacturer (see Fig. 4a) despite the relatively dry operating conditions (see Fig. 4c). The dry operating conditions are assumed to result from inadequate isolation of the air tubes between the stack and the air humidifier.

The efficiencies shown in Fig. 4b are calculated as follows:

$$\eta_{stack} = E_{cell,avg}/E^0_{LHV} \tag{4}$$

$$\eta_{fuel} = \dot{n}_{h,consumed}/\dot{n}_{h,supplied} = N_{cells}\cdot I_{stack}/(2\cdot F\cdot \dot{n}_{h,supplied}) \tag{5}$$

$$\eta_{system} = P_{system,net}/P_{stack} = (P_{stack} - P_{BoP})/P_{stack} \tag{6}$$

$$\eta_{total} = \eta_{stack}\cdot\eta_{fuel}\cdot\eta_{system} = P_{system,net}/(LHV_h\cdot\dot{n}_{h,supplied}) \tag{7}$$

The stack efficiency is calculated relative to the lower heating value of hydrogen (LHV_h = 241.8 kJ/mol [29]) at standard conditions (25 °C, 1.01325 bar):

$$E^0_{LHV} = LHV_h/(2\cdot F) = 1.253\ V \tag{8}$$

The fuel efficiency is the ratio of the fuel consumption rate (i.e. stack current) to the fuel supply rate. The fuel efficiency is quite low at the lowest load levels because of non-optimized purge cycle but reaches normal level (~99%) at load level 4 (131 A) and above. The system efficiency is the ratio of the system (net) power output to the stack (gross) power. The balance of plant (BoP) power consumption is measured with hall sensors. The total efficiency is the product of stack efficiency, fuel efficiency, and system efficiency.

The measured system total efficiency for stack current levels from 25 A to 160 A varies between 37.3% and 43.8%. For a small back-up system, this total efficiency is acceptable, taking into account the possibility to improve efficiency at low load by decreasing the purge rate.

The maximum total efficiency of 43.8% is achieved at load level 3 (82 A). Fig. 5 shows the energy distribution of the fuel supplied to the system at this load level. The BoP consumes 9.7% of the fuel energy and 2.1% of fuel is lost in anode purges. The air blower consumes the majority of BoP power, accounting for 5.1% of the fuel energy content at this operating point. With optimized air blower control, anode purge cycle, and coolant pump control (which is held constant), and without line heaters (which are needed mainly for humidity measurements), the total system efficiency could be notably improved.

Ejector performance

Steady state performance

The anode gas recirculation rate is calculated from the ejector water balance. The flow rate of the practically dry primary gas and the humidities of both the ejector secondary inlet and the ejector outlet are measured. The ejector secondary gas molar flow rate ($n_{s,in}$) can then be computed from the ejector primary gas molar flow rate ($n_{p,in}$) and the water mole fractions at ejector secondary inlet ($x_{w,s,in}$) and ejector outlet (i.e. stack anode inlet, $x_{w,an,in}$), as follows:

$$\dot{n}_{s,in} = \dot{n}_{p,in}\cdot x_{w,an,in}/(x_{w,s,in} - x_{w,an,in}) \tag{9}$$

When also the ejector secondary inlet hydrogen mole fraction ($x_{h,s,in}$) is measured, the recirculation rate in terms of anode inlet hydrogen stoichiometry (λ_h), fuel utilization per pass ($u_{f,pp}$), and entrainment ratio (Ω) can be computed as follows:

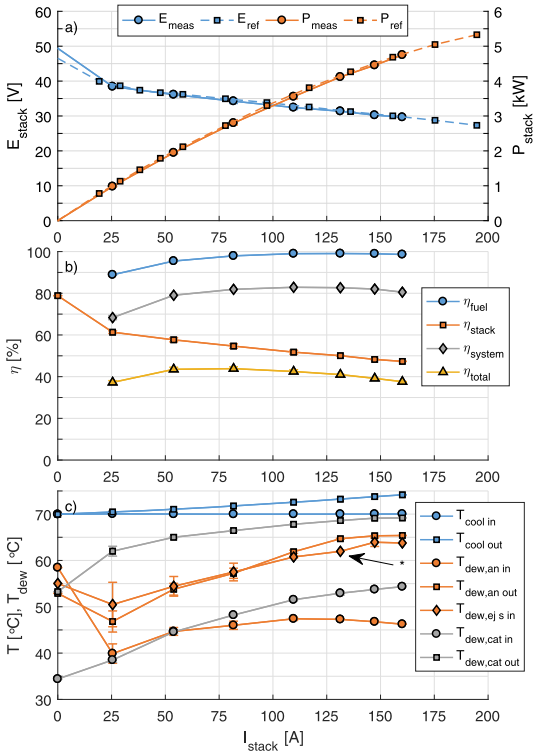

Fig. 4 – Measured time-averaged system performance and operating conditions as function of stack current (I_{stack}). a) Stack voltage (E_{stack}) polarization and power (P_{stack}). b) Efficiencies: fuel (η_{fuel}), stack (η_{stack}), system (η_{system}), and total (η_{total}). c) Operating conditions: coolant inlet and outlet temperatures ($T_{cool\ in}$, $T_{cool\ out}$), dew point temperatures at stack anode inlet ($T_{dew,an\ in}$), stack anode outlet ($T_{dew,an\ out}$), ejector secondary inlet ($T_{dew,ej\ s\ in}$), stack cathode inlet ($T_{dew,cat\ in}$), and stack cathode outlet ($T_{dew,cat\ out}$). The error bars show the variation in time-averaged values between upward and downward polarization curve measurements. *Only data from downward polarization curve is available because of humidity transmitter failure.

$$\lambda_h = \left(\dot{n}_{p,in} + \dot{n}_{s,in} \cdot x_{h,s,in}\right) / \dot{n}_{h,consumed} \tag{10}$$

$$u_{f,pp} = 100/\lambda_h \tag{11}$$

$$\Omega = \dot{m}_{s,in}/\dot{m}_{p,in} = \left(x_{h,s,in} \cdot M_h + \left(1 - x_{h,s,in} - x_{w,s,in}\right) \cdot M_n + x_{w,s,in} \cdot M_w\right)/M_h \cdot \dot{n}_{s,in}/\dot{n}_{p,in} \tag{12}$$

where M_h, M_n, and M_w are the molar weights of hydrogen, nitrogen, and water, respectively. In calculating the ejector entrainment ratio with the above equation, the anode gas is assumed to only contain hydrogen, water, and nitrogen.

Fig. 6 shows the ejector performance recorded during the polarization curve measurement. The time-averaged fuel utilization per pass ($u_{f,pp}$) varies from 40% (±7%) at 25 A stack current to 64% at 160 A stack current. Correspondingly, the time-averaged anode inlet hydrogen stoichiometry (λ_h) varies from 2.6 (±0.4) to 1.6 in the same stack current range. The anode outlet (i.e. ejector secondary inlet) gas inert mole fraction in these measurements was less than 7% on a dry basis.

Table 5 – Range of time-averaged operating conditions during polarization curve measurement.

Anode	Time-averaged value
Stack inlet dew point temperature ($T_{dew,an\ in}$)	37.8–58.5 °C
Stack outlet dew point temperature ($T_{dew,an\ out}$)	44.6–65.4 °C
Ejector secondary inlet dew point temperature ($T_{dew,ej\ s\ in}$)	45.7–64.8 °C
Stack inlet pressure ($p_{an\ in}$)	54–100 mbarg
Stack outlet pressure ($p_{an\ out}$)	40–83 mbarg
Ejector secondary inlet pressure ($p_{ej\ s\ in}$)	38–77 mbarg
Fuel utilization per pass ($u_{f,pp}$)	33–64%
Ejector entrainment ratio (Ω)	2.3–4.5
Cathode	Time-averaged value
Stack inlet dew point temperature ($T_{dew,cat\ in}$)	34.4–54.3 °C
Stack outlet dew point temperature ($T_{dew,cat\ out}$)	53.3–69.2 °C
Stack inlet pressure ($p_{cat\ in}$)	12–124 mbarg
Stack outlet pressure ($p_{cat\ out}$)	−1 to 10 mbarg
Air stoichiometry[a] (λ_{air})	1.9–3.0
Coolant	Time-averaged value
Stack inlet temperature ($T_{cool\ in}$)	70.0–70.1 °C
Stack outlet temperature ($T_{cool\ out}$)	70.0–74.2 °C
Flow rate ($\dot{V}_{cool}$)	20.6–21.0 lpm

[a] Because of periodic air pulses, the measured time-averaged air stoichiometry deviates remarkably from target value especially at low load levels. The measured time-averaged air stoichiometry between air pulses was 1.8–2.1.

The achieved recirculation rate is somewhat lower than expected based on the ejector ex-situ characterization conducted in a previous study [24]. Due to the low stack flow resistance, for which the ejector is not optimized, the ejector operates at a relatively poor exergetic efficiency over much of the range. Nonetheless, the achieved anode gas recirculation rate is above the stack manufacturer specifications ($u_{f,pp} \leq 67\%$ for $I_{stack} \geq 50$ A) over wide stack current range.

The error bars in Fig. 6, showing the variation in time-averaged values between upward and downward measurements, reveal that the variation in fuel utilization per pass and entrainment ratio increase at low load levels. One explanation for this observation is the uncertainty in humidity measurements. Another explanation is the slight variation in operating conditions between downward and upward measurements.

Effect of inert build-up

The inert gas contained in the fuel and diffusing through the stack membrane cause the concentration of inert gas to build up in the anode between purges. On one hand, the added inert concentration should improve stack performance by removing liquid water from gas channels more efficiently due to increased gas viscosity. On the other hand, the added inert

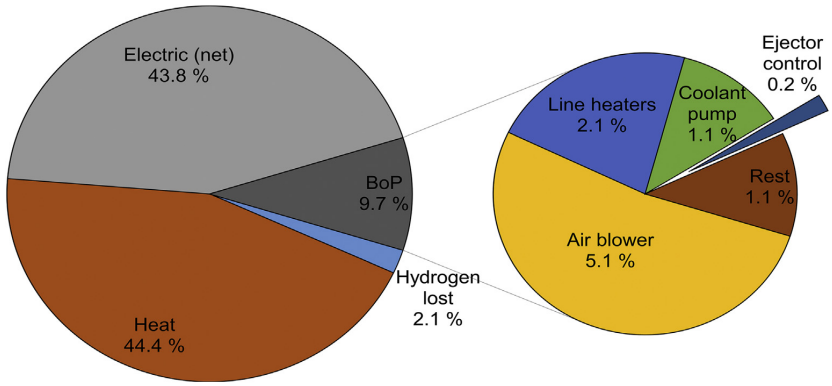

Fig. 5 – Distribution of fuel energy content (LHV_h) at system maximum efficiency point (load level 3, $I_{stack} = 82$ A).

concentration increases anode gas molar weight. Because the ejector operation is based on primary gas momentum transfer over to secondary gas, the added anode gas molar weight decreases the recirculation rate. The decreased recirculation rate is equivalent to decreased gas velocity in the stack and less efficient liquid water removal.

Fig. 7 shows the effect of inert build-up on the fuel utilization per pass, the entrainment ratio, the anode humidities, and the anode pressure drop when the system is operated with 60 mbarg anode inlet pressure and at load levels 1, 4, and 7 (I_{stack} is 27 A, 111 A, and 161 A, respectively). The ejector secondary inlet inert mole fraction on a dry basis ($x_{n,dry,s,in}$) is calculated as follows

$$x_{n,dry,s,in} = x_{n,s,in} / \left(x_{h,s,in} + x_{n,s,in}\right) = x_{n,s,in} / \left(1 - x_{w,s,in}\right) \quad (13)$$

The fuel utilization per pass increases (i.e. mole-based recirculation rate decreases) with increasing inert gas concentration because hydrogen is replaced by the heavier inert gas (Fig. 7a). On the other hand, the ejector entrainment ratio increases (i.e. mass-based recirculation rate increases) for the same reason (Fig. 7b). The effect of inert gas concentration on entrainment ratio is most pronounce at the low load level, as seen from the steepest slope in Fig. 7b. This is in line with the observation made in a previous study that ejector performance is most sensitive to conditions at low primary gas flow rates [24]. The pressure drop (Δp_{ej}) decreases slightly with increasing inert gas mole fraction (Fig. 7e) and decreasing molar recirculation rate despite the increasing mass flow rate.

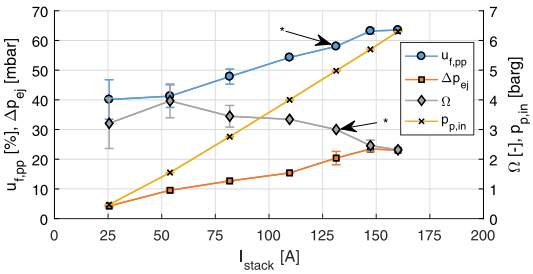

Fig. 6 – Ejector steady state performance as function of stack current: fuel utilization per pas ($u_{f,pp}$), ejector secondary gas pressure lift (Δp_{ej}), entrainment ratio (Ω), and ejector primary pressure ($p_{p,in}$). The error bars show the variation in time-averaged values between upward and downward polarization curve measurements. *Only data from downward curve is available because of humidity transmitter failure.

Fig. 7d shows that the anode inlet (i.e. ejector outlet) humidity decreases with increasing inert gas concentration because of the decreased molar recirculation rate. The change in anode inlet dew point temperature is approximately $\Delta T_{dew,ej,out} = -3$ °C at load level 1 and roughly $\Delta T_{dew,ej,out} = -2$ °C at load levels 4 and 7 for every 0.1 change in dry recirculated gas inert mole fraction ($\Delta x_{n,dry,s,in}$). By contrast, the ejector secondary inlet humidity (which is close to stack outlet humidity) changes only roughly $\Delta T_{dew,ej,s,in} = -1$ °C or less for every 0.1 change in inert dry mole fraction (Fig. 7c). Instead, the stack outlet humidity is more sensitive to the load level and increases notably with increasing load level, as could be expected. The stack inlet humidity, on the other hand, increases with load level 1 to 4 but remains roughly constant when increasing load level from 4 to 7 because of the decreased recirculation rate relative to fuel consumption rate (this is also seen in Fig. 4c).

Fig. 8 shows the effect of inert build-up on the fuel utilization per pass, the entrainment ratio, the anode humidities, and the anode pressure drop when the system is operated with 20, 60, and 150 mbarg anode pressure and at load level 4 (I_{stack} is 111 A). The anode pressure level has a notable effect on ejector performance - the higher the anode pressure level, the higher the recirculation rate both on mole- and mass-basis. The pressure drop (Δp_{ej}) is essentially independent of anode pressure level and decreases again slightly with increasing inert mole fraction.

Opposite to the effect of load level, the anode pressure level has very little or no effect on stack inlet (i.e. ejector outlet) humidity (Fig. 8d). Instead, the stack outlet (i.e. ejector secondary inlet) humidity increases a little with decreasing anode pressure level. This explains why the stack inlet humidity does not increase with increasing anode pressure even

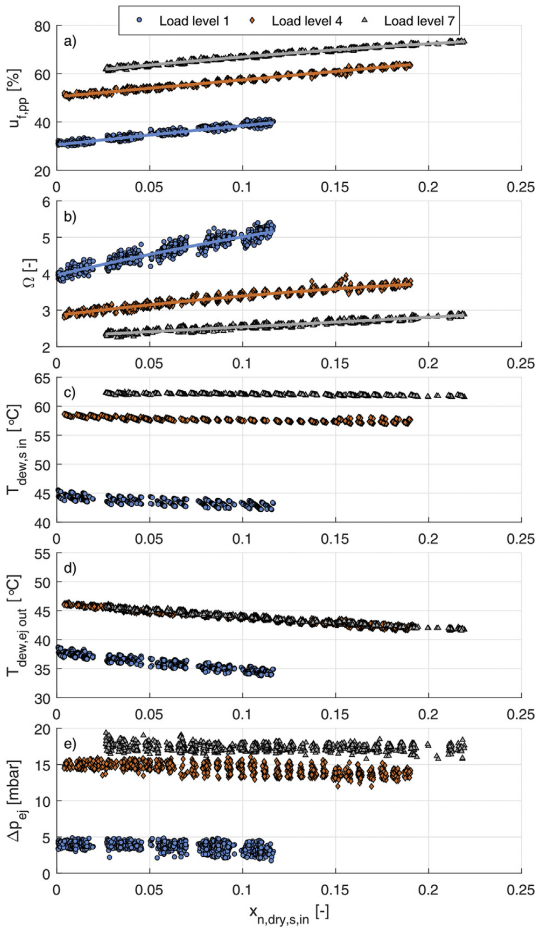

Fig. 7 – Effect of inert mole fraction on a dry basis in ejector secondary inlet gas ($x_{n,dry,s\ in}$) on a) fuel utilization per pass ($u_{f,pp}$), b) ejector entrainment ratio (Ω), c) ejector secondary inlet dew point temperature ($T_{dew,s\ in}$), d) ejector outlet dew point temperature ($T_{dew,ej,out}$), and e) ejector secondary gas pressure lift (Δp_{ej}) at load levels 1, 4, and 7 and 60 mbarg anode inlet pressure. The solid lines on subfigures a) and b) show 2nd order polynomials fitted onto the data.

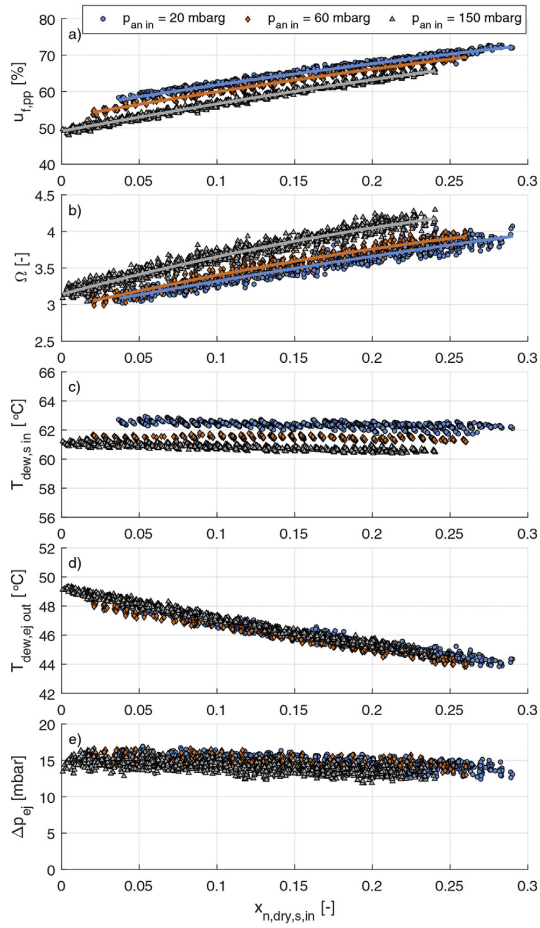

Fig. 8 – Effect of inert mole fraction on a dry basis in ejector secondary inlet gas ($x_{n,dry,s\ in}$) on a) fuel utilization per pass ($u_{f,pp}$), b) ejector entrainment ratio (Ω), c) ejector secondary inlet dew point temperature ($T_{dew,s\ in}$), d) ejector outlet dew point temperature ($T_{dew,ej,out}$), and e) ejector secondary gas pressure lift (Δp_{ej}) at anode inlet pressures 20 mbarg, 60 mbarg, and 150 mbarg and load level 4. The solid lines on subfigures a) and b) show 2nd order polynomials fitted onto the data.

though the recirculation rate increases. The slight increase in stack outlet humidity can be explained with the pressure difference between anode and cathode – a lower anode pressure favors water transportation towards the anode.

System dynamic limitations

Fig. 9a shows the anode inlet pressures during load changes from load level 1 to 7 both with an advance in fuel supply ($\Delta t_{fuel,adv}$ = 0.5 s, 1.0 s, 2.0 s) and without an advance in fuel supply ($\Delta t_{fuel,adv}$ = non). In each case with an advance in fuel supply, the anode inlet pressure first drops to a minimum value upon opening the purge valve (t = 0.0 s, 1.0 s, and 1.5 s, respectively). After 200–300 ms, the anode inlet pressure settles to a level corresponding to the flow resistance from the stack inlet to purge line outlet (~30 mbarg). A very similar temporal behavior of pressures is observed at the anode outlet and the ejector secondary inlet, although the pressure levels are different. The time between the minimum pressure level and the settled pressure level gives the time for the flow to develop fully. This is useful information for determining how much advance in fuel supply is needed to prevent fuel starvation in the stack.

Two seconds after the load increase request (t = 2.0 s), the purge valve is closed and load current is increased

approximately from 27 A to 160 A within milliseconds. At this point, anode pressures increase abruptly because of closing the purge valve. In the case of 0.5 s advance in fuel supply, the anode pressure increases to a higher level than in the cases of 1 s or 2 s advance in fuel supply. This is presumably because of a small deviation in timings of closing the purge valve and increasing the load current, which in the other two cases happen to be almost identical. After the sudden jump, the anode pressure slowly approaches the set point of 60 mbarg due to the controlled load current.

In the case of no advance in fuel supply but with the extra anode volume, the anode pressure makes only a small step due to the abruptly changing fuel consumption rate and the slower development of the fuel supply rate. Repeated measurements reveal that the variation in anode pressure (i.e. the difference between the minimum and maximum anode pressure) during a load change is roughly constant 6 mbar. It is a matter of timing whether the anode pressure will be higher, lower, or the same after the load change. Furthermore, intuitively, the magnitude of the anode pressure variation should be inversely related to the anode volume. Therefore, the approximately 6 mbar pressure variation observed in the setup with extra volume (12.8 dm^3) should translate into approximately 50 mbar pressure variation in the setup without extra volume (1.5 dm^3). This was, however, not tested in the present study.

Fig. 9a shows also the cathode inlet dry air flow rate during load changes from load level 1 to 7. Starting from ~60 slpm (air stoichiometric ratio 2.5 at 27 A load) and accelerating the blower to ~360 slpm (air stoichiometric ratio 2.5 at 160 A load) takes roughly 1.7 s. Thus, in the present setup, the air blower limits the fuel cell ramp rate. However, allowing momentarily a lower air stoichiometric ratio, notably increases the achievable ramp rate. For example, the flow rate corresponding to stoichiometric ratio of 1 at 160 A (~140 slpm) is achieved in less than 1 s. Running the system initially at higher air stoichiometric ratio, allows even faster ramp rates but with the expense of system efficiency at low power.

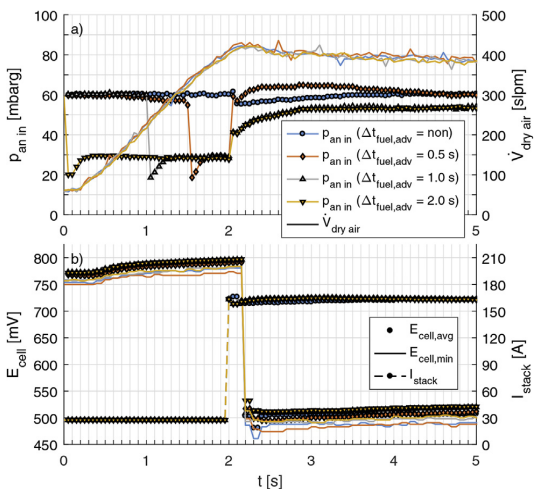

Fig. 9 – System behavior during a load change from level 1 to 7 with advance in fuel supply ($\Delta t_{fuel,adv}$ = 0.5 s, 1.0 s, 2.0 s) and without advance in fuel supply ($\Delta t_{fuel,adv.}$ = non). a) Anode inlet pressure ($p_{an\ in}$) and cathode inlet dry air flow rate ($\dot{V}_{dry\ air}$), b) average and minimum cell voltages ($E_{cell,avg}$ and $E_{cell,min}$) and stack current (I_{stack}).

In measurements with no or 0.5 s advance in fuel supply, the cell voltages are slightly lower compared to measurements done with 1 s or 2 s advance in fuel supply, as seen in Fig. 9b. This could be explained by an insufficient fuel supply during the load change. However, no conclusion about the cause of the lower cell voltages can be made because firstly, there is some variation in the cell voltage between measurements. Secondly, the cell voltages in measurements with no or 0.5 s advance in fuel supply are already slightly lower at the time of the power increase request (t = 0.0 s). Finally, there is some delay in cell voltage measurements (~200 ms) and, thus, completely up-to-date information could not be obtained with the current setup.

Conclusions

A custom-made ejector and a discrete ejector-primary-gas-flow-control-system was assembled into a 5 kW PEMFC system which could be used especially with back-up power applications. System tests were conducted involving both operation at constant load and fast load transients. The discrete ejector flow control solution was shown to be very reliable and cost effective.

The main challenge with the discrete ejector flow control solution is to match the fuel supply rate with the fuel consumption rate to prevent anode under- or over-pressurization. Two anode pressure control strategies were tested: 1) slightly excessive fuel supply combined with a periodic anode purge and 2) automatically controlled load current. Both approaches worked well.

The custom-made ejector employed in this study achieved anode gas recirculation rate ranging from 40% fuel utilization per pass at 25 A stack current to 64% fuel utilization per pass at 160 A stack current. In terms of the anode inlet hydrogen stoichiometry, the recirculation rate ranged from 2.6 to 1.6 in the same current range. Considering the non-optimized ejector geometry, the achieved recirculation rate is acceptable.

The increased inert gas mole fraction in the anode gas was shown to result in decreased mole-based recirculation rate but increased mass-based recirculation rate. The effect of added inert mole fraction was most pronounced at low stack current levels. Because of the decreased recirculation rate, the stack inlet dew point temperature was recorded to decrease 2 °C to 3 °C for every 0.1 change in recirculated gas inert mole fraction on a dry basis.

The dynamic limitations of the system were studied by ramping the stack power from 1 kW to 4.2 kW within seconds. During load changes, instantaneous mismatch in the fuel supply and consumption rates likely occur, hence the timing of the valve control relative to the load control becomes critical, especially when anode gas volume is reduced. A verified and safe approach for this non-pressurized system is to

initiate the fuel supply in advance relative to the consumption and vent out the excess fuel. The power ramp-up was also tested without advancing in fuel supply or opening the purge valve but with a large anode volume. This approach was also successful although there is a short-term risk of fuel starvation when anode gas volume is small.

Acknowledgements

This work has been supported by the Strategic Research Council at the Academy of Finland, project Transition to a Resource Efficient and Climate Neutral Electricity System (ELTRAN) (2015–17) (no. 293437). This research has received funding from the European Union's Seventh Framework Programme (FP7/2007–2013) for the Fuel Cells and Hydrogen Joint Technology Initiative under grant agreement no. 621218.

Symbols and abbreviations

Latin

C	Constant
E	Stack voltage, [V]
F	Faraday constant, [96485 C/mol]
I	Current, [A]
K_v	Flow factor, [m^3/h]
M	Molar weight, [kg/mol]
m	Mass flow rate, [kg/s]
N_i	Number of i
n	Molar flow rate, [mol/s]
P	Power, [kW]
p	Pressure, [(m)bar]
p^{vap}	Vapor pressure, [bar]
RH	Relative humidity, [%]
T	Temperature, [°C]
t	Time, [s]
$\Delta t_{fuel,adv}$	The time between increasing fuel supply rate and increasing load current, [s]
$u_{f,pp}$	Fuel utilization per pass, [%]
V	Volume, [dm^3]
$\dot{V}$	Volumetric flow rate, [m^3/s]
x	Mole fraction, [–]

Greek

Δ	Difference
η	Efficiency [%]
λ	Stoichiometry [–]
Ω	Entrainment ratio [–]

Subscripts

an	Anode
avg	Average
cat	Cathode
cool	Coolant
dew	Dew point
ej	Ejector
h	Hydrogen, H_2
in	inlet
max	Maximum
meas	Measured value
min	Minimum
n	Nitrogen, N_2
out	Outlet
p	Ejector primary inlet
r	Restrictor
ref	Reference value
s	Ejector secondary inlet
w	Water, H_2O

Abbreviations

BoP	Balance of Plant
EPC	Ejector Primary Gas Control system
LHV	Lower Heating Value, = 241.8 kJ/mol for hydrogen at 25 °C and 1.01325 bar(a)
lpm	Liters Per Minute
PEMFC	Proton Exchange Membrane Fuel Cell
slpm	Standard Liters Per Minute (T = 293.15 K, p = 1.01325 bara)

REFERENCES

[1] Jenssen D, Berger O, Krewer U. Anode flooding characteristics as design boundary for a hydrogen supply system for automotive polymer electrolyte membrane fuel cells. J Power Sources 2015;298:249–58. http://dx.doi.org/10.1016/j.jpowsour.2015.08.005.

[2] Pérez LC, Ihonen J, Sousa JM, Mendes A. Use of segmented cell operated in hydrogen recirculation mode to detect water accumulation in PEMFC. Fuel Cells 2013;13:203–16. http://dx.doi.org/10.1002/fuce.201200109.

[3] Reiser CA, Bregoli L, Patterson TW, Yi JS, Yang JD, Perry ML, et al. A reverse-current decay mechanism for fuel cells. Electrochem Solid State Lett 2005;8:A273–6.

[4] Abbou S, Dillet J, Spernjak D, Mukundan R, Borup RL, Maranzana G, et al. High potential excursions during PEM fuel cell operation with dead-ended anode. J Electrochem Soc 2015;162:F1212–20. http://dx.doi.org/10.1149/2.0511510jes.

[5] Ahluwalia RK, Wang X. Buildup of nitrogen in direct hydrogen polymer-electrolyte fuel cell stacks. J Power Sources 2007;171:63–71. http://dx.doi.org/10.1016/j.jpowsour.2007.01.032.

[6] Koski P, Pérez LC, Ihonen J. Comparing anode gas recirculation with hydrogen purge and bleed in a novel PEMFC laboratory test cell configuration. Fuel Cells 2015;15:494–504. http://dx.doi.org/10.1002/fuce.201400102.

[7] Matsuda Y, Hashimasa Y, Imamura D, Akai M, Watanabe S. Accumulation behavior of impurities in fuel cell hydrogen circulation system. Rev Automot Eng 2009;30:167–72. http://dx.doi.org/10.11351/jsaereview.30.167.

[8] Nikiforow K, Karimäki H, Keränen TM, Ihonen J. Optimization study of purge cycle in proton exchange membrane fuel cell system. J Power Sources 2013;238:336–44. http://dx.doi.org/10.1016/j.jpowsour.2012.11.153.

[9] Hosseinzadeh E, Rokni M, Jabbari M, Mortensen H. Numerical analysis of transport phenomena for designing of ejector in PEM forklift system. Int J Hydrogen Energy 2014;39:6664–74. http://dx.doi.org/10.1016/j.ijhydene.2014.02.061.

[10] Vasquez A, Varanauski D, Clark R. Analysis and test of a proton exchange membrane fuel cell power system for space power applications. 2000.

[11] Karnik AY, Sun Jing, Buckland JH. Control analysis of an ejector based fuel cell anode recirculation system. 2006 Am.

Control Conf., IEEE; 2006. p. 6. http://dx.doi.org/10.1109/ACC.2006.1655403.
[12] Bao C, Ouyang M, Yi B. Modeling and control of air stream and hydrogen flow with recirculation in a PEM fuel cell system—I. Control-oriented modeling. Int J Hydrogen Energy 2006;31:1879–96. http://dx.doi.org/10.1016/j.ijhydene.2006.02.031.
[13] Kim M, Sohn Y-J, Cho C-W, Lee W-Y, Kim C-S. Customized design for the ejector to recirculate a humidified hydrogen fuel in a submarine PEMFC. J Power Sources 2008;176:529–33. http://dx.doi.org/10.1016/j.jpowsour.2007.08.069.
[14] Zhu Y, Li Y. New theoretical model for convergent nozzle ejector in the proton exchange membrane fuel cell system. J Power Sources 2009;191:510–9. http://dx.doi.org/10.1016/j.jpowsour.2009.02.014.
[15] Lyndon B. Pressure regulator with internal ejector circulation pump, flow and pressure measurement porting, and fuel cell system integration options. 2011. Houston, TX, United States.
[16] He J, Ahn J, Choe S-Y. Analysis and control of a fuel delivery system considering a two-phase anode model of the polymer electrolyte membrane fuel cell stack. J Power Sources 2011;196:4655–70. http://dx.doi.org/10.1016/j.jpowsour.2011.01.019.
[17] Brunner DA, Marcks S, Bajpai M, Prasad AK, Advani SG. Design and characterization of an electronically controlled variable flow rate ejector for fuel cell applications. Int J Hydrogen Energy 2012;37:4457–66. http://dx.doi.org/10.1016/j.ijhydene.2011.11.116.
[18] Hwang J-J. Passive hydrogen recovery schemes using a vacuum ejector in a proton exchange membrane fuel cell system. J Power Sources 2014;247:256–63. http://dx.doi.org/10.1016/j.jpowsour.2013.08.126.
[19] Dadvar M, Afshari E. Analysis of design parameters in anodic recirculation system based on ejector technology for PEM fuel cells: a new approach in designing. Int J Hydrogen Energy 2014;39:12061–73. http://dx.doi.org/10.1016/j.ijhydene.2014.06.046.
[20] Maghsoodi A, Afshari E, Ahmadikia H. Optimization of geometric parameters for design a high-performance ejector in the proton exchange membrane fuel cell system using artificial neural network and genetic algorithm. Appl Therm Eng 2014;71:410–8. http://dx.doi.org/10.1016/j.applthermaleng.2014.06.067.
[21] Hwang J-J, Cho C-C, Wu W, Chiu C-H, Chiu K-C, Lin C-H. Numerical and experimental investigation into passive hydrogen recovery scheme using vacuum ejector. J Power Sources 2015;275:539–46. http://dx.doi.org/10.1016/j.jpowsour.2014.11.057.
[22] Jenssen D, Berger O, Krewer U. Improved PEM fuel cell system operation with cascaded stack and ejector-based recirculation. Appl Energy 2017;195:324–33. http://dx.doi.org/10.1016/j.apenergy.2017.03.002.
[23] Kim DK, Min HE, Kong IM, Lee MK, Lee CH, Kim MS, et al. Parametric study on interaction of blower and back pressure control valve for a 80-kW class PEM fuel cell vehicle. Int J Hydrogen Energy 2016;41:17595–615. http://dx.doi.org/10.1016/j.ijhydene.2016.07.218.
[24] Nikiforow K, Koski P, Karimäki H, Ihonen J, Alopaeus V. Designing a hydrogen gas ejector for 5 kW stationary PEMFC system – CFD-modeling and experimental validation. Int J Hydrogen Energy 2016;41:14952–70. http://dx.doi.org/10.1016/j.ijhydene.2016.06.122.
[25] Karimäki H, Pérez LC, Nikiforow K, Keränen TM, Viitakangas J, Ihonen J. The use of on-line hydrogen sensor for studying inert gas effects and nitrogen crossover in PEMFC system. Int J Hydrogen Energy 2011;36:10179–87. http://dx.doi.org/10.1016/j.ijhydene.2011.04.230.
[26] Perry RH, Green DW. Section 10 transport and storage of fluids. Perry's chem. eng. handb. 8th ed. McGraw-Hill; 2008. http://dx.doi.org/10.1036/0071511334.
[27] Lohm calculator for gases n.d. http://www.leeimh.com/resources/gas_calculator.htm [Accessed 24 March 2017].
[28] Dillet J, Spernjak D, Lamibrac A, Maranzana G, Mukundan R, Fairweather J, et al. Impact of flow rates and electrode specifications on degradations during repeated startups and shutdowns in polymer-electrolyte membrane fuel cells. J Power Sources 2014;250:68–79. http://dx.doi.org/10.1016/j.jpowsour.2013.10.141.
[29] Perry RH, Green DW. Section 2 physical and chemical data. Perry's chem. eng. handb. 8th ed. McGraw-Hill; 2008. http://dx.doi.org/10.1036/0071511253.

VI

K. Nikiforow, J. Pennanen, J. Ihonen, S. Uski, P. Koski, Power ramp rate capabilities of a 5 kW proton exchange membrane fuel cell system with discrete ejector control, J. Power Sources. 381 (2018) 30–37. doi:10.1016/j.jpowsour.2018.01.090.

Journal of Power Sources 381 (2018) 30–37

Contents lists available at ScienceDirect

Journal of Power Sources

journal homepage: www.elsevier.com/locate/jpowsour

Power ramp rate capabilities of a 5 kW proton exchange membrane fuel cell system with discrete ejector control

K. Nikiforow*, J. Pennanen, J. Ihonen, S. Uski, P. Koski

VTT Technical Research Centre of Finland Ltd, P.O. Box 1000, FI-02044 VTT, Finland

HIGHLIGHTS

- Ejector-based PEMFC system power ramp-rate capabilities were studied.
- Fuel supply manages a 50%–100% power ramp in 0.1 s even in low-volume systems.
- Air supply with 2.5 initial stoichiometry manages a 50%–93% power ramp in 1.0 s.
- Air supply with 7.0 initial stoichiometry manages a 50%–93% power ramp in 0.1 s.

ARTICLE INFO

Keywords:
PEMFC system
Power ramp rate
Dynamic behavior
Ejector
Fuel supply
Air supply

ABSTRACT

The power ramp rate capabilities of a 5 kW proton exchange membrane fuel cell (PEMFC) system are studied theoretically and experimentally for grid support service applications.

The fuel supply is implemented with a fixed-geometry ejector and a discrete control solution without any anode-side pressure fluctuation suppression methods. We show that the stack power can be ramped up from 2.0 kW to 4.0 kW with adequate fuel supply and low anode pressure fluctuations within only 0.1 s.

The air supply is implemented with a centrifugal blower. Air supply ramp rates are studied with a power increase executed within 1 and 0.2 s after the request, the time dictated by grid support service requirements in Finland and the UK. We show that a power ramp-up from 2.0 kW to 3.7 kW is achieved within 1 s with an initial air stoichiometry of 2.5 and within 0.2 s with an initial air stoichiometry of 7.0. We also show that the timing of the power ramp-up affects the achieved ancillary power capacity.

This work demonstrates that hydrogen fueled and ejector-based PEMFC systems can provide a significant amount of power in less than 1 s and provide valuable ancillary power capacity for grid support services.

1. Introduction

Proton exchange membrane fuel cells (PEMFCs) are seen as a valid alternative to diesel generators in backup power and grid balancing applications both in the kW- and MW-range. The main advantages of a PEMFC in these applications are start-up reliability, low start-up costs, ability to respond rapidly to load changes, zero local emissions, and low noise level.

The need for backup power and grid balancing services increases with the amount of variable renewable energy (VRE) in the grid. In particular, the inherent inertia of the system decreases as the penetration of conventional synchronous generators decreases in power systems [1]. The decrease in inertia is mainly due to increasing wind and photovoltaic (PV) solar power generation or electricity imports via high voltage direct current (HVDC) links.

Decreased inertia deteriorates the stability of the power system in case of disturbances. Inertia determines the lowest momentary frequency occurring within a few seconds after a major system frequency disturbance, which typically is caused by the loss of a large power plant or significant transmission connection.

The decrease of inherent inertia can be offset in a number of ways, e.g., keeping a sufficient amount of synchronous generation online in the system and thus curtailing non-synchronous generation or limiting imports via HVDC connections, adding rotating masses like synchronous condensers into the system, or establishing a market for inertia and thus promoting implementation of synthetic inertia. Synthetic inertia could be obtained from non-synchronous units (e.g., wind power plants, solar PV, batteries) by modulating the power output in a manner similar to how synchronous units provide power as inertial response [2]. In Europe, transmission system operators (TSOs) could require non-

* Corresponding author.
E-mail address: kaj.nikiforow@vtt.fi (K. Nikiforow).

https://doi.org/10.1016/j.jpowsour.2018.01.090
Received 1 September 2017; Received in revised form 26 January 2018; Accepted 30 January 2018
Available online 08 February 2018

synchronous Power Park Modules (PPM) to be capable of providing synthetic inertia. This requirement could be applied to PPMs with capacities of a few to tens of megawatts and above depending on the synchronous system [3,4]. Neither inertia requirements nor inertia as an ancillary service is yet widely used.

Inertia is related to the rate of change of frequency (RoCoF) immediately after a disturbance. Frequency containment disturbance reserves (FCR-D) determine the following steady frequency [2,5]. Frequency indicates the balance between system load and power generation and, thus, both power generation and loads can be used for FCR-D.

Historically, load shedding – i.e. fast tripping of loads – has been the means for rapid handling of severe low frequency disturbances due to loss of power supply. In Finland, for example, a tendering for load shedding is employed for system protection because of to the 1600 MW nuclear power production unit that is expected be online in 2019 and will affect the Nordic power system operation security.

In the UK's Enhanced Frequency Response (EFR) market [6], reserve capacity must be activated fully within 1 s and be able to sustain support for a minimum 15 min. Batteries have proven to be a very cost effective way to provide a fast response in the UK EFR tender. The feasibility and applicability of similar fast frequency response systems has been investigated by local authorities, e.g. in Australia [7] and in Texas, U.S [8].

In addition to load shedding and batteries, system protection and EFR could also be implemented by fast generation control reserves with similar control characteristics, i.e., an ability to provide power within 1 s. This creates a new opportunity for fuel cells and, in particular, for PEMFCs, which can achieve a very high power ramp rate.

In Finland, a significant amount of hydrogen is produced as a by-product in chlorine and sodium chlorate factories [9], and the quality of that hydrogen is sufficient for use as fuel in PEMFCs [10]. Using this hydrogen in PEMFC power plants operating at partial load, a significant rapid load response could be provided. However, the ability of PEMFC power plants to provide this ancillary service should be proven by verifying their power ramp rate capability.

A number of factors limit the power ramp rate of hydrogen fueled PEMFC systems, including air supply, fuel supply, and power electronics. These limitations are dependent on the system design and operation. Therefore, the power ramp rate capability can be improved by optimizing the system design and operation.

Air supply is well known to limit the power ramp-up rate in PEMFC systems. In principle, there are three issues: the dynamic capability of the blower/compressor, the gas manifold volume, and the time lag of the control system. Corbo et al. analyzed a 20 kW_e PEMFC system using different air supply strategies. By applying excess air at low loads, a 20%/s power ramp rate was achieved [11]. However, the use of excess air flow rate reduces system efficiency by adding blower power consumption and increases system cost through the need of a more efficient humidifier. In another study, Corbo et al. showed that 10%/s power ramp rate is possible (with minor issues) starting from room temperature [12]. Danzer et al. studied and modeled the control of cathode air excess and pressure in a pressurized PEMFC, showing that with an observer-based multivariable control, a 50%/s power ramp rate is possible [13]. However, the inertia of the compressor was not considered because a mass flow controller supplied the air. The study of Danzer et al. also illustrates that maintaining the cathode pressure close to set-point might be challenging during transients. In pressurized systems, not only does the cathode pressure need to be controlled but also the anode pressure, thus adding complexity. Matraji et al. studied the control of a compressor by modeling and employing a Hardware-In-Loop test bench [14]. According to their results, it takes up to 9 s to increase the air flow rate from 0 to 100%. This long duration may be due to the high inertia of the twin-screw compressor and the limited power of a compressor motor. Based on the literature study, at least a 20–30%/s power ramp rate is possible without extra measures at the air supply side.

The fuel supply also limits the power ramp rate, especially when the system is pressurized and an ejector is employed for anode gas recirculation. In a pressurized system, the anode pressure needs to be controlled to avoid a too high pressure difference over the membrane, leading to possible limitations in power ramp rate. When an ejector is applied, the ejector primary pressure control will further complicate the management of the anode pressure, especially if discrete flow control is applied [15]. Anode gas recirculation is applied in PEMFC systems for fuel humidification and to avoid local fuel starvation [16,17].

A third limitation for the power ramp rate is the thermal management, especially when the stack power density is high. The power densities of present day PEMFC stacks are in the range of 3 kW/dm^3 [18]. When the power is increased from the minimum to the maximum level, the cooling demand may increase up to 5 kW per kilogram of stack mass. This would lead to a temperature increase rate of 2–4 °C/s.

The transients in reactant supply or temperature can also lead to severe degradation of the catalyst layer, as reviewed by e.g. Banerjee [19]. Pei and Chen have reviewed the main factors affecting the lifetime of PEMFC in vehicle applications, and reactant starvation during fast transients is one of the issues [20].

To date, PEMFC systems hydrogen fuel ramp rate capabilities have not been studied, only the air supply capabilities. In addition, in these air supply studies, the focus has been on the time scale of several seconds, not 0.2–2 s, which are needed in many applications, including ancillary services for TSOs.

The present work studies the hydrogen fuel supply ramp rate capabilities of a PEMFC system with an ejector with discrete control. The capabilities of an ejector-based system are studied for the first time without using any anode pressure fluctuation mitigation methods during the transient, such as anode purge [15]. In addition to the fuel supply, the air supply ramp rate capabilities are studied. The work focuses on determining the maximum power increase achievable with a PEMFC system operated at partial load, with the power increase executed within 0.2 or 1–2 s after the request, as suggested by the requirements for ancillary power applications.

2. Methods

2.1. PEMFC system description

Fig. 1 shows the simplified schematic of the PEMFC system employed in this work. The fuel was supplied through a fixed-geometry ejector (E), employed for anode gas recirculation. The ejector primary pressure was controlled using a setup of three solenoid valves and three flow restrictors (EPC), enabling fuel supply at seven discrete flow rates. The fuel supply in the present setup limits the maximum PEMFC power to approximately 4 kW. The load current was fine-tuned to compensate for the possible small variation in fuel supply rate and to maintain a constant anode pressure during steady state operation. Air was supplied with a blower (B) and humidified with a membrane humidifier (MH). A coolant pump (P) recirculated de-ionized water through the stack and through a liquid-liquid heat exchanger (HEX). The PEMFC system was controlled with National Instruments CompactRIO hardware, which was programmed with LabVIEW software. A complete description of the system can be found in previous work [15].

The control software was adopted for the current work, firstly by a higher data acquisition rate (100 Hz), which was triggered prior to a power transient and maintained for 10 s. Secondly, the experiments conducted in this work – the study of system ramp rate capabilities and the control of anode pressure during power transients – relied on exact timing of the fuel valve (in EPC), the air blower, and the electronic load control. Therefore, the control routine was updated to achieve accurate control, with the timing error of 1 ms or below.

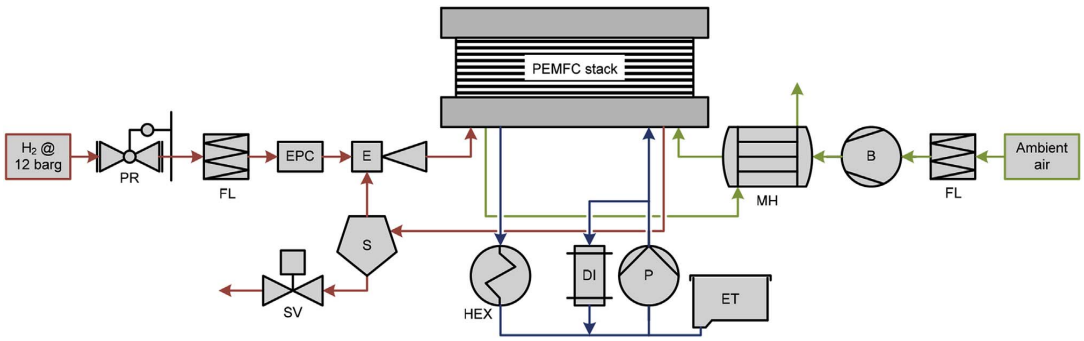

Fig. 1. Simplified PEMFC system scheme. PR: pressure reducer, FL: particle filter, EPC: ejector primary pressure control, E: ejector, BV: buffer volume, S: gas-liquid separator, SV: solenoid valve, B: gas blower, MH: membrane humidifier, P: liquid pump, DI: de-ionizing filter, HEX: liquid-liquid heat exchanger, ET: expansion tank.

2.2. Anode pressure control during power transients

The discrete ejector control has been shown to be a viable solution to achieve fast power ramp rates [15]. A challenge with this solution, however, is to maintain the balance between the hydrogen fuel supply and consumption rate at all times in order to avoid excessive anode pressure fluctuation. The imbalance between fuel supply and consumption can be mitigated by either increasing the anode gas volume or using a long anode purge during the transient.

However, both of these mitigation alternatives have clear drawbacks. Increasing the anode volume will increase the gas exchange time during a system start-up, causing additional degradation [21]. For this reason, a minimum anode volume is preferred. A long anode purge during operation depressurizes the anode side and causes a pressure difference between the anode and cathode, causing unnecessary stresses for the polymer membrane [22]. A long anode purge also causes extra fuel consumption.

It is, therefore, important to study alternative methods for mitigating anode pressure fluctuations that require neither extra anode gas volume nor extra anode gas purging. Precise control of fuel supply timing relative to the load ramp-up is recognized as one such method. Since experimental studies of this approach could damage the system and endanger personal safety, simulations were conducted for the initial study and to assist in designing the system.

The anode gas volume in the current system was measured to be 1.5 dm^3 [15] – a relatively large value compared to the nominal power and current of system (5 kW, 200 A and 50 cells). Thus, the anode volume-to-power ratio for the current system is 0.3 dm^3/kW. A 10 A mismatch in fuel supply and consumption rates leads to only approximately 40 mbar/s pressure change rate in this system. In volume-optimized systems, the anode volume-to-power ratio can be as low as 0.06 dm^3/kW and the corresponding pressure change rate can be 5 times faster. When the mismatch between fuel consumption rate and supply increases (e.g., during load changes), the rate of pressure change can be notably higher and actions must be taken within a fraction of a second.

2.3. Fuel supply modeling

A model for studying the anode dynamics was implemented in Mathworks Simulink employing the thermodynamic function library Thermolib by EUtech Scientific Engineering GmbH. The modeled system was based on the experimental system presented in section 2.1 and comprised three parts: the ejector, the PEMFC stack, and the recirculation loop (Fig. 2).

The ejector was modeled with a lookup table based on experimental data [23]. The ejector's secondary gas flow rate was calculated in the 'Ejector' block based on the primary gas pressure and the pressure difference between ejector outlet and secondary inlet. The ejector primary gas pressure was calculated in the 'Control unit' block, and it was dependent on the combination of valves opened. The control signals for valves were modeled as step functions and they were generated in the 'Control signals'-block. The change of ejector primary pressure (p_p) between two discrete load levels was modeled with a transfer function shown in Fig. 3.

The stack model (implemented in the 'Stack'-block) was based on a PEMFC model-block provided in Thermolib. Essential functionalities of the model were 1) fuel consumption, which was proportional to the load current, and 2) the addition of water due to water transport. During simulations, the stack operating temperature was set at 70 °C and the cathode was fed with air at a stoichiometric ratio of 4.

The 'Recycling' block split the flow into recirculated stream and purged stream in case the purge valve was open. In this study, the anode purge was not employed and the 'Recycling'-block simply recirculated the anode gas to the ejector secondary inlet.

The three model blocks 'Ejector', 'Stack', and 'Recycling' had their specified volumes that, together with in- and out-flow rates, determined their pressure levels. The in- and out-flow rates were determined based on the block pressure levels and flow restrictions between them. The flow restrictions were tuned to correspond to pressure drops in the real system.

The stack load current was fine-tuned with a PI-controller in order to maintain a constant anode pressure. A similar functionality was employed in the real system with the exception that the PI-control was disabled during the transient to better observe the anode pressure behavior.

2.4. Experimental procedure

The experiments were conducted by operating the PEMFC at constant load current (approximately 55 A) with load fine-tuning enabled until a steady state was reached. At this point, the load fine-tuning was disabled, the fast data acquisition was triggered, a ramp-up control sequence was applied, and the load current was increased to approximately 160 A. The PEMFC system operating parameters are listed in Table 1 and the ramp-up control sequences are described below.

Three control sequences were applied for studying fuel supply and air supply ramp rates. A control sequence in this context comprises the initiation of fuel supply ramp, air supply ramp, and load ramp at specified moments in time. In each control sequence, the timing of control actions were varied. Table 2 summarizes each control sequence and more detailed descriptions are given below.

The control sequence named as 'Fuel supply' was employed for studying the fuel supply ramp rate. The timing of load ramp-up relative to the fuel supply ramp-up (t_{lrf}) was varied between −50 ms and +200 ms. The timing of air blower ramp relative to the fuel supply

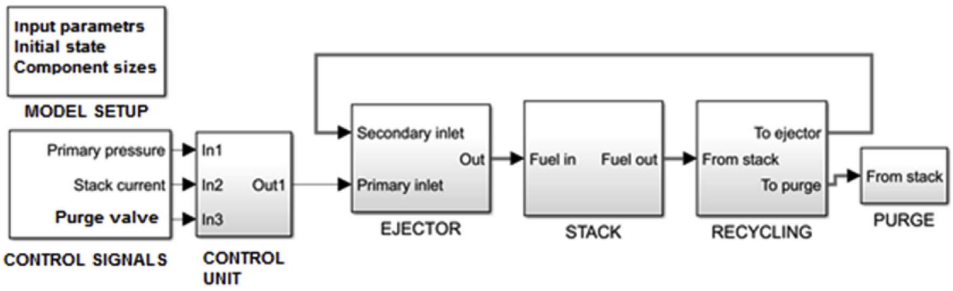

Fig. 2. System model block diagram.

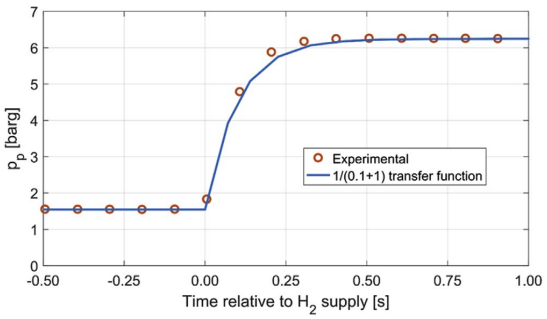

Fig. 3. Measured and modeled transition between two ejector primary pressure (p_p) levels.

Table 1
System operating parameters.

Operating parameter	Target value
Stack current (low power)	55 A (P_{stack} = ~2 kW)
Stack current (high power)	160 A (P_{stack} = ~4 kW)[a]
Anode inlet pressure	0.1 barg
Air stoichiometry	2.5
Coolant inlet temperature	70 °C
Coolant flow rate	~20 lpm

[a] The maximum stack current, 200 A [24], could not achieved because of the ejector control system sizing [15].

Table 2
Control sequence during transients with varying advance in fuel supply, varying advance in air supply, and varying initial air stoichiometry.

Action	Relative time [ms]		
	Fuel supply	Air supply for 1.0 s target	Air supply for 0.2 s target
Increase air stoichiometry	not used	not used	−5000
Initiate air blower ramp-up	−2000	0	0
Initiate fuel supply ramp-up	0	+250, +500, +750, +1000, +1250, +1500, +2000	0
Initiate load ramp-up	−50, 0, +50, +100, +200	+350, +600, +850, +1100, +1350, +1600, +2100	+100

ramp was kept constant at −2.0 s, thereby eliminating the effect of air supply.

The control sequence labeled 'Air supply for 1.0 s target' was employed for studying the maximum achievable power increase within about 1 s. In this sequence, the load ramp-up relative to the air blower ramp-up (t_{lra}) was varied and the initial air stoichiometry was kept at 2.5. The fuel supply ramp was initiated at −100 ms relative to the load ramp because this timing was shown to provide minimum anode pressure fluctuation.

The control sequence labeled 'Air supply for 0.2 s target' was employed for studying the maximum achievable power increase within 0.2 s. This case corresponds to a grid balancing application after a disconnection of a large power unit or import power line. Using this short delay, the initial air stoichiometry was varied between 4.0 and 7.0. The fuel supply ramp was initiated simultaneously with the air blower ramp-up. The load was ramped up 100 ms later. The rest of the 0.2 s target time, i.e., 100 ms, was reserved for the response time of the data transfer and control system in the application.

Each control sequence was repeated 5 to 7 times with each set of parameters, with the exception of experiments that resulted in a deep voltage dip during the transient (experiments with too little time for blower acceleration or too low initial air stoichiometry). These experiments could be conducted only 1 or 2 times because of the control system triggering an emergency shutdown.

3. Results and discussion

3.1. System transient behavior

Fig. 4 displays the high repeatability of measured quantities during seven repetitions of a power transient conducted with the air blower ramp initiated −2000 ms and the load ramp initiated +100 ms relative to the fuel supply ramp-up. These results represent well all measurements in this work.

As seen in Fig. 4a, the load current changes so rapidly that current ramp cannot be captured with the 100 Hz measuring frequency. On the contrary, the stack voltage (Fig. 4b) does not respond instantly to increased current. This results in power peak during the transient, which is followed by a power dip (Fig. 4c). The current increase seen approximately 1 s after the transient is caused by the activation of load fine-tuning.

Compared to the load current ramp, the fuel supply and the air supply ramps are slow. The hydrogen fuel pressure at ejector primary inlet develops in less than 0.5 s (Fig. 4e), while the blower requires approximately 1.5 s for accelerating to the target flow rate (Fig. 4g). The air stoichiometry is computed from the air flow rate and the load current and, thus, changes abruptly with the load current (Fig. 4h).

Fig. 4d shows how the cooling liquid temperature increases after the load change. The stack used in this system (PowerCell S2) is not as volume optimized as automotive stacks. Nonetheless, the coolant outlet temperature increases by 3 °C in 4 s, even though the load change is only 40% of the maximum stack power. In automotive stacks, the rate of change in stack power relative to stack thermal mass can be up to ten

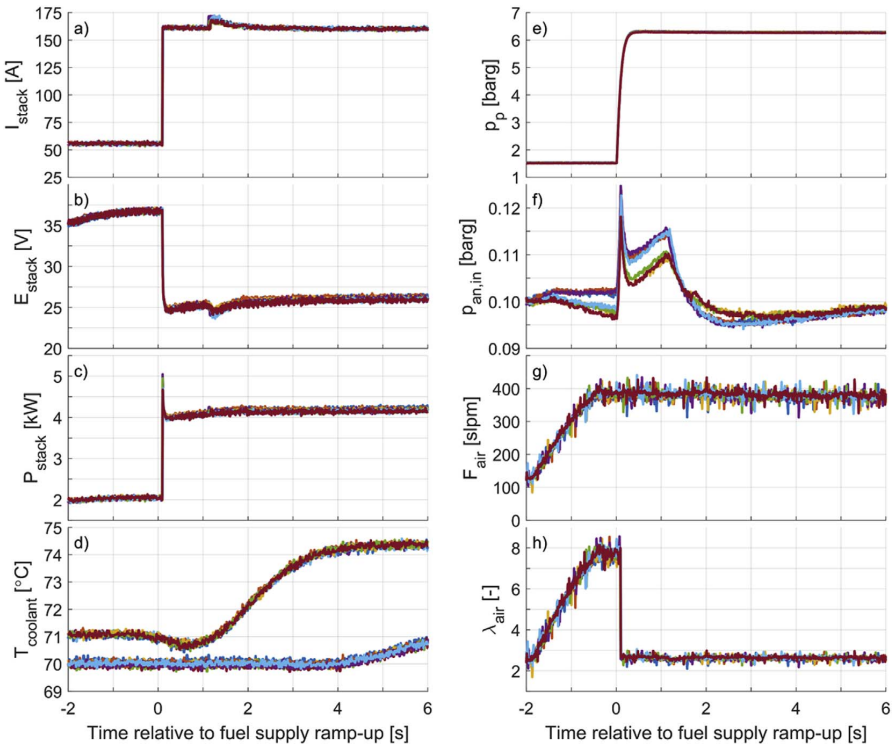

Fig. 4. a) Stack current (I_{stack}), b) stack voltage (E_{stack}), c) stack power (P_{stack}), d) coolant inlet and outlet temperatures ($T_{coolant}$), e) ejector primary inlet pressure (p_p), f) anode inlet pressure ($p_{an,in}$), g) cathode inlet dry air flow rate (F_{air}), and h) air stoichiometry (λ_{air}) during seven repeated transients with air blower ramp-up performed −2000 ms and load ramp-up performed +100 ms relative to hydrogen supply ramp-up.

times larger. This implies a clear risk of stack overheating, unless a feed-forward control method is applied for regulating the coolant flow rate and radiator cooling power.

The variation in anode pressure between experiments (Fig. 4f) is due to disabling the load current fine-tuning at time −2 s relative to the fuel supply ramp-up. From this point on, the anode pressure is not controlled and its value depends on the last load current value. Because of this, the anode pressure relative to the pressure in the beginning of transient ($p_{relative}$) is employed from now on for easier comparison of results. The variation in anode pressure does not affect the fuel supply rate because the flow at the ejector primary nozzle is critical at both current levels employed [15].

3.2. Fuel supply ramp rate

The modeled relative anode pressure profiles ($p_{relative}$) with varying load ramp timings with respect to the fuel supply ramp-up (t_{lrf}) are shown in Fig. 5a. As seen, there is always an anode under- or over-pressurization, or both. This is because the fuel consumption rate changes almost instantaneously with the load current, while the change in fuel flow rate is slower. After the load ramp-up, the pressures in all cases start to approach zero relative pressure because of the load current fine-tuning.

Fig. 5b shows the minimum and maximum simulated relative anode pressure as a function of t_{lrf}. The minimum pressure variation of 24 mbar (−11 to +13 mbar) is achieved with t_{lrf} = +80 ms. With t_{lrf} = +100 ms, the pressure variation is −5 to +19 mbar. If the anode gas volume were to decrease to one fifth, the pressure variation would be five times larger, about 120 mbar. In the current system, a t_{lrf} as low as −100 ms or as high as +200 ms does not cause severe anode pressure fluctuation. Thus, these simulation results were used as reference when planning the experimental part.

The effect of t_{lrf} on anode pressure variation measured experimentally is shown in Fig. 6d. The experimental results accord well with simulated data. Out of the five tested load ramp-up timings, the smallest anode pressure variation of 21 mbar (0 to +21 mbar) was measured with t_{lrf} = +100 ms.

Fig. 6a shows that the minimum stack voltage during transients decreases progressively with decreasing t_{lrf}. All measurements fit this trend perfectly, apart from the sequence with t_{lrf} = +100 ms, which is offset from other measurements by a few hundred millivolts. Nonetheless, ramping up the load as early as 50 ms before initiating the fuel supply (t_{lrf} = −50 ms) does not result in a notable voltage dip. This is because the anode volume functions as a fuel buffer. Hence, a smaller anode volume would presumably result in a more notable voltage dip. However, a smaller anode volume would also result in a higher anode pressure fluctuation, as discussed above. By comparing the anode pressure data and stack voltage data, it can be concluded that the t_{lrf} should be adjusted mainly based on the allowed anode pressure fluctuation.

Because of the small variation in minimum stack voltage between measurements, the minimum stack power also has only small variances (Fig. 6b) – with t_{lrf} = +100 ms the minimum power is 4.0 kW and with all other t_{lrf} the minimum power is 3.9 kW. Thus, the fuel supply can achieve a power ramp-up from 2.0 kW to at least 3.9 kW (a 48% power increase relative to maximum power) in −0.05 to +0.2 s relative to the fuel supply ramp-up.

Fig. 6d shows that a t_{lrf} of +50 ms or less results in anode under-

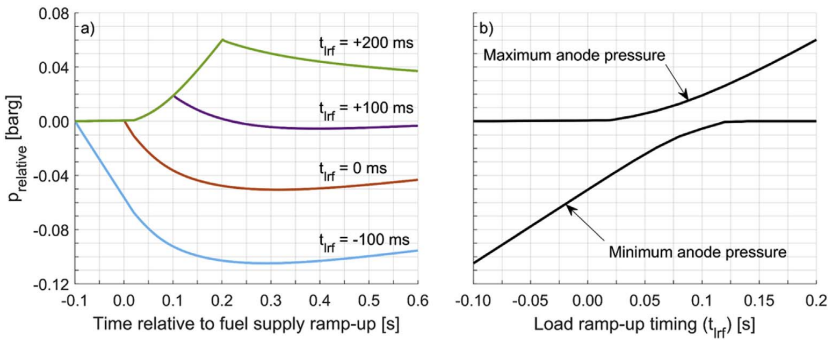

Fig. 5. a) Simulated relative anode pressure ($p_{relative}$) during transients with varying load ramp-up timing relative to fuel supply ramp-up (t_{lrf} = −100 ms…+200 ms). b) The minimum and maximum anode pressure during transients with varying load ramp-up timing relative to fuel supply ramp-up.

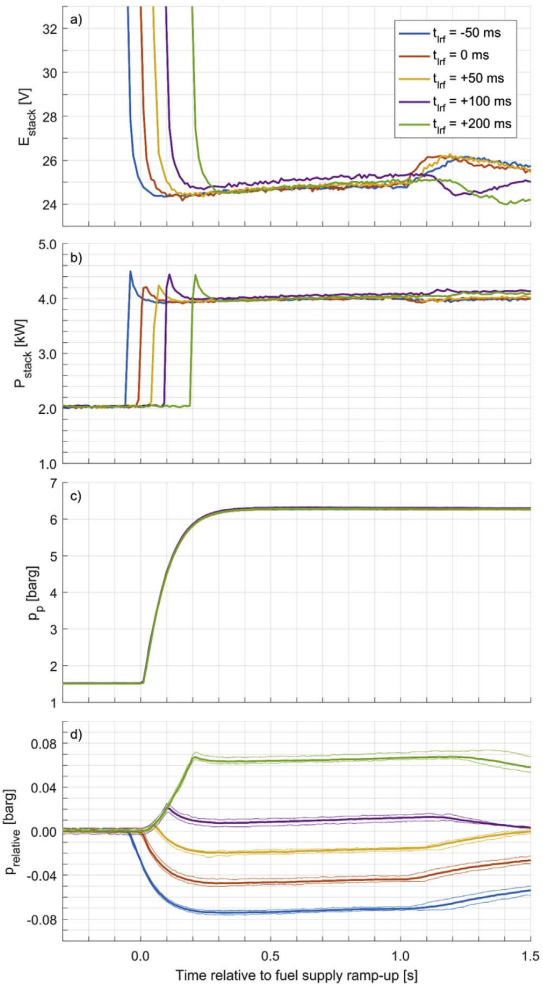

Fig. 6. a) Stack voltage (E_{stack}), b) stack power (P_{stack}), c) ejector primary inlet pressure (p_p), and d) relative anode pressure ($p_{relative}$) during transients with varying load ramp-up timing relative to fuel supply ramp-up (t_{lrf} = −50 ms…+200 ms). The thin lines in figure d show the measured variation in anode pressure between repeated experiments.

pressure. Consequently, when the load fine-tuning is activated, the load current decreases, which results in reduced stack power. This decreases the ancillary power capacity available for sale to the TSO. Therefore, the load ramp-up timing should be chosen to create anode over-pressure, in this case t_{lrf} = +100 ms or t_{lrf} = +200 ms.

The reproducibility of these experiments is very high – the highest and lowest anode pressures measured at the time of load ramp-up in each control sequence in Fig. 6d show a maximum variation of 8 mbar. This indicates that the variation in the opening time of the valves is very small: in the order of 10 ms. A similar conclusion can be made when comparing the evolution of ejector primary pressures after the initiation of fuel supply in Fig. 6c. This low timing variation would be acceptable even in volume-optimized systems using the maximum load step.

3.3. Air supply ramp rate

3.3.1. Varying air blower ramp-up timing for a 1.0 s response

In the studied application, the ancillary power capacity delivered after 1 s forms the basis for the payment from the TSO. Fig. 7 shows the power capacity measured with fixed initial air stoichiometry ($\lambda_{air,0}$ = 2.5) and varying load ramp-up timing relative to the air blower ramp-up (t_{lra}) – not relative to fuel supply ramp-up as in the previous section.

Fig. 7b shows that the earlier the load is ramped up, the higher is the ancillary power capacity. This is contradictory to what could be expected if the stack power is assumed reactant mass transfer limited because the earlier the load is ramped up, the lower is the oxygen concentration at the cathode until a steady state is reached. The observed behavior is believed to be due to water formation at the cathode, the water humidifying the membrane and decreasing resistive losses.

Consistent with the observation of higher stack power with an earlier load ramp-up, the highest stack power (3.7 kW) 1 s after the air blower ramp-up is achieved with a power ramp-up initiated 350 ms after the air blower ramp-up. The power increase corresponds to about 43% of the maximum power. The minimum air stoichiometry during this power transient is 1.2, as seen in Fig. 7c, and a much earlier current ramp-up would result in air under-stoichiometry.

An earlier power ramp-up does not always result in higher power at a given instant. For example, if the target time for the ancillary power is 0.6 s after the trigger, a power ramp-up executed at that very instant or few milliseconds earlier would result in higher power capacity than a power ramp-up executed 350 ms after the trigger, as seen in Fig. 7b. It is concluded that an earlier power ramp-up is beneficial only if it can be performed early enough for the water formation to affect membrane performance. Based on the results shown in Fig. 7b, the time needed for water formation to have an effect is approximately 0.5 s.

The PEMFC system operation should be designed based on lowest performing cell because, at least in typical systems, this will trigger the

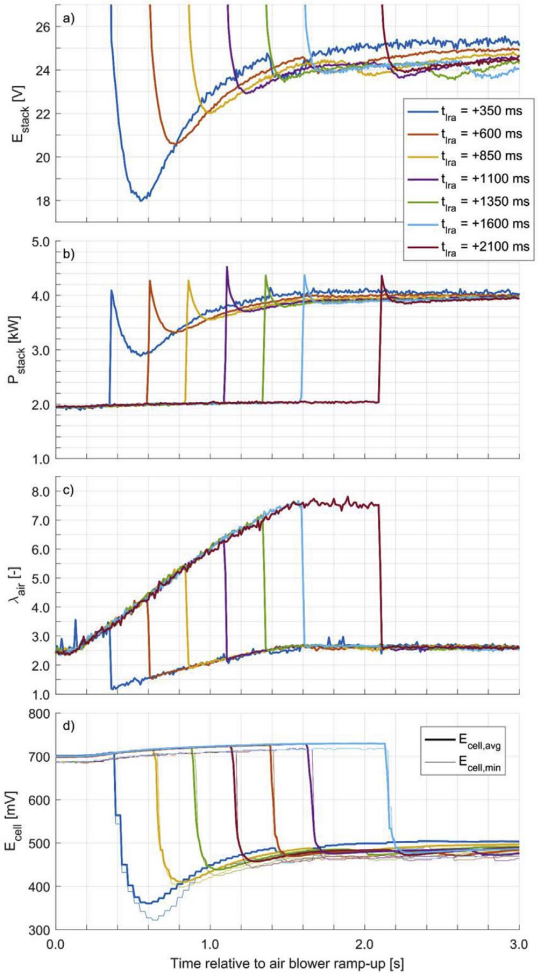

Fig. 7. a) Stack voltage (E_{stack}), b) stack power (P_{stack}), c) air stoichiometry (λ_{air}), and d) average and minimum cell voltage ($E_{cell,avg}$, $E_{cell,min}$) during transients with varying load ramp-up timing relative to air blower ramp-up (t_{Ira} = +350 ms … +2100 ms).

emergency stop. Upon decreasing the load ramp-up timing relative to the air blower ramp-up to +350 ms, a clear decrease in lowest cell voltage compared to average cell voltage can be observed (Fig. 7d). The cell voltages were measured with a CVM operating at 25 Hz read frequency – hence the roughly 40 ms delay in the readings. A very short voltage dip due to limited air supply does not cause catalyst support degradation, but if the limitation is on fuel supply, catalyst support degradation may occur, as shown by Enz et al. [25].

3.3.2. Varying initial air stoichiometry for a 0.2 s response

Running the system with an initial air stoichiometry ($\lambda_{air,0}$) of 2.5 cannot achieve the 55 A–160 A current ramp in 0.1 s (as 0.1 s was reserved for data transfer etc.). To achieve such a rapid current ramp, the system must be operated with a higher initial air stoichiometry. Fig. 8 shows the results with varying the initial air stoichiometry and the load ramp-up time relative to air blower ramp-up (t_{Ira}) fixed at +100 ms.

To achieve a power ramp from 2 kW to 3.7 kW in 0.1 s, an initial air stoichiometry of 7.0 is needed (Fig. 8b). With an initial air stoichiometry of 5.2, a power ramp to 3.5 kW is achieved, which corresponds to

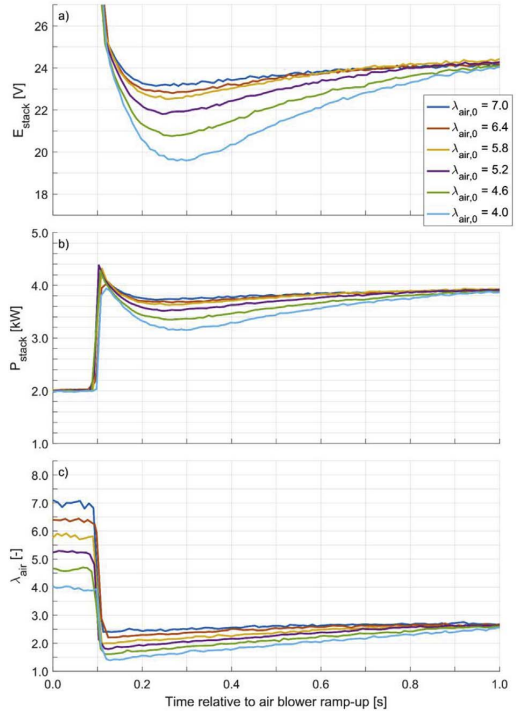

Fig. 8. a) Stack voltage (E_{stack}), b) stack power (P_{stack}), and c) air stoichiometry (λ_{air}) during transients with varying initial air stoichiometry ($\lambda_{air,0}$ = 4.0 … 7.0). Time relative to air blower ramp-up.

a 38% power increase relative to maximum system power. With an initial air stoichiometry of 4.0, the voltage drop is remarkable (Fig. 8a) and a power ramp to only 3.2 kW is achieved because of the low minimum air stoichiometry 1.4 (Fig. 8c).

A high air stoichiometry leads to decreased system efficiency because of air blower power consumption. Further, if a membrane humidifier is employed for air humidification, it should be over-dimensioned. These drawbacks must be evaluated against the benefits from the ancillary services when maximizing the power increase step.

4. Conclusions

The power ramp rate capabilities of a 5 kW PEMFC system using a fixed-geometry ejector with a discrete control solution was studied. The experimental results show that the stack power can be ramped up from 2.0 kW to 4.0 kW (maximum stack power with the current setup) within 0.1 s without problems in fuel supply, even when no mitigation method is applied to dampen the anode pressure fluctuation. Modeling results indicate that if the anode gas volume was reduced by 80%, the anode pressure fluctuation during a similar power ramp could be maintained within 120 mbar. In conclusion, the fuel supply based on ejector with a discrete control does not limit the power ramp rate in the current PEMFC system or in volume-optimized systems.

In the studied system, the air supply limits the power ramp rate because of the slow accelerating air blower. A stack power increase from 2.0 kW to 3.7 kW was achieved in less than 1 s with an initial air stoichiometry of 2.5. A power ramp-up executed earlier results generally in a higher ancillary power capacity even though the encountered low air stoichiometry causes a deep power dip initially. The higher power after the dip is believed to be a consequence of water generation and increased membrane humidity.

When a power ramp from 2.0 kW to 3.7 kW was needed within 0.1 s, an initial stoichiometry of at least 7.0 was necessary. This high air stoichiometry not only consumes much parasitic power, thus lowering the ancillary power capacity of the system, but also necessitates the use of very efficient air humidification to prevent PEMFC dehydration. Therefore, to further increase the power ramp rate capability, additional improvements to the air supply are needed.

Acknowledgements

This work has been supported by the Strategic Research Council at the Academy of Finland, project Transition to a Resource Efficient and Climate Neutral Electricity System (EL-TRAN) (2015–17)" (no. 293437).

This research has received funding from the European Union's Seventh Framework Programme (FP7/2007–2013) for the Fuel Cells and Hydrogen Joint Technology Initiative under grant agreement n° 621218.

Glossary

Latin

E	Voltage, [V]
F	Flow rate, [slpm]
I	Current, [A]
P	Power, [kW]
p	Pressure, [bar]
T	Temperature, [°C]
t	Time, [s]
t_{lra}	Load ramp-up time relative to air blower ramp-up, [s]
t_{lrf}	Load ramp-up time relative to fuel supply ramp-up, [s]

Greek

λ	Stoichiometry [−]

Subscripts

0	Initial
an	Anode
cat	Cathode
in	inlet
min	Minimum
p	Ejector primary inlet

Abbreviations

EFR	Enhanced Frequency Response
FCR-D	Frequency containment disturbance reserves
HVDC	High Voltage Direct Current
lpm	Liters Per Minute
OL3	Olkiluoto 3 nuclear power plant
PEMFC	Proton Exchange Membrane Fuel Cell
PPM	Power Park Module
PV	Photo Voltaic
RoCoF	Rate of Change of Frequency
slpm	Standard Liters Per Minute (T = 293.15 K, p = 1.01325 bara)
TSO	Transmission System Operator
VRE	Variable Renewable Energy

References

[1] P. Tielens, D. Van Hertem, The relevance of inertia in power systems, Renew. Sustain. Energy Rev. 55 (2016) 999–1009, http://dx.doi.org/10.1016/j.rser.2015.11.016.

[2] Nordic TSOs, Challenges and opportunities for the nordic power system, http://www.statnett.no/Global/Dokumenter/Challenges_and_opportunities_Report.pdf, (2016).

[3] European Union, Commission regulation (EU) 2016/631, 68 (2016) 27.04.2016.

[4] ENTSO-E, Need for Synthetic Inertia (SI) for Frequency Regulation - ENTSO-e Guidance Document for National Implementation for Network Codes on Grid Connection, (2017).

[5] ENTSO-E, Nordic balancing philosophy, https://www.entsoe.eu/Documents/Publications/SOC/Nordic/Nordic_Balancing_Philosophy_160616_Final_external.pdf, (2016).

[6] National Grid, Enhanced Frequency Response: Invitation to Tender for Pre-qualified Parties, (2016).

[7] AEMC, System security market frameworks review executive summary system security work program, http://www.aemc.gov.au/getattachment/f510069a-791b-4e4d-8bc0-9e6a216be7a2/Final-report.aspx, (2017) , Accessed date: 28 August 2017.

[8] J. Matevosyan, S. Sharma, S.-H. Huang, D. Woodfin, K. Ragsdale, S. Moorty, P. Wattles, W. Li, Proposed future ancillary services in electric reliability Council of Texas, 2015 IEEE Eindhoven PowerTech, IEEE, 2015, pp. 1–6, , http://dx.doi.org/10.1109/PTC.2015.7232743.

[9] J. Ihonen, Value chain analysis of hydrogen in Finland, http://hdl.handle.net/11250/276892, (2013) , Accessed date: 28 August 2017.

[10] J. Ihonen, P. Koski, V. Pulkkinen, T. Keränen, H. Karimäki, S. Auvinen, K. Nikiforow, M. Kotisaari, H. Tuiskula, J. Viitakangas, Operational experiences of PEMFC pilot plant using low grade hydrogen from sodium chlorate production process, Int. J. Hydrogen Energy 42 (2017) 27269–27283, http://dx.doi.org/10.1016/j.ijhydene.2017.09.056.

[11] P. Corbo, F. Migliardini, O. Veneri, Experimental analysis of a 20 kWe PEM fuel cell system in dynamic conditions representative of automotive applications, Energy Convers. Manag. 49 (2008) 2688–2697, http://dx.doi.org/10.1016/j.enconman.2008.04.001.

[12] P. Corbo, F. Migliardini, O. Veneri, Dynamic behaviour of hydrogen fuel cells for automotive application, Renew. Energy 34 (2009) 1955–1961, http://dx.doi.org/10.1016/j.renene.2008.12.021.

[13] M.A. Danzer, J. Wilhelm, H. Aschemann, E.P. Hofer, Model-based control of cathode pressure and oxygen excess ratio of a PEM fuel cell system, J. Power Sources 176 (2008) 515–522, http://dx.doi.org/10.1016/j.jpowsour.2007.08.049.

[14] I. Matraji, S. Laghrouche, S. Jemei, M. Wack, Robust control of the PEM fuel cell air-feed system via sub-optimal second order sliding mode, Appl. Energy 104 (2013) 945–957, http://dx.doi.org/10.1016/j.apenergy.2012.12.012.

[15] K. Nikiforow, P. Koski, J. Ihonen, Discrete ejector control solution design, characterization, and verification in a 5 kW PEMFC system, Int. J. Hydrogen Energy (2017), http://dx.doi.org/10.1016/j.ijhydene.2017.05.151.

[16] D. Jenssen, O. Berger, U. Krewer, Improved PEM fuel cell system operation with cascaded stack and ejector-based recirculation, Appl. Energy 195 (2017) 324–333, http://dx.doi.org/10.1016/j.apenergy.2017.03.002.

[17] F. Migliardini, T.M. Di Palma, M.F. Gaele, P. Corbo, Hydrogen purge and reactant feeding strategies in self-humidified PEM fuel cell systems, Int. J. Hydrogen Energy 42 (2017) 1758–1765, http://dx.doi.org/10.1016/j.ijhydene.2016.06.196.

[18] A. Martin, L. Jörissen, AutoStack – core – Industry led European consortium to develop next generation automotive stack hardware, 69 (2015) 325335, , http://dx.doi.org/10.1149/06917.0957ecst.

[19] R. Banerjee, S.G. Kandlikar, Two-phase flow and thermal transients in proton exchange membrane fuel cells - a critical review, Int. J. Hydrogen Energy 40 (2015) 3990–4010, http://dx.doi.org/10.1016/j.ijhydene.2015.01.126.

[20] P. Pei, H. Chen, Main factors affecting the lifetime of Proton Exchange Membrane fuel cells in vehicle applications: a review, Appl. Energy 125 (2014) 60–75, http://dx.doi.org/10.1016/j.apenergy.2014.03.048.

[21] J. Dillet, D. Spernjak, A. Lamibrac, G. Maranzana, R. Mukundan, J. Fairweather, S. Didierjean, R.L. Borup, O. Lottin, Impact of flow rates and electrode specifications on degradations during repeated startups and shutdowns in polymer-electrolyte membrane fuel cells, J. Power Sources 250 (2014) 68–79, http://dx.doi.org/10.1016/j.jpowsour.2013.10.141.

[22] R. Borup, J. Meyers, B. Pivovar, Y.S. Kim, R. Mukundan, N. Garland, D. Myers, M. Wilson, F. Garzon, D. Wood, P. Zelenay, K. More, K. Stroh, T. Zawodzinski, J. Boncella, J.E. Mcgrath, M. Inaba, K. Miyatake, M. Hori, K. Ota, Z. Ogumi, S. Miyata, A. Nishikata, Z. Siroma, Y. Uchimoto, K. Yasuda, K.-I. Kimijima, N. Iwashita, Scientific aspects of polymer electrolyte fuel cell durability and degradation, Chem. Rev. 107 (2007) 3904–3951, http://dx.doi.org/10.1021/cr050182l.

[23] K. Nikiforow, P. Koski, H. Karimäki, J. Ihonen, V. Alopaeus, Designing a hydrogen gas ejector for 5 kW stationary PEMFC system – CFD-modeling and experimental validation, Int. J. Hydrogen Energy 41 (2016) 14952–14970, http://dx.doi.org/10.1016/j.ijhydene.2016.06.122.

[24] PowerCell Ab, PowerCell S2 Datasheet, n.d. http://www.powercell.se/wp-content/uploads/2017/05/S2-Data-Sheet.pdf (Accessed 28 August 2017).

[25] S. Enz, T.A. Dao, M. Messerschmidt, J. Scholta, Investigation of degradation effects in polymer electrolyte fuel cells under automotive-related operating conditions, J. Power Sources 274 (2015) 521–535, http://dx.doi.org/10.1016/j.jpowsour.2014.10.127.

Aalto-DD 110/2018
VTT SCIENCE 177

ISBN 978-952-60-8029-1 (printed)
ISBN 978-952-60-8030-7 (pdf)
ISSN 1799-4934 (printed)
ISSN 1799-4942 (pdf)

978-951-38-8642-4 (printed)
978-951-38-8641-7 (pdf)
2242-119X (printed)
2242-1203 (pdf)

Aalto University
School of Chemical Engineering
Department of Chemical and Metallurgical Engineering
www.aalto.fi

BUSINESS + ECONOMY

ART + DESIGN + ARCHITECTURE

SCIENCE + TECHNOLOGY

CROSSOVER

DOCTORAL DISSERTATIONS